UNIVERSITAT DE BARCELONA

# Building Human Spinal Cord Organoids (huSpineOrg) biomodels to study Neural tube defects

Jose Manuel Blanco Ameijeiras

PhD thesis

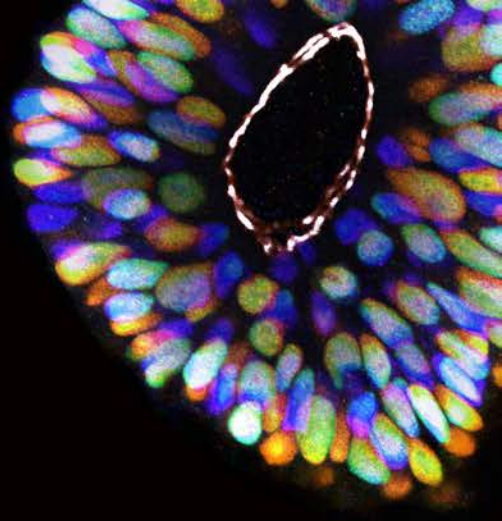

# Building Human Spinal Cord Organoid (huSpineOrg) biomodels to study neural tube defects

José Manuel Blanco Ameijeiras
Barcelona, 2022

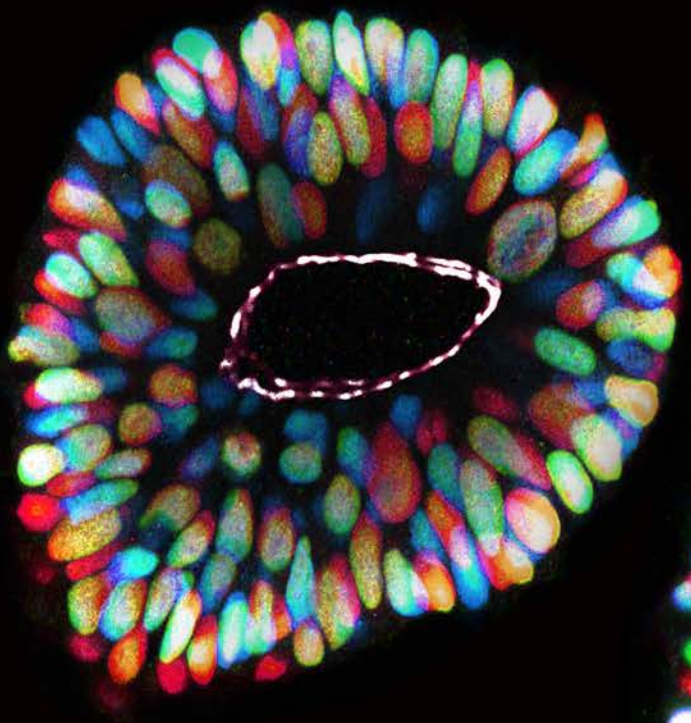

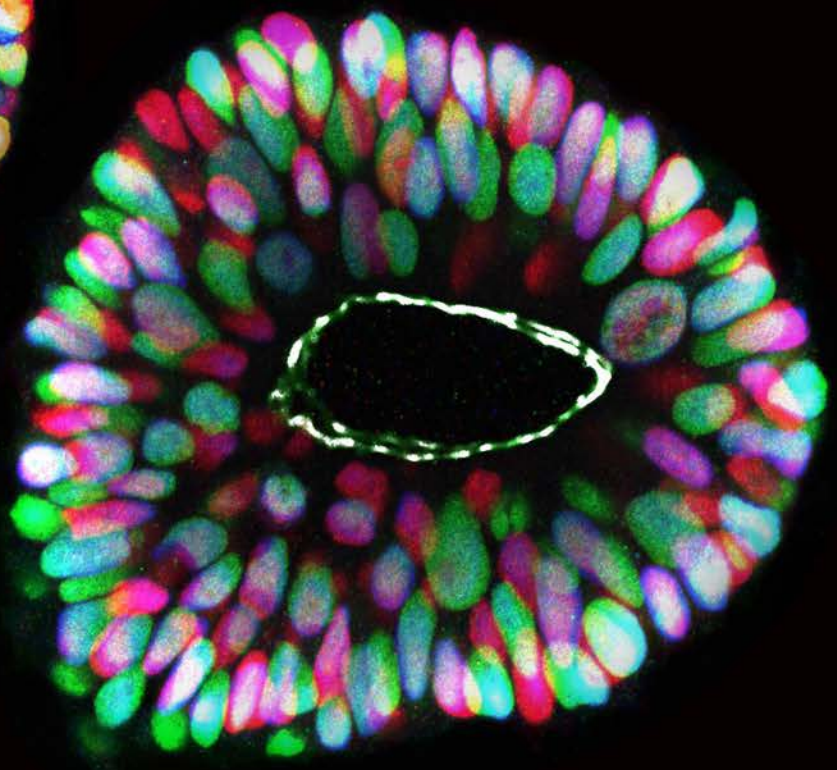

UNIVERSITAT DE BARCELONA

CSIC
CONSEJO SUPERIOR DE INVESTIGACIONES CIENTÍFICAS

Doctoral program in Genetics

Faculty of Biology, University of Barcelona

Research performed at the
Institute of Molecular Biology of Barcelona, CSIC

# Building Human Spinal Cord Organoids (huSpineOrg) biomodels to study neural tube defects

Thesis submitted by

**Jose Manuel Blanco Ameijeiras**

To obtain the

Doctoral degree by the University of Barcelona

Author: Director: Tutor:

Jose M. Blanco Ameijeiras Elisa Martí Gorostiza Florenci Serras Rigalt

Barcelona, December 2022

*"A razón non se come"*

Pepe

# Acknowledgements

Esta tesis supone el final de una etapa en la que siento que he crecido mucho, y no solo académicamente, sino como persona. Esta experiencia como doctorando me ha permitido encontrarme con muchas personas. Todas ellas, en mayor o menor medida han contribuido a este crecimiento, que más allá de los resultados que se resumen en este documento, es para mí lo más importante de esta tesis. A lo largo de estos años ha habido épocas mejores y peores. Agradezco mucho a la gente que ha estado acompañándome en ambas, a mis compañeros de laboratorio, pero también a mi familia y amigos que me han intentado convencer de que disfrutase de los buenos momentos y de que relativizase los malos.

En primer lugar, quiero darte las gracias, Elisa, mi directora de tesis, por haberme recibido en tu laboratorio para realizar esta tesis y por la confianza que has depositado en mí todos estos años. Con nuestros más y nuestros menos por el camino, y aunque muchas veces no hemos estado de acuerdo en absoluto, te agradezco sinceramente que en los momentos claves hayas sabido escucharme y que me hayas apoyado, cuando lo fácil quizás era no hacerlo.

A mis compañeros y excompañeros del laboratorio, muchas gracias por todos los momentos que hemos compartido durante estos años. Los vermuts, las excursiones, las cenas, las ferratas, el surf, los afterworks y la escalada se merecen una mención especial, pero sobre todo mil gracias por haber sido un gran apoyo y fuente de diversión.

A Gwen, por ser una fuente de inspiración y conocimiento infinita. Por ser siempre la voz de la razón que me hace ver las cosas desde una nueva perspectiva. Te he echado mucho de menos en el laboratorio estos últimos años.

A Sus, muchísimas gracias por tu paciencia, por estar siempre disponible para ayudar con cada cosa sea del labo o de la vida. Y por supuesto, muchísimas gracias por tu fichero naranja, la biblia de los protocolos.

A Luci, la persona que me introdujo en cultivos por primera vez, ahora yo soy el loquito de la limpieza y el orden. Creo que estarías tan sorprendida como orgullosa. Muchas gracias por todas las cosas que me has enseñado, pero sobre todo gracias por las risas (por favor, recordemos cuando te fuiste un finde a abrazar arboles con desconocidos). Me alegro muchísimo de haber compartido esta etapa contigo, eres genial.

A Ele, mi mentora (ojalá!), por recibirme con los brazos abiertos cuando llegué al labo. Por invitarme a un montón de planes y presentarme a un montón de gente majísima cuando aún no conocía a casi nadie en la ciudad (empezando por Fer, mi primer climbing buddy en Bcn). Gracias por ser esa persona que a las tantas de la mañana te pide piecito para colarse en la cabina del DJ. Pero sobre todo gracias por ser mi 'amica'.

A Pilar, aunque a veces me supere (sobre todo por las mañanas), muchas gracias por esa energía desbordante que desprendes, que, aunque no lo parezca, se me contagia un poco. Por ser tan buena compi y por todo el apoyo que me has dado. Y sobre todo NO-gracias por contarle a todo el edificio mi "incidente" con el BRA.

A Marsi, qué puedo decir, sin tu ayuda la mayor parte de esta tesis no existiría. Pero más allá de la parte científica, a nivel humano, muchas gracias por tu positividad y todos los buenos ratos que nos das en el labo. Gracias por tomarte tan en serio atender el teléfono, aunque creo que el pobre Samu ya no va tan tranquilo al baño como antes.

A Paula, gracias por tener siempre una sonrisa en la cara y por el ejercicio de supervivencia que compartimos con Marsi en los Pirineos.

Gracias también a las nuevas incorporaciones, Gloria y Axelle, y a los estudiantes que he conocido durante estos años. Especialmente a Giulia por compartir mis momentos de crisis en cultivos y recordarme siempre que 'todo saldrá bien'; y a Henri, por su autenticidad y ganas de aprender y porque sé que siempre tendré un gran amigo esperándome para ir a visitar Galápagos. A Murielle, por enseñarme la lección más valiosa de la tesis.

A todo el laboratorio de Mariona Arbonés. Gracias a Sonia, Isa, Álex, y especialmente a Mariajo, por todas las sesiones de terapia cuando vienen mal dadas y por hacerme de pared cuando los experimentos no salían. Gracias por intentar hacerme relativizar los problemas que me parecían inabarcables.

A Marian Martínez y todo su grupo: Raquel, Stella, Simona, Marta Vicioso, Marta Artés y Samu. Ha sido un placer compartir espacio todos estos años.

Al laboratorio de Nuria Verdaguer: Pablo, Cris, María, Sergi y especialmente a Diego, por toda su ayuda con los clonajes. Eres una enciclopedia de la biología molecular.

To the people from Mathias Lutolf's lab, who kindly hosted my internship and made me feel at home since the first moment. Special mention deserved by JiSoo, who taught me how to work with ESC, and cooked the best Korean bbq ever for me. I hope to see you soon again.

A Susana de la Luna y Borja Balbastre por todo el feedback y ayuda que me proporcionaron con el BioID.

A la gente de los afterwork, M&M (Marcos y Mónica), Alexis, Blanca, Laura, Marta Artés, Samu, Nuria, Mónica Salinas, María, Omar, Mar, Pilar, Paula. Aunque no iba a todos los que debería, siempre es un placer desconectar (y travestirme) con vosotros.

A Ramiro y Elena, por todos esos cafecitos de media mañana que venían tan bien para despejarse un poco.

A Elena Rebollo, por todas esas horas peleándonos con las pelis. Sin tu ayuda hubiese sido imposible poner a punto casi toda la microscopía que hay en esta tesis. También gracias a Antonia, por cada "Jose, bonito, ¿que tal?" que alegraba cada mañana.

No puedo terminar esta sección sin mencionar a Marcos, mi 'maestro'. Muchas gracias por las sesiones de escalada, baloncesto y paseos en bicicleta por Edimburgo. Tú me enseñaste que la ciencia es cacharrear y explorar. Y sobre todo me inculcaste que el motor de la ciencia tiene que ser la curiosidad y no el ego. Eres una persona excepcional, tendría que haber un clon tuyo en cada laboratorio del mundo.

A la gente de loquedigavarelamelapela, muchas gracias por todas esas cañas y pulgas de lomo y queso de media mañana, por las escapadas a Fonsagrada (aunque algunas salieron un poco caras), los biocelta-biodepor, las churrascadas y demás. Especial mención merecen los compimochos, Sergio y Martamon porque, aunque no nos veamos todo lo que me gustaría, ni respondo al WhatsApp todo lo rápido que debería, siempre estáis ahí y cuando nos juntamos es como si no hubiese pasado el tiempo.

A todos los integrantes de la ABSS, la liga de baloncesto más exclusiva del mundo, especialmente a Joni, Óscar y Andrés/Pip. Por todos esos playoffs perdidos, los ojos piratas, las faltas que no me pitáis (que no son pocas) y las bofetadas que vendrán.

A la gente de Vv, Mauro, Boris, Suso, Nardo, Samu, Lucas, Paco, Charly y Nava. Gracias por alegrarme tantos veranos, por todos los Naseiros y por todos los carritos. Sois gente excepcional.

A los fractales, por ser gente de la integración máxima, apoyarme a lo largo de estos años de tesis y sobre todo por ser la gente más fiestas que conozco.

A mi segunda familia, Lucas, Macaca y Kalvo. Gracias por aguantar mi mal humor los días malos, por hacerme terapia, por toda esa comida riquísima que me preparáis, por esos lolitos tontos, por todas esas horas de Anatomía de Grey, y por los "all bad". Gracias por atravesar la pared de Javi con un taladro, por ir pisando fuerte por la vida, por abollar la pared del salón de Urquinaona (nunca me perdonaré habérmelo perdido), por el champiñón en el bidé, por la tele a todo volumen porque el director así lo quería, e infinidad de cosas más... ¡Estoy deseando celebrar esta tesis con vosotros!

A María, antes de darte las gracias debo pedirte perdón por todos esos fines de semana en los que no podía hacer planes o llegaba tarde/me iba temprano para hacer experimentos. Muchas gracias por entenderme, apoyarme y quererme tanto. Somos personas muy diferentes, pero siento que me complementas a la perfección (cacahuetes).

To Fabrice, thanks a lot for your support both, emotional and logistic. Let's not forget that you managed to get me a house with jacuzzi in Lutry, and that is a plus.

A meus avós moitas gracias por aturarme de cativo, que ben sei que non debeu ser fácil criar a un anano chorón coma min. Gracias por ese chicle que me dabades cada mañan antes de ir á escola, por ese ovo que me poñiades no leite no inverno, e por levarme no carretillo cada vez que ibas á verdura. Gracias por facer de min un neno feliz e por seguir queréndome aínda que me faga moitas tatuaxes.

A meus pais. Estivérades lonxe ou perto, eu sempre vos sentín o meu lado e sígovos sentindo. Gracias por apoiarme sempre e ter esa fe cega en min. Vos ensináchesme moitas leccións, todas infinitamente máis importantes que as ESC, os organoides e os centrosomas. Mami, eres un exemplo de constancia e sacrificio. Cada día demóstrasme que nada é demasiado, que nada é imposible. A tua forza de vontade é infinita, e so espero que sexa xenético e me transmitiras unha pouca. Pepe, cando penso no amor, penso en ti. Cada dia da túa vida é unha demostración de amor incondicional. Non podería estar máis orgullo de que sexas meu pai.

Por ultimo, a miña irmán, Sonia. Moitas gracias por todos os consellos, por facerme os disfraces cando era pequeno, por todos eses días de entrenar por videochamada, por facer equipo comigo fronte o pavo. Gracias por facer mellor e mellores a todo e todos os que te rodean. Es a miña persoa favorita.

# Abstract

The Central nervous system (CNS) originates from the coordinated events that result into neural specification and the morphogenic events that shape the neural tube (NT). Then, the embryonic NT should grow and generate all the cell diversity present in the healthy organ. The morphogenic events that shape the NT occur in two consecutive, radically different processes referred as primary and secondary neurulation, that can be followed at different anterio-posterior levels in the Spinal cord (SpC). The posterior NT is formed by secondary neurulation, in a process concomitant to body axis elongation and mediated by the specification of nueromesodermal progenitors (NMPs). Defects in this process lead to caudal neural tube defects (NTDs).

In the first chapter of this thesis, a new human 3D *in vitro* model for posterior SpC is set up. In these human organoid models, the neural specification, the morphogenesis of the NT, and its grow can be followed. Here, it is characterized a human organoid model were human embryonic stem cells (hESC) are guided into NMPs, expressing *SOX2* and *BRA* and then into neural progenitor cells (NPCs), which maintain the *SOX2* and lose *BRA* expression as it happens *in vivo*. Moreover, the NPCs are organized as an epithelium surrounding a central lumen. NPCs locate the centrosome and cilia at the lumen surface, where the polarity complexes are organized mimicking the polarity features of NPCs characterized in vivo. Additionally, in parallel to this epithelialization, the cell rearranges that shape the hollow NT formation in vivo, like the cell intercalation driving lumen resolution, can be followed in this organoid model.

In the second chapter of this thesis, a screening to identify new mature centrosome components that would be potentially control the NPCs proliferation/differentiation rates was done independently with an *in vivo*, using the chick embryo as model, and an *in silico* approach. Unfortunately, the *in vivo* approach faced technical limitations intrinsic of the chick embryo model that prevent any successful identification of new candidates. However, the *in silico* approach provided a list of candidates to start their functional analysis.

# Resumen

El desarrollo del sistema nervioso central (SNC) depende de la especificación del tejido neural y una serie de eventos morfogénicos que lo organizan en un tubo neural (NT). A partir de ahí, ese NT deberá crecer y generar toda la diversidad celular que presenta el organo sano y le confiere su funcionalidad. Los eventos morfogénicos que dan forma al NT ocurren en dos procesos consecutivos radicalmente diferentes denominados neurulación primaria y secundaria, que pueden seguirse a diferentes niveles antero-posteriores en la médula espinal (SpC). El NT posterior se forma por neurulación secundaria, en un proceso simultaneo a la elongación del embrión y mediado por la especificación de progenitores nueromesodérmicos (NMP). Los defectos en este proceso conducen a defectos del tubo neural caudal (NTDs).

En el primer capítulo de esta tesis, se establece *in vitro* un nuevo modelo 3D de SpC posterior humana. En estos organoides, se puede seguir la especificacion neural, los procesos morfogeneticos de la formación del NT y su crecimiento. Aquí, se caracteriza un modelo de organoides humanos en el que las células madre embrionarias humanas (hESC) se guían hacia NMP, expresando *SOX2* y *BRA*, que a continuación se diferencian en células progenitoras neurales (NPC). Estas últimas mantienen la *SOX2* y pierden la expresión de *BRA* como sucede *in vivo*. Además, los NPC organizan un epitelio que rodea un único lumen central. Los NPC presentan su centrosoma y cilio en la superficie del lumen, donde los complejos de polaridad se organizan mimetizando las características de polaridad apical observadas *in vivo*. Además, en estos organoides se pueden seguir los reordenamientos celulares de los procesos morfogénicos que eventualmente forman un tubo neural hueco.

En el segundo capítulo de esta tesis, se realizó un *screening* para identificar nuevos componentes de maduración del centrosoma que potencialmente controlarian el equilibrio de proliferación/diferenciación de los NPC. Este *screening* se realizó de forma independiente *in vivo*, utilizando el embrión de pollo como modelo, e *in silico*. Desafortunadamente, el enfoque *in vivo* enfrentó limitaciones técnicas intrínsecas del modelo que impidieron la identificación de nuevos candidatos. Sin embargo, el enfoque *in silico* proporcionó una lista de candidatos sobre los que comenzar un análisis funcional.

# Contents

# Glossary

BB- Basal body

BM- basement membrane

BMP- Bone Morphogenetic Proteins

CLE- caudal lateral epiblast

CNS- Central nervous system

CTCF- Corrected total cell fluorescence

DA- Distal appendage

DAB- Distal appendage blade

DAM- Distal appendage matrix

DCMP- daughter centriolar maturation proteins

DCPs- daughter centriolar proteins

ECM- extracellular matrix

FP- Floor plate

GOF- gain of function

hESC- human embryonic stem cell

hpe- Hours post electroporation

ImC- Y-linkers intermediate components

InC- Y-linkers inner componets

INM- Interkinetic nuclear migration

IP- immunoprecipitation

iPSC- induced pluripotent stem cell

LOF- loss of function

MCPH- autosomal recessive primary microcephaly

MET- mesenchymal-to-epithelial transition

MET- mesenchymal-to-epithelial transition

MP- Mesodermal progenitor

MTOC- Main microtubule-organizing centre

MTs- Microtubles

MZ- Mantle zone

NMP- Neuromesodermal progenitor cell

NPC- Neural progenitor cell

NT- Neural tube

NTDs- Neural tube defects

OC- Y-linkers outter componets

PCM-Pericentriolar material

RA- Retinoid acid

RP- Roof plate

SDA- Subdistal appendage

SHH- Sonic Hedgehog

SpC- Spinal Cord

TGF$\beta$- Transforming Growth Factor beta

TZ- Transition zone

VZ- Ventricular zone

$\gamma$-TuRC- $\gamma$-tubulin ring complex

# Introduction

## Building the CNS during embryonic development

### Definition of the SpC

The central nervous system (CNS) is comprised of the brain and spinal cord (SpC). Collectively, it coordinates our conscious and unconscious bodily processes, such as cognition, movement, emotion, sensation, respiration and learning. Building the CNS during embryonic development requires a series of sequential and coordinated events including; (a) the formation of a neural tube (NT), (b) the growth of the embryonic organ to acquire the proper size, and (c) the generation of cell diversity to acquire the vast array of neural cells requite to build a functional organ. In this PhD thesis, the two first processes had been studied using the SpC as tissue model.

The SpC is generated over an extended period in a head to tail sequence, therefore, it has been an ideal model for studying the temporal sequence of the different events that control NT formation. Besides, as it will be discussed in the following section, early in development the progenitor cells that form the NT are conserved all along the CNS. Thus, CNS growth and cell diversity generation mechanisms can be assessed in the SpC. Decades of work with different vertebrate animal models has provided a detailed understanding of many aspects of the molecular, cellular and morphogenetic aspects underlying SpC generation, development, function and repair. All this knowledge pave to way for the optimization of new human SpC organoid systems for study the organ formation and physiology in a human context.

### Embryonic origin of the SpC: the NT, a conserved structure along the Anterior to Posterior axis

Along the entire anterio-posterior axis of the CNS, the lumen of the NT is covered by a single type of neuroepithelial cells, termed Neural Progenitor Cell (NPC), from which all neural cell types will be generated (Figure 1A). Each cell extends a basal process to the

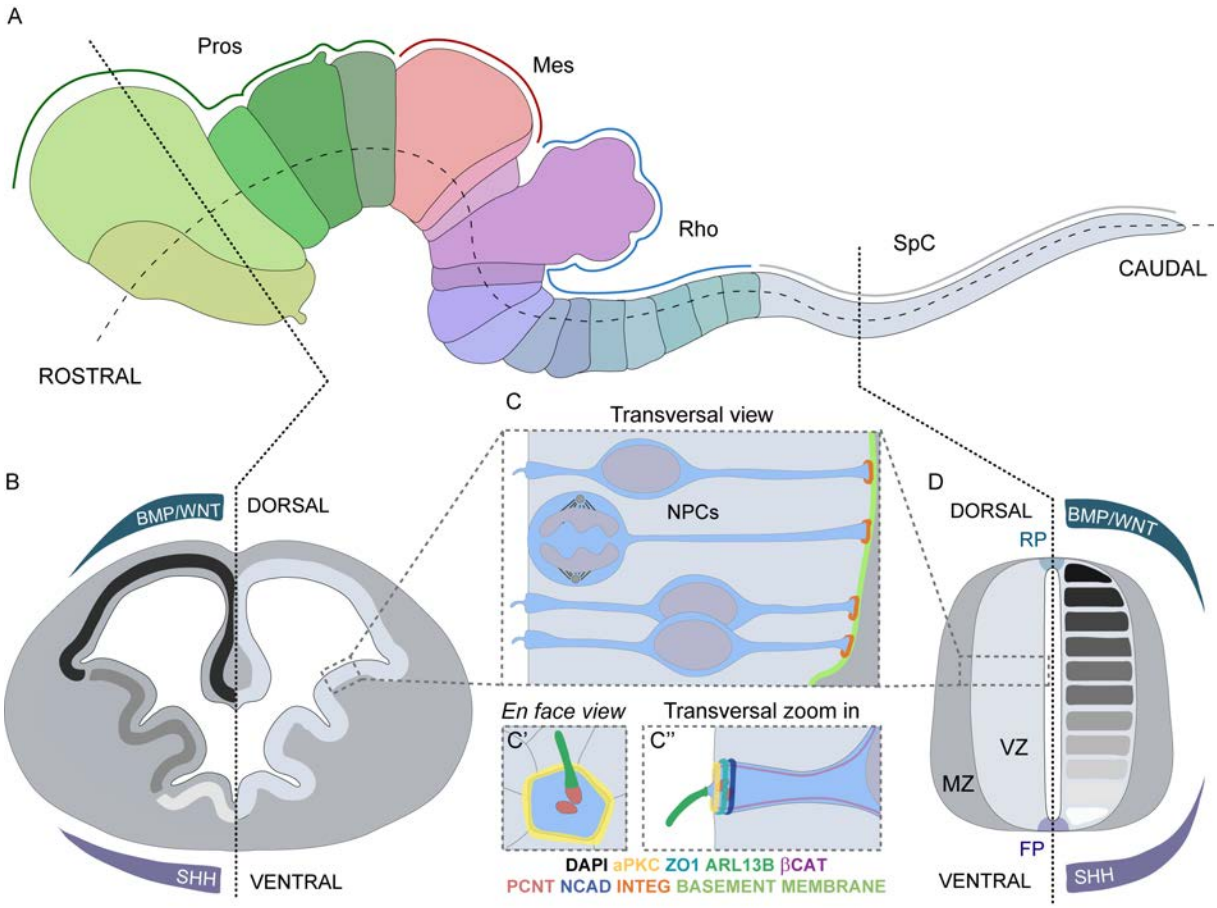


**Figure 1: Early in development, the embryonic CNS is composed by NPCs all along the anterio-posterior axis. (A)** Diagram of a vertebrate embryo CNS, showing rostral to caudal regionalization into the forebrain (Pros), midbrain (Mes), hindbrain (Rho), and the spinal cord (SpC). **(B)** Diagram of a transverse section through the telencephalon. The main telencephalic subdivisions along the dorsal ventral axis are generated in response to dorsal BMP/WNT and ventral SHH patterning signals. **(C)** Detailed view of dividing NPCs that occupy the ventricular zone (VZ) lining the entire neural tube lumen. NPCs are present as elongated cells that contact both the ventricle surface and the BM, with their nuclei adopting distinct positions along the apico-basal axis. **C'** *En face* view drawing of the NPC apical end foot. **C' '** Transversal zoom in drawing of the NPC apical foot. DAPI (gray), aPKC (yellow), ZO1 (cyan), ARL13B (green), $\beta$CAT (purple), PCNT (red), NCAD (dark blue), INTEGRINS (orange), and BM (pistachio). **(D)** Diagram showing a transverse section through the SpC. The progenitor populations generated along the dorsal-ventral axis, highlighted with a greyscale on the right, are established by the conserved activity of extrinsic secreted signals (dorsal BMP/WNT and ventral SHH). The relative position of NPCs (in the VZ) and post-mitotic neurons (in the mantle zone, MZ) is shown. FP, floor plate; RP, roof plate. Adapted from (Saade *et al.*, 2018).

basement membrane (or basal lamina) (BM) and an apical process to the lumen of the NT, and their nuclei adopt distinct positions along the apico-basal cell axis, according to the progression of the cell cycle (Figure 1C). Their nuclei move in a basal direction during $G_1$ phase of the cell cycle, while apical nuclear migration happens during $G_2$ phase to organize all mitosis at the luminal surface. Collectively, these oscillatory nuclear movements are referred to as interkinetic nuclear migration (INM) (Sauer, 1935; Langman, Guerrant and Freeman, 1966; Taverna and Huttner, 2010; Molina and Pituello, 2017; Saade *et al.*, 2018). The rationale behind this striking feature of neuroepithelial cells has been classically explained by the capacity to pack more progenitor cells within a limited space (Sauer, 1935; Langman, Guerrant and Freeman, 1966). Although, numerous examples of INM perturbations correlating with neurogenesis modifications are present in the literature (Murciano *et al.*, 2002; Baye and Link, 2007; Del Bene *et al.*, 2008; Del Bene, 2011; Formosa-Jordan *et al.*, 2013; Hu *et al.*, 2013), whether INM also has an instrumental role in determining the cell fate of neural progenitors remains an open question.

NPCs are fully apico-basally polarized cells, with intercellular junctions in their apical pole and a basal end foot contacting the BM. They present apical junctional complexes composed by discrete micro-domains where NCAD (adherens junction protein) and the ZO1/OCLN complex (tight junction proteins) occupy internal positions, while the PAR/aPKC complex concentrates more apically (Aaku-Saraste, Hellwig and Huttner, 1996; Chenn *et al.*, 1998; Afonso and Henrique, 2006; Marthiens and Ffrench-Constant, 2009) (Figure 1C' and 1C' '). On the other hand, INTEGRINS are basally localized contacting the BM mainly composed of LAMININ, FIBRONECTIN, among other protein content (Figure 1C).

Although later in development, cephalic NPCs are organized into two germinal layers with different proliferation capacities (Wilsch-Brauninger, Florio and Huttner, 2016; Florio, Borrell and Huttner, 2017; Heide, Long and Huttner, 2017; Johnson and Walsh, 2017) (Figure 1B); at early developmental stages, the key features of NPC expansion are conserved between brain and SpC (Saade *et al.*, 2018) (Figure 1D). Besides, during body axis elongation CNS growth is not only due to NPCs proliferation, but also to cell rearrangements (Bénazéraf and Pourquié, 2013; Neijts *et al.*, 2014; Loganathan *et al.*, 2016; Steventon *et al.*, 2016), that mainly happen at the caudal end of the SpC in coordination with body axis elongation.

## Differential genetic NPCs specification mechanisms in anterior and posterior regions

Even though the final fate and cell properties are indistinguishable, the mechanisms of genetic specification of NPCs differ depending on the anterior-posterior level. The pre-

vailing view of vertebrate CNS formation proposes two different embryonic origins for making anterior and posterior CNS progenitors; while the anterior neural plate is generated by neural induction in the medial anterior ectoderm (Figure 2A), the posterior neural plate generation is mediated by progenitor cells with a dual fate, the neuromesodermal progenitor cells (NMPs) (Tzouanacou *et al.*, 2009) (FigureFigure 2B).

In the anterior regions of the CNS, NPCs are generated through direct neural induction of ectodermal tissue in middle dorsal ectoderm. Several lines of evidence demonstrate a crucial role for SMAD signaling during neural induction. BMP and TGF$\beta$ inhibitors had been identified as a critical neural-inducing factors in both amphibian and mammalian models (Marshal *et al.*, 1991; Hemmati-Brivanlou and Melton, 1992; Smith and Harland, 1992; Sasai *et al.*, 1994; Valenzuela *et al.*, 1995; Patel *et al.*, 1996; Connolly, Patel and Cooke, 1997; Stottmann *et al.*, 2006; Ybot-Gonzalez *et al.*, 2007; Lee *et al.*, 2007; Elkabetz *et al.*, 2008; Eom *et al.*, 2012). Both BMP and TGF$\beta$ signalling inhibition come from subjacent tissues, the notochord or endoderm in the most anterior regions, and had a central role in the neutralization of the ectoderm to form the anterior NT (Figure 2A').

NMPs arise within the caudal lateral epiblast (CLE) through a mechanism that is separable from that which establishes neural fate in the anterior epiblast (Gouti, Metzis and Briscoe, 2015; Henrique *et al.*, 2015). NMPs are responsible for the embryo elongation, they co-express *SOX2* and *BRA* showing a dual neuro-mesodermal fate (Olivera-Martinez *et al.*, 2012; Gouti *et al.*, 2014, 2017; Henrique *et al.*, 2015; Tsakiridis and Wilson, 2015). As such those cells give rise to both the NT and the surrounding mesodermal tissues, during body axis elongation (Figure 2B). Both WNT and FGF signaling have been implicated in *BRA* induction in NMPs (Yamaguchi *et al.*, 1999; Martin and Kimelman, 2008), elongation of the body axis (Aulehla *et al.*, 2003; Olivera-Martinez and Storey, 2007; Wilson, Olivera-Martinez and Storey, 2009), and in posteriorizing cells by inducing the *CDX* transcription factors that promote the expression of more posterior *HOX* genes (van den Akker *et al.*, 2002; Nordström *et al.*, 2006; van de Ven *et al.*, 2011; Mazzoni *et al.*, 2013; Amin *et al.*, 2016). RA may also have a role in the establishment of NMPs, since primitive streak and node cells transiently express the retinoic acid (RA)-synthesizing enzyme ALDH1A2 (Ribes *et al.*, 2009) and mouse embryos lacking ALDH1A2 have defects in axis elongation (Niederreither *et al.*, 1999). Moreover, inhibition of BMP signaling is required for *SOX2* transcription in the CLE (Takemoto *et al.*, 2006). In mouse and chick embryos, some BMP and TGF$\beta$ inhibitors (NOGGIN, CHORDIN and FOLLISTATIN) are expressed in the anterior primitive streak, emerging notochord and newly formed somites close to posterior neural tissue (Albano *et al.*, 1994; Liem, Jessell and Briscoe, 2000; Chapman *et al.*, 2002).

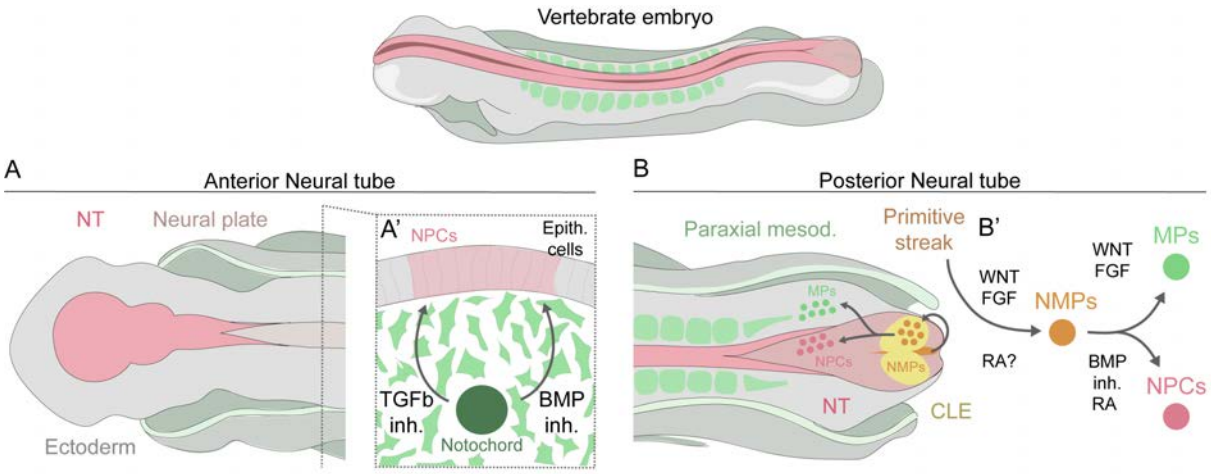


**Figure 2: NPCs genetic specification mechanism is different in anterior and posterior NT. (A)** Drawing of the dorsal view of an anterior embryo region showing the NT closed in the most anterior cephalic vesicles and the open neural plate in the immediate caudal region. **A'** Shows a drawing of a transversal section where the ectoderm is represented in gray and the neural plate in pink. Inhibition signals from the notochord to orchestrate the neural plate specification in the medial ectoderm. **B** Drawing of the dorsal view of an anterior embryo region showing the primitive streak (orange) and the CLE (yellow) responsible of the embryo elongation in the most posterior region. There, the NMPs specified to then commit with the neural (pink) or the mesodermal (green) lineages depending on the signal they sense. **B'** Shows a schematic representation of the different signals involved in the NPCs specification and commitment.

After NMPs specification, in the caudal NT, a subset of them must commit with the neural lineage to give rise to the NPCs that will form the NT *per se.* Those will downregulate *BRA* while maintaining *SOX2* expression. Conversely, WNT signaling promotes the NMPs commitment with the mesodermal lineage (mesodermal progenitors, MPs) (Martin and Kimelman, 2012; Garriock *et al.*, 2015), as *Wnt3a* loss of function (LOF) experiments in both mice and zebrafish lead to a depletion of mesodermal tissue (Yoshikawa *et al.*, 1997; Martin and Kimelman, 2008; Garriock *et al.*, 2015). In opposition to WNT and FGF signaling, RA synthesized in neighboring paraxial mesoderm mediates the transition to NPCs, repressing expression of *Fgf8*, *Wnt8a*, *Wnt8c* and *Wnt3a* (Shum *et al.*, 1999; del Corral *et al.*, 2003; Sirbu and Duester, 2006; Olivera-Martinez and Storey, 2007; Cunningham *et al.*, 2015) (Figure 2B').

## Morphogenesis of the SpC; primary and secondary neurulation

The morphogenic events that shape the vertebrate NT occur in two consecutive, radically different processes referred as primary and secondary neurulation, that can be followed at different anterio-posterior levels in the SpC. Building of the anterior NT is initiated soon

after gastrulation by primary neurulation, while the posterior NT is formed by secondary neurulation, in a process that is more extended in time and it is concomitant to body axis elongation (Greene and Copp, 2014). The primary and secondary NT join end-to-end (Shum and Copp, 1996). The border between primary and secondary neurulation is defined by the position where posterior neuropore is closed.

**Primary neurulation**

During primary neurulation a subgroup of the ectodermal cells are transformed and organized into a hollow nerve cord, the neural tube. The morphogenic process has been divided in four consecutive and partially overlapping events: (1) formation of the neural plate; (2) shaping of the neural plate; (3) bending of the neural plate to form the neural groove and the neural folds; and (4) fusion of the neural folds to close the neural groove and form the neural tube (Smith and Schoenwolf, 1997) (Figure 3A). Although there are slight interspecific differences, these basic events of primary neurulation are conserved in amphibians, reptiles, birds, and mammals (Gallera, 1971; Smith and Schoenwolf, 1991; Morriss-Kay, Wood and Chen, 1994; Peeters *et al.*, 1998; Davidson and Keller, 1999). Primary neurulation also presents some peculiarities dependent on the anterio-posterior level of the tissue, due to the anatomical differences of the final CNS (Shum and Copp, 1996; Lowery and Sive, 2004).

(1) The formation of the neural plate is induced by the notochord (and in the most anterior levels by the endoderm). Neural plate formation begins with a thickening of the ectoderm that will become the neural plate. Cells in that region increase in height, undergo pseudostratification and begin to express unique molecular markers (Smith and Schoenwolf, 1989, 1997; Keller *et al.*, 1992) (Figure 3A').

(2) Subsequently, the lateral neural plate undergoes anterior-posterior lengthening, mediolateral narrowing and further apico–basal thickening. On the contrary, the midline neural plate anchors to the underlying notochord and its cells become shorter and wedge-shaped. This shaping events set the conditions so upon bending, the neural plate will generate a tubular-like structure instead of an spherical vesicle (Keller, Shook and Skoglund, 2008) (Figure 3A'').

(3) The bending of the NT begins the internalization of the neural plate, forming in most of the cases an open neural tube, hemitubular structure partially rolled up but where the folds have not yet fused (Lowery and Sive, 2004) (Figure 3A'''). There are different strategies to accomplish it, depending on the organism or even on the antero-posterior level (Schroeder, 1970; Sakai, 1989; Keller, 1991; Smith and Schoenwolf, 1997; Davidson and Keller, 1999; Lowery and Sive, 2004).

(4) Primary neurulation finishes with the closure of the NT, as the epidermal ectoderm

detaches from the adjacent neuroepithelium and fuses achieving the internalization of the neural tissue. Concomitantly, the two detached neural folds from both sides fuse together beneath the epidermal ectoderm, establishing the RP of the NT (Mak, 1978; Lawson and England, 1998). In the embryo, NT closure initiates at distinct closure points and progresses from them by zipping the open neural groove, in both anterio-posterior and posterior-anterior directions (Cearns *et al.*, 2016) generating the final NT (Figure 3A’’’’).

### Secondary neurulation

Although the morphogenesis of the nervous system is a major area of research, so far the majority of studies have been focused on the primary neurulation while secondary NT formation remains largely unknown. The posterior region of the embryo derives from tissue of the undifferentiated tail bud by a process of body axis elongation, including the caudal elongation of the NT, after more cranial regions have developed (Holmdahl, 1925; Schoenwolf and Delongo, 1980; Nakao and Ishizawa, 1984; Griffith, Wiley and Sanders, 1992). The tail bud is composed of NMPs, which at the onset of secondary neurulation are mesenchymal cells, as they show no epithelial apico-basal polarity, although they express the adherens junction marker *NCAD* (Duband, 2010).

Later in the 80’s, using scanning and transmission electron microscopy as well as light microscopy of plastic sections (Schoenwolf and Delongo, 1980; Schoenwolf and Kelley, 1980), the four basic morphogenetic processes involved in secondary neurulation were established using the chick embryo as a model: (1) NMPs condense to form a solid medullary cord, (2) undergo mesenchymal-to-epithelial transition (MET), (3) open small lumina and (4) cavitate to finally form a single epithelial tube (Criley, 1969; Griffith, Wiley and Sanders, 1992; Catala, Teillet and Le Douarin, 1995; Colas and Schoenwolf, 2001; Shimokita and Takahashi, 2011) (Figure 3B).

(1) Chick secondary neurulation starts with the aggregation of mesenchymal tail bud cells on the midline to form a densely packed cylinder of cells, the medullary cord, in a process that occurs in an anterior-posterior fashion (Schoenwolf and Delongo, 1980; Catala, Teillet and Le Douarin, 1995; Catala *et al.*, 1996; Yang *et al.*, 2003) (Figure 3B’).

(2) Subsequently, the segregated NMPs undergo MET, that involves the formation of a layer of extracellular matrix (ECM) between adjacent organ rudiments (deposit of BM), the formation of intercellular junctions and the establishment of apico-basal cell polarity (Schoenwolf and Delongo, 1980; Yang *et al.*, 2003; Shimokita and Takahashi, 2011). The first cord cells to undergo MET are located dorsally and peripherally contacting the recently formed BM, and subsequently, the epithelializa-

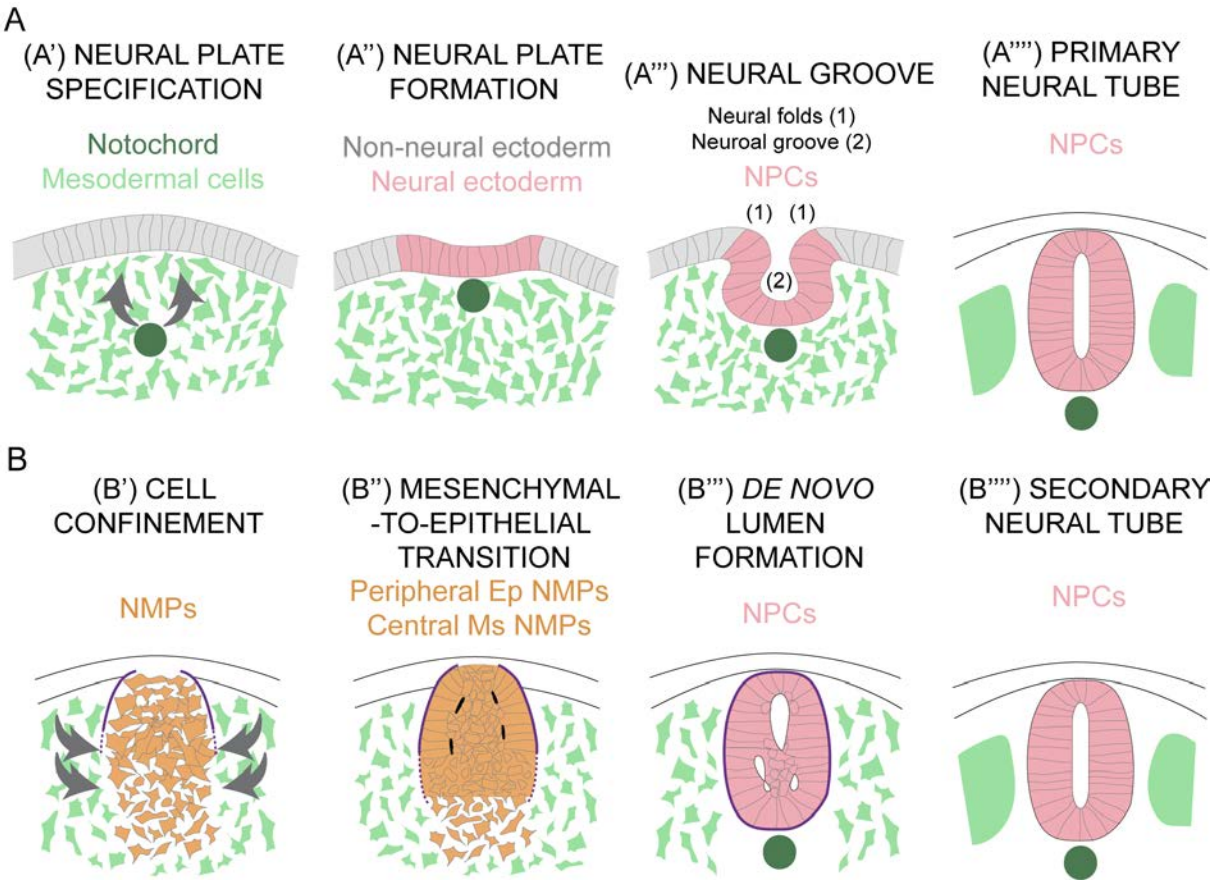


**Figure 3: Primary and Secondary neurulation processes.** **(A)** Drawing of transversal sections of an embryo undergoing primary neurulation. **(A')** The notochord produces the molecular signals that will induce the neural commitment of the ectoderm above. **(A'')** Once, the neural plate is specified, neural cells undergo a morphological transformation that allows the beginning of the neural plate bending. **(A''')** The folding of the NT begins the internalization of the neural plate, forming a central neural groove and two lateral neural folds. **(A'''')** Finally, NT closes with the fusion of the neural folds underneath the epidermal ectoderm. **(B)** Drawing of transversal sections of an embryo undergoing secondary neurulation. **(B')** NMPs are condensed and confined in the center of the tissue forming a solid medullary **(B'')** Cells located dorsally and at the periphery of the medullary cord undergo the MET, although the cells in the center of the tissue remain mesenchymal and small lumina open up between the peripheral epithelial and central mesenchymal cell populations. **(B''')** The small cavities formed grow as the MET progresses. **(B'''')** Finally those cavities coalesce to form a neural tube with a single central lumen.

tion propagates ventrally as the BM deposit progress. Small intercellular junctions first form at the basal outer ends of the elongating peripheral cells and then at their apical inner ends (Schoenwolf and Delongo, 1980; Schoenwolf and Kelley, 1980). The centrally located cells retain mesenchymal features, characteristic of the undifferentiated tail bud (Figure 3B'').

(3) Small lumina soon form between the peripheral epithelial and the central mesenchymal cell populations. These small lumina vary in number, size, shape and dorso-ventral location, even though the first lumen often appears dorsally displaced (Schoenwolf and Delongo, 1980) (Figure 3B''').

(4) Finally, cavities coalesce to form a central single lumen. For that to happen, central cells must be cleared from the luminal space (Schoenwolf and Delongo, 1980) (Figure 3B''''). The clearance mechanisms of the central cells had been recently reported to be mediated by central cells intercalating in the epithelium (Gonzalez-Gobartt *et al.*, 2021).

Although the major conclusions have been drawn from studies in chick (Schoenwolf and Delongo, 1980; Shimokita and Takahashi, 2011; Dady *et al.*, 2014), secondary neurulation has been also studied in both mice and human embryos (Schoenwolf, 1984; Nievelstein *et al.*, 1993; O'Rahilly and Muller, 1994; Saitsu *et al.*, 2004; Shum *et al.*, 2010).

A comparative analysis of those studies reveals that the precise position of the caudal neuropore, the place where primary and secondary NTs fuse, is variable in different organisms. In human embryos, that junction is apposed at the lumbosacral level (O'Rahilly and Muller, 1994, 2002; Saitsu *et al.*, 2004; Saitsu and Shiota, 2008). Likewise, the caudal neuropore locates at the transition from the thoracic to the lumbosacral vertebrae in chick and quail embryos (Criley, 1969; Catala *et al.*, 1996; Le Douarin, Teillet and Catala, 1998; Dady *et al.*, 2014). On the contrary, secondary neurulation only occurs at the level of the tail in mice embryos (Schoenwolf, 1984; Nievelstein *et al.*, 1993; Shum *et al.*, 2010). Besides, contrary to other amniotes like mice, both types of neurulation can be observed in parallel in the developing human embryo (Muller and O'Rahilly, 1987; O'rahilly and Muller, 1994; Nakatsu, Uwabe and Shiota, 2000; O'Rahilly and Muller, 2002). Finally, in the human junctional region, tail bud mesenchymal cells are incorporated into the ventral part of the primary neural tube by MET, an event that has also been observed in developing chick embryos, but has not been reported in mice embryos (Saitsu and Shiota, 2008; Dady *et al.*, 2014).

### Neural tube defects

Neural tube defects (NTDs) are severe birth defects of the CNS due to a failure in the process of neurulation. They affect an average of 1 in every 1000 established pregnancies

worldwide (Morris *et al.*, 2016). Around 30% of individuals with birth defects die before the first year of life (Malcoe *et al.*, 1999; Dolk, Loane and Garne, 2010). Surviving individuals beyond one year of age are often destined for a life of ill health with repeated medical and surgical interventions. NTDs are classified depending on the degree of exposure of the neural tissue to the amniotic fluid into open and closed NTDs.

Open NTDs result from a failure of primary neurulation leading to the exposure of the neuroepithelium and its degeneration *in utero* and loss of neurological function below the lesion level. The severity of open NTDs vary with the level of the body axis affected (Copp and Greene, 2013; Copp *et al.*, 2015).

Closed NTDs occur when secondary neurulation is disturbed. In this case, the defects are skin covered and not exposed to the external environment. They range from the asymptomatic spina bifida occulta to the more severe closed spinal dysraphism, in which the distal spinal cord is tethered to surrounding non-neural tissues. It has been hypothesized that spinal cord tethering arises from faulty cell specification of neural and mesodermal lineages (Copp *et al.*, 2015).

NTDs have a multifactorial aetiology, involving multiple genes and several environmental factors. Genetic factors account for 70% of the variance in neural tube defects prevalence (Leck, 1974) and the recurrence risk for siblings increases compared to the general population and gradually decreases in more distant relatives. The best-known non-genetic factor is diminished folate one-carbon metabolism or availability (Burren *et al.*, 2008).

## Dorsal–Ventral Patterning of the NT; the role of morphogenetic signals and the impact on the generation of cell diversity

Once the genetic neural specification and the tissue dynamics collectively coordinate the formation of a hollow NT, the NPCs progressively acquire different identities along the dorsal–ventral axes of the NT. This patterning event allows the generation of the tremendous variety of neuronal and glial cells that compose the functional vertebrate CNS. Since the SpC is the anatomically simplest and most conserved region of the vertebrate CNS, it has been instrumental in the understanding of the patterning mechanisms within the growing organ.

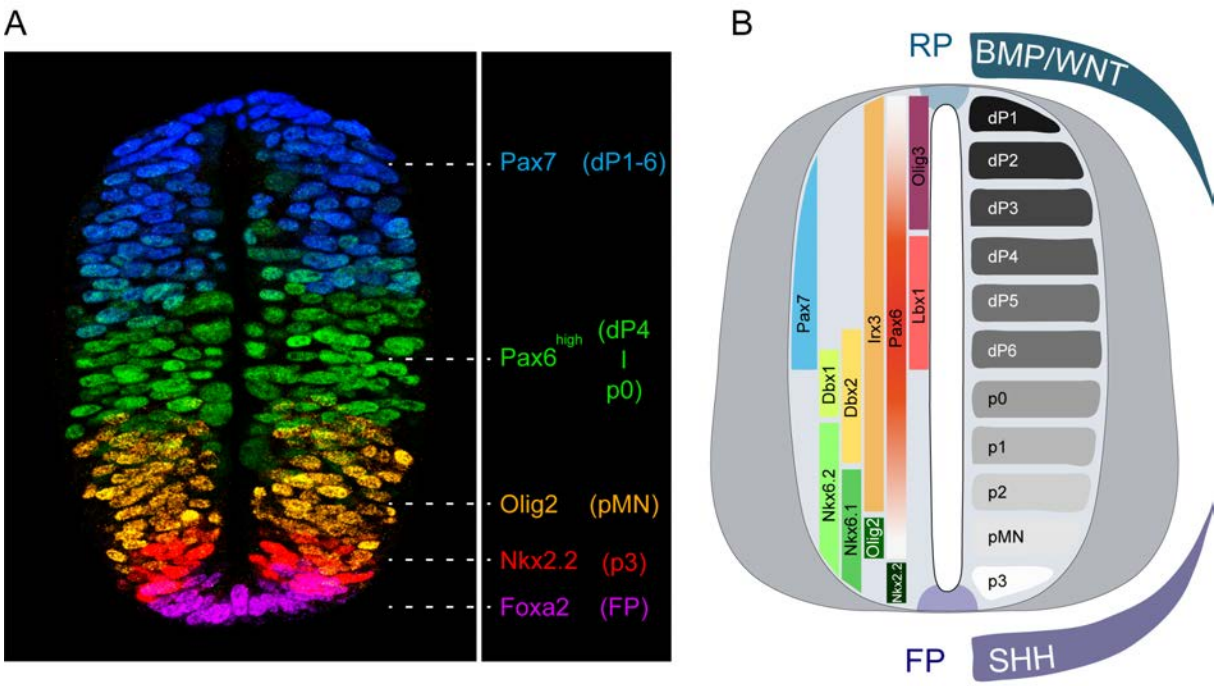


**Figure 4: Dorsal–ventral patterning of the vertebrate developing spinal cord at early stages. (A)** Photographic reconstruction of immunostainings performed on chick neural tube sections at HH16, showing how combinations of expression of progenitor proteins subdivide the neural tube into distinct domains. **(B)** Schematic representation of a transversal section of a chick neural tube at stage HH16. Left side shows expression of several ventral and dorsal progenitor proteins patterning the neural tube along the DV axis. Right side presents the subdivision of the neural tube into 11 distinct domains of neural progenitors, including (from ventral to dorsal): p3, pMN, p2-0 and dP6-1. Image adapted from (Le Dreau and Marti, 2012).

The NPCs acquisition of a specific neural cell fate depends on their initial spatial coordinates within the neural plate, which defines their exposure to specific local environmental signals that progressively restrict its developmental potential (Le Dréau and Martí, 2012). Those local signals are proteins with morphogenetic activities secreted from two opposed signaling centers: (1) Sonic Hedgehog (SHH) from the ventral FP, and (2) members of WNT and the BMP families from the dorsal RP (Patten and Placzek, 2002; Le Dreau and Marti, 2012). However, additional activities have also been assigned to members of TGF$\beta$ family (Pituello, Yamada and Gruss, 1995; Liem, Tremml and Jessell, 1997; Garcia-Campmany and Marti, 2007) as well as RA (del Corral *et al.*, 2003; Novitch *et al.*, 2003; Wilson and Maden, 2005).

These local signals direct cell fate by activating or repressing the expression of determinants of the dorso-ventral patterning, which, in turn, control the genetic network for the specific function of each neural cell population. Determinants of dorso-ventral identities include members of the homeodomain and the basic-helix–loop–helix families of transcrip-

tion factors (Figure 4A, B). As the result of these patterning events, the developing SpC is divided into 11 discrete domains of NPCs: five ventral domains (from ventral to dorsal, p3, pMN, p2-0) and six dorsal domains (from dorsal to ventral dP1–6) (Figure 4B). Each of them is determined by a particular transcription factor code, that determines the neuronal subtype progeny they will produce (extensively reviewed in Le Dreau & Martí, 2012) (Figure 4B).

## Growth of the NT; the role of specialized modes of division of NPCs and the impact on tissue growth

Growth of the embryonic NT requires a finely tuned balance between the different modes of divisions that NPCs undergo: (1) symmetric proliferative divisions ensure expansion of the progenitor pool by generating two daughter cells with identical progenitor potential, (2) asymmetric divisions generate one daughter cell with progenitor potential and one daughter cell with a more restricted potential, which is then committed to neuronal differentiation, and (3) symmetric neurogenic divisions depletes the progenitor pool by generating two daughter cells committed to neuronal differentiation (Saade *et al.*, 2013; Le Dreau *et al.*, 2014). Early in development the symmetric proliferative divisions are dominant to allow the expansion of the NPCs population. Later on, once the NPCs pool had reached the critical size to generate all the neural cells required to form a functional and healthy CNS, the neurogenic divisions prevail to guarantee the generation of neurons needed for proper functioning (Saade *et al.*, 2013; Le Dreau *et al.*, 2014). Thus, a premature switch from the symmetric proliferative to the asymmetric neurogenic mode of division has dramatic effects on the CNS growth and function.

Interestingly, cell division in general is intrinsically asymmetric as a consequence of differences in the centrosomes that are passed on to the daughter cells since, before entering mitosis, the centrosome replicates in a semi-conservative manner, forming one centrosome that retains the mother centriole and another that receives the daughter centriole (extensively explained in the section 2.2) (Blanco-Ameijeiras, Lozano-Fernández and Martí, 2022).

This centrosome asymmetry can influence the fate of NPC divisions and, hence, the expansion and shrinking of the progenitor pool. It has been reported in the developing mouse cortex (Wang *et al.*, 2009; Paridaen, Wilsch-Brauninger and Huttner, 2013) and in the chick SpC (Saade *et al.*, 2017; Tozer *et al.*, 2017) that the centrosome retaining the old mature centriole is preferentially inherited by the NPC, whereas the centrosome containing the immature centriole is inherited by the delaminating and differentiating neuron, which leaves the VZ (Saade *et al.*, 2018).

Different mechanisms could be mediating the instructive role of the centrosome matura-

tion in the NPCs fate commitment. Centrosome maturation is characterized by a drastic expansion of the pericentriolar material (PCM) and a robust increase in MTOC activity. These might play instructive roles in the outcome of the cell division, since the removal of PCM and subdistal appendage (SDA) components such as PCNT, WDR62, ASPM and NIN (Wang *et al.*, 2009; Buchman *et al.*, 2010; Gai *et al.*, 2016; Jayaraman *et al.*, 2016; Saade *et al.*, 2017), is sufficient to cause premature depletion of NPCs from the VZ and to impair CNS growth. Centrosome asymmetry is also reflected in notable differences in the recruitment of signaling components affecting the signaling pathways activity in the daughter cells and ultimately their fate. For instance, MIB1, a component of the NOTCH pathway, is enriched at the daughter centrosome during mitosis and gets inherited by the prospective neuron in asymmetric divisions (Tozer *et al.*, 2017). Centriole maturation affects the NPCs capacity to quickly reassembles a cilium and responds to external stimuli, such as other growth factors (Anderson and Stearns, 2009). For instance, in dividing NPCs, a portion of the ciliary membrane is preferentially attached to the mother centriole during mitosis and asymmetrically inherited by the daughter cell retaining the progenitoasr character (Paridaen, Wilsch-Brauninger and Huttner, 2013).

Hence, from a centrosome perspective, the default outcome of any cell division should be asymmetric, which in the case of NPC is preventing tissue growth. Overcoming these centrosome-associated asymmetries would be required to promote symmetric proliferative divisions and embryonic CNS growth.

# The multiple roles of Centrosome in the control of tissue growth

## Definition of Centrosome

The centrosome is a small, non-membranous organelle capable of self-replication, composed of two centrioles and surrounded by the PCM. Centrosomes perform several critical functions in animal cells, which include serving as the main microtubule- organizing centre (MTOC), the basal body (BB) of cilia and a platform for intracellular signalling, as well as organizing the mitotic spindle during cell division (Arquint, Gabryjonczyk and Nigg, 2014; Blanco-Ameijeiras, Lozano-Fernández and Martí, 2022).

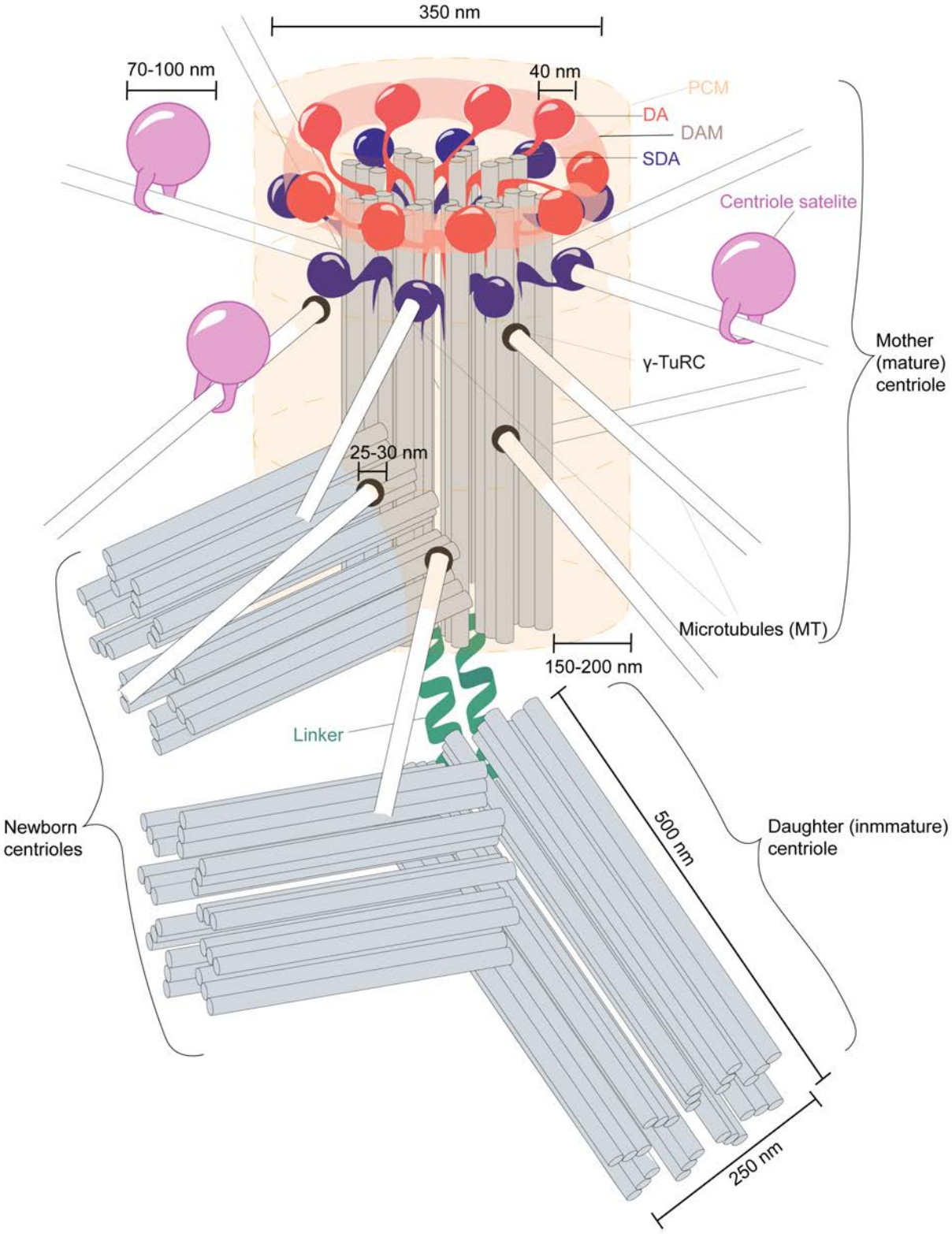
350 nm
70-100 nm
40 nm
PCM
DA
DAM
SDA
Centriole satelite
γ-TuRC
Mother
(mature)
centriole
25-30 nm
Microtubules (MT)
150-200 nm
Linker
Newborn
centrioles
500 nm
Daughter (inmmature)
centriole
250 nm

**Figure 5: 3D reconstruction of a mature centrosome in the $G_2$ phase of the cell cycle.** The mother (mature) centriole is decorated with distal (DA, terracotta) and subdistal appendages (SDA, purple), as well as pericentriolar material (PCM, pale yellow). Proteins filling the space between DA constitute the distal appendage matrix (DAM, pale terracotta). Centriolar triplet microtubules are illustrated in grey- blue. Mother and daughter centrioles are connected through a proteinacous linker (green), and newborn centrioles emerge from each pre-existing centriole. Microtubules (MTs) nucleated by the mature centriole emerge from the $\gamma$-tubulin ring complex ($\gamma$-TuRC, dark grey) and centriolar satellites (lavender) travel along the MTs. Image from (Blanco-Ameijeiras, Lozano-Fernández and Martí, 2022).

Centrioles are cylindrical structures that are ∼500 nm long and have a diameter of 250 nm in vertebrate cells (Winey and O'Toole, 2014) (Figure 5). They are composed of triplets of microtubules (MTs) organized around a central cartwheel with an evolutionarily conserved nine- fold symmetry (Azimzadeh and Marshall, 2010). Typically, two centrioles are joined perpendicularly by their proximal ends, a connection that is sustained by the proteinaceous centrosome linker in conjunction with MT forces (Panic *et al.*, 2015). Of these two centrioles, only one is fully mature, exhibiting two characteristic accessory structures, the distal appendages (DAs) and the SDAs; this centriole is termed the mother (or mature) centriole. In most cases, both appendages show the nine-fold symmetry of the centriole wall, with the head-like structures radially disposed around the MT triplets (Ibrahim *et al.*, 2009; Bowler *et al.*, 2019).

The heads of both the DA and SDA are ∼40 nm in length and extend for ∼100 nm from the centriole wall (Ibrahim *et al.*, 2009; Bowler *et al.*, 2019) (Figure 5). In cilia, DAs (also known here as transition fibers) are the platform that allows a transition zone (TZ) to be established, which contains a ring-like protein structure that extends for ∼120 nm along the ciliary axis with a nine-fold symmetry, and which connects MTs with the ciliary membrane (Shi *et al.*, 2017) (Figure 5). The daughter centriole, the younger of the two centrioles, is less mature and lacks SDAs and DAs; however, it has several daughter centriolar proteins (DCPs) that are recruited to nascent centrioles in order to regulate their elongation and homeostasis (Zou *et al.*, 2005; Mahjoub, Xie and Stearns, 2010; Li *et al.*, 2012) (Figure 6).

The PCM, a proteinaceous material surrounding the mother centriole, forms a cylindrical structure devoid of MTs that assembles around the centriole and is the focal point of MT nucleation (Jana, 2021). It is organized into concentric protein layers that attach to the mother centriole via pericentrin, a large protein that forms fibrils orientated with its C-terminal domain adjacent to the centriole wall and its N-terminus extending outwards into the PCM (Lawo *et al.*, 2012; Mennella *et al.*, 2012; Woodruff, Wueseke and Hyman,

2014). These PCM protein layers accommodate the $\gamma$-tubulin ring complex ($\gamma$-TuRC) (Moritz *et al.*, 2000), which is ∼25–30 nm in diameter and the origin of MT nucleation (Conduit, Wainman and Raff, 2015). The size of the PCM varies widely as it undergoes dynamic changes (∼150–200 nm from the centriole wall) (Fry *et al.*, 2017) (Figure 5).

How protein exchange and replacement occur between the centrosome and the cytoplasm has long remained unclear. However, it now appears that centriolar satellites (CSs), spherical granular structures of ∼70–100 nm in diameter (Tollenaere, Mailand and Bekker-Jensen, 2015), are responsible for centrosome protein transport (Bärenz, Mayilo and Gruss, 2011) (Figure 5).

## Centrosome duplication in tune with the cell cycle

Centrosomes possess a self-replicative capacity that, like DNA replication, is coordinated with the cell cycle. In order to guarantee that there is a constant number of centrosomes in the cell, cycling cells establish two layers of control: (1) cell cycle control, whereby each centriole duplicates exactly once per cell cycle, and (2) copy number control, whereby only one new centriole forms alongside each pre-existing one (Nigg and Stearns, 2011). The main events of canonical centrosome duplication during the cell cycle are: (1) procentriole formation during $G_1$, (2) elongation of the procentriole during S phase, (3) centrosome maturation during $G_2$, and (4) centrosome separation as the cell enters mitosis (extensively reviewed in Blanco-Ameijeiras, Lozano-Fernández and Martí, 2022).

(1) During $G_1$, the centrosomal proteins CEP192 and CEP152 make up the inner components of the PCM and are sequentially recruited to the wall of the daughter centriole. CEP192 promotes the recruitment of CEP152 and the Polo kinase PLK4 (Kim *et al.*, 2013), and once at the centriole, CEP152 competes with CEP192 to restrict PLK4 to the CEP152-containing proximal end of the centriole (Park *et al.*, 2014). PLK4 is targeted for proteasomal degradation unless it binds to STIL (Cunha-Ferreira *et al.*, 2009, 2013; Rogers *et al.*, 2009). STIL interaction with PLK4, allows the centriolar loading of the coiled-coil protein SAS6 (encoded by SASS6) for cartwheel assembly (Moyer *et al.*, 2015). Subsequently, the formation of a STIL–SAS6 complex establishes a negative-feedback loop by restricting PLK4 stabilization to a single focus, guaranteeing copy number control (Ohta *et al.*, 2014; Kim *et al.*, 2016) (Figure 6A).

(2) The cartwheel structure serves as a template for centriole elongation. MT nucleation and its stabilization in the nine-fold symmetry requires the cartwheel–MT connection to be established, ensuring that elongation can occur during the S phase. This connection probably takes place through CEP135, which can bind to SAS6 (Lin *et al.*, 2013) and to MTs (Kraatz *et al.*, 2016). Moreover, CEP135 recruits CPAP

(also known as CENPJ), to the centriole wall (Lin *et al.*, 2013). In turn, CPAP will recruit CEP120, which allows CCDC52 (also known as SPICE1) to be incorporated into the MT stabilization complex (Comartin *et al.*, 2013). Centriole length is negatively regulated by CP110 (also known as CP110) and CEP97, which cap the distal end of centrioles (Spektor *et al.*, 2007; Schmidt *et al.*, 2009) (Figure 6B).

(3) During late $G_2$ and the mitotic prophase, the centrosome recruits PCM components that enhance its MT-nucleating capacity to guarantee correct spindle pole formation during mitosis (Meraldi and Nigg, 2002). In addition to PCM recruitment, DAs and SDAs are assembled at the $G_2$ phase of the cell cycle. This maturation process initiates the breaking of the intrinsic centrosome molecular asymmetries. Up until the $G_2$/M transition, centrosome separation is prevented by a flexible proteinaceous linker that bridges the centriole walls via CEP135 (Lin *et al.*, 2013). Besides binding to the MT triplets of the centriole wall, it interacts with the linker protein CNAP1 (also known as CEP250) (Kim *et al.*, 2008). CNAP1 segregates into two pools at the proximal ends of the maternal and daughter centriole (Fry *et al.*, 1998), which operate as anchor points for the rootlet fibres, formed by CROCC, that join the centrioles (Bahe *et al.*, 2005; Yang, Adamian and Li, 2006). A further component of the proteinaceous linker is CEP68, which is a filament modulator that regulates the thickness of the rootlet fibres (Vlijm *et al.*, 2018). Although CNAP1, CROCC and CEP68 are the best studied components of the linker, LRRC45 and CNTLN are also associated with this structure (He *et al.*, 2013; Fang *et al.*, 2014). In addition to the proteinaceous linker, forces generated by sliding of anti-parallel MTs (induced by kinesin KIF25) collaborate tethering the centrioles together until mitosis (Jean *et al.*, 1999; Decarreau *et al.*, 2017) (Figure 6C).

(4) At the end of $G_2$, the proteinaceous linker is disrupted to allow the two centrosomes to separate and polarize at mitosis. The stability of the proteinaceous linker is mainly regulated by the kinase NEK2 and the phosphatase PP1 (Helps *et al.*, 2000; Agircan, Schiebel and Mardin, 2014; Fry, Bayliss and Roig, 2017). Besides the dissolution of the proteinaceous linker, KIF11 generates outward forces that antagonize KIF25 activity on the MT, contributing to centrosome separation (Kapitein *et al.*, 2005). The two separated centrosomes nucleate the mitotic spindle. From centriole duplication until anaphase, centrioles remain tightly engaged. During anaphase, the protease separase is activated in order to guarantee sister chromatid separation, and it also acts on centrosomes, leading to centriole disengagement (Tsou and Stearns, 2006) (Figure 6D).

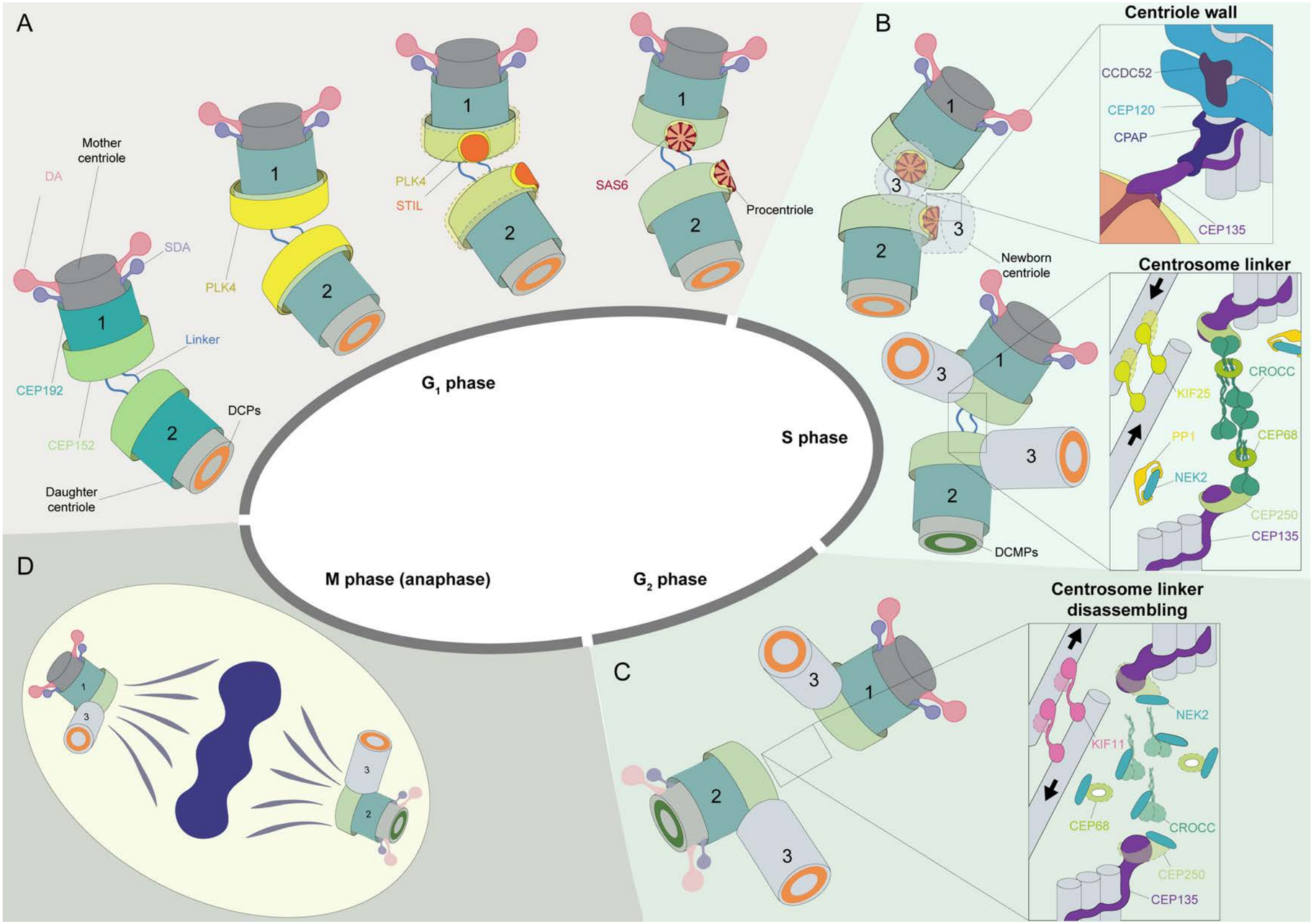


**Figure 6: Self-replication and maturation of the centrosome during the cell cycle. (A)** In the mature centrosome, mother and daughter centrioles are connected through a proteinacous linker (mid-blue). The mother centriole (1) is decorated with DA (terracotta) and SDA (dark-blue). Upon entering the cell cycle, CEP192 and CEP152 (inner components of the PCM), are recruited to the daughter centriole (2). On the daughter centriole, DCPs (orange ring) regulate centriole elongation. Restriction of PLK4 and STIL to a single focus ensures that only one procentriole cartwheel forms from a pre-existing centriole in $G_1$ phase. **(B)** Elongation of the newborn centriole (3) during S phase. The centriole wall expanded view shows proteins contributing to cartwheel–MT stabilization. Newborn centriole elongation terminates in S phase with the addition of DCPs. The transition from daughter to new mother centriole includes the loss of DCPs and the recruitment of new daughter centriole maturation proteins (DCMP, green ring). The expanded view shows proteins in the centrosome linker connecting centriolar MTs. **(C)** Daughter centriole maturation into a new 'mother' by the assembly of DAs and SDAs occurs during the $G_2$ phase of the cell cycle. Centrosome separation, caused by the disassembly of the linker (see expanded view) occurs at the end of $G_2$. **(D)** Two molecularly distinct centrosomes nucleate the mitotic spindle. Centriolar MTs and PCM are not shown for clarity. Image from (Blanco-Ameijeiras, Lozano-Fernández and Martí, 2022).

## Mature centriole build the cilium

Along cell cycle, the immature centrioles of the cells receiving permissive signals to do so, remove their DCPs and start a maturation process. This process leads to the assembling of some structures that confer the organelle with new functional capacities and impact the fate of the cell.

### DA and SDA assembly initiates centriole maturation.

The centriole maturation begins with the removal of specific newborn centriolar proteins, the DCPs, that allows OFD1 recruitment, triggering DA formation and leading to the gradual maturation of the daughter centriole (Wang *et al.*, 2018). Components of DAs are assembled in a hierarchical manner, in an inner-to-outer fashion to form a fully mature DA. Then, DAs adopt a pinwheel-like structure with a spherical head that connects through a thin stem to two MT triplets of the centriole wall (Wang *et al.*, 2018) (Figure 7A). That stem is composed by ODF2 (Tateishi *et al.*, 2013; Huang *et al.*, 2017; Kashihara *et al.*, 2019; Chong *et al.*, 2020), and CEP83 (Yang *et al.*, 2018). CEP83 is required for the recruitment of CEP89, SCLT1, FBF1 and CEP164 to appendages, without affecting the distribution of ODF2 (Tanos *et al.*, 2013). CEP89, SCLT1, LRRC45, FBF1, CEP164, TTBK2 and the recently characterized centrosome proteins ANKRD26 and PIDD1, are all known components of the DA head (Tanos *et al.*, 2013; Yang *et al.*, 2018; Bowler *et al.*, 2019; Lo *et al.*, 2019; Burigotto *et al.*, 2021; Evans *et al.*, 2021) (Figure 7C). In addition, super-resolution imaging of DAs has shown that there are also proteins filling the space between each pinwheel blade, constituting a new ultrastructural element, the distal appendage matrix (DAM) (Yang *et al.*, 2018). The correct localization of CEP164 and LRRC45 in the DA are required for DAM formation (Yang *et al.*, 2018). Owing to its outer localization at the DA, ANKRD26 might also contribute to forming the DAM (Bowler *et al.*, 2019) (Figure 7A).

SDA assembly follows the DA formation. Protein components of the SDA are also recruited gradually in a hierarchical manner; inner, intermediate and outer components are recruited to form fully mature SDAs with a spherical head that connects to two MT triplets of the centriole wall through a conical structure. C2CD3 initiates the recruitment of ODF2 and likely a few additional inner SDA components (Thauvin-Robinet *et al.*, 2014; Wang *et al.*, 2018). The base of the conical SDA is formed by CC2D2A, ODF2 and CEP128, which form the inner SDA layer (Ishikawa *et al.*, 2005; Tateishi *et al.*, 2013; Veleri *et al.*, 2014; Kashihara *et al.*, 2019). Subsequently, CCDC120, CEP110 (also known as CNTRL), CCDC68 and NDEL1 interact with ODF2 and CEP128, establishing an intermediate layer (Tateishi *et al.*, 2013; Huang *et al.*, 2017; Kashihara *et al.*, 2019; Chong *et al.*, 2020). Interestingly, CEP89 is a DA protein implicated in ciliogenesis (Sillibourne

*et al.*, 2011; Tanos *et al.*, 2013) and is also present in SDAs (Chong *et al.*, 2020). Finally, ninein and CEP170 form an outer layer, which interacts with at least CCDC120 and CCDC68 (Huang *et al.*, 2017) (Figure 7C).

**Mature centrioles serve the base upon which cilia is assemble.**

Cilium assembly requires a mature centriole, which provides a template with nine-fold symmetry on which the axonemal structure of the cilium can be built. The DA is involved in the assembly of the TZ (Bornens, 2012; Clare *et al.*, 2014). The TZ is situated just above the DA and comprises the most proximal region of the cilium that separates the BB from the axoneme. It also adopts a ring-like protein structure composed of repetitive units, the Y-linkers, which conects ciliary MT doublets with the ciliary membrane (Gilula and Satir, 1972) (Figure 7A). Y-linkers are organized in three layers: an inner layer of proteins located close to the MT doublets of the axoneme, an outer layer of transmembrane proteins in the ciliary membrane, and an intermediate layer of proteins in between (extensively reviewed in Blanco-Ameijeiras, Lozano-Fernández and Martí, 2022). In addition to these layers, CEP290 provides the base upon which Y-linker components assemble by occupying the space between the axoneme and the plasma membrane (Craige *et al.*, 2010; Yang *et al.*, 2015).

The proposed inner components (InC) of the Y-linkers are RPGRIP1L (also known as NPHP8), NPHP4 and NPHP1 (Jauregui and Barr, 2005; Sang *et al.*, 2011; Yang *et al.*, 2015; Shi *et al.*, 2017; Blanco-Ameijeiras, Lozano-Fernández and Martí, 2022). They form the RPGRIP1L–NPHP1–NPHP4 complex that is located above CEP290 in the TZ and contacts the MTs doblets (Sang *et al.*, 2011; Williams *et al.*, 2011; Czarnecki and Shah, 2012) (Figure 7B).

For the intermediate layer of Y-linkers, so far only a single component (ImC) has been characterized, MKS1 (Yang *et al.*, 2015). However, B9D1, B9D2 and AHI1 had been proposed to be also part of the intermediate layer due to some protein domains shared with MKS1, lack of transmembrane regions and a complex organization with MKS1 (MKS1–B9D1–B9D2–AHI1 complex) (Dowdle *et al.*, 2011; Zhang and Aravind, 2012; Remans *et al.*, 2014; Blanco-Ameijeiras, Lozano-Fernández and Martí, 2022) (Figure 7B).

Finally, TMEM231, TMEM67 and TCTN2 are outer components (OC) of Y-linkers (Yang *et al.*, 2015; Shi *et al.*, 2017); they are transmembrane proteins that, through their intracellular domains, likely interact with intermediate layer components. These proteins act as anchors that connect the Y-linker base with the membrane, ultimately joining the ciliary membrane to the MT doublets and regulating the access of membrane proteins to the ciliary membrane (Yang *et al.*, 2015) (Figure 7B).

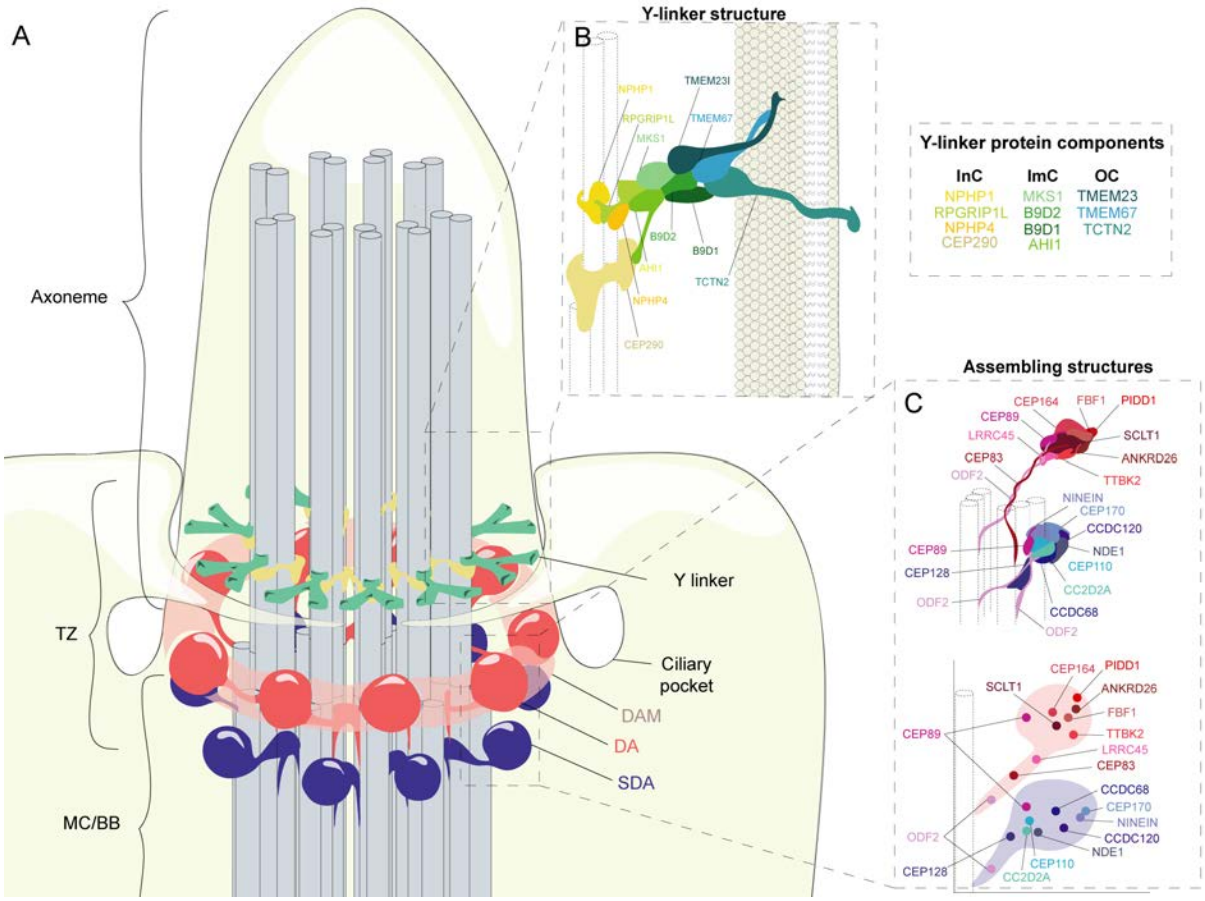


**Figure 7: Mature centriole organization at the BB of the cilium.** **(A)** Microtubule triplets of the BB extend as doublets into the axoneme. This transition from triplets to doublets occurs at the TZ, where Y-linkers connect microtubules to the extracellular membrane. **(B)** The relative position of protein complexes forming the Y-linkers that connect microtubule doublets to the plasma membrane. Proteins identified in the Y-linker InC (yellow/beige), the ImC (greens), and the OC (blues) are listed. **(C)** The relative positioning of DA (red) and SDA (blue) protein complexes as they associate to centriolar microtubule triplets. Image from (Blanco-Ameijeiras, Lozano-Fernández and Martí, 2022).

## The role of cilia in morphogen signalling

As it has been discussed in section 1.5 of this introduction, the morphogenetic activity of secreted proteins (e.g. members of the SHH, WNT and BMP families) generates the cell diversity needed for building a healthy CNS. However, these factors appear to also modulate the mode of cell division adopted by NPCs controlling the proliferation-differentiation balance, and ultimately tissue growth. In the NPCs the sensing organelle for the secreted morphogens is the primary cilia, since it works as an antenna-like structure, where the morphogens receptors are enriched, pointing to the ventricle (Anderson and Stearns, 2009). Thus, upon NPCs division the maturity of the centrosome will dra-

matically impact the time the daughter cell will need to assemble a cilia and sense the morphogen ques that as it is described below are instructive for its cell fate.

SHH signaling regulates the NPCs mode of division in the motor neuron progenitor domain division within the developing spinal cord. It has been reported that maintaining SHH signaling is sufficient to maintain symmetric proliferative divisions and prevent the neurogenic mode of cell division (Saade *et al.*, 2013). Similarly, the BMP signaling pathway also play major roles in regulating growth of the developing vertebrate nervous system (Le Dreau and Marti, 2012). Indeed, the canonical BMP effectors Smad1/5 activity determine the mode of cell division adopted by NPCs from the interneuron dorsal domains (Le Dreau *et al.*, 2014). Finally, *in vitro* studies showed that a localized WNT signal can induce oriented cell divisions that generate distinct cell fates in embryonic stem cells (Habib *et al.*, 2013).

### Centrosome dysfunction and microcephaly

As it had been explained above, centrosome maturity has a central role in NPCs mode of division commitment and ultimately, this determine the CNS growth capacity. The consequences of centrosome dysfunction during development and how they contribute to human diseases are highlighted by the study of autosomal recessive primary microcephaly (MCPH). MCPH is a genetically heterogeneous neurodevelopmental pathology characterized by a small CNS at birth. The patients present a non-progressive intellectual disability. So far, 20 MCPH-causative loci had been mapped (MCPH1-MCPH20) in various populations around the globe. 12 out of them encode centriole/centrosome or kinetochore/spindle pole proteins that are involved in centriole biogenesis, centrosome maturation, cytokinesis, centromere and kinetochore function (Table 1). This indicates that centrosome dysfunction is one of the main causes of MCPH (Nano and Basto, 2017; Jayaraman, Bae and Walsh, 2018). Moreover, additional microcephaly phenotypes are associated with centrosome proteins, including CEP63, PCNT, NIN, POC1A, establishing a strong genetic link between centrosome dysfunction during development and the aetiology of microcephaly. Furthermore, these observations highlight the central role of the centrosome in the CNS growth (Table 1).

## Models to study neural development

### The chick embryo NT, a classical model to study vertebrate CNS development

The use of chick embryos as animal model goes as far back in time as classical Greece, when Aristoteles “discovered” the chick embryo as the ideal object for embryological studies.

| Locus | Gene product | Protein function and localization | OMIM |
|---|---|---|---|
| MCPH1 | MCPH1 | Regulates chromosome condensation | 607117 |
| MCPH2 | WDR62 | Localizes to the centrosome and to the nucleus | 613583 |
| MCPH3 | CEP215 | Localizes to the centrosome and to the spindle poles during mitosis | 608201 |
| MCPH4 | CASC5 | Localizes to the kinetochore | 609173 |
| MCPH5 | ASPM | Essential for mitotic spindle assembly/function | 605481 |
| MCPH6 | CENPJ | Localizes to the centrosome, regulates microtubule assembly and nucleation | 609279 |
| MCPH7 | STIL | Localizes to PCM, regulates centriole duplication | 181590 |
| MCPH8 | CEP135 | Forms the core centriole structure, regulates early centriole assembly | 611423 |
| MCPH9 | CEP152 | Core protein of the centrosome | 613529 |
| MCPH10 | ZNF335 | Component of the trithorax H3K4-methylation chromatin remodeling complex | 610827 |
| MCPH11 | PHC1 | Component of the polycomb repressive complex-1 (PRC1) | 602978 |
| MCPH12 | CDK6 | Localizes to the centrosome, plays a role in cell cycle progression | 603368 |
| MCPH13 | CENPE | Kinetochore-associated kinesin-like motor protein | 117143 |
| MCPH14 | SAS6 | Functions in procentriole formation | 609321 |
| MCPH15 | MFSD2A | Sodium-dependently sophosphatidylcholine transporter | 614397 |
| MCPH16 | ANKLE2 | Regulates reassembly of the nuclear envelope at anaphase | 616062 |
| MCPH17 | CIT | Essential for cytokinesis | 605629 |
| MCPH18 | WDFY3 | Organizes misfolded ubiquitinated proteins into bodies to be degraded by autophagy | 617485 |
| MCPH19 | COPB2 | Subunit of the Golgi coatomer complex, necessary for retrograde intracellular trafficking | 606990 |
| MCPH20 | KIF14 | Microtubule-associated motor, plays an important role in cell division | 611279 |
| SCKL6 | CEP63 | Centrosomal protein | 614724 |
| SCKL7 | NIN | Centrosomal protein, reforms interphase centrosomal architecture after mitosis | 608684 |
| MOPD2 | PCNT | Localizes to the centrosome | 605925 |
| SOFT | POC1A | Localizes to centrioles, functions in centriole duplication and/or maintenance | 61473 |

**Table 1: The MCPH1-20 loci, their gene products and protein functions.** Adapted from (Saade *et al.*, 2018)

Ever since, it has been used as a classical embryological model for development because of its ready availability, similarity to the human embryos, and amenability to embryological and surgical manipulations. Early in the 50s, an exhaustive preparation of a series of normal stages of the chick embryo, following its development all along the incubation, serve the practical purpose of identifying and designating embryos developmental stages on the basis of external characters (Hamburger and Hamilton, 1951).

However, with the arrival of the molecular era, distinct experimental limitations of the model came out, mostly due to the difficulty of performing targeted mutagenesis or transgenic studies. Fortunately, since the 90s a number of new methods for transient transgenesis have been developed in the chick embryo (Itasaki, Bel-Vialar and Krumlauf, 1999; Ishii and Mikawa, 2005) and shortly after the chicken genome was sequenced (Hillier et al., 2004). Thus, although germ line transgenesis had not been very successful in the chick embryo, transient spatiotemporally targeted gene alterations and genomic sequencing have established the chick embryo as the model where apply genetics in concert with classical embryological techniques. This provides a unique tool to explore the role of developmentally important gene regulatory networks.

Although, in recent times other model organisms, such as the mouse and zebrafish, have been in greater demand because of increased genetic resources (Burt, 2005), the chick embryo genetic toolset is catching up with other models while it still presents some important advantages: easy to manipulate without *in utero* surgery, fast embryonic development, almost no maintenance, and low economic cost, for instance.

Even though it is not a mammalian model; the chick embryo is still a human comparable model. This is highlighted in the case of the secondary neurulation, since as it has been explained at the beginning of the introduction, chick caudal SpC formation resemble better the human secondary neurulation than murine models, for instance. It is because of that that the chick embryo was the main animal model used for both the initial characterization of the process (Schoenwolf and Delongo, 1980; Shimokita and Takahashi, 2011; Alwyn Dady *et al.*, 2014) and for the mechanisms identification (Gonzalez-Gobartt *et al.*, 2021).

## Tissue engineering, an emerging model to study human CNS development

*In vitro* tissue and organ engineering builds on the advances in developmental and cell biology and in the understanding of how cells interact one another -multicellular self-organization- and with their environment –the ECM- to assemble a given tissue.

From early 1900s, developmental biologists have selected different model organisms to study tissue and organ morphogenesis. Important innovations developed along the last

two decades, such as the isolation of human embryonic stem cells (hESCs) (Thomson *et al.*, 1998) and the reprogramming of human somatic cells into induced pluripotent stem cells (iPSCs) (Takahashi and Yamanaka, 2006), have added instrumental cellular sources to understand organ formation in a human context, as these cells can recapitulate the fundamental principles of human-specific tissue and organ morphogenesis.

As a result of these findings, it is now possible to generate a large number of *in vitro* organoids, spheroids and 3D cell cultures recapitulating the essence of tissues and organs development, not only from "healthy" cells but also from iPSCs derived from patients suffering from a wide variety of genetic or acquired pathologies. These "new experimental models" represent unprecedented tool kits for the discovery of novel therapeutic targets, drug screening, and regenerative medicine, as well as for the study of human physiology and pathogens. Despite these enormous advances, many challenges still remain to be solved. In general, among other problems, organoids still present reproducibility deficits, represent imperfect structures of the corresponding organs, in some cases present a limited differentiation of all specific cell types, and may have limited interaction with the surrounding matrix. Besides, they cannot interact with other organs, although there are attempts to establish "assembloids" (co-cultures of different structures), or to use organoids in complex organ-on-a-chip systems (Ergün and Wörsdörfer, 2022).

Understanding the development and pathologies of the human CNS is a major goal of neurodevelopmental biology. Much of our current understanding in this area has been derived from the examination of post-mortem and pathological specimens, developing non-human primates and mouse models (Di Lullo and Kriegstein, 2017). However, these tissue specimens and model systems cannot fully capture the unique and dynamic features of human CNS development. To date, a variety of protocols for CNS organoid generation have been published, many of which aim to model cortical development (Kadoshima *et al.*, 2013; Lancaster *et al.*, 2013; Qian *et al.*, 2016; Birey *et al.*, 2017). However, protocols have also been published for modeling the development of the hippocampus (Sakaguchi *et al.*, 2015), midbrain (Jo *et al.*, 2016; Qian *et al.*, 2016; Monzel *et al.*, 2017), hypothalamus (Qian *et al.*, 2016), cerebellum (Muguruma *et al.*, 2015; Qian *et al.*, 2016), SpC (Haremaki *et al.*, 2019; Zheng *et al.*, 2019), anterior pituitary (Suga *et al.*, 2011) and retina (Eiraku *et al.*, 2008; Suga *et al.*, 2011).

The advantages of using a simple tissue as a model, are still relevant in the human organoid context. Moreover, SpC is still as informative as more complex structures for studying the neural specification, neural tube formation, patterning establishment and CNS growth; since the mechanisms of these processes are conserved at early developmental stages all along the anterior-posterior axis of the CNS (detailed in previous sections). Besides, simpler tissue structures are easier to guide *in vitro*, which improves most of the liabilities

of the organoids models, specially the reproducibility.

Although there are some protocols for human anterior SpC organoid (Haremaki *et al.*, 2019; Zheng *et al.*, 2019); there has not been published so far any protocol for human posterior SpC organoids. As it has been explained above, even though the final structure is indistinguishable, the process of neural specification and the formation of the neural tube are different in anterior and posterior SpC. Since defects in secondary neurulation are associated with diseases that has a high prevalence in births (Morris *et al.*, 2016), develop a human model to study it is necessary for reveal the aetiology and mechanisms of those pathologies.

# Aims

The aim of this thesis is to unravel the cellular events and molecular networks driving SpC formation and its growth, using the classical chick embryo as *in vivo* model, and establishing organoids as *in vitro* models to study human Spinal Cord formation.

The specific objectives of this thesis are:

- To generate a human *in vitro* 3D model for SpC.
- To use this organoid models to study secondary neurulation and associated NTDs.
- To identify the proteome landscape of centrosome maturation in NPCs.
- To assess the role of centrosome proteins in the control of neural tissue growth.

# Material and methods

## Material

### Chick embryos

Fertilized eggs from the White-Leghorn strain of chickens were incubated horizontally at 38.5°C in an atmosphere of 70% humidity. Embryos were staged following morphological criteria (Hamburger and Hamilton, 1951).

### Cell lines

Both hiPSC and hESC lines were cultured under a standard feeder-free condition in mTeSR1 medium (STEMCELL Technologies #85850) with daily medium exchange. Cells were passaged every 3-5 days (depending on the confluence) as follows:

- Cells were rinsed 2 x in PBS (Fisher Scientific #10010015).
- Cells were incubated in PBS-EDTA 0.5mM (Sigma #20-158) for 4 min at 37$^{o}$C.
- Detached multicellular clumps were collected in mTeSR1 and diluted between 1/4 and 1/10.
- Clumps were transferred to a six-well tissue culture plate (Corning #353046) (6WP) precoated with 1% lactate dehydrogenase–elevating virus (LDEV)–free hESC-qualified BM matrix Matrigel (Corning #354277) for 30 min to 2h.

| **Name** | **Cell line derivation** | **Source** | **Cell type** | **Sex** | **RRID** |
|---|---|---|---|---|---|
| *RUES2* | Rockefeller University Embryonic Stem Cell Lines; NIH Registration number 0013 | WiCell | ES human | Female | CVCL_B810 |
| *H9 (WA09)* | University of Wisconsin - Dr. James Thomson | WiCell | ES human | Female | CVCL_9773 |

**Table 2: Cell lines.**

All cell lines used in this study (Table 2) had a passage number of <P100. They were tested negative for mycoplasma contamination.

## DNA constructs

The pCS2:H2B-GFP, pCS2:membrane-GFP, and pCAGGS:_ires_GFP (pCIG) vectors were used at a concentration of 0.5 $\mu$g/$\mu$l as controls for electroporation (Le Dreau *et al.*, 2014; Attardo *et al.*, 2008, Megason and McMahon, 2002).

The Myc-BioID2-MCS was used as negative control for the unspecific proximity labelling of the BioID2 system (Kim *et al.*, 2016). The neighbouring proteomic environment of CEP89, CEP164 and CP110 was analysed using the Myc-BioID2-CEP89, Myc-BioID2-CEP164 and Myc-BioID2-CP110 vectors which were generated on house (as described in the following section). Those vectors consist of a Myc tag on frame with the BioID2 enzyme fused to the different bait proteins. The four vectors were electroporated at 2mg/mL in the chick embryo neural tube at stage HH14-16.

The vectors p3XFLAG-CMV8-CP110, pEGFP-C1-CEP123/89 and pRcCMV myc-CEP164 were used for the cloning process (Lee *et al.*, 2017; Sillibourne *et al.*, 2013; Graser *et al.*, 2007). The sequences of the bait proteins were subcloned into the Myc-BioID2-MCS empty vector.

| **Recombinant DNA** | **Reference/Source** |
|---|---|
| pCAGGS:_ires_GFP | (Megason and McMahon, 2002) |
| pCS2:H2B-GFP | (Le Dréau *et al.*, 2014a) |
| pCS2:membrane-GFP | (Attardo *et al.*, 2008) |
| pCAG-PBase | (Chen and LoTurco, 2012) |
| PBCAG-eGFP | (Chen and LoTurco, 2012) |
| Myc-BioID2-MCS | (Addgene #74223) |
| p3XFLAG-CMV8-CP110 | (Lee *et al.*, 2017) |
| pEGFP-C1-CEP123/89 | (Sillibourne *et al.*, 2013) |
| pRcCMV myc-CEP164 | (Graser *et al.*, 2007) |
| Myc-BioID2-CP110 | Inhouse subclonned |
| Myc-BioID2-CEP89 | Inhouse subclonned |
| Myc-BioID2-CP164 | Inhouse subclonned |
| PB-OFD1-3xFLAG | Externalized clonning service |
| PB-3xFLAG-SSX2IP | Externalized clonning service |

**Table 3: DNA constructs.**

The piggyBac™ transposon system was used to integrate a GFP sequence into the genome of the hESC. piggyBac transposase vector (pCAG-PBase) was co-nucleofected with a piggyback transposon GFP vector (PBCAG-eGFP) (Chen *et al.*, 2016) to generate hESC mosaic cultures that ultimately are used to generate mosaic organoids with GFP+ and GFP- cells that allow a better characterization of cell rearrangements along the secondary neurulation process and organoid *in vivo* imaging.

Moreover, the pCAG-eGFP was also used as electroporation control for the *gain of function* of OFD1 and SSX2IP. OFD1 and SSX2IP were overexpressed using the PB-OFD1-3xFLAG and the PB -3xFLAG-SSX2IP vectors. They consist of three in tandem FLAG tags in frame with the sequence of the protein. Vectors were generated in an external cloning service (as described in the following section). The vectors were electroporated at 2mg/mL in the chick embryo neural tube at stage HH14-16.

## Counter-stains and antibodies.

| Antibody | Source | # Catalogue | Host Species | Dilution |
|---|---|---|---|---|
| SOX2 | R&D | AF2018-SP | Goat polyclonal IgG | 1:500 |
| aPKC | Santa Cruz | SC-17781(H-1) | Mouse monoclonal IgG | 1:500 |
| T/Bra | R&D | AF2085 | Goat polyclonal IgG | 1:500 |
| cCaspase-3 | BD Biosci. | 559565 | Rabbit monoclonal IgG | 1:500 |
| FOP(FGFR1OP) | O. Rosnet | Gift | Rabbit monoclonal IgG | 1:1000 |
| CP110 | Proteintech | 12780-1-AP | Rabbit polyclonal IgG | 1:500 |
| CEP89 | OriGene | AP50762PU-N | Rabbit polyclonal IgG | 1:500 |
| CEP164 | C. Morisson | | Mouse monoclonal IgG | 1:500 |
| N-cadherin | ZYMED | 13-2100 | Rat monoclonal IgG | 1:500 |
| Laminin-111 | Sigma | L9393 | Rabbit polyclonal IgG | 1:500 |
| Centrin2 | Merk Milipore | 04-1624 | Mouse monoclonal IgG | 1:500 |
| Phospho-Histone3 | Sigma | H9908 | Rat monoclonal IgG | 1:500 |
| PCNT | Abcam | ab4448 | Rabbit polyclonal IgG | 1:500 |
| N-Cadherin | BioLegend | 350802 | Mouse monoclonal IgG | 1:500 |
| ARL13B | ProteinTech | 17711-1-AP | Rabbit polyclonal igG | 1:500 |
| CDX2 | Abcam | ab76541 | Rabbit monoclonal IgG | 1:500 |
| ZO-1 | Invitrogen | 339111 | Mouse monoclonal IgG | 1:500 |
| SOX2 | Invitrogen | 481400 | Rabbit polyclonal IgG | 1:1000 |
| HUC/D | Molecular probes | A-21271 | Mouse monoclonal IgG | 1:1000 |
| TUJ1 | Sigma | T8578-25UL | Mouse monoclonal IgG | 1:500 |
| YAP | Santa Cruz | sc-101199 | Mouse monoclonal IgG | 1:250 |

**Table 4: Primary antibodies.**

| Antibody | Source | # Catalogue | Host Species | Dilution |
|---|---|---|---|---|
| Alexa 488 anti-rabbit | ThermoFisher Sci. | A-21206 | Donkey IgG | 1:1000 |
| Alexa 488 anti-mouse | ThermoFisher Sci. | A-21202 | Donkey IgG | 1:1000 |
| Alexa 488 anti-goat | ThermoFisher Sci. | A-11055 | Donkey IgG | 1:1000 |
| Alexa 488 anti-rat | ThermoFisher Sci. | A-21208 | Donkey IgG | 1:1000 |
| Alexa 555 anti-rabbit | ThermoFisher Sci. | A-31572 | Donkey IgG | 1:1000 |
| Alexa 555 anti-mouse | ThermoFisher Sci. | A-31570 | Donkey IgG | 1:1000 |
| Alexa 555 anti-rat | ThermoFisher Sci. | A78945 | Donkey IgG | 1:1000 |
| Alexa 633 anti-rabbit | ThermoFisher Sci. | A-21070 | Goat IgG | 1:1000 |
| Alexa 633 anti-mouse | ThermoFisher Sci. | A-21052 | Goat IgG | 1:1000 |
| Alexa 633 anti-rat | ThermoFisher Sci. | A-21434 | Goat IgG | 1:1000 |
| Streptavidin 488 | ThermoFisher Sci. | S11223 | | 1:1000 |
| Streptavidin 568 | ThermoFisher Sci. | s11226 | | 1:1000 |
| Streptavidin 800 | Li-cor | 926-32230 | | 1:1000 |

**Table 5: Secondary antibodies.**

Counter-stains were added during incubation with secondary antibody. DAPI (1:5000) was used to visualise nuclei (Sigma-Aldrich, #D9542). TRITC conjugated phalloidin was used to visualize F-actin/tissue structure (Sigma-Aldrich, #P1951) (sometimes incubated both with primary and secondary to improve the signal). Primary and secondary antibodies were used as explained in the sections of immunostaining (Table 3, 4)

## Public repositories

The BioGRID database was used for the protein interaction analysis as part of the centrosome superinteractor screening. It contains 725,012 non-redundant curated interactions in Homo sapiens (updated Nov 2021) (Oughtred *et al.*, 2021).

# Methods

## Subcloning strategies

The CP110 sequence was removed from the p3XFLAG-CMV8-CP110 vector with restriction enzymes. Vector was digested with SalI (ThermoFisher #FD0644) and SmaI (ThermoFisher #FD0663). The Myc-BioID2-MCS vector was open with XhoI (ThermoFisher #FD0694) and EcoR32I (V) (ThermoFisher #FD0303). Digested vector were run in an electrophoresis gel to isolate by size the bands of interest. Those bands were purified with the NucleoSpin Gel and PCR Clean-up (Macherey-nagel #740609-50). CP110 sequence was ligated to the Myc-BioID2 backbone vector with DNA T4 ligase (ThermoFisherScientific #EL0014) and subsequently transformed in DH5-alpha competent cells (ThermoFisherScientific #18265017). Clonning success was asses by colony PCR. Finally, the Myc-BioID2-CP110 was sequence with the primers detailed in the Table 5.

| Primer name | Sequences |
|---|---|
| BioID2 sequentiation | F: GCAAGATCACCGGCAAGCTG |
| Poly(A) sequentiation | R: CTACTCAGACAATGCGATGC |
| CP110 inner sequentiation | F: CAGCAACCCCACAAGAAACT<br>R: GGAGTGAGTCCGCTTGAGAC |
| CEP89 inner sequentiation | F: TGGTGGATGAAAATGATGGA<br>R: TGCAGGACTGTCAGCTTCTC |
| CEP164 inner sequentiation | F: CCAGAGTGTCCACAGCTCAA<br>R: ATGGCCGACTTCATCTCATC |
| CEP164 inner sequentiation (2) | F: GGATCCTGAGGAGAAGGTG |

**Table 6: Sequencing primers.**

The CEP89 sequence was removed from the pEGFP-C1-CEP123/89 vector with restriction enzymes. Vector was digested with SalI (ThermoFisher #FD0644) and BamHI (ThermoFisher #FD0054). In this case, the Myc-BioID2-MCS vector was open with XhoI (ThermoFisher #FD0694) and BamHI (ThermoFisher #FD0054). The rest of the process went as explained above.

The CEP164 sequence was removed from the pRcCMV myc-CEP164 vector with restriction enzymes. Both vectors were digested with EcoRI (ThermoFisher #FD0274) and KpnI (ThermoFisher #FD0524). The rest of the process went as explained above.

The cloning of the OFD1 and the SSX2IP was externalized with the company GeneWiz (Astrazeneca Life Science). They synthetize the provided sequence for the genes adding three in tandem FLAG tags in frame and restriction sites for EcoRI in both ends to clone the inserts in the PBCAG-eGFP substituting the eGFP sequence. Clonning success was asses by vector sequencing.

## SpC organoids differentiation guidance

Due to the number of passages, most of the organoid experiments were carried out with the RUES2 cell line. Although, no significant differences were observed when organoids differentiation guidance was done with the other cell lines. Guidance went as follows:

- Cells were rinsed 2 x in PBS (Fisher Scientific #10010015).
- Cells were incubated in StemPro™ Accutase™ (ThermoFisherScientific #A1110501) for 3 min at 37$^{o}$C.
- Cell suspension was recovered in 3mL of mTesR1 with Y27632 2HCl 10$\mu$M (Selleckchem #S1049).
- Cell suspension was spin down and cell density adjusted to 10 x $10^6$ cells/mL.

| Name | Source | # Catalogue | Pathway | [ ] |
|---|---|---|---|---|
| CHIR99021 | Milipore | 361571-5MG | WNT inductor | 3$\mu$M |
| bFGF | Thermo Fisher | PMG0031 | FGF activator | 12ng/mL |
| Y27632 | Selleckchem | S1049 | ROCK inhibitor | 10$\mu$M |
| SB431542 | StemCell | 72234 | TGF$\beta$ inhibitor | 10$\mu$M |
| LDN | Sigma | SML0559-5MG | BMP inhibitor | 10$\mu$M |
| All-trans RA | StemCell | 72264 | RA activator | 100nM |

**Table 7: Drugs.**

- $10^5$ cells were incorporated to 150$\mu$L of Matrigel on ice.
- A droplet of 10uL of the Matrigel cell suspension was pipetted per well in a twenty-four-well tissue culture plate (Corning #353046) (24WP).
- Droplet plates were incubated for 13 min at 37$^{o}$C to subsequently add 0,5mL of mTeSR1 with Y27632 2HCl 10$\mu$M.

The following days mTeSR1 is substituted by N2B27-based neural induction medium comprised of: Advance DMEM/F12 (Gibco #31331-028):Neurobasal medium (1:1; Gibco #21103-049), 0,5× N2 (Gibco #17502-001), 0,5× B27 (Gibco #17504-001), 1× nonessential amino acids (Gibco #11140-035), 1x Sodium Piruvate (Gibco #11360-088), 0,5x GlutaMax (Gibco #35050-038), and 0,1 mM $\beta$-mercaptoethanol (Gibco #31350-010). Media was supplemented with the appropriate drugs as indicated in each experiment. For references and concentrations of the drugs see Table 6. Media was changed every day and plates were kept at 37$^{o}$C and 5% of $CO_2$.

## Spheroids preassembling

To study the epithelialization and lumen resolution processes, solid aggregates were generated before the Matrigel induction process. This was achieved with a two-day spheroid preassembling protocol that was carried out as follows:

- Cells were rinsed 2 x in PBS (Fisher Scientific #10010015).
- Cells were incubated in PBS-EDTA 0.5mM (Sigma #20-158) for 4 min at 37$^{o}$C.
- Detached multicellular clumps were collected in mTeSR1.
- Approximately $10^6$ cells forming clumps were seeded in a 6WP with mTesR1 and kept shaking at 150rpm at 37$^{o}$C and 5%CO2.
- 3$\mu$M CHIR99021 (Milipore # 361571) was added to the media the following day.
- One day after, spheroids from each well were collected, spin down and re-suspended between 50-80$\mu$L of Matrigel to generate droplets in 24WPs and complete the

organoid guidance as it is detailed in the previous section.

## Genetic manipulation

### Chick embryo *in ovo* electroporation

*In ovo* electroporation was performed at stage HH14 (54 hours post fertilization (hpf), 22 somite stage) and the embryos were recovered at the times indicated (between 16-48 hours post electroporation (hpe). Embryos were electroporated with purified plasmid DNA (0,05-1 $\mu$g/ml in H2O (Sigma-Aldrich, W4502)) with Fast Green FCF (Sigma-Aldrich, F7258) (50 ng/ml). Before manipulation, 5ml of albumen was removed from the egg with a syringe and a window was opened at the top of the shell to visualize the embryo (Stern 1993; Selleck 1996). 200$\mu$l of 1% Penicillin/Streptomycin (P/S) (Gibco, 15070063) were poured on top of the embryo to improve electrode conductivity. DNA solution was then injected into the ventricle of the neural tube with a glass capillary (GD-1, Narishige; made with Narishige PC-10 glass capillary puller) by blowing air through an aspirator tube (Sigma-Aldrich, A5177-5EA). Subsequently, the platinum electrodes (CUY610P1.5-1, Nepagene) were placed either side of the embryo to perform the electroporation using an Intracel Dual Pulse (TSS10) electroporator, delivering five 50 ms pulses of 20-30V. The window in the shell was finally sealed with plastic tape and embryos were incubated until the desired stage.

### hESC electroporation

Nucelofection of undifferentiated hESC were carried out as follows:

- Cells were rinsed 2 x in PBS.
- Cells were incubated in StemPro™ Accutase™ for 3 min at 37ºC.
- Cell suspension was recovered in 3mL of mTesR1 with Y27632 2HCl 10$\mu$M.
- Cell suspension was spin down and cell density was quantified.
- 8 x $10^5$ cells were resuspended in 100$\mu$L of Human Stem Cell Nucleofector® Solution (Lonza # VPH-5002) with 4$\mu$g of PBase and 4$\mu$g of PB-GFP DNA vectors.
- Solution is transferred to an electroporation cuvette (Lonza # VPH-5002) to subsequently been inserted into the Nucleofector® 2b Device (Lonza #AAB-1001) to apply program A-012.
- Cell were recovered in mTesR1 with Y27632 2HCl 10$\mu$M to subsequently being seeded in 2D for maintenance or directly to generate matrigel droplets and undergo organoid guidance.

## *En face* chicken embryo preparations

For better visualization of the apical feet of the NPCs, an *en face* or open-book dissections were performed. Chick embryos were removed from the egg at stage HH10-22 and fixed in 4% paraformaldehyde (PFA) (Sigma-Aldrich, 16005) in 1x PBS for 2 hours at room temperature (RT) or 4 h at 4°C. After fixation, the embryos were pinned down dorsal up in a dissecting pad made of Sylgard Silicone Elastomer (World Precision Instruments #SYLG184). Using two tungsten wire tools homemade, the neural tube is open at the roof plate to subsequently be dissected from the paraxial mesoderm and the ventral non-neural tissue. Open neural tube with the apical feet of the NPCs exposed are then collected and process.

## Immunohistochemistry

### *En face* tissue preparation for immunohistochemistry

Immunostaining of *en face* samples was carried out as follows:

- Dissected neural tubes were permeabilized 1h in PBS SDS 0.1%.
- Dissected neural tubes were incubated in blocking solution (PBS, 0.1% Triton-X-100, 10% BSA) for at least 30min at RT.
- Dissected neural tubes were incubated in antibody solution (1% BSA in PBT) with primary antibody at least overnight at 4ºC with gentle shaking.
- Following incubation, dissected neural tubes were washed 3 x 10 min in PBT.
- Tissue was then incubated in secondary antibodies in antibody solution overnight at 4ºC with gentle shaking.
- Dissected neural tubes were initially washed 3 x 10 min in PBT washes and transferred to a cover glass. Neural tubes are then manipulated with tungsten tools to expose the apical side to the cover glass. Subsequently, liquid is removed as much as possible and RapiClear 1.52 (SUNJin Lab #RC147001) is added on top. Finally, a porta with a $\mu$well sticker (iSpacer 0.15mm SUNJin Lab #IS016) is placed on top.

### Free-floating sections for immunohistochemistry

Immunostaining of transversal vibratome sections was carried out as follows:

- Chick embryos were removed from the egg at st HH10-22 and fixed in 4% PFA in 1xPBS for 2 hours at room temperature (RT) or 4 h at 4°C.
- Embryos were embedded in plastic moulds with a warm 5% agarose - 10% sucrose

matrix and cooled down to solidify.

- Agarose embryo-blocks were sectioned at 50-100$\mu$m thickness in a Leica Vibratome (VT1000S), obtaining free-floating transversal sections.
- Sections were washed 3 x 5 min in PBT (PBS + 0.1% Triton-X-100).
- Sections were incubated in blocking soluion (10% BSA in PBT) for at least 30min at RT.
- Sections were incubated in antibody solution (1% BSA in PBT) with primary antibody overnight at 4ºC with gentle shaking.
- Following incubation, sections were washed 3 x 10 min in PBT.
- Sections were then incubated in secondary antibodies in antibody solution for 2 hours at room temperature.
- Finally, embryos were initially washed 3 x 10 min in PBT washes and transferred to water for glass-slide mounting, and covered by Mowiol (Sigma-Aldrich, 81381) or RapiClear 1.52 (SUNJin Lab #RC147001) and a glass-coverslip.

Various primary antibodies were used (See Table 4) in combination with Alexa® Fluor (488, 555, 633) conjugated secondary antibodies (1:1000, Invitrogen).

**In droplet organoids immunohistochemistry**

Immunostaining of organoids droplets was carried out as follows:

- Media was removed and organoids droplets were rinsed 2 with PBS.
- Organoids droplets were fixed in 4% PFA in 1xPBS for 1 hour at RT.
- Organoids droplets were rinsed 3 x with PBS.
- Organoids droplets were permeabilized 1-3h in PBS SDS 0.1%.
- Organoids droplets were rinsed 3 x with PBS.
- Organoids droplets were incubated in blocking soluion (10% BSA in PBT) overnight at 4ºC.
- With a metal spatula organoids droplets were deatached from the bottom of the 24WP and transferred to Eppendorf tubes.
- Organoids droplets were incubated in antibody solution (1% BSA in PBT) with primary antibody overnight at 4ºC in rotation.
- Following incubation, organoids droplets were washed 3 x 5 min with PBS.

- Organoids droplets were then incubated in secondary antibodies in antibody solution overnight at 4ºC in rotation.
- Finally, organoids droplets were initially washed 3 x 10 min in PBS washes. Each droplet was then transferred to a porta with a $\mu$well sticker (iSpacer 0.2mm SUN-Jin Lab #IS016) where liquid is removed as much as possible and RapiClear 1.52 (SUNJin Lab #RC147001) is added on top. Finally, a glass coverslip is placed on top.

#### Free-floating organoids immunohistochemistry

Alternatively, organoids can be removed from the matrigel before the fixation and the immunohistochemistry. The free-floating organoids immnustaining was carried out as follows:

- Media was removed and organoids droplets were rinsed with PBS.
- Organoid droplets were incubated with Colagenase IV (3mg/mL) and Dispase (1mg/mL) in HBSS at 37ºC and 5% $CO_2$ for 30 mins with gentle agitation.
- Matrigel dissolution was facilitated with up and down pipetting. Finally, organoids were collected in N2B27 and spin down to fix in PFA 4%.
- Inmunostaining procedure goes as has been described above for the droplets.
- Free-floating organoids were spin down and ressuspended directly in RapiClear 1.52 (SUNJin Lab #RC147001). Then they were transfer to a porta with a $\mu$well sticker (iSpacer 0.2mm) and a glass coverslip is placed on top.

## Fluorescence Associated Cell Sorting (FACS)

FAC sorting of chicken embryos was carried out as follows:

- Between 20 and 30 HH14 embryos were recovered 16-20h after co-electroporation with the H2B-GFP and Myc-BioID2-CEP89, Myc-BioID2-CEP164 and Myc-BioID2-CP110 vector constructs. Neural tubes were dissected in cold PBS and kept in PBS-Glucose 0.1% on ice.
- Neural tubes were dissociated in pre-heated trypsin-EDTA (Sigma-Aldrich #T4049) for 12min at 37ºC.
- Enzymatic cell dissociation was complemented with mechanical dissociation through up-and-down pipetting.
- Dissociation was stopped with PBS-Glucose 0.1% Horse Serum 20%. Samples were

filtered using Cell Strainer snap cap tubes (Corning #352235) and kept in ice.

- Samples were sorted on a FACS Aria III (BD) with the 70 $\mu$m tip to reduce as much as possible the final volume.
- At least 200000 cells for each bait where collected in Protein LowBind® Tubes (Eppendorf #0030108116). Samples were then frozen in liquid nitrogen and store at -80ºC until processed.

## Protein Immunoprecipitation

Protein immunoprecipitation from chicken FACS cells samples was carried out as follows:

- Frozen cells were gently thaw on ice and re-suspended at RT with lysis buffer (50 mM Tris·Cl, pH 7.4; 150 mM NaCl; 1 mM EDTA, 1% NP-40 (w/v); 0.5% deoxycholic acid (w/v); 0.1% SDS (w/v); 1 mM DTT; 2 mM sodium orthovanadate (Na3VO4); 30 mM Sodium pyrophosphate (Na4P2O7); 25 mM sodium fluoride (NaF); and 1× protease inhibitor cocktail (cOmplete™ Mini, EDTA-free (Roche # 11836170001)).
- Samples were incubated at RT with Benzonase Nuclease (250U, Milipore #E1014) for 15 mins.
- Triton X-100 was added to reach 2% concentration and samples were kept in rotation for 45mins at 4ºC.
- Samples were sonicated in two sessions (5 cycles of 30sec ON, 30sec OFF each) with a pre-cooled (4ºC) Bioruptor® Pico sonication device (Diagenode #B01060010).
- Samples were centrifuged for 30 minutes at 16,500 x g, 4°C. Protein samples were recovered in the supernatant.
- Using a magnetic rack (DynaMag-2 magnet, Thermo Fisher Scientific, #12321D) Streptavidin-blocked magnetic beads (Streptavidin-Blocked Magnetic Particles, GE Healthcare #GE21152104010350) were washed and resuspended in equilibration buffer (50 mM Tris·Cl, pH 7.4; 150 mM NaCl; 1 mM EDTA, 1% NP-40 (w/v); 0.5% deoxycholic acid (w/v); 0.1% SDS (w/v); 1 mM DTT).
- Beads were added to the sample and kept in rotation over-night (ON) at 4ºC.

For samples that would be send to LC-MC after immunoprecipitation we process the beads as follows:

- Beads were washed 10 min with 1mL lysis buffer.
- Beads were washed 4 x 10 min with 1mL 50mM ammonium bicarbonate (pH=8).

- Beads were re-suspended in 50mM ammonium bicarbonate (pH=8) and processed to LC-MS.

For samples that would be analysed by western blot after immunoprecipitation we process the beads as follows:

- Beads were washed 10 min with 1mL lysis buffer.
- Beads were washed 4 x 10 min with 50 mM Tris·Cl, pH 7.4
- Beads were boiled in SDS-PAGE sample buffer (65 mM Tris-HCl pH 6.8; 2.5 % SDS; 0.002 % Bromophenol Blue; 0.7135 M (5%) $\beta$-mercaptoethanol; and 10 % glicerol) at 98$^{o}$C for 10 min.
- Beads were removed using the magnetic rack and samples stored at -80$^{o}$C upon analysis.

## Western blot for protein separation and determination

Western blot assays on chicken embryo samples were carried out as follows:

- Protein samples were resolved by SDS-PAGE (7% separation gel and 5% stacking gel). At 100V for 20 min and then 125V.
- Protein samples were subsequently transferred to nitrocellulose membranes by wet electrobloting. At 50V fixed, $\sim$180mA, 4$^{o}$C overnight.
- Ponceau staining is done to confirm the protein transference to the membrane.
- Membranes were washed 3 x 5-15 min in PBS, 0.2% Tween at RT with gentle shacking.
- Membranes were blocked in PBS; 0.2% Tween; and 10% milk (w/v) at RT with gentle shaking for 1h.
- Membranes were incubated in antibody solution (PBS; 0.2% Tween; and 0.5% milk (w/v)) with primary antibody at RT with gentle shaking for 3h.
- Membranes were washed 3 x 5-15 min in PBS, 0.2% Tween at RT with gentle shacking.
- Membranes were incubated in antibody solution (PBS; 0.2% Tween; and 0.5% milk (w/v)) with secondary antibody at RT with gentle shaking for 1h.
- Membranes were washed 3 x 5-15 min in PBS, 0.2% Tween at RT with gentle shacking.

- Membranes were allowed to dry, and the fluorescence was detected on an Odyssey Infrared Imaging System (LI-COR). The molecular weights were calculated using Bio-Rad Precision Molecular Weight Markers.

## Dotblot analysis for protein determination

Dotblot assays on chicken embryo samples were carried out as follows:

- A homemade microfiltration system, similar to Bio-Dot® and Bio-Dot SF Microfiltration Apparatus (Bio-Rad) was set up and used for loading the sample in the nitrocellulose membrane.
- Membranes were washed 3 x 5-15 min in PBS, 0.2% Tween at RT with gentle shacking.
- Membranes were blocked in PBS; 0.2% Tween; and 10% milk (w/v) at RT with gentle shaking for 1h.
- Membranes were incubated in antibody solution (PBS; 0.2% Tween; and 0.5% milk (w/v)) with primary antibody at RT with gentle shaking for 3h.
- Membranes were washed 3 x 5-15 min in PBS, 0.2% Tween at RT with gentle shacking.
- Membranes were incubated in antibody solution (PBS; 0.2% Tween; and 0.5% milk (w/v)) with secondary antibody at RT with gentle shaking for 1h.
- Membranes were washed 3 x 5-15 min in PBS, 0.2% Tween at RT with gentle shacking.
- Membranes were allowed to dry, and the fluorescence was detected on an Odyssey Infrared Imaging System (LI-COR).

Biotinylated BSA (Vector laboratories, #B-2007-10) was used as positive control in the dot blots as indicated in the results section.

## Mass Spectrometry (MS)

Protein samples were attached to streptavidin-blocked magnetic beads (Streptavidin-Blocked Magnetic Particles, GE Healthcare #GE21152104010350) in Ammonium bicarbonate 50mM pH8. Samples are digested on-beads with Trypsin Gold mass spectrometry grade (Promega #V5280). C18 tips (PolyLC) columns (ThermoFisher #89870) are used for the clean-up process to finally elude the samples in 3% acetonitril 1% formic acid.

Nanoscale liquid chromatography (NanoLC) was done in a Evosep One (EV-1000, Evosep)

with Evotip (Evosep) trap columns and EV1106 (150 $\mu$m $\times$ 150 mm, 1.9 $\mu$m) (Evosep) analytical columns. EasySpray source (1900V, positive) (Thermo Scientific) allowed the NanoLC-MS coupling. MS was done using a Orbitrap Eclipse™ Tribrid (Thermo Scientific) with the software Xcalibur vs 4.2.28.14 (ThermoFisher).

Data analysis was done using the SEQUEST HT algorithm within the Proteome Discoverer software v2.5.0.400 (ThermoFisher Scientific). Gallus gallus from Uniprot (released on 2021/06) and Contaminants (released on 2017) were used as reference databases.

## Image Acquisition of fixed samples

### Confocal microscopy

Samples were imaged on an inverted Zeiss LSM-780 confocal microscope, equipped with an Argon multiline gas laser at 488 nm, a DPSS laser at 561 nm and a HeNe laser at 633nm. The objectives used were a ZEISS 40X (oil, NA 1.3, 0.2mm working distance) and a ZEISS 63X (oil, NA 1.4, 0.18mm working distance).

### Fluorescence microscopy

Samples were imaged on an inverted Leica DMI8 microscope equipped with Spectra-X Light Engine: 6 solid-state LEDs. The objective used was a LEICA (oil, NA 1.4/0.7, 0.09mm working distance).

Instant computational clearing algorithm were used in image post-processing to remove out-of-focus light in real-time to enhance optical sectioning.

## Image Acquisition of *in vivo* samples

### Mounting

One organoid droplet was seeded per bottom-plastic dish (ibidi $\mu$-Dish 35mm, high; #81156) as described in Organoid differentiation guidance or Spheroid preassembling sections. Dishes were kept at 37$^{o}$C and 5%$CO_2$.

### Staining

Organoids used for *in* vivo time-lapse imaging are a GFP+ cells mosaic, generated as explained in hESC nucleofection section.

To facilitate lumen and cell shape identication *in vivo,* 50-200nM SiR-actin (SPIROCHROME, #SC001) was added to sample media between 6 and 24 hours before imaging. It is a fluorogenic, cell permeable and highly specific probe for F-actin compatible with GFP and mCherry fluorescent proteins.

### Spinning-disk time-lapse microscopy

Samples were imaged on an inverted Nikon Ti-E microscope stand including the Perfect Focus System (PFS) equipped with 405, 488, 561 and 637 nm laser lines. The objective used was a CFI Plan Apochromat Lambda S LWD (water, NA 1.14, 0.59mm working distance).

Images were taken every 15mins for 24 to 72h. Laser were set in low power mode at 1-2%. Image acquisition was done at high speed with a resolution of 2048x2048 and binning 3x3.

## Image analysis and quantification

### General image analysis

Raw confocal data was exported to ImageJ/FiJi (`http://rsbweb.nih.gov/ij/`) (Rueden *et al.*, 2017; Schindelin *et al.*, 2012) (RRID: SCR_003070) to be processed and analysed. Projections of z-stacks are maximum projections unless otherwise indicated. Figures and schemes were generated using Adobe Illustrator CC2018 (RRID: SCR_014199).

3D reconstructions were generated using the 3D viewer plugin included in the ImageJ/Fiji.

### Proliferation index

Sox2 antibody was used to identify NPCs in fixed st HH20-22 and HH24 transversal sections. We counted both the number of Sox2+ cells and the number of total DAPI cells in control and candidate proteins gain of function conditions. Percentages were then calculated and presented in GraphPad Prism 8 bar graphs (mean ± SD/s.e.m.).

### Neurogenesis index

HuC/D antibody was used to identify differentiating neurons in fixed st HH20-22 and HH24 transversal sections. We counted both the number of HuC/D cells and the number of total DAPI cells in control and candidate proteins gain of function conditions. Percentages were then calculated and presented in GraphPad Prism 8 bar graphs (mean ± SD/s.e.m.).

### Apoptotic index

Cleaved-Caspase3 (cCaspase3) antibody was used to detect apoptosis in fixed organoids. We counted both the number of cCapase3+ cells and the number of total DAPI cells for central cells and epithelialized cells. Percentages were then calculated and presented in GraphPad Prism 8 bar graphs (mean ± SD/s.e.m.).

### Mitotic index

Phospho-histone 3 (PH3) antibody was used to detect mitotic cells in fixed organoids. We counted both the number of PH3+ cells and the number of total DAPI cells. Percentages were then calculated and presented in GraphPad Prism 6 bar graphs (mean ± SD/s.e.m.).

### BioID2 bait proteins endogenous localization

CEP89, CEP164 and CP110 antibodies were used to detect the endogenous subcellular localization of the bait proteins. FOP and centrin2 antibodies were used as pancentriolar markers to identify the centrioles of each cell. Finally, NCad antibody allows the isolation of the apical pole of each NPC.

Based on the biogenesis of the centrosome, we were able to distinguish the cells in G2/S from the cells in G1. Cells in G1 present 2 centrioles identify as 2 Centrin2 staining dots in the apical feet of the NPCs, and 1 FOP staining dot in the apical feet of the NPCs. Meanwhile in G2/S present 4 centrioles identify as 4 Centrin2 staining dots in the apical feet of the NPCs, and 2 FOP staining dots in the apical feet of the NPCs.

At early stages (HH10-12), chicken NPCs mainly undergo proliferative symmetric division, where both centrosomes must be mature. At later stages (HH22-23), chicken NPCs mainly undergo neurogenic divisions, where only one or none centrosome must be mature.

We compare the endogenous bait proteins association to the centrioles at early and later stages to assess their behaviour as mature/non-mature centrosome markers. Results are presented in GraphPad Prism 8 stacked bar plots that represent the frequency of the different behaviours.

### Cell shape

$\beta$Cat antibody was used to visualize cell shape in fixed organoids. Cells were delimited with the polygon selection tool and cell shape was quantified by measuring cell aspect ratio (AR), a parameter included in ImageJ Shape descriptors. AR is calculated dividing major axis diameter between minor axis diameter, with a value of 1.0 indicating a perfect circle. As the value increase over 1, it indicates an increasingly elongated shape. Results are presented in GraphPad Prism 8 violin plots.

### Centrosome positioning

Centrosomes were visualized with PCNT antibody and DAPI was used to stain the nucleus in organoid samples. The straight line tool of ImageJ was used to draw a line from the centrosomes to the edge of the nucleus and the distance was measured. Results are presented in GraphPad Prism 8 violin plots.

### Ciliary length

Length of the primary cilium was quantified in anti-Arl13B stained organoids. A straight or segmented line was drawn onto the Arl13B staining of each cell and length was measured with the ImageJ command. Results are represented in GraphPad Prism 8 violin plots showing all points, median and interquartile range.

### Relative localization of proteins

ZO1 and aPKC antibodies were used to assess apical components organization. An intensity profile was generated from a line drawn along the cell's major axis for ZO1, aPKC and DAPI. Thus, the relative apico-basal position is assessed. Results are plotted in GraphPad Prism 8 XY graphs. Similarly, YAP antibodie and Phalloidin and DAPI stainings were used to assess differences between nuclear and cytoplasmic YAP. An intensity profile was generated from a line drawn along the cell for YAP, Phalloidin and DAPI. Results are plotted in GraphPad Prism 8 XY graphs.

## Statistical analysis

Statistical analysis was performed using the GraphPad Prism 8 (RRID: SCR_002798). Significance was assessed by performing the Mann-Whitney test when comparing two populations or the Kruskal-Wallis when comparing more than two. In this later case, Dunn's multiple comparisons test was also run. (*$p<0.05$, **$p<0.01$, ***$p<0.001$ and ****$p<0.0001$).

## *In silico* screening for new centrosome maturation protein candidates

To generate a cloud of protein interactions in mature centriole structures a bibliographical search of proteins reported in the literature to be localized to mature centriole structures (Blanco-Ameijeiras, Lozano-Fernández and Martí, 2022) was combined with a search on public repositories for protein interactions. The BioGRID database (Oughtred *et al.*, 2021), that contains 725,012 non-redundant curated interactions in Homo sapiens (updated Nov 2021), was used to interrogate for the interactome of DAs (10 selected proteins), SDAs (10 selected proteins) and cilia BB (11 selected proteins) to generate a preliminary cloud of proteome interactions in the mature centrioles. A short list of superinteractor proteins with reported repetitive interactions ($\geq$12) was selected from that cloud. These protein list contains the superinteractor candidates which are candidate new centrosome maturation proteins potentially with functional relevance in the organization of specialized NPC divisions, and the control of tissue growth.

# Results

## Building human SpC organoids

### Neural lineage restriction of NMPs during posterior SpC formation in the chick embryo.

SpC cells are produced during vertebrate embryo elongation by axial stem cells known as NMPs (Tzouanocou et al., 2009). Besides, these dual fate progenitors will also generate the trunk mesodermal tissues. NMPs are identified by the expression of transcription factors *SOX2*, *BRA*, and *CDX1*, *2*, and *4* (Gouti *et al.*, 2017). NPCs emerging from NMPs downregulate BRA but maintain high *SOX2* expression (Kondoh and Takemoto, 2012; Olivera-Martinez *et al.*, 2012; Gouti *et al.*, 2014; Tsakiridis and Wilson, 2015; Wymeersch *et al.*, 2016).

The lineage restriction process can be followed in the same stage HH15 chick embryo, by analyzing BRA and SOX2 protein expression at several axial levels (Figure 8A-E). A strong decrease of BRA expression was observed along SN (median±IQR log10 of BRA CTCF tailbud elongation = 3.6±0.2; cell confinement = 3.3±0.5; lumen initiation=3.0±0.3; lumen resolution = 2.3±0.4; SNT = 0.8±0.5: Figure 8A'-E', F). Concomitantly, there is an increase of SOX2 levels during this process (median±IQR log10 of Sox2 CTCF tailbud elongation = 2.5±0.2; cell confinement = 3.0±0.3; lumen initiation = 3.3±0.2; lumen resolution = 3.4±0.2; SNT = 3.4±0.2: Figure 8A' '-E' ',F), consequent with the progressive generation of NPCs. Thus, BRA+ SOX2+ NMPs convert to NPCs by downregulating *BRA* and upregulating *SOX2* in a process that had been reported to be dependent of the BM (Gonzalez-Gobartt *et al.*, 2021).

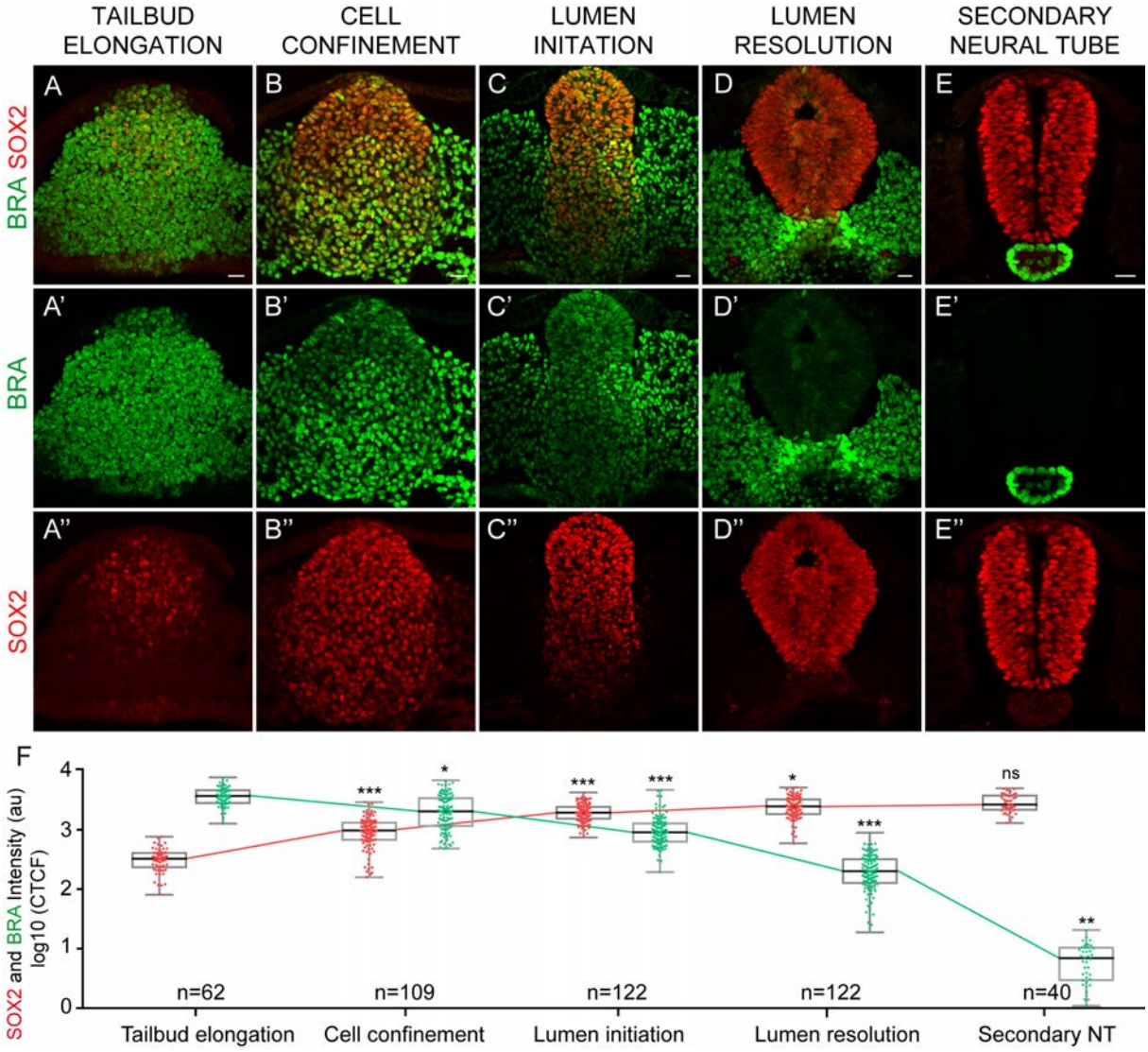


**Figure 8: Lineage restriction of NMPs into NPCs is characterised by *BRA* downregulation and *SOX2* upregulation. (A-E)** Selected images of transverse sections at the indicated secondary neurulation phase in the caudal chick embryo, stained for BRA (green) and SOX2 (red). Scale bars = 20 $\mu$m. **(F)** Plots fluorescence nuclear intensity of BRA and SOX2 at the indicated tissue remodelling events (horizontal bold lines show the median; n=62, 109, 122, 122, 40 cells from 10 embryos; *p<0.05, **p<0.01, ***p<0.001 Kruskal-Wallis test). Adapted from Gonzalez-Gobartt *et al.*, 2021.

## Generation of human SpC organoids that mimic the lineage restriction of NMPs.

To begin to emulate the extrinsic signals operating in vivo during body axis elongation, hESCs were seeded in matrigel, that will mimic the BM, and cultured in neural induction medium (N2B27) that was transiently (48 hours) supplemented with the WNT agonist CHIR (CHIR99021) and with basic Fibroblast Growth Factor (bFGF) (Figure 9A). Consistent with previous studies in mouse ES cells and mouse epiblast cells (Edri *et al.*, 2019), this resulted in the rapid exiting of pluripotency, monitored by the absence of SOX2 expression (Figure 9A'; day3 1/22), and by the presence of the mesodermal gene BRA (Figure 9A'; day3 17/19). This 48h WNT/FGF pulse appeared to be insufficient to induce the neural identity, even in longer culture periods, since the presence of SOX2+ cells were only scattered in the growing multicellular cysts (Figure 9A'' and A'''; day5 6/19; day7 9/21). In addition, this 48h WNT/FGF pulse was insufficient to maintain the mesenchymal progenitor identity, since BRA+ cells gradually disappeared (Figure 9A; day5 4/16; day7 0/16). These cells formed multicellular cysts in which cells were prevented to epithelialize and to self-organize around a lumen, and the subcellular localization of polarity proteins was randomized (Figure 9A; aPKC). Hence, even though in vivo the WNT/$\beta$-CATENIN signalling is capable to promoting differentiation to mesodermal tissue at the expense of spinal cord neural differentiation (Martin and Kimelman, 2012; Veenvliet *et al.*, 2020), in vitro, this pulse WNT /FGF treatment may not be insufficient for the NMP cell conversion. Another hypothesis is that the mesenchymal fate is favour enough to prevail over the neural with this treatment. In this case, *BRA* expression would not be observed because in the mesenchymal lineage *BRA* expression is downregulated and replaced by other genes, such as *TBX6* or *MSGN1* (Gouti *et al.*, 2017).

Members of the BMP/TGF$\beta$ signalling pathway are present and active during vertebrate body axis elongation and secondary NT formation (Gonzalez-Gobartt *et al.*, 2021). In addition, it had been reported in studies *in vitro*, both in 2D (Chambers *et al.*, 2009; Verrier *et al.*, 2018) and 3D cultures (Haremaki *et al.*, 2019; Zheng *et al.*, 2019), that the double BMP/TGF$\beta$ inhibition resulted in the rapid neural conversion. hESCs were next cultured in neural induction medium in which BMP and TGF$\beta$ signalling was transiently inhibited (48h treatment with the BMP type I receptor ALK1-3, 6 inhibitor LDN193189, and the TGF$\beta$ type I receptor ALK4,5,7 inhibitor SB431542). This resulted in the organization of multicellular cysts, consistently composed by SOX2+ cells (Figure 10B; day3 22/22; day5 23/23; day7 21/21). Concomitant with the neural lineage restriction of hESCs, these SOX2+/BRA- cells epithelialize as showed by the apical localization of aPKC, and self-organize around a single central lumen (Figure 10B). However, this 48h pulse BMP/TGF$\beta$ inhibition was insufficient to guide a complete neural conversion, since the presence of Bra+ cells increased in longer culture periods, indicating the persistence

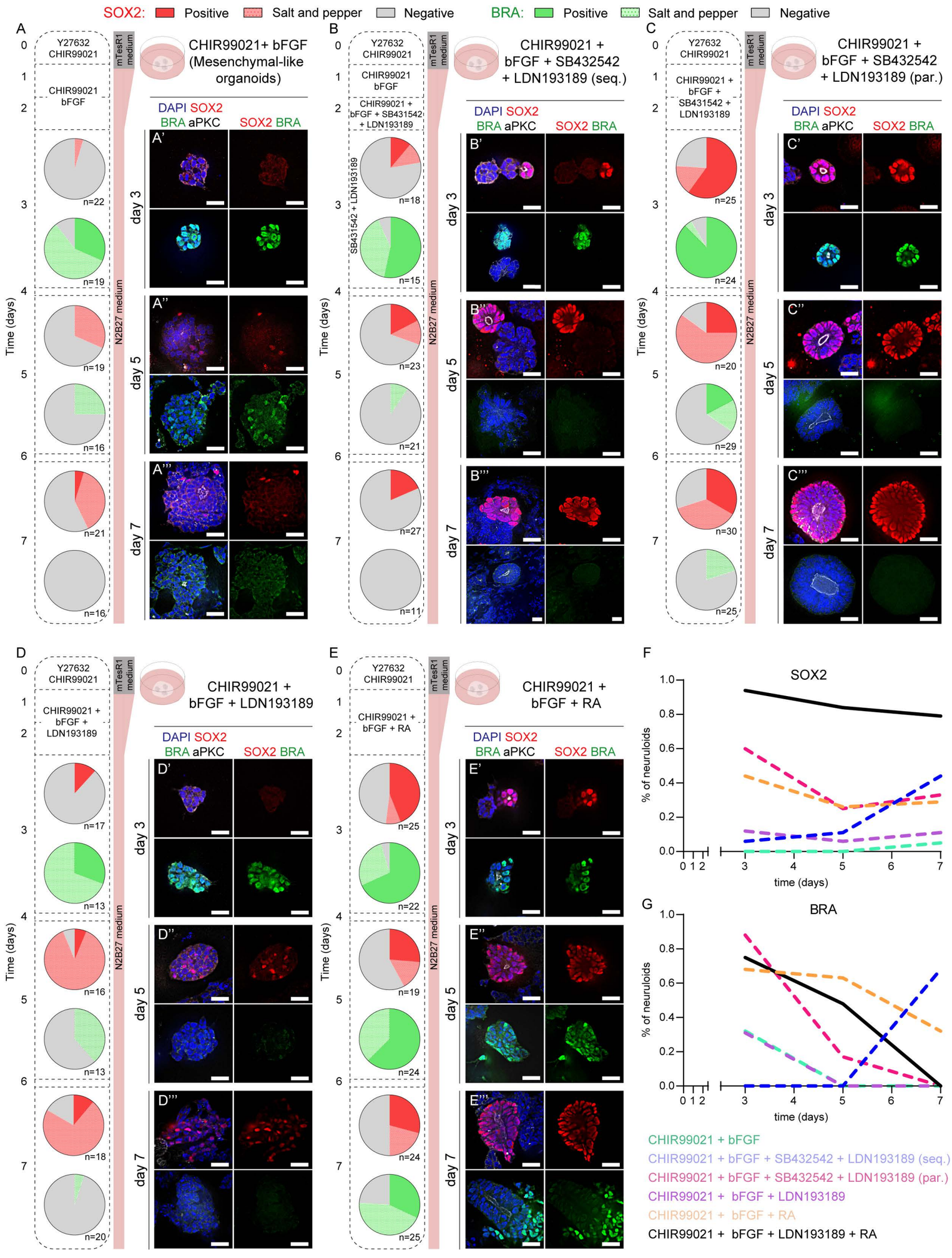
SOX2: Positive Salt and pepper Negative
BRA: Positive Salt and pepper Negative
A
B
C
D
E
F
G
Y27632 CHIR99021
CHIR99021 bFGF
CHIR99021 + bFGF + SB431542 + LDN193189
CHIR99021 + bFGF + LDN193189
CHIR99021 + bFGF + RA
mTesR1 medium
N2B27 medium
Time (days)
CHIR99021+ bFGF (Mesenchymal-like organoids)
CHIR99021 + bFGF + SB432542 + LDN193189 (seq.)
CHIR99021 + bFGF + SB432542 + LDN193189 (par.)
CHIR99021 + bFGF + LDN193189
CHIR99021 + bFGF + RA
DAPI SOX2 BRA aPKC
SOX2 BRA
day 3
day 5
day 7
n=22
n=19
n=16
n=21
n=16
n=18
n=15
n=23
n=21
n=27
n=11
n=25
n=24
n=20
n=29
n=30
n=25
n=17
n=13
n=16
n=13
n=18
n=20
n=25
n=22
n=19
n=24
n=24
n=25
% of neuruloids
time (days)
SOX2
BRA
CHIR99021 + bFGF
CHIR99021 + bFGF + SB432542 + LDN193189 (seq.)
CHIR99021 + bFGF + SB432542 + LDN193189 (par.)
CHIR99021 + bFGF + LDN193189
CHIR99021 + bFGF + RA
CHIR99021 + bFGF + LDN193189 + RA

**Figure 9: Signalling screening for hESCs lineage restriction to NMPs and ultimately to NPCs in 3D cultures.** Human organoids were generated from hESC culture in 3D and supplemented with different drugs. Organoids are stained for SOX2 (red), BRA (green) and aPKC (grey) at day 3 (A'-E'), day 5 (A''-E'') and day 7 (A'''-E'''). Scale bars = 30 $\mu$m. **(A)** Selected images of organoids transiently supplemented with CHIR99021 (WNT agonist) and bFGF. **(B)** Selected images of organoids transiently supplemented with CHIR99021 and bFGF to subsequently be supplemented with LDN193189 (BMP inhibitor) and SB431542 (TGF$\beta$ inhitor). **(C)** Selected images of organoids transiently supplemented with LDN193189 and SB431542, CHIR99021 and bFGF. **(D)** Selected images of organoids transiently supplemented with CHIR99021, bFGF and LDN193189. **(E)** Selected images of organoids transiently supplemented with CHIR99021, bFGF and RA. **(A-E)** Pie charts represent the proportion of organoids expressing different levels of SOX2 (red) and BRA (green) for each treatment and timing. The data that these graphs represent is detailed in Table 8. **(F)** Plots together the proportion of organoids with SOX2 signal at day 3, 5 and 7 of culture. Black solid line represents the reference treatment for posterior SpC organoids (Figure 10). **(G)** Plots together the proportion of organoids with BRA signal at day 3, 5 and 7 of culture. Black solid line represents the reference treatment for posterior SpC organoids (Figure 10).

of NMP-like cell identity (Figure 10B; day3 5/22; day5 20/30; day7 14/30). Thus, to boost a stable neural conversion, BMP/TGF$\beta$ signalling was next inhibited for the entire culture period (Figure 11A). This treatment is referred as maintained treatment, in opposition to transient treatment, for now on in the text. This resulted in the formation of multicellular organoids consistently composed by SOX2+ cells, in which the proportion of BRA+ cells were maintained low (Figure 11A; SOX2+ cells: day 3 16/16; day 5 18/18; day 7 13/13; BRA+ cells: day 3 0/13; day5 2/13; day7 1/9), indicating a lineage restriction similar to that occurring in vivo during caudal spinal cord formation (Gonzalez-Gobartt *et al.*, 2021). However, several morphometric parameters (Figure 11B) including, the area (data not shown; day3 = 1202.9±1598.15; day5 (transitory) = 5302±3160.3; day5 (maintained) = 3478.4±1983.7; day7 (transitory) = 9013.2±4883.1; and day7 (prolonged) = 4394.1±3476.4) and circularity of the spinal organoids (Figure 11C; day3 = 0.94±0.02; day5 (transitory) = 0.95±0.02; day5 (maintained) = 0.92±0.07; day7 (transitory) = 0.96±0.03; and day7 (prolonged) = 0.8±0.18), the number (data not shown; median±IQR number of cells per organoid day3 = 9±7.75; day5 (transitory) = 26±15.5; day5 (maintained) = 29±17; day7 (transitory)=80±40.75; day7 (prolonged) = 56±48) and area of the cells (Figure 11D; day3 = 138.7±30; day5 (transitory) = 168.7±19.8; day5 (maintained) = 126.3±28.8; day7 (transitory) = 105.6±12.2; and day7 (prolonged) = 69.6±15.5), and the lumen area (Figure 11E; day3 = 77.6±178.3; day5 (transitory) = 323.6±402.2; day5 (maintained) = 219.1±252.5; day7 (transitory) = 545.6±402; and day7

(prolonged) = 579.6±563.8), were inconsistent when BMP/TGF$\beta$ were permanently inhibited. Based on these observations different combinations of extrinsic signals were tested to optimize an *in vitro* elongating embryo environment that might better resemble the physiology of the tissue.

Next, hESCs were cultured in neural induction medium that was transiently (48h) supplemented with the caudalization condition (WNT/FGF) and sequentially exposed for additional 48h to the neural induction condition (BMP/TGF$\beta$ inhibition) (Figure 9B). Three days after this treatment, organoids were formed in which the presence of SOX2+ cells were occasional (Figure 9B'; day3 4/18), while the majority contained BRA+ cells (Figure 9B'; day3 14/15). Even though in longer culture periods the presence of BRA+ cells were dramatically reduced (Figure 9B'' and B'''; day5 2/21; day7 0/11), the proportion of SOX2+ cells did not increase concomitantly (Figure 9B'' and B'''; day5 7/23; day7 5/27). Moreover, in these culture conditions, the organization of a single central lumen was not reliable (Figure 9B. These results suggest that *SOX2* levels of expression might be insufficient to repress WNT/$\beta$CATENIN activity, which is in turn maintaining high *BRA* expression and the mesenchymal phenotype within these neural organoids (Blassberg *et al.*, 2022).

Therefore, we sought to expose hESC to the caudalization and the neural induction conditions at the same time. hESC were transiently (48h) supplemented with the neural induction medium with WNT/FGF and with the BMP/TGF$\beta$ inhibition simultaneously (Figure 9C). Three days after this treatment, organoids were formed in which the presence of SOX2+ cells (Figure 9C'; day3 19/25), and the presence of Bra+ cells (Figure 9C'; day3 22/24) were consistent. Under this culture condition, lineage restriction towards the neural fate resembles that of the in vivo NMP cells (Figure 8), in which the presence of BRA+ cells are gradually reduced (Figure 9C'' and C'''; day5 10/29, day7 5/25) in favour of the presence of SOX2+ cells (Figure 9C'' and C'''; day5 17/20, day7 21/30)(Gonzalez-Gobartt *et al.*, 2021). However, a significant proportion of multicellular cysts maintained in these culture conditions are prevented to self-organize and to resolve a single central lumen (Table 8; day5, ˜38.6%, n=44; day7, ˜36.2%, n=47) indicating that the extrinsic signals to which these cells are exposed are not fully mimicking the environment of the elongating embryo chick embryo, since TGF$\beta$ signalling is required for the resolution of a single central lumen during secondary NT formation (Gonzalez-Gobartt *et al.*, 2021).

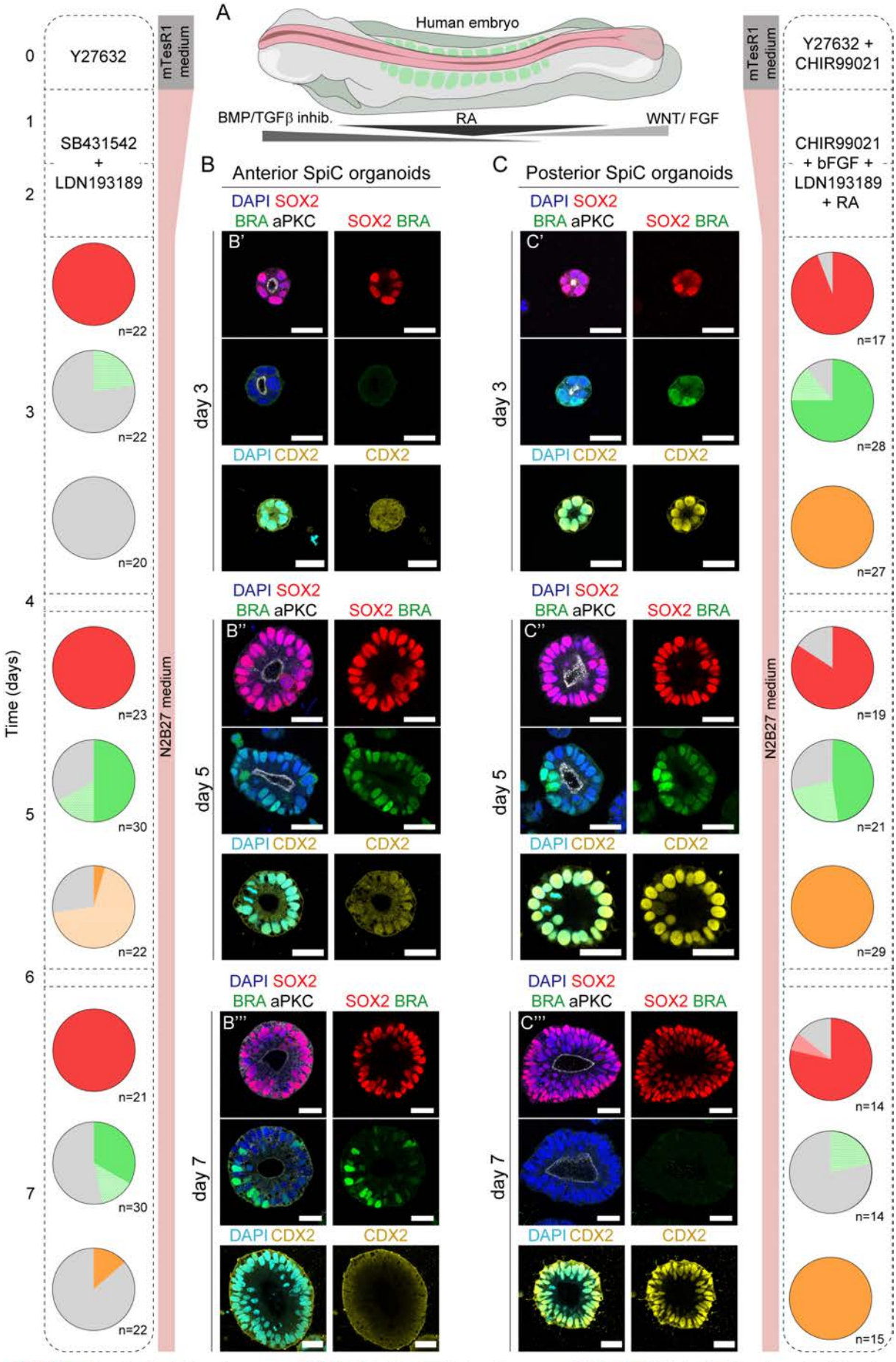
A
Human embryo
BMP/TGFβ inhib.
RA
WNT/ FGF
B
Anterior SpiC organoids
C
Posterior SpiC organoids
DAPI SOX2
BRA aPKC
SOX2 BRA
DAPI CDX2
CDX2
B'
B''
B'''
C'
C''
C'''
day 3
day 5
day 7
Time (days)
0
1
2
3
4
5
6
7
Y27632
SB431542
+
LDN193189
Y27632 +
CHIR99021
CHIR99021
+ bFGF +
LDN193189
+ RA
mTesR1
medium
N2B27 medium
n=22
n=22
n=20
n=23
n=30
n=22
n=21
n=30
n=22
n=17
n=28
n=27
n=19
n=21
n=29
n=14
n=14
n=15
SOX2: Positive
Salt and pepper
BRA: Positive
Salt and pepper
CDX2: High int.
Low int.
Negative

**Figure 10: Generation of human SpC organoids with different anterior-posterior identities.** **(A)** Drawing of an embryo where primary neurulation is closing the neural tube at cranial while NT is formed by secondary neurulation at caudal. The morphogens gradients modulating neurulation are represented underneath. **(B)** Selected images of organoids transiently supplemented with LDN193189 (BMP inhibitor) and SB431542 (TGF$\beta$ inhitor). Organoids are stained for SOX2 (red), BRA (green) and aPKC (grey) (B') and CDX2 (yellow) (B'') at day 3, day 5 and day 7. Scale bars = 30 $\mu$m. **(C)** Selected images of organoids transiently supplemented with CHIR99021 (WNT agonist), bFGF and LDN193189, and RA. Organoids are stained for SOX2 (red), BRA (green) and aPKC (grey) (B') and CDX2 (yellow) (B'') at day 3, day 5 and day 7. Scale bars = 30 $\mu$m. **(B-C)** Pie charts represent the proportion of organoids expressing different levels of SOX2 (red), BRA (green) and CDX2 (yellow) for each treatment and timing. The data that these graphs represent is detailed in Table 8.

To test its role in the process, TGF$\beta$ activity was maintained in the culture conditions, by transiently (48h) supplementing the neural induction medium with WNT/FGF and BMP inhibition (Figure 9D). However, under this culture condition, lineage restriction towards the neural fate failed to resemble that of the in vivo NMP cells, since the presence of BRA+ cells are gradually reduced (Figure 9D; day3 13/13; day5 5/13, day7 1/20), but this was only accompanied by the scattered presence of SOX2+ cells in most of the cell aggregates (Figure 9D; day3 2/17; day5 15/16, day7 15/18). Moreover, these cells failed to acquire an epithelial polarity and to self-organize around a single central lumen.

In the elongating embryo, RA plays an instructive role opposing WNT activity and regulating the balance between the NMP fate and the neural identity (Figure 2B') (Gouti *et al.*, 2017). To mimic this embryonic environment, hESC were next exposed to the neural induction medium that was transiently (48h) supplemented with WNT/FGF, BMP inhibition, and RA. Three days after this treatment, hESCs efficiently formed small organoids consistently composed by NMP-resembling cells expressing SOX2 (Figure 10C'; day3 16/17) as well as BRA (Figure 10C'; day3 25/28). In addition, the temporal evolution of these spinal cord organoids also resembled the lineage restriction of NMP in vivo, since they comprised the presence of SOX2+ cells (Figure 10C'' and C'''; day5 16/19, day7 12/14) concomitant to the gradual reduction of BRA+ cells (Figure 10C'' and C'''; day5 15/21, day7 3/14). Moreover, the organoids efficiency self-organize to resolve a single central lumen (Table 8; day5, ˜72.3%, n=47; day7, ˜62.5%, n=24), hence resembling both the cell identity and the morphogenesis of the caudal spinal cord.

In order to test whether the BMP inhibition were dispensable to the formation of these organoids, hESCs were grown in the neural induction medium that was transiently (48h) supplemented with the caudalization condition (WNT/FGF) and RA (Figure 9E). Three

| | SOX2 | | | BRA | | | Ventricle | | |
|---|---|---|---|---|---|---|---|---|---|
| **Treatment (N2B27 transiently supplemented with...)** | **day 3** | **day 5** | **day 7** | **day 3** | **day 5** | **day 7** | **day 3** | **day 5** | **day 7** |
| Wnt activator and FGF | 1/22 | 6/19 | 9/21 | 17/19 | 4/16 | 0/16 | | | |
| BMP and TGF$\beta$ inhibitors | 22/22 | 23/23 | 21/21 | 5/22 | 20/30 | 14/30 | 49/54 | 52/58 | 52/53 |
| BMP and TGF$\beta$ inhibitors (mainteined) | 16/16 | 18/18 | 13/13 | 0/13 | 2/13 | 1/9 | 49/54 | 47/62 | 53/54 |
| Wnt activator and FGF and subsequently with BMP and TGF$\beta$ inhibitors | 4/18 | 7/23 | 5/27 | 14/15 | 2/21 | 0/11 | 3/18 | 4/41 | 4/31 |
| BMP and TGF$\beta$ inhibitors, Wnt activator and FGF | 19/25 | 17/20 | 21/30 | 22/24 | 10/29 | 5/25 | 29/57 | 17/44 | 17/47 |
| BMP inhibitor, Wnt activator and FGF | 2/17 | 15/16 | 15/18 | 13/13 | 5/13 | 1/20 | | | |
| BMP inhibitor, RA, Wnt activator and FGF | 16/17 | 16/19 | 12/14 | 25/28 | 15/21 | 3/14 | 28/42 | 34/47 | 15/24 |
| RA, Wnt activator and FGF | 13/25 | 8/19 | 12/24 | 21/22 | 25/25 | 19/25 | | | |

**Table 8: Summary of the drug screening for SN human spinal cord organoids.**

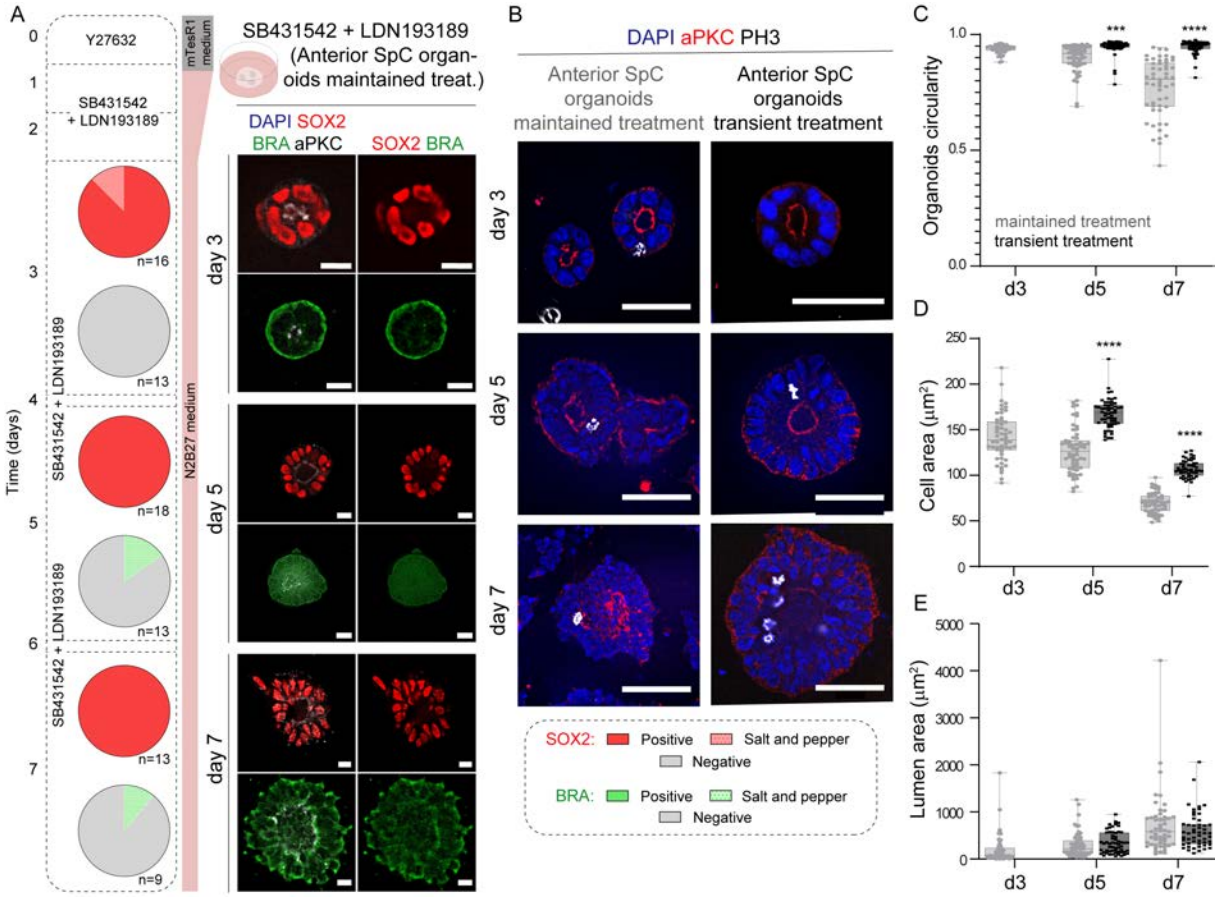


**Figure 11: Prolonged inhibition of BMP/TGF$\beta$ signalling induce consistent lineage restriction but does not efficiently reproduce several morphometric parameters of the neural tissue.** **(A)** Selected images of organoids supplemented with LDN193189 (BMP inhibitor) and SB431542 (TGF$\beta$ inhitor) during the whole culture time. Organoids are stained for SOX2 (red), BRA (green) and aPKC (grey) at day 3, day 5 and day 7. Scale bars = 20 $\mu$m. Pie charts represent the proportion of organoids expressing different levels of SOX2 (red) and BRA (green). The data that these graphs represent is detailed in Table 8. **(B)** Selected images of organoids supplemented with LDN193189 and SB431542 during the whole culture time (maintained treatment) and transiently (transient treatment). Organoids are stained for aPKC (red) and PH3 (grey) at day 3, day 5 and day 7. Scale bars = 50 $\mu$m. **(C)** Plots organoids circularity in both treatments at day 3, 5 and 7. (horizontal bold lines show the median; n=53-60 organoids; *** p<0.001; **** p<0.0001 two-way ANOVA). **(D)** Plots the mean area of the cells in the organoid in both treatments at day 3, 5 and 7. (horizontal bold lines show the median; n=53-60 organoids; **** p<0.0001 two-way ANOVA). **(E)** Plots the area of the organoid lumen in both treatments at day 3, 5 and 7. (horizontal bold lines show the median; n=53-60 organoids). (n=53-60 organoids).

days after this treatment, organoids were formed in which the presence of SOX2+ cells were irregular (Figure 9E', day3 13/25) while the presence of BRA+ cells were consistent (Figure 9E', day3 21/22). The temporal evolution of these organoids did not resemble the lineage restriction of NMP *in vivo*, since the presence of BRA+ cells were maintained (Figure 9E'' and E'''; day5 25/25, day7 19/25) and the presence of SOX2+ cells failed to increase (Figure 9E'' and E'''; day5 8/19, day7 12/24).

Thus, when compared with all the screened treatments for posterior/caudal spinal cord organoids (Table 8), the caudalization condition (WNT/FGF) with RA and BMP inhibition, consistently show high SOX2 expression along time (black in Figure 9F), while the other treatments present low to mild expression. Moreover, at the beginning of the culture organoids treated with WNT agonist, FGF, RA and BMP inhibition show high *BRA* expression (black in Figure 9G), accordingly with a ESC to NMP lineage restriction. Subsequently, *BRA* expression is downregulated until day 7 when it is almost absent (black in Figure 9G), accordingly with a NMP to NP lineage restriction.

Because mouse ESC differentiated in the absence of WNT generate neural cells with a caudal limit corresponding to the hindbrain (Metzis *et al.*, 2018), whether this was conserved in human cells was assessed. In organoids generated from hESCs that were cultured in conditions in which BMP/TGF$\beta$ activity was inhibited, the presence of CDX2+ cells were rare (Figure 10B; day3 0/20; day5 1/22; day7 3/22), indicating an anterior neural identity of these SpC organoids. However, SpC organoids generated from hESCs that were cultured in the presence of WNT/FGF, BMP inhibition, and RA, consistently show a robust *CDX2* expression (Figure 10C; day3 = 27/27; day5 = 29/29; day7 = 15/15) indicating a caudal regional identity of these human spinal cord organoids (Metzis *et al.*, 2018).

Altogether these screening revealed that the self-assembling properties of hESC can be guided towards the generation of SpC organoids, with defined anterior and posterior identities.

## NMPs undergo MET to organize a pseudostratified epithelium during chick posterior SpC formation.

The cellular composition and tissue architecture of the embryonic neural tube is highly comparable along the entire anterior to posterior axis, even though it is built by different cell lineages that undergo two very different morphogenetic processes (Metzis *et al.*, 2018; Saade *et al.*, 2018). At the caudal spinal cord, the secondary NT morphogenesis includes *de novo* formation of a lumen initiated by the MET that generate epithelial cells (Saitsu and Shiota, 2008; Gonzalez-Gobartt *et al.*, 2021). That process can be followed along the cranio-caudal axis in stage HH15 chick embryos (Figure 8). It had been reported

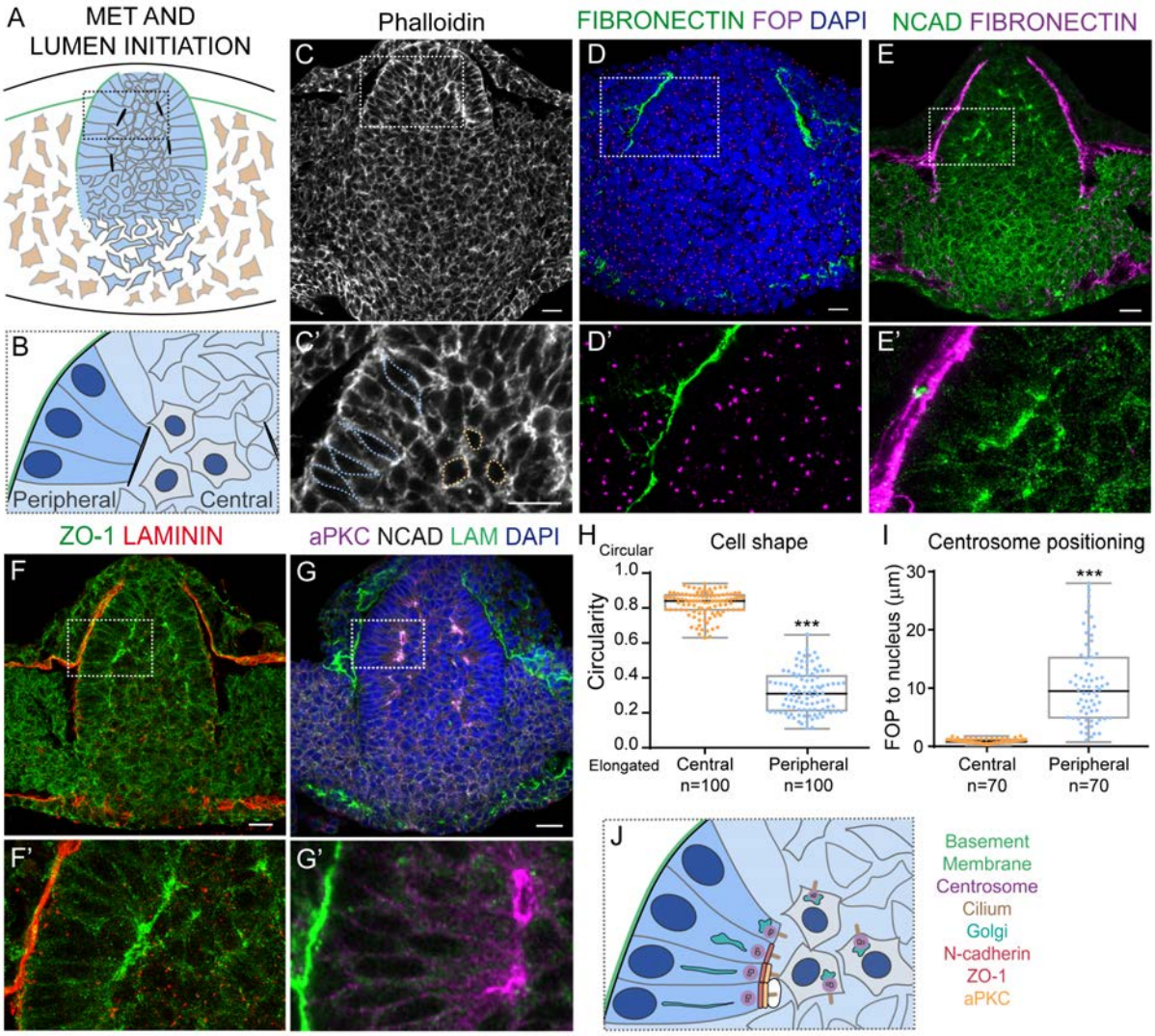


[H]

**Figure 12: MET in NMPs undergoing SN in the chick embryo. (A, B)** Schemes showing the cellular processes occurring during MET in the SNT. **(C)** Selected images of transversal sections stained for the ACTIN cytoskeleton (grey). Higher magnifications are shown in **C'**. Scale bars = 20 $\mu$m. **(D)** Selected images of transverse sections showing FIBRONECTIN deposition (green) and centrosome positioning (purple). Higher magnifications of the boxed regions are shown in **D'**. Scale bars = 20 $\mu$m. **(E, F)** Selected images of transversal sections stained for the indicated apical and basal polarity proteins. Higher magnifications of the boxed regions are shown in **E'-F'**. Scale bars = 20 $\mu$m. **(G)** Selected image of transverse sections at the lumen initiation stage stained for aPKC (purple), NCAD (grey) and LAMININ (green). A higher magnification of the boxed region appears in **G'**. Scale bars = 20 $\mu$m. **(H)** Plots circularity in central and peripheral cord cells (horizontal bold lines show the median; n=100, 100 cells from 10 embryos; ***p<0.001 Mann-Whitney test). **(I)** Plots the distance from FOP staining to the nucleus in central and peripheral cord cells (horizontal bold lines show the median; n=70, 70 cells from 10 embryos; ***p<0.001 Mann-Whitney test). **(J)** Scheme of polarising PSNT cells. The centrosome is the first organelle to be apically localised and then the Golgi, NCAD/ZO1 and finally aPKC follow it. The BM and INTEGRINS basally line the MET undergoing cells. Adapted from Gonzalez-Gobartt et al., 2021.

both in MDCK cells growing in 3D culture (Martin-Belmonte *et al.*, 2008; Bryant *et al.*, 2014), and in the early mouse embryo (Bedzhov and Zernicka-Goetz, 2014), that the orientation of epithelial polarity depends on the interaction of the cells with the ECM.

Similarly, in the developing secondary NT, the first cells to acquire epithelial polarity are those in contact with the forming BM, the ones located dorsally and in the periphery of the cord (Figure 12A, B). Thus, upon MET initiation in the chick embryo secondary NT, there are: (1) epithelialized cells, close to the BM in the periphery of the tissue, referred in the text as peripheral cells; and (2) no-epithelialized cells, far from the BM, in the centre of the secondary NT, referred in the text as central cells (Figure 12A, B). To characterize the subcellular events accompanying; cell epithelialization, cell shape, centrosome positioning, and polarity protein localisation at early MET stages were assessed in both central and peripheral cells (Figure 12C-G).

During MET in the secondary NT, cells change their shape from polygonal to elongated as they polarized and form first a columnar and later a pseudostratified epithelium (median±IQR circularity central cells=0.8±0.1 vs peripheral cells=0.3±0.2: Figure 12C, C' and H). The perinuclear centrosome becomes apically localised, as determined by the distance from FOP labelled centrosomes (Yan, Habedanck and Nigg, 2006) to the nucleus (median±IQR distance central cells=0.9±0.5$\mu$m vs peripheral cells=9.7±10.3$\mu$m: Figure 12D, D', and I). The high variability found in peripheral cell centrosome-to-nucleus distance associates to the onset of INM, which separates or brings together the centrosome and the nucleus depending on the phase of the cell cycle (Sauer, 1935; Langman, Guerrant and Freeman, 1966). Finally, cell epithelialization includes the organization of the apical membrane in discrete micro-domains where NCAD and the ZO1/OCCLUDIN complex occupy internal positions, while aPKC concentrates at the most apical domain (Aaku-Saraste, Hellwig and Huttner, 1996; Chenn *et al.*, 1998; Afonso and Henrique, 2006; Marthiens and Ffrench-Constant, 2009). Thus, apical proteins such as NCAD or ZO1 are progressively accumulated in the apical pole of the cell (Figure 12E-G, J).

Hence, during chick SNT, NMPs neural lineage restriction must be accompanied by subcellular rearrangements that allow their polarization to ultimately form a neuroepithilium.

## Human SpC Organoids are organized by polarized cells exhibiting features such as those of the SpC neural progenitor cells.

To test whether the subcellular events that accompany NMP epithelialisation in human SpC organoids, were comparable to those occurring *in vivo* (Gonzalez-Gobartt *et al.*, 2021), cell shape, the centrosome position, the cilia length, and the distribution of polarised proteins were analysed in synthetically generated human SpC organoids with different anterior-to-posterior identities.

During MET in the caudal spinal cord, the shape of the cells shifted from polygonal to elongated (Gonzalez-Gobartt *et al.*, 2021). Compared to hESCs cultured in the presence of WNT/bFGF (median ±IQR major axis/minor axis of cells = 1.48±0.49), that are used as negative control since they present a mesenchymal-like organization, the shape of those cells cultured in neural induction medium and guided for either the anterior or the posterior SpC identities, elongate (median ±IQR major axis/minor axis of anterior cells = 3.88±1.97 vs posterior cells =4.37±1.71, Figure 13A, A', B, B' and C). Concomitant to cell elongation, the perinuclear centrosome relocated apically, as witnessed by its localization lining the organoid lumen, labelled by NCAD expression (Figure 13D, D', E and E'). *En face* organoid imaging revealed NCAD localized to the NPC apical belt and the central localization of a single PCNT labelled centrosome (Figure 13D'' and E''). Quantification of the distance of the PCNT labelled centrosomes from the nucleus showed their apical localization in elongated cells (median ±IQR distance mesenchymal cells = 1.46 ±0.63 $\mu$m vs NPCs in anterior organoids= 10.18±11.54 $\mu$m vs NPCs in posterior organoids =

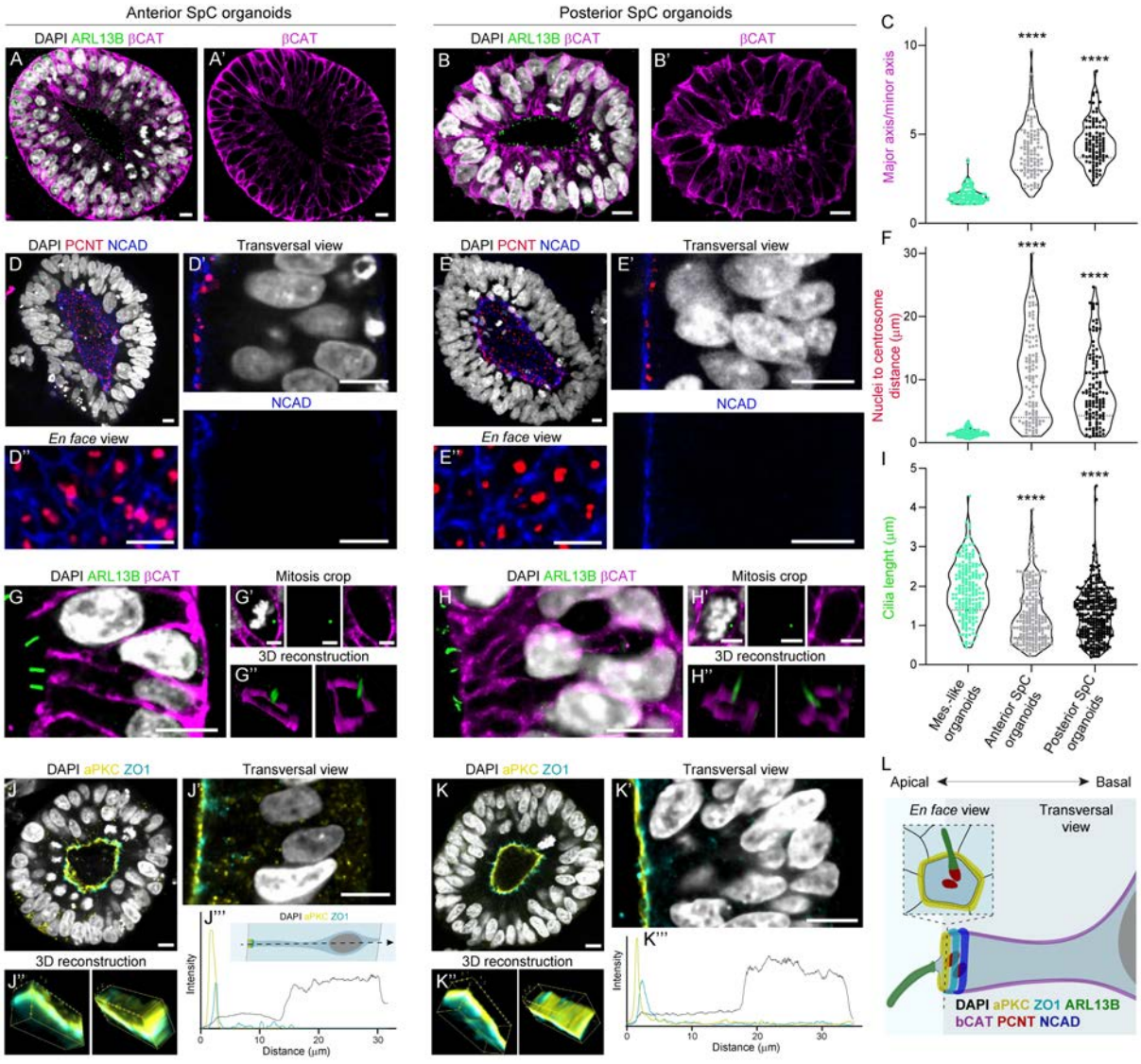

**Figure 13: Human Spinal Cord Organoids are organized by epithelial polarized cells.** Selected images of anterior SpC identity **(A)** or posterior SpC **(B)** organoids stained for ARL13B (green) and $\beta$CAT (magenta). Scale bars = 10 $\mu$m. Selected images of the $\beta$CAT staining along are shown in **A'** and **B'**. **(C)** Plots major axis/ minor axis of the cell (aspect ratio) in organoids with mesenchymal-like identity, anterior, and posterior SpC identity (horizontal bold lines show the median; n=100, 100 cells from 5 organoids; ****p<0.0001 Kruskal-Wallis test and Dunn's multiple comparison test). Selected images of anterior SpC **(D)** or posterior SpC **(E)** organoids stained for for PCNT (red) and NCAD (blue). Higher magnifications of transversal views are shown in **D'** and **E'**. Scale bars = 10 $\mu$m. *En face* views are shown in **D''** and **E''**. Scale bars = 5 $\mu$m. **(F)** Plots nuclei to centrosome distance in cells from organoids with mesenchymal identity, anterior, and posterior SpC identity (horizontal bold lines show the median; n=187, 187 cells from 5 organoids; ****p<0.0001 Kruskal-Wallis test and Dunn's multiple comparison test). Selected images of transversal views of anterior SpC identity **(G)** or posterior SpC **(H)** organoids stained for ARL13B (green) and bCAT (magenta). Scale bars = 10 $\mu$m. Higher magnifications of mitosis in transversal views are shown in **G'** and **H'**. Scale bars = 5 $\mu$m. 3D reconstructions of the apical end foot of the cells are shown in **G''** and **H''**. **(I)** Plots cilia length in cells from organoids with mesenchymal identity, anterior, and posterior SpC identity (horizontal bold lines show the median; n=100, 100 cells from 5 organoids; ****p<0.0001 Kruskal-Wallis test and Dunn's multiple comparison test). Selected images of transversal views of anterior SpC identity **(J)** or posterior SpC **(K)** organoids stained for aPKC (yellow) and ZO1 (cyan). Higher magnifications of transversal views are shown in **J'** and **K'**. Scale bars = 10 $\mu$m. 3D reconstructions of the apical surface of the epithelium are shown in **J''** and **K''**. **(J''' and K''')** Plots the fluorescence intensity to the distance from the organoid lumen (zero). Yellow line representss aPKC, cyan line represents ZO1 and grey line represents DAPI. **(L)** Scheme of polarized organoid cells in transversal and *en face* view. The centrosome (red) is apically localised. Cilia (green) is nucleated from the centrosome pointing to the lumen of the tissue. Apical polarity components are organized in the apical end foot, being aPKC (yellow) apical to ZO1 (cyan) and NCAD (blue). bCAT (magenta) is localized in the cell mebrane.

7.21±7.55 $\mu$m. Figure 13F). The wide variation in the centrosome-to-nucleus distance might be related to the onset of INM, which separates or brings together the centrosome and the nucleus depending on the phase of the cell cycle, as occurs in vivo in the embryonic neural tube (Sauer, 1935; Langman, Guerrant and Freeman, 1966; Saade *et al.*, 2018).

A hallmark of neuroepithelial cells is the single primary cilium at their apical surface, which is nucleated by the BB (Blanco-Ameijeiras, Lozano-Fernández and Martí, 2022). In the embryo NT this cilium extends into the lumen, where it is able to detect the growth factors that control CNS growth (Saade *et al.*, 2018). Both anterior and posterior spinal

cord organoids exhibited a lumen surface that is decorated with primary cilia, identified by the expression of the small GTPase ADP-ribosylation factor-like 13b (ARL13B) that specifically associates with the ciliary membrane (Paridaen, Wilsch-Bräuninger and Huttner, 2013; Saade *et al.*, 2017) (Figure 13G, H). 3D reconstructions of the apical end foot of the organoid cells revealed bCAT localized to the NPC apical belt and the central localization of a single ARL13B+ labelled cilia (Figure 13G'' and H'' ). In vivo, in NPCs, the cilia length varied as a function of the cell cycle phase and nuclear position (Saade *et al.*, 2020). The primary cilia of human NPCs generated in vitro exhibit similar length and dynamics as those decorating the embryo NT (Saade *et al.*, 2020), as measured by the length of ARL13B labelled cilia protruding from the centrioles at the lumen of the organoids (median ±IQR distance mesenchymal cells = 1.86±0.98 $\mu$m vs NPCs in anterior organoids = 1.11±1.03 $\mu$m: NPCs in posterior organoids = 1.29±0.92 $\mu$m Figure 13I). Moreover, both anterior and posterior organoid cells reproduce the ciliary membrane inheritance behaviour during mitosis reported in mouse neocortex stem cells (Paridaen, Wilsch-Bräuninger and Huttner, 2013), since the ciliary membrane is endocytosed at mitosis onset and persisted through mitosis at one spindle pole to subsequently being asymmetrically inherited by one daughter cell (Figure 13G' and H').

NPCs epithelialization involves the reorganization of the apical membrane into discrete micro-domains where the junctional complexes (NCAD, $\alpha$CAT, and $\beta$CAT) are located in the subapical domain, the zonular proteins (ZO1, AFADIN, and ACTIN) occupy an intermediate position, and the fate-determining factors (PAR3, aPKC, and PROMININ1) are confined to the most external domain (Aaku-Saraste, Hellwig and Huttner, 1996; Chenn *et al.*, 1998; Afonso and Henrique, 2006; Marthiens and Ffrench-Constant, 2009). *En face* and transversal imaging of the organoids revealed NCAD and bCAT localized to the NPCs apical belt (Figure 13A', B', D', D'', E' and E'' ). Besides, co-staining of aPKC and ZO1 revealed that hESCs cultured in both, the anterior and in the posterior neural induction conditions, organize membrane microdomains lining the lumen and closely resembling those of the NPC in vivo, in which the aPKC microdomain faces the organoid lumen and localizes external to the ZO1 membrane domain (Figure 13J, K). Altogether these analyses revealed that both anterior and posterior human SpC organoids are built by NPCs that exhibit a cell/tissue architecture that is highly similar to that of the embryonic NT (Figure 13L).

Next, the cellular dynamics of these human SpC organoids were tested. To that end, hESC were electroporated using the piggyBac™ transposon system (pCAG-PBase), with a GFP vector (PBCAG-eGFP). GFP-expressing hESCs were cultured in conditions guiding the formation of posterior SpC organoids, and imaged under an Andor Dragonfly 505 confocal microscope. This system allows SpC organoids to grow at the approximate same rate as they do in normal culture conditions, and it also permits fluorescently labelled

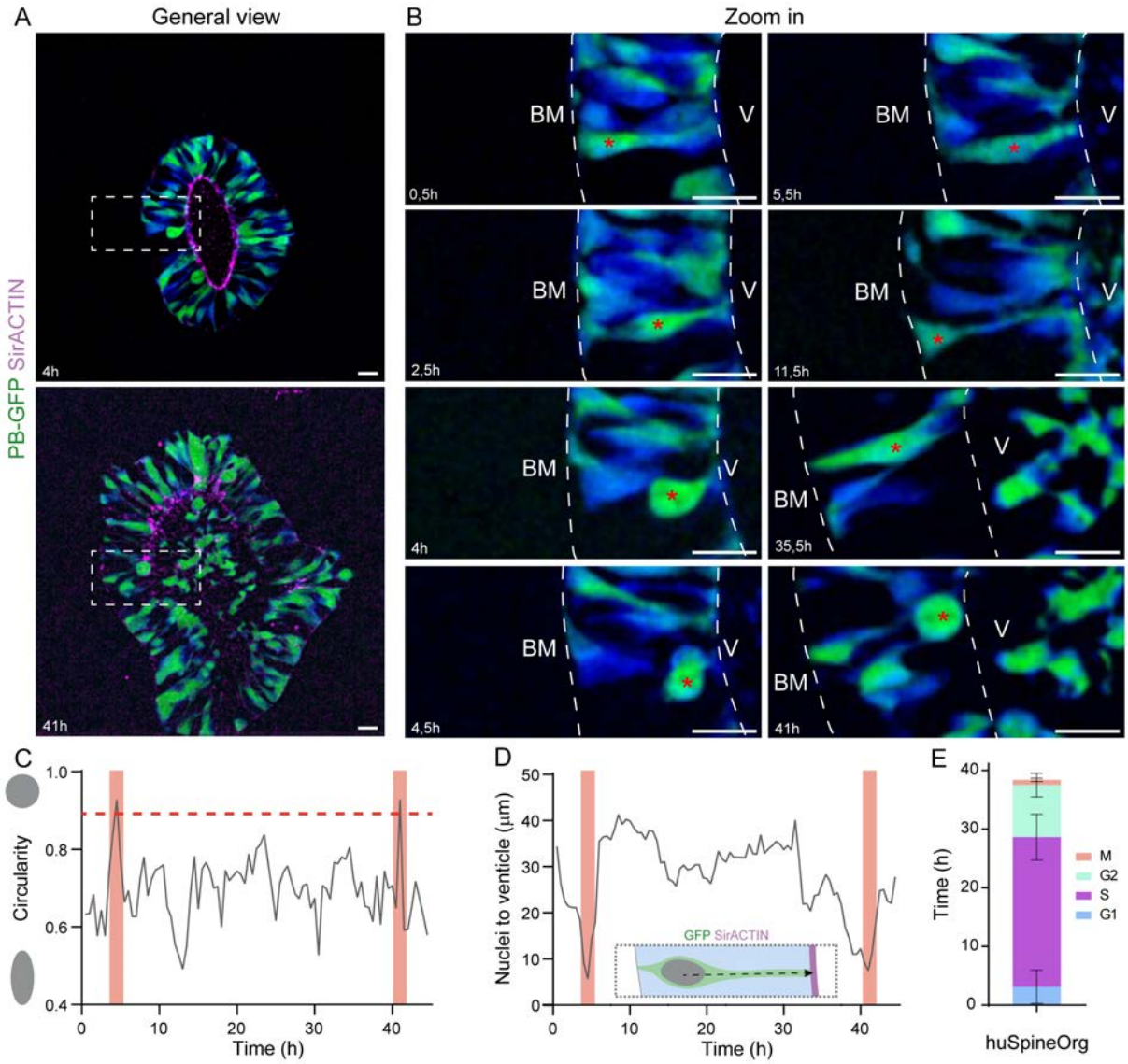


**Figure 14: NPCs forming human posterior SpC organoids undergo INM. (A)** Images of the general view of the selected organoid at the beginning and the end of the time-lapse. Organoids are stained for ACTIN (magenta) and GFP (green to blue). Scale bars = 10 $\mu$m. **(B)** Zoom in of the sequential time point following a NPCs (marked with the red asterisk) undergoing INM in the SpC organoid showed in A. Organoids are stained for GFP (green to blue). Scale bars = 10 $\mu$m. **(C)** Plots the changes in circularity that the cell undergoes in the time-lapse showed in B. Pink areas highlight the mitosis time points. **(D)** Plots the changes in the distance from the nuclei of the cell to the lumen surface in the time-lapse showed in B. Pink areas highlight the mitosis time points. **(E)** Plots the cell cycle length estimation from the time-lapses (n=5).

electroporated cells to be tracked over time (Figure 14A). In vitro these proliferating NPCs present the stereotypic INM movement pattern, synchronized with the cell cycle. GFP+ cells contacting the ventricle showed high circularity associated to the rounded nucleus at mitosis (M) (Figure 14A). During $G_1$ the nucleus is traveling basally and the cell present two feet contacting apical and basal. During S, the nucleus is contacting basal and the cell present and apical foot, and during $G_2$ the nucleus is traveling apically and the cell present two feet contacting apical and basal (Figure 14A). Tracking GFP+ cells allowed the estimation of the total cell cycle length in 40 hours, as the time taken between cell shape changes (Figure 14B), as well as the time taken to transit from the organoid lumen to the basal end and back to the lumen (Figure 14C). Moreover, these cell tracking allowed the estimation of the duration of the different phases of the cell cycle (Figure 14D). Altogether, these data showed the robustness of the in vitro generated human SpC organoids, not only in terms of cell identity, but also in cellular and tissue dynamics, and prompted us to take advantage of these biomodels to study the biological bases of neural tube defects.

## Lumen resolution in posterior SpC organoids requires YAP activity

During the formation of the posterior SpC in the elongating embryo, concomitant to NMPs epithelialization, small lumen foci emerge at a distance equivalent to one-cell from the forming BM. These multiple small lumens resolve into a single central lumen by the intercalation of central cells (Figure 3B’’’’) (Gonzalez-Gobartt *et al.*, 2021). Resembling the *in vivo* process, these results showed the capacity of hESC to self-polarize and self-organize around a single central lumen. Because in these culture conditions, hESC are all in contact to the BM-like provided by matrigel, these organoids are devoid of central cells retaining the mesenchymal polarity.

Hence to better emulate the extrinsic conditions operating in vivo during body axis elongation, GFP-expressing hESCs cultured in neural induction medium, were maintained in agitation (48h), to allow the formation of cell aggregates exhibiting mesenchymal features (Figure 15A’). Twenty-four hours (24h) after transferring these cell aggregates into 3D matrigel, and cultured in neural induction medium that was supplemented with WNT/FGF, BMP inhibition and RA, SpC organoids are formed in which peripheral cells elongate and acquire epithelial polarity, while central cells retain mesenchymal polarity (Figure 15A’’). Moreover, under these culture conditions, small lumen foci emerged at a distance equivalent to one-cell from the matrigel (Figure 15A’’). When maintained in culture for

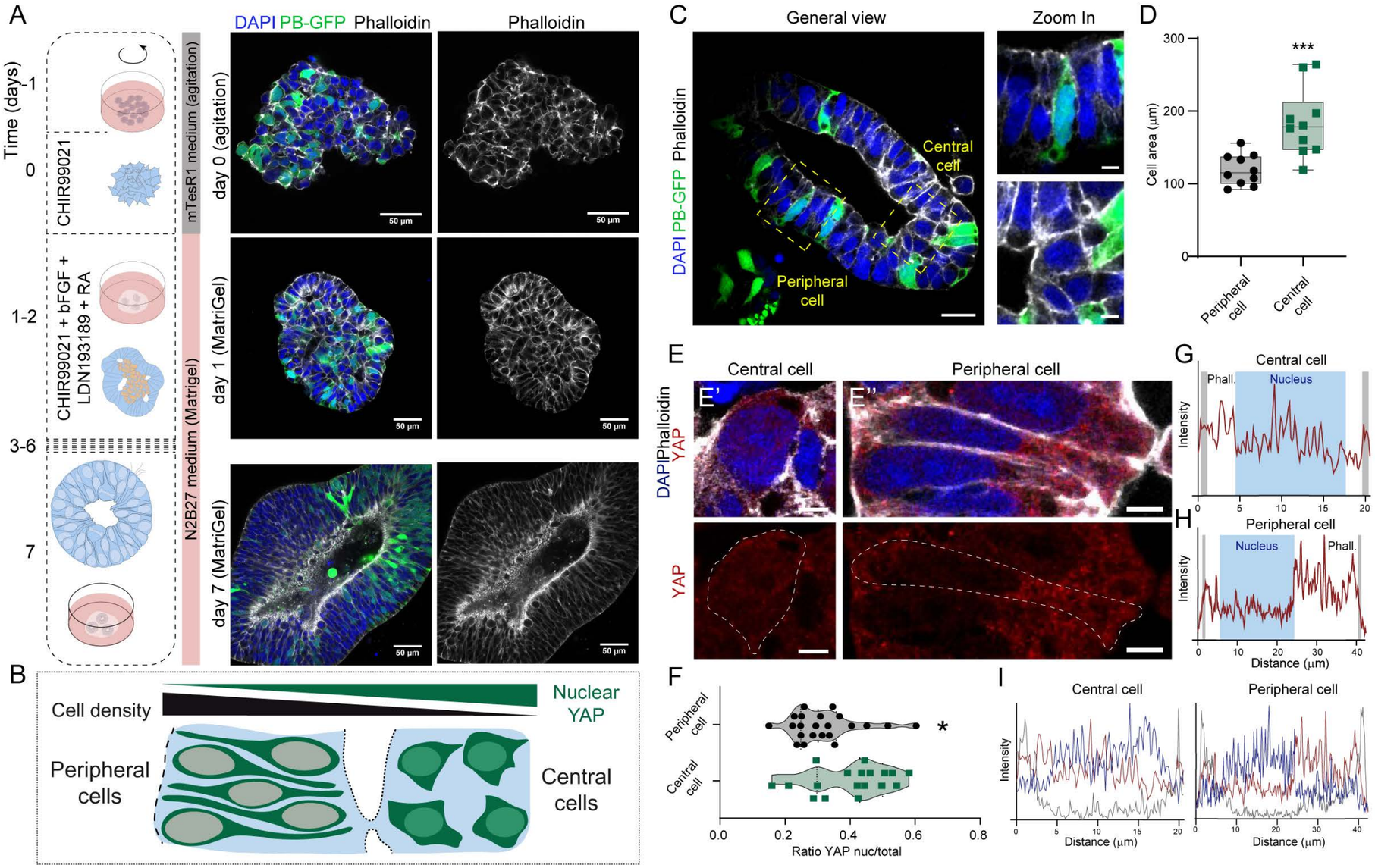


**Figure 15: Lumen resolution in human posterior SpC organoids is associated with an increase in cell density and decrease in nuclear YAP. (A)** Selected images of the general view of posterior SpC organoids maintained 48h in agitation and then transferred to a Matrigel droplet. Organoids are stained with Phalloidin (grey), GFP (green) and DAPI (blue). Scale bars = 50 $\mu$m. **(B)** Schemes representing the processes occurring during cell intercalation into the neuroeptithelial cells. The nuclear YAP is inversely proportional to the cell density. **(C)** Selected image of the general view of posterior SpC organoids maintained 48h in agitation and then maintained in a Matrigel droplet for 24h. Scale bars = 20 $\mu$m. Zoom in of peripheral and central cells. Scale bars = 5 $\mu$m. Organoids are stained with Phalloidin (grey), GFP (green) and DAPI (blue). **(D)** Plots the mean area occupied by peripheral and central cells (horizontal bold lines show the median; n=10, 10 images from 5 organoids; ***p<0.001 Mann-Whitney test). **(E)** Selected images of peripheral **(E')** and central cells **(E")** from posterior SpC organoids maintained 48h in agitation and then maintained in a Matrigel droplet for 24h. Organoids are stained with Phalloidin (grey), YAP (red) and DAPI (blue). Dot line represents the limits of the cells based on the phalloidin staining. Scale bars = 5 $\mu$m. **(F)** Plots the ratio of the integrated density of the nuclear YAP over the integrated density of YAP in the whole cell. (horizontal bold lines show the median; n=23 (peripheral cells) n=18 (central cells), from 7 organoids; *p<0.05 Mann-Whitney test). **(G)** Plots the fluorescence intensity of YAP (red line) to the distance from the organoid lumen (zero) for the peripheral cell showed in E'. Grey boxes represents the limits of the cell based on the Phalloidin staining, blue box represents the nuclei localization based on DAPI staining. **(H)** Plots the fluorescence intensity of YAP (red line) to the distance from the organoid lumen (zero) for the central cell showed in E''. Grey boxes represents the limits of the cell based on the Phalloidin staining, blue box represents the nuclei localization based on DAPI staining. **(I)** Plots the fluorescence intensity to the distance from the organoid lumen (zero) for the peripheral and central cells showed in E. Grey line represents Phalloidin, blue line represents DAPI and red line represents YAP.

few days, those multiple lumina ultimately coalesce in single central lumen (Figure 15A'''). Altogether these posterior SpC organoids closely emulated the morphogenetic events occurring during posterior SpC formation in the human embryo (Saitsu and Shiota, 2008).

We have recently reported that during chicken embryo secondary neurualtion the central cells present a lower density, so they occupied bigger areas, than the peripheral cells (Figure 15B) (Gonzalez-Gobartt *et al.*, 2021). Remarkably, in these posterior SpC organoids, a difference in cell density was appreciated, from low in the central areas to high cell density in the peripheral NPCs (median ±IQR central cell area = 178 ±66,3 $\mu$m vs peripheral cell area = 115 ±37,8 $\mu$m; Figure 15C-D).

Cell density directly regulates the activity of the Hippo pathway and its downstream effector the Yes-associated protein (YAP) (Piccolo, Dupont and Cordenonsi, 2014; Elosegui-Artola *et al.*, 2017; Nardone *et al.*, 2017) (Figure 15B). Hence, the endogenous levels of YAP protein were tested in the human posterior SpC organoids comparing peripheral and central cells. Immunostaining for the endogenous YAP protein revealed that the active YAP (nu- clear/total ratio) was high in the central cells compared with the peripheral cells (median ± IQR ratio YAP nuclear/total peripheral cells = 0.30 ± 0.108 versus central cells = 0.43 ± 0.202; Figure 15E-F). Moreover, this difference in the nuclear YAP between central and peripheral cells is also illustrated by the YAP intensity profile. In the peripheral cells is observed a drop in YAP intensity that spatially correlates with the DAPI staining (Figure 15G, I) while in the central cells there is no correlation between YAP and DAPI signalling (Figure 15H, I).

These prompted us to test the requirement of YAP activity during the process of lumen resolution in these posterior human SpC organoids. Compared to control conditions, GFP-expressing hESCs aggregates cultured in the presence of dasatinib C-SRC/YAP1 inhibitor (DASA) (Hsu *et al.*, 2018), generated a multilumen phenotype and were prevented to resolve a single lumen (Figure 16A-B). During day 1 and 2 of culturing the organoids in matrigel there is no significant differences in the proportion of multilumen organoids observed in control (Figure 16A', A'') and DASA (Figure 16B', B'') conditions. However, DASA organoids present slightly smaller lumina than controls, assessed by the ratio of the lumen perimeter mean over the organoid perimeter (Figure 16C). At day 3 in matrigel, the control organoids already undergo lumen resolution and they present a single central lumen (Figure 16A'''). Meanwhile, at that culture time, most of the organoids treated with DASA organize a multiple lumen (Figure 16B'''). At day 4 in matrigel, the organoids treated with DASA still organize multiple lumen in a high proportion (Figure 16B'''') in contrast with the control organoids that consistently organize a single central lumen (Figure 16A''''). At day 3 and 4, the control organoids show a sharp increase in the ratio of the lumen perimeter mean over the organoid perimeter, caused by the fusion of the

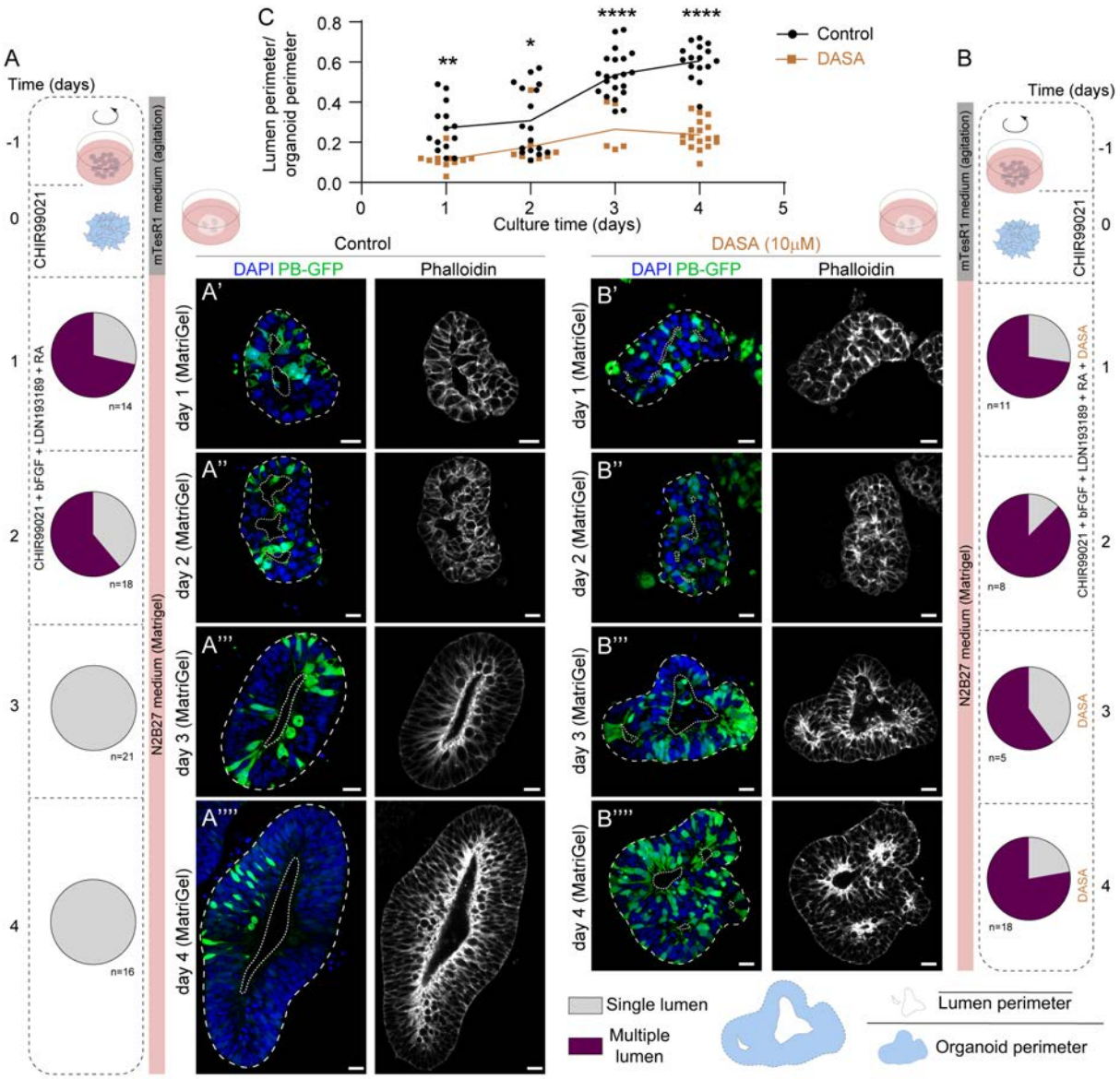


**Figure 16: Lumen resolution in human posterior SpC organoids requires YAP activity.** Selected images of the general view of posterior SpC organoids maintained 48h in agitation and then transferred to a Matrigel droplet in control conditions **(A)** or with a YAP inhibitor DASA **(B)**. Organoids are stained with Phalloidin (grey), GFP (green) and DAPI (blue). Scale bars = 20 $\mu$m. Pie charts represent the proportion of organoids with single (grey) and multiple (purple) lumen. White dot line delimitates the lumen perimeter while, the white discontinuous like delimitates the organoid perimeter. **(C)** Plots the ratio of the lumina perimeter mean over the organoid perimeter at day 1, day 2, day 3 and day 4 of culture in control (black) and DASA (organge) (horizontal bold lines show the median; * $p<0.05$, ** $p<0.005$, **** $p<0.0001$, two-way ANOVA).

multiple lumens concomitant with the lumen resolution (Figure 16C). Contrarily, the DASA treated organoids at day 3 and 4 still present a low ratio of the lumen perimeter mean over the organoid perimeter, since the lumen resolution has not taken place (Figure

16C). All in all, these data confirms the role of YAP signalling in lumen resolution during secondary neurulation.

# Proteome landscape of centrosome maturation in neural progenitor cells.

## Identification of bait proteins for the proximity labelling (BioiD2) screening.

Based on the published data, here we selected two proteins associated to the mature centrosome appendages (CEP89, and CEP164), as bait proteins for the screening of the protein landscape of mature centriole. CEP89 was selected as mature centrosome bait, since it presents a central localization in both DAB and SDA. In both cases CEP89 is located between the stem and the head of the structures (Blanco-Ameijeiras, Lozano-Fernández and Martí, 2022) (represented in grass green in Figure 7, 17A). Additionally, CEP164 was selected as mature centrosome bait since it is located in the outer compartment of the DA (Tanos *et al.*, 2013; Yang *et al.*, 2018; Bowler *et al.*, 2019; Lo *et al.*, 2019) (represented in green pine in Figure 7, 17A). Moreover, it is located in the transition in between the DAB and the DAM (Bowler *et al.*, 2019). Thus, CEP164 neighbouring proteome could give new insights on the proteomic composition of the DAM and its interaction with the DAB, since these substructures had been recently described.

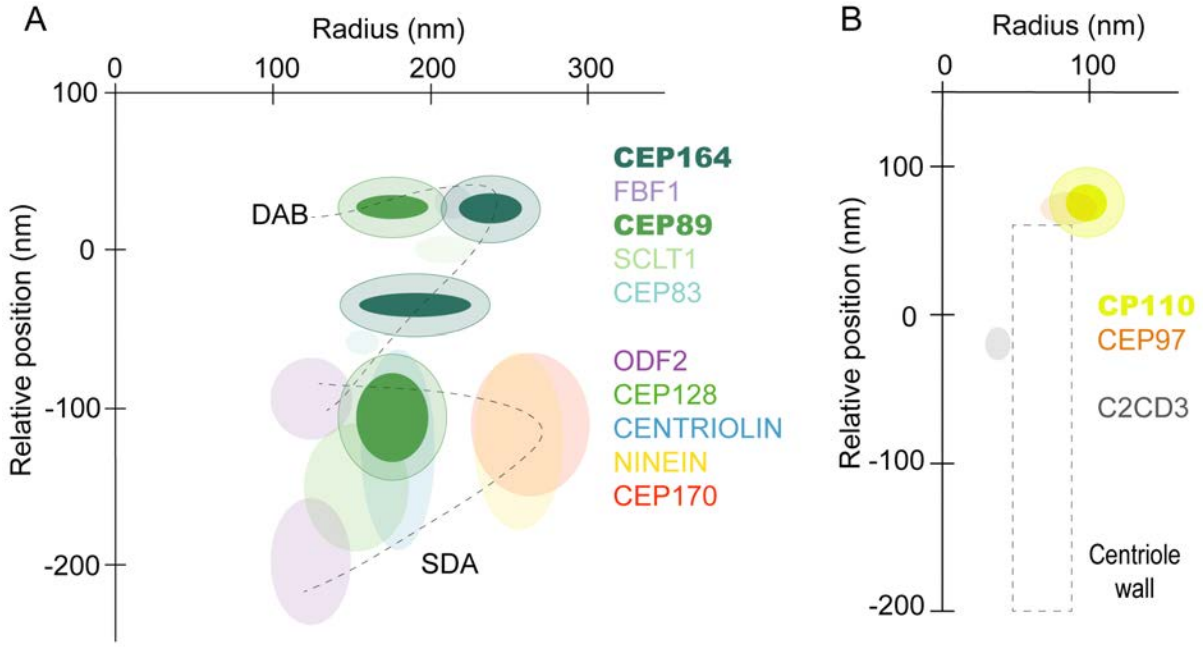

**Figure 17: Centriole structures protein map. (A)** Protein map of the distal and subdistal proteins (adepted from Chong et al., 2020). Selected mature centriole bait proteins are represented in bright grass green (CEP89) and bright green pine (CEP164). **(B)** Protein map of the DCPs (addapted from Yang et al., 2018). Selected immature centriole bait protein (CP110) is represented in bright yellow. In both cases, lighter halos represent the biotinylation activity radio of the BioID2 (bait protein radio plus 20nm) while the brighter perimeter represent space occupied by the bait protein fused with the BioID2 (bait protein radio plus 8nm).

So far, at the centriole ultrastructural level it has not been described yet any appendage exclusive of immature centrioles. However, they do present some proteins specifically enriched in comparison with its mature homologous, the DCPs. CP110 is one of these DCPs, it is located in the distal part of the centriole upon elongation until the maturation structures are assembled (Spektor *et al.*, 2007) (represented in yellow in Figure 17Band in orange in the Figure 6). Therefore, it could provide a proteomic picture of the distal part of the centrioles that are not mature. Thus, CP110 was selected as immature centrosome bait to identify new potential DCPs at the distal end of centrioles.

## Distribution of the selected baits in NPCs of the chick embryo NT

Early in development (HH12 chick embryos), NPCs undergo mainly proliferative symmetric divisions resulting in both daughter cells remaining as NPCs, and promoting tissue growth (Saade *et al.*, 2013; Le Dréau *et al.*, 2014b). Later in development (HH23 chick embryos) there is a switch towards neurogenesis so that upon cell division at least one daughter cell will undergo neuronal differentiation instead of remaining as a NPC. Since the mechanisms that control these specialized cell divisions of the NPCs correlates with the maturation of the centrosome (Wang *et al.*, 2009; Paridaen, Wilsch-Brauninger and Huttner, 2013; Saade *et al.*, 2017; Tozer *et al.*, 2017), we expected that in HH12 chick embryos mature centriole proteins are symmetrically distributed in both centrosomes before entering mitosis, while in HH23 chick the mature centriole proteins are absent in one (asymmetric neurogenic division) or both centrosomes (symmetric neurogenic division).

To monitor the dynamics of the selected bait proteins during centrosome duplication and maturation, *en face* chick embryo NT preparations were generated at these two developmental stages; HH12 and HH23 (Figure 18A). anti-FOP (FGFR1 Oncogene Partner (Yan, Habedanck and Nigg, 2006) and anti-CENTRIN2 (Satisbury, 1995) were used as a centriole markers. FOP staining appears as a single dot at $G_1$ and as two dots at $S/G_2$, since FOP immunostaining cannot resolve individual centrioles by confocal microscopy

(Figure 18A'). However, CENTRIN2 immunostaining appears as two dots at $G_1$ and four at $S/G_2$, since this staining resolve individual centrioles (Figure 18A' ').

At the $G_1$ phase of the cell cycle, prior to centrosome duplication, HH12 chick embryos show CEP89 largely associated with both centrioles labelled with CENTRIN2 (58,2%, Figure 18B, B', B' ' and Q,). Later in development (HH23) CEP89 staining associated with either one centriole (46,4%, Figure 18C, C', C' ' and Q) or none centriole (33%, Figure 18Q,). The analysis of CEP164 showed co-localization with FOP-labelled centrosomes (100%, Figure 18D, D', D' ' and Q), in early (HH12) NPCs. At later developmental stages (HH23), NPCs maintain CEP164 mainly associated with the centrosome (63,2%, Figure 18Q) but appears a subpopulation of NPCs that present no CEP164 centrosome association (36,9%, Figure 18E, E', E' ' and Q). Regarding CP110, the immature centriole protein selected as bait, the vast majority of the NPCs showed it associated with only one centriole labelled with CENTRIN2 (90,6%, Figure 18G, G', G' ' and Q), at the G1 phase of the cell cycle in early NPCs (HH12). Later, at HH23, CP110 is mainly associated with both centrioles (69,2%, Figure 18F, F', F' ' and Q).

At the $S/G_2$ phase of the cell cycle, NPCs have four centrioles due to the centriole duplication, that the CENTRIN2 staining is able to resolve as four dots. In early HH12 embryos, NPCs show CEP89 associated with two centrioles (74,1%, Figure 18H, H', H' ' and S). By contrast, the proportion of cells with CEP89 associated with two centrioles decreases at HH23 (34,4%, Figure 18S), and a high proportion of NPCs show CEP89 associated with one centriole (43,7%, Figure 18I, I', I' ' and S) or show no centriole association (21,9% Figure 18J, J', J' ' and S). The analysis of CEP164 revealed that at early stages (HH12), NPCs mostly show CEP164 associated with two FOP foci (79,5%, Figure 18K, K', K' ' and S), and that later in development (HH23 stage) the proportion of NPCs with CEP164 associated with two FOP foci decreases significantly (37,2%, Figure 18S), since most of them have CEP164 associated with one foci (46,5%, Figure 18L, L', L' ' and S) or show no centriole association (16,3% Figure 18M, M', M' ' and S). Regarding CP110, the immature centriole protein selected as bait, in early NPCs (HH12 embryos) CP110 appeared mostly associated with two centrioles (76,5%, Figure 18P, P', P' ' and S). By contrast, the proportion of cells with CP110 associated with three centrioles prevail at HH23 (53,8%, Figure 18O, O', O' ' and S). Meanwhile the subpopulation of NPCs with CP110 associated to all the four centrioles increases (15,4%, Figure 18N, N', N' ' and S).

Altogether, this analysis indicate that early NPCs symmetric proliferative division correlated with an enhanced CEP89 and CEP164-centriole association, as it is expected to

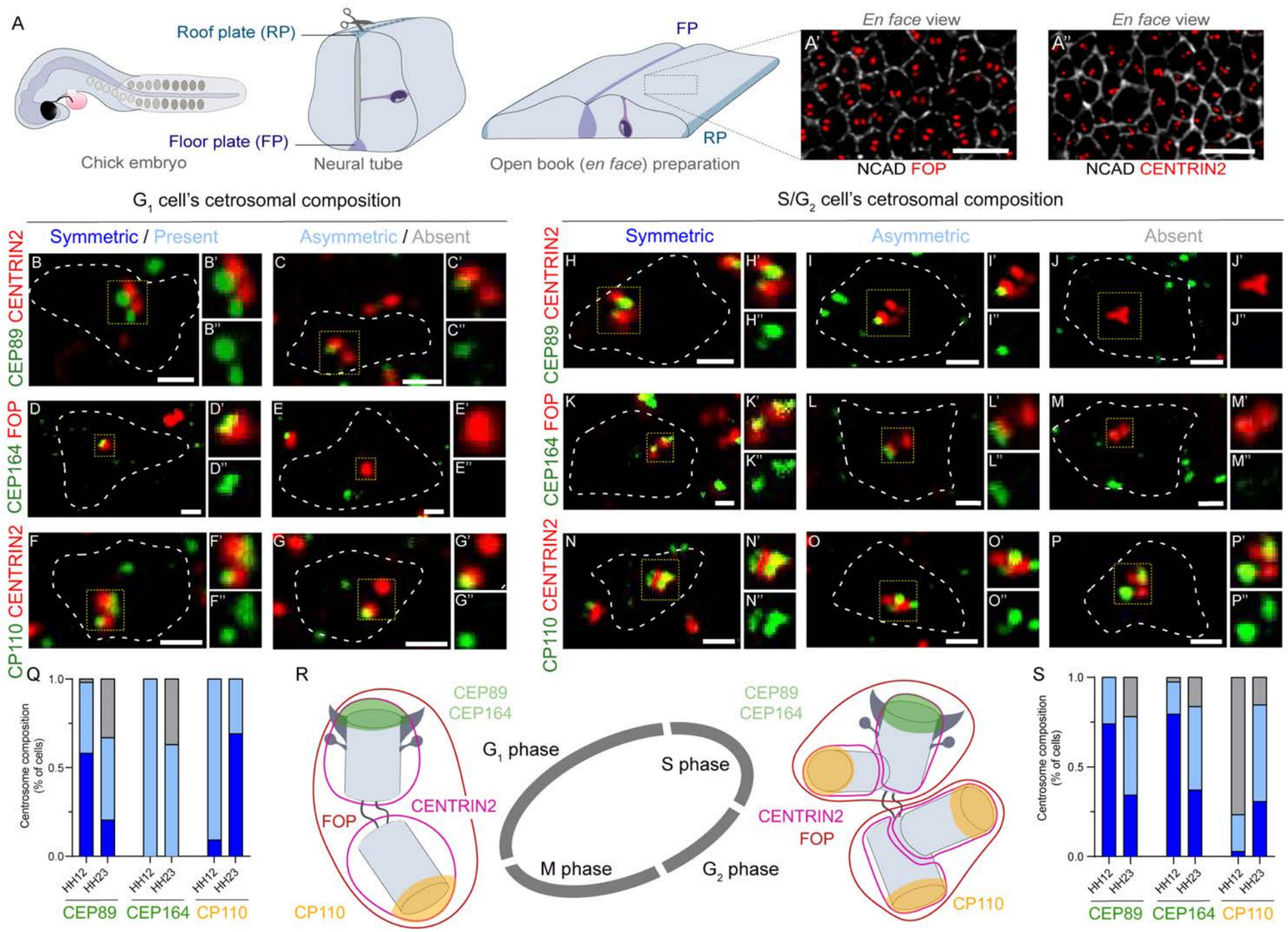


**Figure 18: CEP89 and CEP164 are endogenously associated to mature centrioles, while CP110 is associated to immature centrioles in chick embryo NPCs. (A)** Drawing of a stage HH14 chick embryo NT before and after *en face* dissection. These preparations allow the apical view of the NPCs feet, where the centrosomes can be stained with FOP (A') or CENTRIN2 (A''). Selected images of the different centriole association behaviours of CEP89 at $G_1$ **(B, C)** and $S/G_2$ **(H-J)**. Higher magnifications of the yellow boxed regions are shown in **B', C'**, **B'', C''**, **H'-J'** and **H''-J''**. Selected images of the different centriole association behaviours of CEP164 at $G_1$ **(D, E)** and $S/G_2$ **(K-M)**. Higher magnifications of the yellow boxed regions are shown in **D'**, **E'**, **D''**, **E''**, **K'-M'** and **K''-M''**. Selected images of the different centriole association behaviours of CP110 at $G_1$ **(F, G)** and $S/G_2$ **(N-P)**. Higher magnifications of the yellow boxed regions are shown in **F'**, **G'**, **F''**, **G''**, **N'-P'** and **N''-P''**. Discontinuous white lines were drawn over a NCAD staining to represent the apical foot limits of the NPC. Centrioles (red) are stained with CENTRIN2 (for CEP89 and CP110 images) and FOP (for CEP164 images). Yellow boxes limit the zoom in area in each case. Scale bars = 1um. **(Q)** Plots the proportions of NPCs with each behaviour at stage HH12 and HH23 during $G_1$ (for CEP89: at HH12 n=55 cells from 5 embryos, at HH23 n=97 cells from 5 embryos) (for CEP164: at HH12 n=18 cells from 5 embryos, at HH23 n=19 cells from 5 embryos) (for CP110: at HH12 n=32 cells from 5 embryos, at HH23 n=26 cells from 5 embryos). **(R)** Summary drawing showing the CEP89, CEP164 (green) association to mature centrioles and the CP110 (yellow) association to the immature centrioles during the cell cycle of a NPCs committed with to asymmetric division. Centriole staining resolution is represented in red for FOP and violet for CENTRIN2. **(S)** Plots the proportions of NPCs with each behaviour at stages HH12 and HH23 during $S/G_2$ (for CEP89: at HH12 n=27 cells from 5 embryos, at HH23 n=32 cells from 5 embryos) (for CEP164: at HH12 n=39 cells from 5 embryos, at HH23 n=44 cells from 5 embryos) (for CP110: at HH12 n=34 cells from 5 embryos, at HH23 n=26 cells from 5 embryos).

happen with the mature centriole proteins. While upon neurogenesis, its centriole association decreases since, neurogenic mitosis take place when centrosome maturation is partially or completely missing (Figure 18R). Although this is observed at both $G_1$ and $S/G_2$ NPCs, it is more evident in $S/G_2$ since the cell is closer to entering mitosis. In opposition to what was observed for CEP89 and CEP164, CP110 association with the centrioles increases upon the neurogenic switch in NPCs (Figure 18R). This localization dynamics match what would be expected for a centrosome immature protein.

Thus, it can be concluded that CEP89 and CEP164 indeed present mature centriole associated proteins dynamics in the chick embryo NPCs, while CP110 present immature centriole dynamics. Moreover, they act as *bona fide* maturation markers all along the cell cycle, since we observed the appropriate dynamics both at $G_1$ and $S/G_2$. Although we did not assess their distribution during mitosis, since it is the shortest phase of the cell cycle in NPCs (Saade *et al.*, 2013; Le Dreau *et al.*, 2014), the potential noise that those cells could introduce in the final proteomic analysis can be negligible.

## Myc-BioID2-CEP89, Myc-BioID2-CEP164 and Myc-BioID2-CP110 subcellular localization and proximity labelling in the chick embryo NT.

Once CEP89, CEP164 and CP110 were selected and validated in the chick embryo NT as centrosome proteins specific of mature and immature centrioles, their sequences were subcloned into a Myc-BioID2-MCS vector. Hence, each bait was fused to a Myc tag and to the BioID2 at the N terminal. Bait proteins in this fusion will localize the biotinylation enzyme in the proteomic subcellular environment of interest. There, the BioID2 will be active incorporating biotin to the neighbouring proteins in a few nm radio.

Although the three selected bait proteins endogenously behave as expected in the chick embryo NT, their fusion with the BioID2 enzyme may affect their distribution or even affect the enzymatic activity of the BioID2. To rule that out that, BioID2 constructs were electroporated in the chick embryo NT and their localization and activity was monitored with Streptavidin conjugated with a fluorophore. Streptavidin will identify the biotinylated proteome labelled by proximity (and the bait protein fused to the BioID2 *per se* since it will be also self-biotinylated).

All, CEP89, CEP164 and CP110 when fused with BioID2 show a centrosome localization (Figure 19A-C), as the endogenous proteins. However, the proteome labelled by proximity to the enzymatic activities showed slight differences as described below.

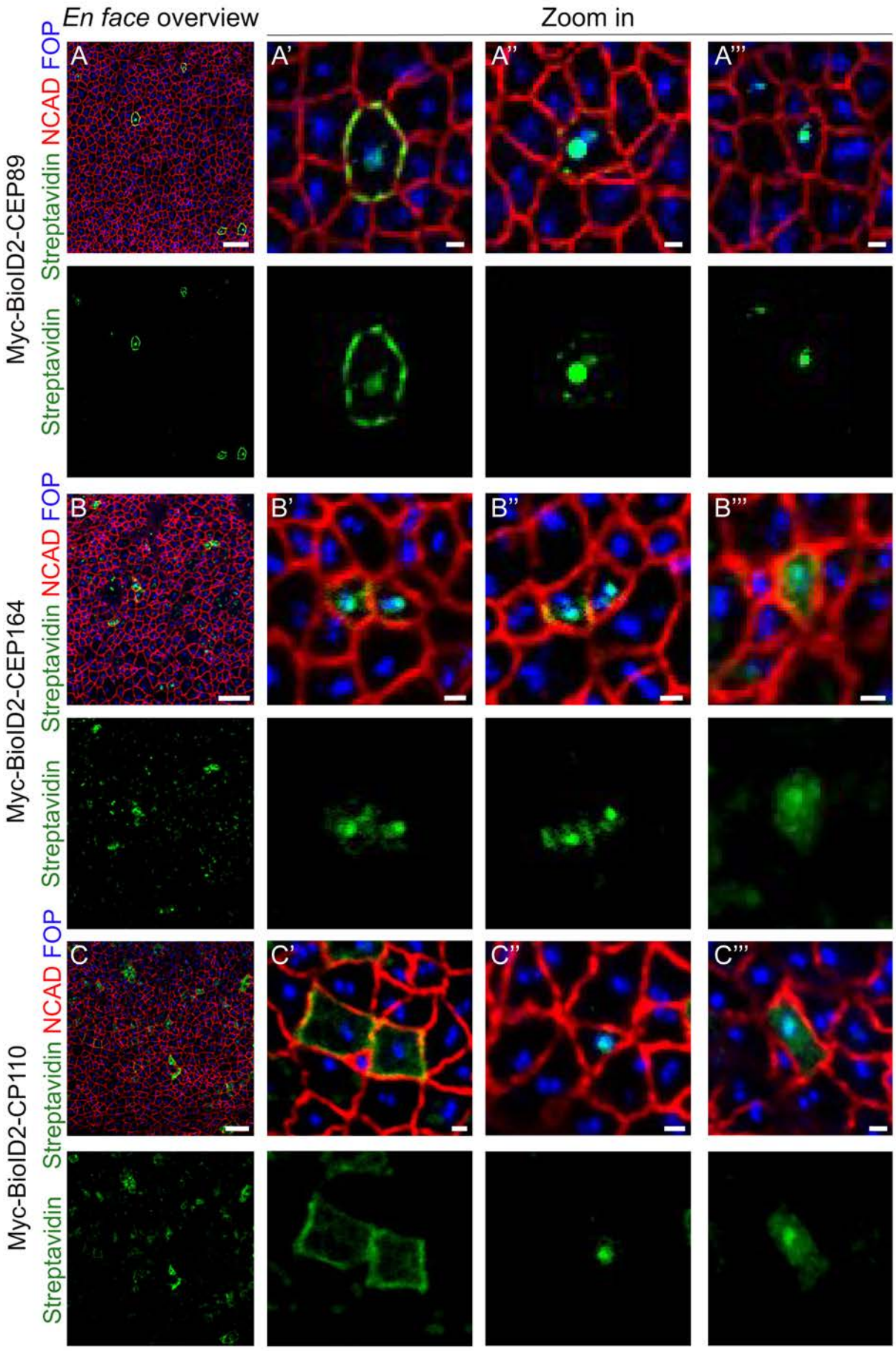
*En face* overview
Zoom in
Myc-BioID2-CEP89
Streptavidin NCAD FOP
Streptavidin
Myc-BioID2-CEP164
Streptavidin NCAD FOP
Streptavidin
Myc-BioID2-CP110
Streptavidin NCAD FOP
Streptavidin
A
A'
A''
A'''
B
B'
B''
B'''
C
C'
C''
C'''

**Figure 19: Upon BioID2 fusion the bait proteins still show centrosome localization.** Selected images of *en face* general view of Myc-CEP89-BioID2 **(A)**, Myc-CEP164-BioID2 **(B)** and Myc-CP110-BioID2 **(C)** electroporated chick embryo NT. Streptavidin (green) marks the biotinylation activity of the BioID2, FOP staining (blue) marks centrosome while NCAD (red) delimitates the apical foot of each NPCs. Scale bars = 10 $\mu$m. **(A'-C', A''-C'' and A'''-C''')** Selected zoom in images from NPCs electroporated with the BioID2 constructs showing the different centrosome distributions for each protein bait. Scale bars = 1 $\mu$m.

Upon Myc-BioID2-CEP89 electroporation, some NPCs show a single biotinylation focus that specifically co-localize with the centrosome (Figure 19A'''). In addition to the centrosome localization, biotinylated proteins may also form a ring that co-localizes with the NCAD at the apical end foot of NPCs (Figure 19A'). This apical ring of biotinylated proteins may correspond to centrosome components traveling along the MT ring that aligns with the apical ACTIN cable and adherens-junctions (as previously reported for some centrosome components by Kasioulis et al., 2017; Moss et al., 2007; Shao et al., 2020). There are some intermediate scenarios where proteins biotinylated by Myc-BioID2-CEP89 have a centrosome focus and a partial biotinylation of the apical ring (Figure 19A'').

Similarly, NPCs electroporated with Myc-BioID2-CEP164 showed biotinylation at the centrosome in the apical end foot of the cell (Figure 19B'), or at the centrosome and partially at apical ring (Figure 19B''). In addition, a subpopulation of NPCs showed centrosome biotinylation together with faint biotinylation covering most of the apical area (Figure 19B'''), that could correspond to centriole satellite trafficking, since reminds the reported localization of centriole satellites components such as AZ1 or PCM1 (Kubo and Tsukita, 2003; Chamling *et al.*, 2014).

Lastly, upon Myc-BioID2-CP110 electroporation some NPCs show biotinylation at the periphery of the apical end foot of the cell (Figure 19C'), at a single focus that specifically co-localize with the centrosome (Figure 19C''), as well as diffuse biotinylation that extends in most of the apical area (Figure 19C''').

Although there are slightly different biotinylation distributions, all in all the three BioID2 constructs have a centrosome specific activity biotinylating the proteomic environments of interest.

## Proximity labelling of centrosome proteome in the chick embryo NT encountered technical limitations

Isolation of the proteome of interest requires the immunoprecipitation (IP) of the biotinylated proteins. To optimize IP from chick embryo NT, we generated protein extracts

from non-electroporated chick embryo trunks (8 to 10 embryos per sample), since there is endogenous biotinylation in the tissue. Additionally, biotinylated BSA was incorporated in parallel as positive control. Upon IP, most of the biotinylated proteins are retained in the elution fraction in both the biotinylated BSA and the chicken embryo NT protein extracts (Figure 20A). This is even more evident when the proteins are separated by WB (Figure 20B).

The centrosome BioID2 constructs were co-electroporated with H2B-GFP, as electroporation control, since the BioID2 has no fluorescence signal. Subsequently, the samples were FAC sorted to isolate the electroporated subpopulation of NPCs, in order to reduce the noise that might be introduced by endogenous biotinylated proteins (Figure 20C). As the mature/immature centrosome association of the selected baits is maintained along the cell cycle (Figure 18Q, S), there is no need to sort the cells at any specific phase. Thus, from 25 to 30 chick embryo trunks, 100.000 to 250.000 GFP+ cells were isolated and processed for protein extraction, IP and MS (Figure 20C).

To the best of our knowledge this was the first time that a BioID2 proximity labelling assay was carried out in the chick embryo NT. Then, as positive control human *in vitro* samples were included in the experimental pipeline. Those samples were HEK293 cells transfected with the centrosome BioID2 constructs by our collaborators Dr. Balbastre and Prof. De la Luna (CRG, Barcelona).

Both chick and human data were compared against a published BioID2 dataset of CEP89 (Gupta *et al.*, 2015), independently generated with a different construct and experimental pipeline. Most of the published protein prays (Figure 20D') were also detected in our human samples (Figure 20D' '). This validates the Myc-BioID2-CEP89 construct and the experimental pipeline that we generated, since it is able to reproduce the published data with a different construct for the same bait and BioID enzyme.

However, chick data does not overlap with the human data (Figure 20D' ' '). Moreover, there is no centrosome associated protein detection in the chicken samples, which goes against the immunohistochemistry data (Figure 19). Thus, it seems that the BioID2 biotinylated proteins are not detected in the chicken samples for same reason independent of the construct and the purification process. In order to further discard any contamination enrichment in the chick samples that could mask the specific hits, common contaminants detected in human (Figure 20D') versus chick (Figure 20D' ') samples were compared, observing no significant differences.

Similarly, almost no centrosome associated protein were detected in the case of Myc-Cep164-BioID2 and Myc-CP110-BioID2 (data not shown). All this, point to some tissue specific limitations further explained in the discussion section.

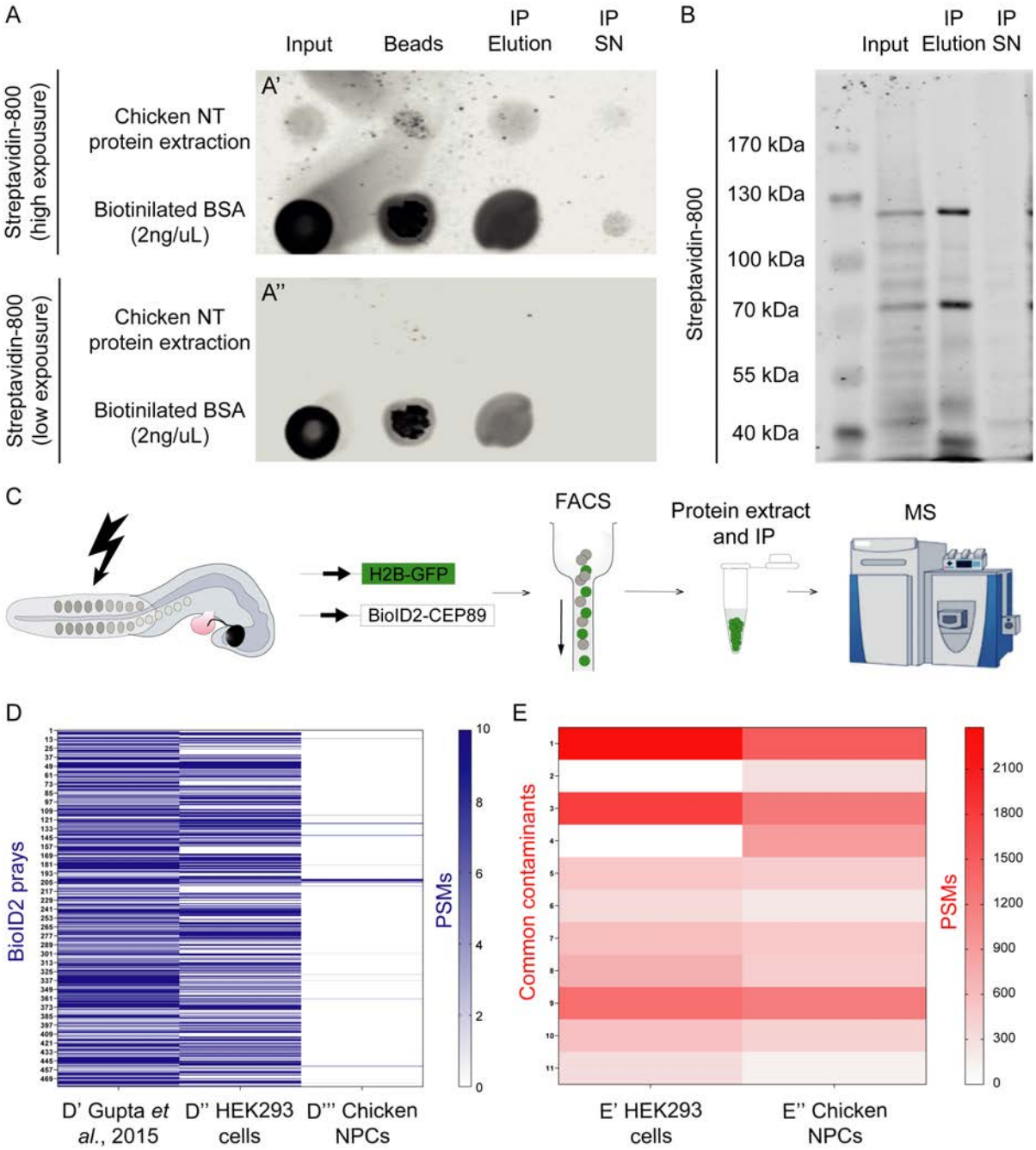


**Figure 20: MS results from the BioID2 analysis are not conclusive in chick embryo NT samples.** **(A)** Dot blot of chick embryo protein extract IP with Streptavidin beads. Membrane is imaged at low **(A')** and high exposure **(A'')** settings. **(B)** Western blot of chick embryo protein extract IP with Streptavidin beads. **(C)** Schematic drawing of the experimental procedure optimized for the proximity labelling analysis of the centrosome composition in chick embryo NT samples. **(D)** Heat map of the MS results comparing CEP89 proximity proteome from **(D')** published data on human cell lines with a different BioID2 construct (Gupta *et al.*, 2015), **(D'')** data on human cell lines with the in house generated BioID2 construct, and **(D''')** data on chick embryo NT with the in house generated BioID2 cosntruct. Color intensity responds to the number of PSMs for each pray protein detected. **(E)** Heat map of the common contaminants detected in both the human **(E')** and chick **(E'')** samples. Color intensity responds to the number of PSMs for each contaminant protein detected.

## *In silico* screening of mature centrosome proteins and *in vivo* characterization of the candidates.

Since possible technical limitations for the *in vivo* proximity labelling screening were envisioned, the experimental approach was combined with a complementary *in silico* screening pipeline. This *in silico* approach was designed to identify candidate proteins to be part of the centrosome mature structures that may have an instructive role in the organization of symmetric divisions in NPCs and hence in the control of CNS tissue growth.

To that end, a bibliographical search of proteins reported in the literature to be localized to mature centriole structures was combined (Figure 7) with a search on public repositories for protein interactions. The BioGRID database, that contains 725,012 non-redundant curated interactions in Homo sapiens (updated Nov 2021), was used to interrogate for the interactome of DAs (10 selected proteins), SDAs (10 selected proteins) and cilia BB (11 selected proteins). This generate a preliminary cloud of proteome interactions in the mature centrioles. The screening approach was based in the premise that: if a protein interaction with the components of a specific structure is overrepresented, it is reasonably probable that this protein is also a member of such structure. Thus, in this specific case, proteins that had been reported to interact with several components of the mature centrosome structures (DA, SDA and Y-linker), probably are also components of those (Figure 21A). Ultimately conferring the centrosome maturation properties and impacting the fate of the NPC.

The so far characterized components of the DA, SDA and Y-linker structures were used as reference for the mature centrosome structures proteins (Blanco-Ameijeiras, Lozano-Fernández and Martí, 2022). The reported interactions of those proteins were taken from the BioGRID database (Oughtred *et al.*, 2021). Interactors were then sorted for the number of centrosome maturation components interaction. In Figure 21Bis showed the reported interactions of SSX2IP and OFD1 with several reference centrosome mature proteins. These are two of the candidate proteins identify by their overrepresented interaction with the reference centrosome mature proteins, name from now on in the text as *superinteractors*. The top 14 *superinteractors* were obtained setting up an arbitrary cut off of 12 out of 31 interactions with the reference mature centrosome components (Table 9).

Reviewing the published literature on those *superinteractors,* 12 out of the 14 candidate proteins (CEP128, PCM1, CEP170, OFD1, CEP131, SSX2IP, HAUS8, NDC80, NINL, CCDC138, CEP135 and NIN) had been reported to be somehow related with centrosome structures (Staples *et al.*, 2012; Bärenz *et al.*, 2013; Bachmann-Gagescu *et al.*, 2015; Hori and Toda, 2016; Helgeson *et al.*, 2018; L. Wang *et al.*, 2018; Mönnich *et al.*, 2018; Gheiratmand *et al.*, 2019; Chong *et al.*, 2020; Schweizer *et al.*, 2021; Blanco-Ameijeiras,

Lozano-Fernández and Martí, 2022). Moreover, among these candidate proteins there are some that are also part of the reference centrosome mature proteins, which validate our premise that if a protein interacts with several components of a structure is reasonably probable to be part of that structure.

Once identified, overexpression constructs were generated for those *superinteractor* candidates. Gain of function (GOF) experiments were then carried out to test their functional role in the regulation of the specialized NPCs modes of division. As a readout for the global fate commitment, the pan-neuronal markers HuC/D was assessed by immunohistochemistry upon over-expression of SSX2IP and OFD1. If they have an instructive role in the maturation of the centrosome and ultimately in the control of the NPCs modes of division (proliferative vs neurogenic divisions), a reduction in the neurogenesis would be observed upon overexpression of those proteins.

Preliminary results assessing the capacity of *superinteractor* proteins to modulate neurogenesis showed that SSX2IP overexpression (in HH14 chick embryo NT) was sufficient to reduce neurogenesis (HuC/D+ cells) at 24hpe (Figure 21C). 17,4% (± 9,4 SD; n=8, Figure 21E) of the PB-GFP control electroporated cells are positive for HuC/D (Figure 21C'), while 5,3% (± 3,4 SD; n=14, Figure 21E) of the PB-SSX2IP-3XFLAG electroporated cells are positive for HuC/D (Figure 21C' '). However, at 48 hpe there are no significant differences in the percentage of neuronal differentiating cells (Figure 21D, E). OFD1 overexpression, however, was insufficient to reduce neurogenesis in HH14 chick embryo NT (HuC/D+ cells) either at 24 or 48hpe (Figure 21F-H). Although these preliminary results might indicate some activity of these *superinteractor* proteins in regulating neurogenesis, the results are very weak. Thus, more candidates need to be tested, and complementary readouts need to be assessed to prove the hypothesis, as it is further detailed in the discussion section.

| | | Centrosome interactions | | | |
|---|---|---|---|---|---|
| **Protein** | **Subcellular compartment** | **DA (t=10)** | **SDA (t=10)** | **Cilia (t=10)** | **Total** |
| CEP128 | Inner compartment of the SDA | 6 | 7 | 4 | 17 |
| PCM1 | Centriolar satellites | 6 | 7 | 3 | 16 |
| CEP170 | Outter compartment of the SDA and centriole proximal end | 4 | 9 | 3 | 16 |
| OFD1 | DA and SDA assembler complex at the centriole distal end and centriole satellites | 4 | 8 | 3 | 15 |
| CEP131 | Centriole core and centriole satellites | 4 | 7 | 3 | 14 |
| SSX2IP | BB and centriole satellites | 4 | 7 | 3 | 14 |
| HAUS8 | Centriole lumen and spindle pole | 3 | 7 | 4 | 14 |
| NDC80 | Kinetochore-MTs interphase | 5 | 6 | 2 | 13 |
| NINL | SDA and TZ | 4 | 6 | 3 | 13 |
| CCDC138 | BB and centriole satellites | 3 | 7 | 3 | 13 |
| CEP135 | Procentriole | 5 | 5 | 2 | 12 |
| NIN | Outter component of the SDA | 4 | 6 | 2 | 12 |
| GPATCH1 | Spliceosomes | 3 | 6 | 3 | 12 |
| WDR83 | Vesicles, nucleoplasm and centriole satellites | 3 | 6 | 3 | 12 |

**Table 9: Superinteractors identified, their subcelular localization and centrosome interactions.**

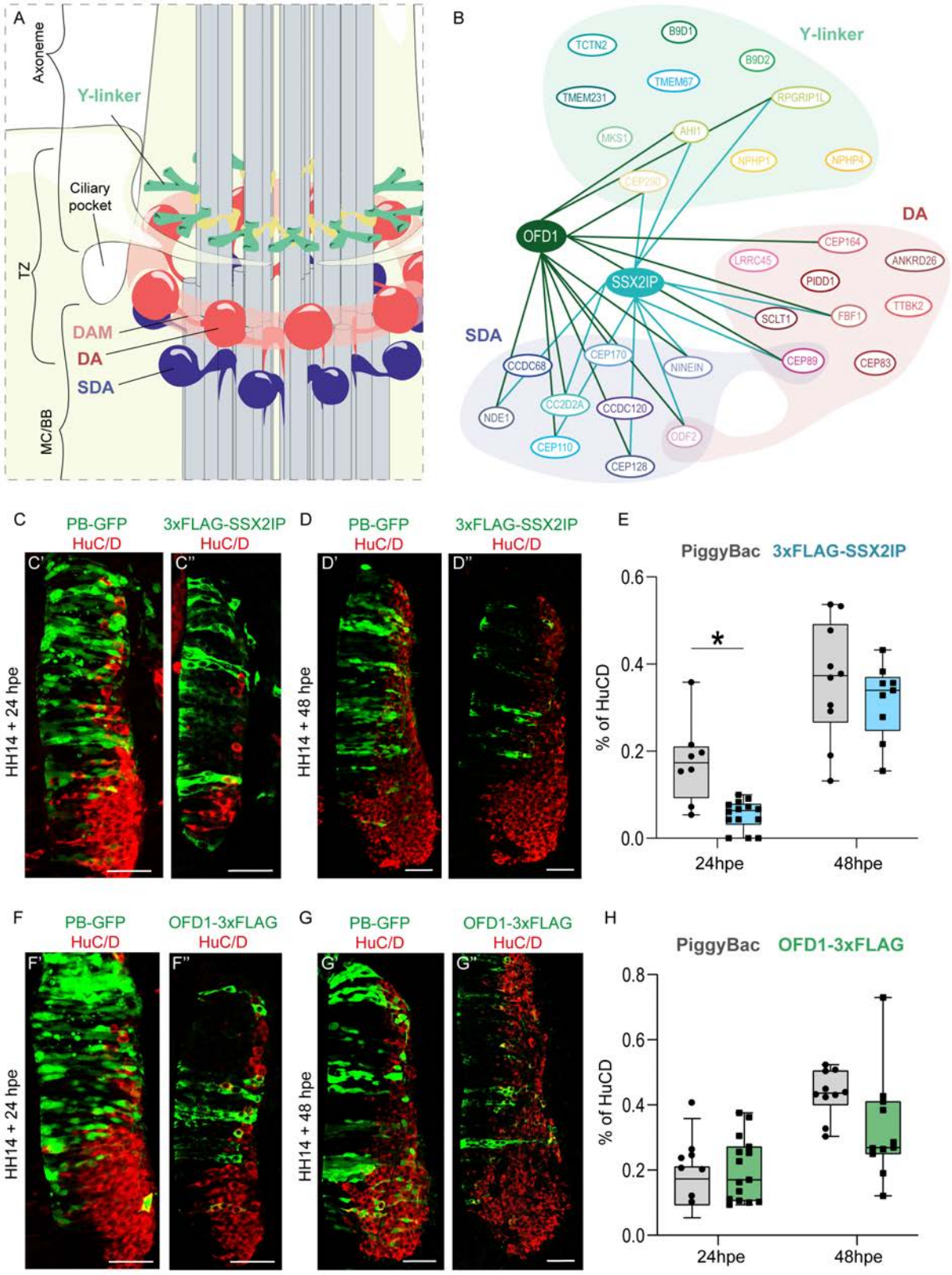
A
Axoneme
Y-linker
Ciliary pocket
TZ
DAM
DA
SDA
MC/BB
B
Y-linker
B9D1
TCTN2
B9D2
TMEM67
TMEM231
RPGRIP1L
MKS1
AHI1
NPHP1
NPHP4
CEP290
DA
OFD1
CEP164
LRRC45
ANKRD26
SSX2IP
PIDD1
TTBK2
SCLT1
FBF1
SDA
CEP170
CCDC68
NINEIN
CEP89
CEP83
CC2D2A
CCDC120
NDE1
ODF2
CEP110
CEP128
C
PB-GFP HuC/D
3xFLAG-SSX2IP HuC/D
C'
C''
HH14 + 24 hpe
D
PB-GFP HuC/D
3xFLAG-SSX2IP HuC/D
D'
D''
HH14 + 48 hpe
E
PiggyBac 3xFLAG-SSX2IP
% of HuCD
0.6
0.4
0.2
0.0
*
24hpe
48hpe
F
PB-GFP HuC/D
OFD1-3xFLAG HuC/D
F'
F''
HH14 + 24 hpe
G
PB-GFP HuC/D
OFD1-3xFLAG HuC/D
G'
G''
HH14 + 48 hpe
H
PiggyBac OFD1-3xFLAG
% of HuCD
0.8
0.6
0.4
0.2
0.0
24hpe
48hpe

**Figure 21: Overrepresented interactions with the so far characterized proteins of the centrosome maturation structures are good candidates for being part of those structures and centrosome maturation proteins *per se*.** **(A)** Drawing of the maturation structures of the centriole in the base of the cilia. Y-linker are represented in aquamarine, DA in red and SDA in blue. **(B)** Network representation of OFD1 (solid green ellipse) and SSX2IP (solid blue ellipse) interactions with the protein components of the mature centrosome structures. Those are two example of the *superinteractor* proteins identified *in silico*. The subcellular localization of the reference proteins (solid white ellipses) is taken from Blanco-Ameijeiras et al., 2022. Interactions are taken from the BioGRID database (Oughtred *et al.*, 2021). **(C-D)** Selected images of transverse sections of HH14 stage chick embryos NT at 24 hpe **(C)** and 48 hpe **(D)** electroporated with PB-GFP (control) **(C'-D')** and PB-SSX2IP-3xFLAG (2ug/uL) **(C''-D'')** (green), showing differentiating neurons stained with HuC/D antibody (red). Scale bars = 50um. **(E)** Plots percentage of electroporated cells HuC/D+ in control and PB-SSX2IP-3xFLAG electroporated cells (horizontal bold lines show the median; n=8-14 tissue slices from 6 embryos/condition;* p>0.05 two-way ANOVA). **(F-G)** Selected images of transverse sections of HH14 stage chick embryos NT at 24 hpe **(F)** and 48 hpe **(G)** electroporated with PB-GFP (control) **(F'-G')** and PB-OFD1-3xFLAG (2ug/uL) **(F''-G'')** (green), showing differentiating neurons stained with HuC/D antibody (red). Scale bars = 50um. **(H)** Plots percentage of electroporated cells HuC/D+ in control and PB-OFD1-3xFLAG electroporated cells (horizontal bold lines show the median; n=8-14 tissue slices from 6 embryos/condition;* p>0.05 two-way ANOVA).

# Discussion

CNS development requires the specification of neural tissue and the morphogenic events that shape it into a hollow NT. Then, the embryonic NT should grow and generate all the cell diversity present in the healthy and functional organ. Since it perfectly recapitulates the early CNS development and due to their simplicity, the SpC is the most suitable tissue model to study these sequence of events.

In the first chapter of this thesis, a new human 3D *in vitro* model for anterior and posterior SpC is set up. In these human organoid models, the neural specification, morphogenic NT formation and its grow can be followed. Most importantly, the posterior SpC human organoids fill a gap in the field. Although secondary NT formation was studied in the past (Schoenwolf and Delongo, 1980; Shimokita and Takahashi, 2011; Dady *et al.*, 2014), it was mostly using animal models. Since human specific peculiarities had been described (Muller and O'Rahilly, 1987; O'rahilly and Muller, 1994; Nakatsu, Uwabe and Shiota, 2000; O'Rahilly and Muller, 2002; Saitsu and Shiota, 2008; Dady *et al.*, 2014) and NTDs have high prevalence in births (Morris *et al.*, 2016), study this process in a 3D human context is very relevant. In this work it is characterized a human organoid model were hESC are guided into NMPs, expressing *SOX2* and *BRA* and then into NPCs, which maintain the *SOX2* and lose *BRA* expression as it happens *in vivo.* Moreover, the NPCs are organized as an epithelium surrounding a central lumen. NPCs located the centrosome and cilia at the lumen surface, where the polarity complexes are organized mimicking the polarity features of NPCs characterized *in vivo.* Additionally, in parallel to this epithelialization, the cell rearranges that shape the hollow NT formation *in vivo*, like the cell intercalation driving lumen resolution (Gonzalez-Gobartt *et al.*, 2021), can be also followed in this new human SpC organoid model (data not shown).

In the second chapter of this thesis, a screening to identify new mature centrosome components that would be potentially controlling the NPCs proliferation/differentiation rates (Saade *et al.*, 2018) was done independently with an *in vivo*, using the chick embryo as model, and an *in silico* approach. Unfortunately, the *in vivo* approach faced technical limitations intrinsic of the chick embryo model that prevent any successful identification

of new candidates. However, the *in silico* approach provided a list of candidates to start their functional analysis, that is still on going.

## Further genetic validation is needed to definitely confirm the anterior and posterior SpC specification of the human SpC organoid models.

To optimize the human SpC organoid model, the sequence of events that shape the CNS *in vivo* were sequentially reproduced. First, a drug guidance protocol was set up to differentiate *in vitro* the hESC into NPCs both directly, and through NMPs generation. To do so, a signaling modulation screening was performed in the hESC.

For the direct NPCs differentiation, the double SMAD inhibition guidance protocol had been broadly used in both 2D and 3D cultures for neural specification, (Chambers *et al.*, 2009). It is based on the role of BMP and TGF$\beta$ inhibition signals reported *in vivo* to guide the neural plate formation in the anterior regions of the embryo (Marshal *et al.*, 1991; Hemmati-Brivanlou and Melton, 1992; Smith and Harland, 1992; Sasai *et al.*, 1994; Valenzuela *et al.*, 1995; Patel *et al.*, 1996; Connolly, Patel and Cooke, 1997; Stottmann *et al.*, 2006; Ybot-Gonzalez *et al.*, 2007; Lee *et al.*, 2007; Elkabetz *et al.*, 2008; Eom *et al.*, 2012). However, the posterior NPCs specification had not been characterized *in vitro.* Moreover, in the posterior regions of the embryo, the neural specification is mediated by the NMPs generation which make the signaling modulation more complex (Figure 2). In this work, the signaling pathways reported to guide *in vivo* the NMPs generation and commitment with NPC differentiation were emulated with drug supplementation *in vitro.* Besides testing several drug combinations, few supplementation strategies were also assessed. Initially, since *in vivo*, the posterior NT formation is mediated by NMPs generation, sequential drug treatments for NMPs and for NPCs specification were tested (Figure 9B). However, they proof to be quite inefficient compared to simultaneous treatments. This is probably due to the fact that if maintained for too long, the signals that specify NMPs promote mesodermal differentiation (Martin and Kimelman, 2012; Garriock *et al.*, 2015).

As read out of this screening for neural specification, the endogenous expression levels of SOX2 and BRA were monitored, as well as the epithelial morphology. Those readouts allow a crude genetic identification of the cells and their commitment with the embryonic cell lineages through immunostaining. Although, *a posteriori* validation is often needed, having fast and cheap initial readouts are key points to set up an efficient screening protocol. In this case, a RNA seq is going to be performed to definitely validate the anterior and posterior SpC identity of the human SpC organoids.

## Grafting the human organoids.

Although in this thesis, the SpC identities are guided through constant concentration of drugs that emulate morphogen signaling pathways (Wnt, FGF, BMP, TGF$\beta$ and RA), physiologically those signaling pathways are modulated by gradients of the proteins (Christian, 2012; Le Dréau and Martí, 2012). This difference may have an impact on the self-assembly capacity of the cells, for instance in the symmetry breaking and patterning establishment within the organoid. It would be interesting to assess whether doing the neural guidance with gradients could further optimize the model.

To establish such gradients, the easiest approach would be to use beads coated with the guidance drugs (Ben-Reuven and Reiner, 2020). When placed near to the organoids, the bead would generate a gradient of those drugs. However, the concentration and gradient distance cannot be tightly controlled, which would difficulty the optimization and reproducibility of the approach. Solving these limitations, there had been published some chip devices that allow more control over the gradient properties (Koh and Hagiwara, 2022). However, those devices significantly scale the complexity of the protocol and their cost.

Alternatively, to solve the limitations of both beads and chips, use an animal embryo model as a living bioreactor may allow the guidance for SpC organoids generation in a more physiological context, where the morphogens are distributed in gradients in the different axes, with the proper concentration and distances. Thus, with this approach, organoids would be grafted in the host embryos, where the primordium of the NT might have been previously removed by dissection.

Regarding the choice of the animal model, historically, the chicken embryo had been extensively used as a grafting model for studding CNS development (Alvarado-Mallart, 2000) because of its accessibility and easy manipulation, as well as low economic cost. Thus, the chicken embryo would be a good candidate for serve as bioreactor for the organoids. Indeed, it had been already used for assessing the integration of dissociated dorsal SpC rosettes already specified (Dady *et al.*, 2022).

## hESC achieved the MET as they commit with the neural lineage.

*In vivo* during secondary neurulation concomitantly with the neural specification the cells undergo a MET (Gonzalez-Gobartt *et al.*, 2021). Although the epithelial morphology was assessed as a readout for the neural specification screening, a further characterization of the polarity features is needed in order to confirm the MET. This initial epithelial morphology assessment is limited to a ventricle opening visualized by aPKC staining (Figure 9-11).

During chick secondary neurulation the MET starts with the apical localization of the centrosome, followed by the NCAD and ZO1 accumulation in the apical end foot of the NPCs. Finally, the aPKC is located immediately apical to the ZO1 domain (Figure 12). In both the anterior and posterior human SpC organoid models optimized in this thesis, the apical organization of the centrosome, cilia and the apical complex components (NCAD, ZO1 and aPKC) observed *in vivo* are reproduced. However, the sequence of events for the apical polarity organization had not been assessed *in vitro*, since without the pre-aggregation step, the MET happened too fast. However, with this last modification of the protocol, the sequence of apical polarization can be assessed experimentally and indeed further experiments will be carried out for that.

The nuclei of the cells organized in a pseudostratified epithelium undergo INM, as they travel between apical and basal, in coordination with the cell cycle. Thus, INM is a further emergent feature upon MET. In both the anterior and posterior human SpC organoid models, the nuclei to centrosome distance present a wide variability when compared with the mesenchymal-like organoids (Figure 13F). Since in the SpC organoids, the centrosome is located in the apical end foot of the NPCs during interphase, these variability of the distance to the nuclei may represent cells undergoing INM in different phases of the cell cycle. On the contrary, in the mesenchymal-like organoids during interphase the centrosome is at the same distance to the nuclei. To further confirm these cell dynamics in the SpC organoids, live imaging was performed and INM migration was indeed followed along cell cycle and used as landmark to do an estimation of the cell cycle phases length (Figure 14).

## Compartmentalization of the posterior SpC organoid make it more affordable and useful.

BM is a triggering signal for MET in the secondary NT formation. During chick embryo secondary neurulation, the BM is deposited in the periphery of the medullary cord following a dorsal to ventral gradient. The cells that are contacting it will epithelialize while the central cells that do not reach the BM remain with a mesenchymal morphology. These central cells are responsible for the multiple lumen formation and their clearing allow the lumen resolution, the two last events of secondary neurulation.

As it has been just mentioned, without the pre-aggregation step the organoids open a lumen almost immediately. This is due to the fact that the matrigel in culture works as an artificial BM. Thus, when the hESC are seeded in small clamps of cells (between 1 and 4 cells per clamp approximately), all the cells are in contact with the matrigel and immediately undergo the MET, open a single lumen very early. In order to better mimic the events taking place in vivo, this setback was solved with the pre-aggregation step that

guarantee that when seeded into matrigel the hESC aggregates are big enough so not all the cells contact it. Thus, emulating the multiple lumen formation and lumen resolution observed during chick secondary neurulation.

Although the pre-aggregation step protocol reproduces the multiple lumen formation and lumen resolution in this organoid system, the posterior SpC organoids protocol without the pre-aggregation perfectly emulates the neural specification and MET. Besides, the final tissue had the same features observed *in vivo* in the caudal NT. This simpler version of the protocol is shorter and requires less equipment, thus it is a cheaper and faster model that allows the study of those secondary neurulation events.

Since, time and money are two important issues of organoid model usage in science, this compartmentalization of the secondary neurulation process allows the usage of different versions of the protocol depending on the scientific question of each experiment, ultimately making the model more efficient.

## Human organoids are responsive to dorso-ventral patterning signals.

Once the NT is formed, NPCs are going to acquire specific neural fates depending on their exposure to specific local environmental signals that will progressively restrict their developmental potential and allows the generation of the neural cells diversity needed in a heathy CNS (Le Dréau and Martí, 2012). The exposure of environmental signals depends on the NPCs position in the dorso-ventral axis of the embryo, which determines the different progenitor domains during dorso-ventral patterning. Although the triggering signals for the dorso-ventral patterning come from the surrounding tissue, two NT intrinsic signaling centers are eventually specified, the FP and the RP.

*In vitro* there are few examples of NT organoid protocols that respond to patterning signals (Meinhardt *et al.*, 2014; Zheng *et al.*, 2019) and establish signaling centers in the tissue that break its symmetry. It had been tested weather the SpC organoid models set up and characterized in this work are also responsive to environmental signals to break the symmetry and organize a dorso-ventral patterning. The data was not included in the thesis since it is very preliminary and further experiments need to be done, but it had been observed that a short pulse of RA in the anterior SpC organoids is sufficient to induce the formation of a FOXA2 FP-like structure. It would be interesting to assess whether this also happen in the posterior SpC organoids and how well resolve is the patterning (e.g. how many NPCs domain they organize?).

## NPCs proliferate and differentiate in the human organoids.

These SpC organoid models, once completed the neurulation process, are able to proliferate and increase in size through symmetric proliferative divisions, as the tissue grows maintaining the NPCs identity. Eventually they are also able to undergo neurogenic differentiation, since it had been observed that at later culture time, there are cells positive for TUJ1 (data not shown), a postmitotic pan-neuronal marker.

A further characterization of the dynamics of proliferation *versus* neurogenesis will be important to characterize this SpC organoids as a model for CNS growth. The chicken embryo NT data gathered in previous works of the group can be used as reference data for SpC proliferation/neurogenesis balance. Whether in the organoids the neurogenesis switch takes place in a tightly restricted timing would significantly impact the applicability of the models. Its tightly time regulation would imply a neurogenesis synchrony in the organoids droplets that would facilitate the analysis of factors that modulate the onset of the neurogenesis and therefore the CNS growth.

Actually, they could even be used for the validation of the centrosome maturation candidates identified with the *in silico* approach in the second chapter of this thesis, assessing its relevance for human CNS growth. Besides, the SpC organoids could be used to perform the proximity labeling screening for mature and immature centrosome components. Although it would be an *in vitro* approach, SpC organoids provide a 3D human tissue organization, that potentially make the results more clinically relevant.

## Bait candidates for mature and immature centrosome.

For the screening of new centrosome components that may impact the NPCs commitment with proliferation and neurogenesis, both mature and immature centrosome components already characterized had been used as bait proteins for the proximity labeling approach. Although the idea was to identify new centrosome components that confer the centrosome with maturation properties, some competence mechanisms had been reported along the maturation process, where immature specific components must be removed from the centriole as the first step of maturation (Blanco-Ameijeiras, Lozano-Fernández and Martí, 2022). For instance, CP110 interacts directly with CEP97 to form a DCP complex, which needs to be removed from the distal end of the daughter centriole before the final phase of centriole maturation (Spektor *et al.*, 2007). Thus, a pathological condition where there is a malfunction of the centrosome maturation process can be caused by both defective mature and immature centrosome components. Ultimately, this malfunction would drive a premature differentiation of the NPCs generating a CNS growth failure, and MCPH-like phenotypes.

Hence, MCPH can be genetically caused by mutations in both mature and immature centrosome components and a better proteomic characterization of both is relevant to improve its genetic diagnosis capacity.

## Technical limitations of the chick model for BioID2 proximity labeling assays.

Unfortunately, as it had been described in the results of the second chapter of this thesis, the proximity labelling approach for the centrosome components screening cannot be done in the chick embryo NT. This is due to two main technical limitations for the BioID2 assay specific of the chick embryo NT that may not affect other models: (1) chick NPCs had intermediate to lower transfection efficiency, and (2) the chicken model has a limited cell gathering capacity. Both of them cooperate to significantly reduce the enrichment of the BioID2 biotinylated proteins per sample, that subsequently cannot be identified by MS.

Firstly, chick embryo electroporation only affects to one side of the NT. Moreover, in the electroporated side, the proportion of electroporated cells is limited (20-40%). (Figure 22A). These efficiency problems had been tried to bypass by increasing the number of embryos per condition and by FAC sorting of the electroporated NPCs. However, in light of the MS results, this strategy had been proven to be unsuccessful. This is at least partially explained by the different electroporation efficiency of the H2B-GFP (electroporation control) and the BioID2 constructs. Although the electroporation control gets transfected in 30,98% (±0,13 (SD); n=12) of the NPCs in the electroporation side, the Myc-BioID2-CEP89 gets transfected in only 11,82% (±0,06 (SD); n=11) (Figure 4B). Since the purification of the electroporated subpopulation of NPCs is based on the H2B-GFP signal, BioID2+ cells are diluted with BioID2- cells. Besides, the NPCs had endogenous biotinylated proteins that could mask the BioID2 proximity labelled proteins if the BioID2- dilution is high enough. However, the endogenous biotinylated proteins seem to be much less abundant that the BioID2 biotinylated proteins (Figure 22A). Thus, this dilution of the BioID2 biotinylated proteins, although relevant, it is unlikely to be main factor explaining the negative results obtained by MS.

Other factor that may cooperate with the electroporation efficiency problem is the total amount of cells gathered. In the *in vitro* culture cell lines approach, millions of cells transfected with the BioID2 constructs are pulled together per sample. Meanwhile, in the chick embryo NT experimental pipeline, hundreds of thousands cells transfected with the electroporation control are FAC sorted from pulls of 25 to 30 embryos. Only around 5% of the dissociated cells from chick embryo trunks are electroporated with the H2B-GFP (Figure 22C). Thus, the total amount of BioID2 biotinylated proteins is significantly lower in the *in vivo* chick embryo NPCs samples. Although the number of embryos could be

increased to improve those numbers, due to the electroporation limitations it is no feasible to reach an amount of BioID2 biotinylated proteins comparable to the *in vitro* cell culture assays.

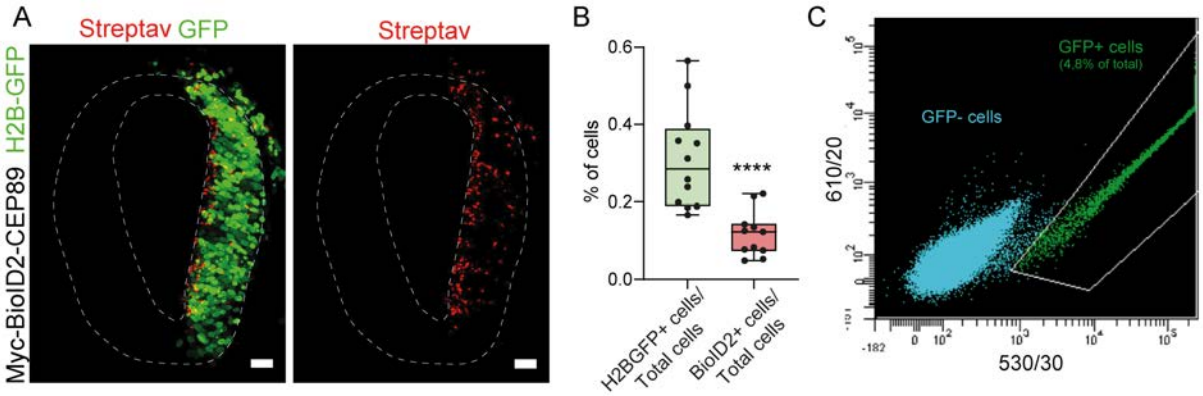


**Figure 22:** Myc-BioID2-CEP89 gets electroporated at a lower efficiency than electroporation control **(A)** Selected images from transversal section of chick embryos NT co-electroporated with Myc-BioID2-CEP89 and H2B-GFP (green). Biotinylated proteins are detected with Streptavidin (red). Dash line draws the NT using DAPI staining as reference. Scale bars = 20um. **(B)** Plots the percentage of cells electroporated with H2B-GFP in the electroporated side versus the percentage of cells electroporated with Myc-BioID2-CEP89 in the electroporated side. (horizontal lines show the median; n=12, 12 sections from 5 embryos; ****p<0.0001 Mann-Whitney test). **(C)** FAC sorting plot showing the gating used for GFP+ cells isolation.

All in all, these technical limitations make the chicken embryo NT an inappropriate model for BioID2 proximity labelling approach with the current technology. However, there are some modifications in the experimental pipeline that could mitigate those technical constrains. By substituting the Myc tag of the BioID2 construct with a fluorescent protein, there would be no need to include an electroporation control. Thus, the limitations derived from the differences in the electroporation efficiency would be removed. However, the size of the fusion protein would dramatically increase, since most of the fluorescence proteins are approximately the same size as the BioID2 (˜20kDA). This could affect the localization of the bait protein or its interactions, thus, introducing noise in the screening. Alternatively, the fluorescent protein sequence could be added after an IRES sequence included in the BioID2 plasmid downstream the BioID2 fusion protein sequence, mimicking a polycistronic mRNA. The drawback of this strategy would be that the fluorescent protein expression would be less efficient that the BioID2 fusion protein, improving the enrichment but restricting even further the cell gathering capacity.

## Alternative models to do the *in vivo* approach.

Although most BioID studies have applied proximity labeling to *in vitro* cell culture systems, there are few examples in the literature where *in vivo* approaches had been explored using mice, Zebrafish or Drosophila (Spence et al., 2019; Feng et al., 2020; Rudolph et al., 2020; Mannix et al., 2019; Cho et al., 2020, Pronobis et al 2021). However, in all those *in vivo* approaches, the fusion protein was genetically engineered by knock in, which implies substituting the bait protein by the fusion protein BioiD2-bait. This significantly improves the enrichment limitations that we observed in the chicken experimental approach, since all the cells that would express the endogenous protein will have the BioID2 activity.

However, the generation and maintenance of the knock in lines is much more expensive and time consuming that the chicken embryo electroporation. Another drawback derived from the knock in engineering is the time control of the BioID2 activity. Since we had observed that in the chicken the biotinylation activity of the enzyme works with the endogenous levels of biotin, if that also happens in the zebrafish or mice knock in, there will be no time restriction for the proximity labelling. Thus, due to the high dynamism of centrosome maturation, the MS will detect biotinylated proteins that used to be in the proteomic landscape of the centrosome, but may not be in there anymore; introducing noise to the results.

## *In silico* analysis identify new candidates.

Due to technical limitations found for the chick embryo *in vivo* approach, the screening for the proteomic landscape of mature and immature centrosome was finally tackled with an *in silico* approach. From that analysis, a list of candidate proteins to be associated with the mature centriole were sorted out, the *superinteractors*. Subsequently, those candidates must be functionally validated for its role in the CNS growth.

For the functional validation, the neurogenesis was assessed by HuC/D immunostaining upon GOF of the *superinteractor* in chick embryo NT. This show mostly negative results in the few candidates analysed so far. However, different readouts should be also explored to have more conclusive results on the CNS growth modulation capacity of the candidates. HuC/D are pan-neuronal markers that are quite downstream on a potential CNS growth modulation that allow some compensation effects that could mask a phenotype. Assess the mode of division commitment of the NPCs upon GOF of the *superinteractor* may be a more accurate readout, since the candidates are proposed to modulate the maturation of the centrosome, which would be directly instructive for the mode of division. Thus, this readout would be more direct that neurogenesis.

Moreover, since the maturation structures of the centriole are assembled in a build in

fashion (extensively described in the introduction), it is possible that for the GOF to show an effect on centrosome maturation (and ultimately in the CNS growth) some candidates must be co-overexpressed. Thus, different combinations of the candidates must be also tested together.

Finally, although we start the validation inducing a GOF of the candidates since it is technically easier to do generate the needed genetically engineering tools, candidates should also be validated through LOF. In the future, shRNA vectors will be generated and electroporated in the chick embryo NT for that purpose.

# Conclusions

(1) hESC can be *in vitro* guided to acquire the neuro-mesodermal progenitor identity.

(2) hESC can self-organize into NT like structures.

(3) hESC can be in vitro guided to build SpC organoids with different anterior-posterior identities.

(4) The cellular and subcellular organization of human SpC organoids mimic the features of the embryonic NPCs.

(5) Posterior SpC Organoids can be guided to mimic tissue dynamics similar to those occurring during secondary neurulation in the chick embryo.

(6) Posterior SpC Organoids required YAP activity to resolve a single central lumen.

(7) Posterior SpC Organoids are suitable biomodels to study human SpC development and associated NTDs.

(8) The chick embryo neural tube has technical limitations to perform an *in vivo* proximity labelling screening for centrosome proteins.

(9) The *in silico* screening identified a cluster of *superinteractor* centrosome proteins, that might contribute to centrosome maturation.

# Bibliography


Aaku-Saraste, E., Hellwig, A. and Huttner, W.B. (1996) 'Loss of occludin and functional tight junctions, but not ZO-1, during neural tube closure--remodeling of the neuroepithelium prior to neurogenesis.', *Developmental biology*, 180(2), pp. 664–679. Available at: https://doi.org/10.1006/dbio.1996.0336.

Afonso, C. and Henrique, D. (2006) 'PAR3 acts as a molecular organizer to define the apical domain of chick neuroepithelial cells', *J Cell Sci*, 119(Pt 20), pp. 4293–4304. Available at: https://doi.org/10.1242/jcs.03170.

Agircan, F.G., Schiebel, E. and Mardin, B.R. (2014) 'Separate to operate: Control of centrosome positioning and separation', *Philosophical Transactions of the Royal Society B: Biological Sciences*, 369(1650). Available at: https://doi.org/10.1098/rstb.2013.0461.

van den Akker, E. *et al.* (2002) 'Cdx1 and Cdx2 have overlapping functions in anteroposterior patterning and posterior axis elongation', *Development*, 129(9), pp. 2181–2193. Available at: https://doi.org/10.1242/dev.129.9.2181.

Albano, R.M. *et al.* (1994) 'Expression of inhibin subunits and follistatin during postimplantation mouse development: decidual expression of activin and expression of follistatin in primitive streak, somites and hindbrain', *Development*, 120(4), pp. 803–813. Available at: https://doi.org/10.1242/dev.120.4.803.

Alvarado-Mallart, R.M. (2000) 'The chick/quail transplantation model to study central nervous system development', *Progress in Brain Research*, 127, pp. 67–98. Available at: https://doi.org/10.1016/S0079-6123(00)27006-4.

Amin, S. *et al.* (2016) 'Cdx and T Brachyury Co-activate Growth Signaling in the Embryonic Axial Progenitor Niche', *Cell Reports*, 17(12), pp. 3165–3177. Available at: https://doi.org/10.1016/j.celrep.2016.11.069.

Anderson, C.T. and Stearns, T. (2009) 'Centriole age underlies asynchronous primary cilium growth in mammalian cells', *Curr Biol*, 19(17), pp. 1498–1502. Available at:

https://doi.org/10.1016/j.cub.2009.07.034.

Arquint, C., Gabryjonczyk, A.M. and Nigg, E.A. (2014) 'Centrosomes as signalling centres', *Philosophical Transactions of the Royal Society B: Biological Sciences*, 369(1650). Available at: https://doi.org/10.1098/rstb.2013.0464.

Attardo, A. *et al.* (2008) 'Live imaging at the onset of cortical neurogenesis reveals differential appearance of the neuronal phenotype in apical versus basal progenitor progeny', *PLoS ONE* [Preprint]. Available at: https://doi.org/10.1371/journal.pone.0002388.

Aulehla, A. *et al.* (2003) 'Wnt3a plays a major role in the segmentation clock controlling somitogenesis', *Developmental Cell*, 4(3), pp. 395–406. Available at: https://doi.org/10.1016/S1534-5807(03)00055-8.

Azimzadeh, J. and Marshall, W.F. (2010) 'Building the centriole', *Current Biology*, 20(18), pp. R816–R825. Available at: https://doi.org/10.1016/j.cub.2010.08.010.

Bachmann-Gagescu, R. *et al.* (2015) 'The Ciliopathy Protein CC2D2A Associates with NINL and Functions in RAB8-MICAL3-Regulated Vesicle Trafficking', *PLoS Genetics*, 11(10), pp. 1–28. Available at: https://doi.org/10.1371/journal.pgen.1005575.

Bahe, S. *et al.* (2005) 'Rootletin forms centriole-associated filaments and functions in centrosome cohesion', *Journal of Cell Biology* [Preprint]. Available at: https://doi.org/10.1083/jcb.200504107.

Bärenz, F. *et al.* (2013) 'The centriolar satellite protein SSX2IP promotes centrosome maturation', *Journal of Cell Biology*, 202(1), pp. 81–95. Available at: https://doi.org/10.1083/jcb.201302122.

Bärenz, F., Mayilo, D. and Gruss, O.J. (2011) 'Centriolar satellites: Busy orbits around the centrosome', *European Journal of Cell Biology*, 90(12), pp. 983–989. Available at: https://doi.org/10.1016/j.ejcb.2011.07.007.

Baye, L.M. and Link, B.A. (2007) 'Interkinetic nuclear migration and the selection of neurogenic cell divisions during vertebrate retinogenesis', *Journal of Neuroscience*, 27(38), pp. 10143–10152. Available at: https://doi.org/10.1523/JNEUROSCI.2754-07.2007.

Bedzhov, I. and Zernicka-Goetz, M. (2014) 'Self-organizing properties of mouse pluripotent cells initiate morphogenesis upon implantation', *Cell*, 156(5), pp. 1032–1044. Available at: https://doi.org/10.1016/j.cell.2014.01.023.

Ben-Reuven, L. and Reiner, O. (2020) 'Toward spatial identities in human brain organoids-on-chip induced by morphogen-soaked beads', *Bioengineering*, 7(4), pp. 1–17. Available at: https://doi.org/10.3390/bioengineering7040164.

Bénazéraf, B. and Pourquié, O. (2013) 'Formation and Segmentation of the Vertebrate Body Axis', *Annual Review of Cell and Developmental Biology*, 29(1), pp. 1–26. Available at: https://doi.org/10.1146/annurev-cellbio-101011-155703.

Del Bene, F. *et al.* (2008) 'Regulation of neurogenesis by interkinetic nuclear migration through an apical-basal notch gradient', *Cell*, 134(6), pp. 1055–1065. Available at: https://doi.org/10.1016/j.cell.2008.07.017.

Del Bene, F. (2011) 'Interkinetic nuclear migration: Cell cycle on the move', *EMBO Journal*, 30(9), pp. 1676–1677. Available at: https://doi.org/10.1038/emboj.2011.114.

Birey, F. *et al.* (2017) 'Assembly of functionally integrated human forebrain spheroids', *Nature*, 545(7652), pp. 54–59. Available at: https://doi.org/10.1038/nature22330.

Blanco-Ameijeiras, J., Lozano-Fernández, P. and Martı, E. (2022) 'Centrosome maturation – in tune with the cell cycle', *Journal of Cell Science*, 135(2). Available at: https://doi.org/10.1242/jcs.259395.

Blassberg, R. *et al.* (2022) 'Sox2 levels regulate the chromatin occupancy of WNT mediators in epiblast progenitors responsible for vertebrate body formation', *Nature Cell Biology*, 24(5), pp. 633–644. Available at: https://doi.org/10.1038/s41556-022-00910-2.

Bornens, M. (2012) 'The centrosome in cells and organisms', *Science* [Preprint]. Available at: https://doi.org/10.1126/science.1209037.

Bowler, M. *et al.* (2019) 'High-resolution characterization of centriole distal appendage morphology and dynamics by correlative STORM and electron microscopy', *Nature Communications*, 10(1). Available at: https://doi.org/10.1038/s41467-018-08216-4.

Bryant, D.M. *et al.* (2014) 'A molecular switch for the orientation of epithelial cell polarization', *Dev Cell*, 31(2), pp. 171–187. Available at: https://doi.org/10.1016/j.devcel.2014.08.027.

Buchman, J.J. *et al.* (2010) 'Cdk5rap2 interacts with pericentrin to maintain the neural progenitor pool in the developing neocortex', *Neuron*, 66(3), pp. 386–402. Available at: https://doi.org/10.1016/j.neuron.2010.03.036.

Burigotto, M. *et al.* (2021) 'Centriolar distal appendages activate the centrosome-PIDDosome-p53 signalling axis via ANKRD26', *The EMBO Journal*, 40(4), pp. 1–22. Available at: https://doi.org/10.15252/embj.2020104844.

Burren, K.A. *et al.* (2008) 'Gene-environment interactions in the causation of neural tube defects: folate deficiency increases susceptibility conferred by loss of Pax3 function.', *Human molecular genetics*, 17(23), pp. 3675–3685. Available at: https://doi.org/10.

1093/hmg/ddn262.

Burt, D.W. (2005) 'Chicken genome: Current status and future opportunities', *Genome Research*, 15(12), pp. 1692–1698. Available at: https://doi.org/10.1101/gr.4141805.

Catala, M. *et al.* (1996) 'A spinal cord fate map in the avian embryo: while regressing, Hensen's node lays down the notochord and floor plate thus joining the spinal cord lateral walls', *Development*, 122(9), pp. 2599–2610. Available at: https://www.ncbi.nlm.nih.gov/pubmed/8787735.

Catala, M., Teillet, M.A. and Le Douarin, N.M. (1995) 'Organization and development of the tail bud analyzed with the quail-chick chimaera system', *Mech Dev*, 51(1), pp. 51–65. Available at: https://www.ncbi.nlm.nih.gov/pubmed/7669693.

Cearns, M.D. *et al.* (2016) 'Microtubules, polarity and vertebrate neural tube morphogenesis', *J Anat*, 229(1), pp. 63–74. Available at: https://doi.org/10.1111/joa.12468.

Chambers, S.M. *et al.* (2009) 'Highly efficient neural conversion of human ES and iPS cells by dual inhibition of SMAD signaling', *Nature Biotechnology*, 27(3), pp. 275–280. Available at: https://doi.org/10.1038/nbt.1529.

Chamling, X. *et al.* (2014) 'The Centriolar Satellite Protein AZI1 Interacts with BBS4 and Regulates Ciliary Trafficking of the BBSome', *PLoS Genetics*, 10(2). Available at: https://doi.org/10.1371/journal.pgen.1004083.

Chapman, S.C. *et al.* (2002) 'Analysis of Spatial and Temporal Gene Expression Patterns in Blastula and Gastrula Stage Chick Embryos', *Developmental Biology*, 245(1), pp. 187–199. Available at: https://doi.org/10.1006/dbio.2002.0641.

Chen, F. and LoTurco, J. (2012) 'A method for stable transgenesis of radial glia lineage in rat neocortex by piggyBac mediated transposition', *Journal of Neuroscience Methods*, 207(2), pp. 172–180. Available at: https://doi.org/10.1016/j.jneumeth.2012.03.016.

Chenn, A. *et al.* (1998) 'Intrinsic polarity of mammalian neuroepithelial cells.', *Molecular and cellular neurosciences*, 11(4), pp. 183–193. Available at: https://doi.org/10.1006/mcne.1998.0680.

Chong, W.M. *et al.* (2020) 'Super-resolution microscopy reveals coupling between mammalian centriole subdistal appendages and distal appendages', *eLife*, 9(e53580). Available at: https://doi.org/10.7554/eLife.53580.

Christian, J.L. (2012) 'Morphogen gradients in development: From form to function', *Wiley Interdisciplinary Reviews: Developmental Biology*, 1(1), pp. 3–15. Available at: https://doi.org/10.1002/wdev.2.

Clare, D.K. *et al.* (2014) 'Basal foot MTOC organizes pillar MTs required for coordination of beating cilia', *Nature communications* [Preprint]. Available at: https://doi.org/10.1038/ncomms5888.

Colas, J.F. and Schoenwolf, G.C. (2001) 'Towards a cellular and molecular understanding of neurulation', *Dev Dyn*, 221(2), pp. 117–145. Available at: https://doi.org/10.1002/dvdy.1144.

Comartin, D. *et al.* (2013) 'CEP120 and SPICE1 cooperate with CPAP in centriole elongation', *Current Biology*, 23(14), pp. 1360–1366. Available at: https://doi.org/10.1016/j.cub.2013.06.002.

Conduit, P.T., Wainman, A. and Raff, J.W. (2015) 'Centrosome function and assembly in animal cells', *Nature Reviews Molecular Cell Biology*, 16(10), pp. 611–624. Available at: https://doi.org/10.1038/nrm4062.

Connolly, D.J., Patel, K. and Cooke, J. (1997) *Chick noggin is expressed in the organizer and neural plate during axial development, but offers no evidence of involvement in primary axis formation, I.*

Copp, A.J. *et al.* (2015) 'Spina bifida', *Nat Rev Dis Primers*, 1, p. 15007. Available at: https://doi.org/10.1038/nrdp.2015.7.

Copp, A.J. and Greene, N.D.E. (2013) 'Neural tube defects--disorders of neurulation and related embryonic processes.', *Wiley interdisciplinary reviews. Developmental biology*, 2(2), pp. 213–227. Available at: https://doi.org/10.1002/wdev.71.

del Corral, R.D. *et al.* (2003) 'Opposing FGF and Retinoid Pathways Control Ventral Neural Pattern, Neuronal Differentiation, and Segmentation during Body Axis Extension', *Neuron*, 40(1), pp. 65–79. Available at: https://doi.org/10.1016/S0896-6273(03)00565-8.

Craige, B. *et al.* (2010) 'CEP290 tethers flagellar transition zone microtubules to the membrane and regulates flagellar protein content', *Journal of Cell Biology*, 190(5), pp. 927–940. Available at: https://doi.org/10.1083/jcb.201006105.

Criley, B.B. (1969) 'Analysis of embryonic sources and mechanims of development of posterior levels of chick neural tubes', *J Morphol*, 128(4), pp. 465–501. Available at: https://doi.org/10.1002/jmor.1051280406.

Cunha-Ferreira, I. *et al.* (2009) 'The SCF/Slimb Ubiquitin Ligase Limits Centrosome Amplification through Degradation of SAK/PLK4', *Current Biology*, 19(1), pp. 43–49. Available at: https://doi.org/10.1016/j.cub.2008.11.037.

Cunha-Ferreira, I. *et al.* (2013) 'Regulation of autophosphorylation controls PLK4 self-

destruction and centriole number', *Current Biology*, 23(22), pp. 2245–2254. Available at: https://doi.org/10.1016/j.cub.2013.09.037.

Cunningham, T.J. *et al.* (2015) 'Retinoic Acid Activity in Undifferentiated Neural Progenitors Is Sufficient to Fulfill Its Role in Restricting Fgf8 Expression for Somitogenesis', *PLOS ONE*. Edited by M. Mallo, 10(9), p. e0137894. Available at: https://doi.org/10.1371/journal.pone.0137894.

Czarnecki, P.G. and Shah, J. V. (2012) 'The ciliary transition zone: From morphology and molecules to medicine', *Trends in Cell Biology*, 22(4), pp. 201–210. Available at: https://doi.org/10.1016/j.tcb.2012.02.001.

Dady, A *et al.* (2014) 'Junctional neurulation: a unique developmental program shaping a discrete region of the spinal cord highly susceptible to neural tube defects', *J Neurosci*, 34(39), pp. 13208–13221. Available at: https://doi.org/10.1523/JNEUROSCI.1850-14.2014.

Dady, Alwyn *et al.* (2014) 'Junctional Neurulation: A unique developmental program shaping a discrete region of the spinal cord highly susceptible to neural tube defects', *Journal of Neuroscience*, 34(39), pp. 13208–13221. Available at: https://doi.org/10.1523/JNEUROSCI.1850-14.2014.

Dady, A. *et al.* (2022) 'Human spinal cord in vitro differentiation pace is initially maintained in heterologous embryonic environments', *eLife*, 11, pp. 1–32. Available at: https://doi.org/10.7554/elife.67283.

Davidson, L.A. and Keller, R.E. (1999) 'Neural tube closure in Xenopus laevis involves medial migration, directed protrusive activity, cell intercalation and convergent extension.', *Development (Cambridge, England)*, 126(20), pp. 4547–4556.

Decarreau, J. *et al.* (2017) 'The tetrameric kinesin Kif25 suppresses pre-mitotic centrosome separation to establish proper spindle orientation', *Nature Cell Biology* [Preprint]. Available at: https://doi.org/10.1038/ncb3486.

Dolk, H., Loane, M. and Garne, E. (2010) 'The prevalence of congenital anomalies in Europe.', *Advances in experimental medicine and biology*, 686, pp. 349–364. Available at: https://doi.org/10.1007/978-90-481-9485-8_20.

Le Douarin, N.M., Teillet, M.A. and Catala, M. (1998) 'Neurulation in amniote vertebrates: a novel view deduced from the use of quail-chick chimeras', *Int J Dev Biol*, 42(7), pp. 909–916. Available at: https://www.ncbi.nlm.nih.gov/pubmed/9853821.

Dowdle, W.E. *et al.* (2011) 'Disruption of a ciliary B9 protein complex causes meckel syndrome', *American Journal of Human Genetics* [Preprint]. Available at: https://

doi.org/10.1016/j.ajhg.2011.06.003.

Le Dreau, G. *et al.* (2014) 'The strength of SMAD1/5 activity determines the mode of stem cell division in the developing spinal cord', *J Cell Biol*, 204(4), pp. 591–605. Available at: https://doi.org/10.1083/jcb.201307031.

Le Dréau, G. *et al.* (2014a) 'The strength of SMAD1/5 activity determines the mode of stem cell division in the developing spinal cord', *Journal of Cell Biology*, 204(4), pp. 591–605. Available at: https://doi.org/10.1083/jcb.201307031.

Le Dréau, G. *et al.* (2014b) 'The strength of SMAD1/5 activity determines the mode of stem cell division in the developing spinal cord', *Journal of Cell Biology* [Preprint]. Available at: https://doi.org/10.1083/jcb.201307031.

Le Dreau, G. and Marti, E. (2012) 'Dorsal-ventral patterning of the neural tube: a tale of three signals', *Dev Neurobiol*, 72(12), pp. 1471–1481. Available at: https://doi.org/10.1002/dneu.22015.

Le Dréau, G. and Martí, E. (2012) 'Dorsal-ventral patterning of the neural tube: A tale of three signals', *Developmental Neurobiology*, 72(12), pp. 1471–1481. Available at: https://doi.org/10.1002/dneu.22015.

Duband, J.-L. (2010) 'Diversity in the molecular and cellular strategies of epithelium-to-mesenchyme transitions: Insights from the neural crest.', *Cell adhesion & migration*, 4(3), pp. 458–482. Available at: https://doi.org/10.4161/cam.4.3.12501.

Edri, S. *et al.* (2019) 'Neuro-mesodermal progenitors (NMPs): A comparative study between pluripotent stem cells and embryo-derived populations', *Development (Cambridge)*, 146(12). Available at: https://doi.org/10.1242/dev.180190.

Eiraku, M. *et al.* (2008) 'Self-Organized Formation of Polarized Cortical Tissues from ESCs and Its Active Manipulation by Extrinsic Signals', *Cell Stem Cell*, 3(5), pp. 519–532. Available at: https://doi.org/10.1016/j.stem.2008.09.002.

Elkabetz, Y. *et al.* (2008) 'Human ES cell-derived neural rosettes reveal a functionally distinct early neural stem cell stage (Genes and Development (2008) 22, (152-165))', *Genes and Development*, 22(9), p. 1257. Available at: https://doi.org/10.1101/gad.1616208.1995.

Elosegui-Artola, A. *et al.* (2017) 'Force Triggers YAP Nuclear Entry by Regulating Transport across Nuclear Pores', *Cell* [Preprint]. Available at: https://doi.org/10.1016/j.cell.2017.10.008.

Eom, D.S. *et al.* (2012) 'Bone morphogenetic proteins regulate hinge point formation during neural tube closure by dynamic modulation of apicobasal polarity', *Birth Defects*

*Res A Clin Mol Teratol*, 94(10), pp. 804–816. Available at: https://doi.org/10.1002/bdra.23052.

Ergün, S. and Wörsdörfer, P. (2022) 'Organoids, Assembloids and Embryoids: New Avenues for Developmental Biology, Disease Modeling, Drug Testing and Toxicity Assessment without Animal Experimentation', *Organoids*, 1(1), pp. 37–40. Available at: https://doi.org/10.3390/organoids1010004.

Evans, L.T. *et al.* (2021) 'ANKRD26 recruits PIDD1 to centriolar distal appendages to activate the PIDDosome following centrosome amplification', *The EMBO Journal*, 40(4), pp. 1–18. Available at: https://doi.org/10.15252/embj.2020105106.

Fang, G. *et al.* (2014) 'Centlein mediates an interaction between C-Nap1 and Cep68 to maintain centrosome cohesion', *Journal of Cell Science* [Preprint]. Available at: https://doi.org/10.1242/jcs.139451.

Florio, M., Borrell, V. and Huttner, W.B. (2017) 'Human-specific genomic signatures of neocortical expansion', *Curr Opin Neurobiol*, 42, pp. 33–44. Available at: https://doi.org/10.1016/j.conb.2016.11.004.

Formosa-Jordan, P.A.U. *et al.* (2013) 'Lateral inhibition and neurogenesis: Novel aspects in motion', *International Journal of Developmental Biology*, 57(5), pp. 341–350. Available at: https://doi.org/10.1387/ijdb.120259jf.

Fry, A.M. *et al.* (1998) 'C-Nap1, a novel centrosomal coiled-coil protein and candidate substrate of the cell cycle-regulated protein kinase Nek2', *Journal of Cell Biology*, 141(7), pp. 1563–1574. Available at: https://doi.org/10.1083/jcb.141.7.1563.

Fry, A.M. *et al.* (2017) 'Recent advances in pericentriolar material organization: Ordered layers and scaffolding gels', *F1000Research*, 6(0). Available at: https://doi.org/10.12688/f1000research.11652.1.

Fry, A.M., Bayliss, R. and Roig, J. (2017) 'Mitotic regulation by NEK kinase networks', *Frontiers in Cell and Developmental Biology* [Preprint]. Available at: https://doi.org/10.3389/fcell.2017.00102.

Gai, M. *et al.* (2016) 'ASPM and CITK regulate spindle orientation by affecting the dynamics of astral microtubules', *EMBO Rep*, 17(10), pp. 1396–1409. Available at: https://doi.org/10.15252/embr.201541823.

Gallera, J. (1971) 'Primary Induction in Birds', in, pp. 149–180. Available at: https://doi.org/10.1016/B978-0-12-028609-6.50008-X.

Garcia-Campmany, L. and Marti, E. (2007) 'The TGFbeta intracellular effector Smad3 regulates neuronal differentiation and cell fate specification in the developing spinal cord',

*Development*, 134(1), pp. 65–75. Available at: https://doi.org/10.1242/dev.02702.

Garriock, R.J. *et al.* (2015) 'Lineage tracing of neuromesodermal progenitors reveals novel Wnt-dependent roles in trunk progenitor cell maintenance and differentiation.', *Development (Cambridge, England)*, 142(9), pp. 1628–1638. Available at: https://doi.org/10.1242/dev.111922.

Gheiratmand, L. *et al.* (2019) 'Spatial and proteomic profiling reveals centrosome-independent features of centriolar satellites', *The EMBO Journal*, 38(14), pp. 1–22. Available at: https://doi.org/10.15252/embj.2018101109.

Gilula, N.B. and Satir, P. (1972) 'The ciliary necklace a ciliary membrane specialization', *Journal of Cell Biology* [Preprint]. Available at: https://doi.org/10.1083/jcb.53.2.494.

Gonzalez-Gobartt, E. *et al.* (2021) 'Cell intercalation driven by SMAD3 underlies secondary neural tube formation', *Developmental Cell*, 56(8), pp. 1147-1163.e6. Available at: https://doi.org/10.1016/j.devcel.2021.03.023.

Gouti, M. *et al.* (2014) 'In vitro generation of neuromesodermal progenitors reveals distinct roles for wnt signalling in the specification of spinal cord and paraxial mesoderm identity', *PLoS Biol*, 12(8), p. e1001937. Available at: https://doi.org/10.1371/journal.pbio.1001937.

Gouti, M. *et al.* (2017) 'A Gene Regulatory Network Balances Neural and Mesoderm Specification during Vertebrate Trunk Development', *Developmental Cell*, 41(3), pp. 243-261.e7. Available at: https://doi.org/10.1016/j.devcel.2017.04.002.

Gouti, M., Metzis, V. and Briscoe, J. (2015) 'The route to spinal cord cell types: a tale of signals and switches', *Trends Genet*, 31(6), pp. 282–289. Available at: https://doi.org/10.1016/j.tig.2015.03.001.

Graser, S. *et al.* (2007) 'Cep164, a novel centriole appendage protein required for primary cilium formation', *Journal of Cell Biology*, 179(2), pp. 321–330. Available at: https://doi.org/10.1083/jcb.200707181.

Greene, N.D. and Copp, A.J. (2014) 'Neural tube defects', *Annu Rev Neurosci*, 37, pp. 221–242. Available at: https://doi.org/10.1146/annurev-neuro-062012-170354.

Griffith, C.M., Wiley, M.J. and Sanders, E.J. (1992) 'The vertebrate tail bud: three germ layers from one tissue.', *Anatomy and embryology*, 185(2), pp. 101–113. Available at: https://doi.org/10.1007/bf00185911.

Gupta, G.D. *et al.* (2015) 'A Dynamic Protein Interaction Landscape of the Human Centrosome-Cilium Interface', *Cell*, 163(6), pp. 1484–1499. Available at: https://doi.

org/10.1016/j.cell.2015.10.065.

Habib, S.J. *et al.* (2013) 'A localized Wnt signal orients asymmetric stem cell division in vitro', *Science*, 339(6126), pp. 1445–1448. Available at: https://doi.org/10.1126/science.1231077.

Hamburger, V. and Hamilton, Howard L (1951) 'A series of normal stages in the development of the chick embryo', *Journal of Morphology* [Preprint]. Available at: https://doi.org/10.1002/jmor.1050880104.

Hamburger, V. and Hamilton, Howard L. (1951) 'A series of normal stages in the development of the chick embryo', *Journal of Morphology*, 88(1), pp. 49–92. Available at: https://doi.org/10.1002/jmor.1050880104.

Haremaki, T. *et al.* (2019) 'Self-organizing neuruloids model developmental aspects of Huntington's disease in the ectodermal compartment', *Nature Biotechnology*, 37(10), pp. 1198–1208. Available at: https://doi.org/10.1038/s41587-019-0237-5.

He, R. *et al.* (2013) 'LRRC45 Is a Centrosome Linker Component Required for Centrosome Cohesion', *Cell Reports*, 4(6), pp. 1100–1107. Available at: https://doi.org/10.1016/j.celrep.2013.08.005.

Heide, M., Long, K.R. and Huttner, W.B. (2017) 'Novel gene function and regulation in neocortex expansion', *Curr Opin Cell Biol*, 49, pp. 22–30. Available at: https://doi.org/10.1016/j.ceb.2017.11.008.

Helgeson, L.A. *et al.* (2018) 'Human Ska complex and Ndc80 complex interact to form a load-bearing assembly that strengthens kinetochore–microtubule attachments', *Proceedings of the National Academy of Sciences of the United States of America*, 115(11), pp. 2740–2745. Available at: https://doi.org/10.1073/pnas.1718553115.

Helps, N.R. *et al.* (2000) 'NIMA-related kinase 2 (Nek2), a cell-cycle-regulated protein kinase localized to centrosomes, is complexed to protein phosphatase 1', *Biochemical Journal* [Preprint]. Available at: https://doi.org/10.1042/0264-6021:3490509.

Hemmati-Brivanlou, A. and Melton, D.A. (1992) 'A truncated activin receptor inhibits mesoderm induction and formation of axial structures in Xenopus embryos', *Nature*, 359(6396), pp. 609–614. Available at: https://doi.org/10.1038/359609a0.

Henrique, D. *et al.* (2015) 'Neuromesodermal progenitors and the making of the spinal cord', *Development*, 142(17), pp. 2864–2875. Available at: https://doi.org/10.1242/dev.119768.

Hillier, L.W. et al. (2004) 'Sequence and comparative analysis of the chicken genome provide unique perspectives on vertebrate evolution', *Nature*, 432(7018), pp. 695–716.

Available at: https://doi.org/10.1038/nature03154.

Holmdahl, D.E. (1925) 'Experimentelle Untersuchungen uber die Lage der Grenze primarer und sekundarer Korperentwicklung beim Huhn.', *Anat Anz*, (59), pp. 393–396.

Hori, A. and Toda, T. (2016) 'Regulation of centriolar satellite integrity and its physiology', *Cellular and Molecular Life Sciences*. Birkhauser Verlag AG, pp. 213–229. Available at: https://doi.org/10.1007/s00018-016-2315-x.

Hsu, P.C. *et al.* (2018) 'The role of yes-associated protein (YAP) in regulating programmed death-ligand 1 (PD-L1) in thoracic cancer', *Biomedicines*, 6(4), pp. 1–10. Available at: https://doi.org/10.3390/biomedicines6040114.

Hu, D.J. *et al.* (2013) 'Dynein recruitment to nuclear pores activates apical nuclear migration and mitotic entry in brain progenitor cells', *Cell*, 154(6), pp. 1300–1313. Available at: https://doi.org/10.1016/j.cell.2013.08.024.

Huang, N. *et al.* (2017) 'Hierarchical assembly of centriole subdistal appendages via centrosome binding proteins CCDC120 and CCDC68', *Nature Communications*, 8. Available at: https://doi.org/10.1038/ncomms15057.

Ibrahim, R. *et al.* (2009) 'Electron tomography study of isolated human centrioles', *Microscopy Research and Technique*, 72(1), pp. 42–48. Available at: https://doi.org/10.1002/jemt.20637.

Ishii, Y. and Mikawa, T. (2005) 'Somatic transgenesis in the avian model system', *Birth Defects Research Part C: Embryo Today: Reviews*, 75(1), pp. 19–27. Available at: https://doi.org/10.1002/bdrc.20033.

Ishikawa, H. *et al.* (2005) 'Odf2-deficient mother centrioles lack distal/subdistal appendages and the ability to generate primary cilia', *Nature Cell Biology*, 7(5), pp. 517–524. Available at: https://doi.org/10.1038/ncb1251.

Itasaki, N., Bel-Vialar, S. and Krumlauf, R. (1999) ' "Shocking" developments in chick embryology: electroporation and in ovo gene expression', *Nature Cell Biology*, 1(8), pp. E203–E207. Available at: https://doi.org/10.1038/70231.

Jana, S.C. (2021) 'Centrosome structure and biogenesis: Variations on a theme?', *Seminars in Cell and Developmental Biology*, 110(January), pp. 123–138. Available at: https://doi.org/10.1016/j.semcdb.2020.10.014.

Jauregui, A.R. and Barr, M.M. (2005) 'Functional characterization of the C. elegans nephrocystins NPHP-1 and NPHP-4 and their role in cilia and male sensory behaviors', *Experimental Cell Research* [Preprint]. Available at: https://doi.org/10.1016/j.yexcr.2005.01.008.

Jayaraman, D. *et al.* (2016) 'Microcephaly Proteins Wdr62 and Aspm Define a Mother Centriole Complex Regulating Centriole Biogenesis, Apical Complex, and Cell Fate', *Neuron*, 92(4), pp. 813–828. Available at: https://doi.org/10.1016/j.neuron.2016.09.056.

Jayaraman, D., Bae, B.-I. and Walsh, C.A. (2018) 'The genetics of primary Microcephaly', *Annual Review ofGenomics and Human Genetics*, (19), pp. 177–200. Available at: https://doi.org/10.1146/annurev-genom-083117-021441.

Jean, C. *et al.* (1999) 'The mammalian interphase centrosome: Two independent units maintained together by the dynamics of the microtubule cytoskeleton', *European Journal of Cell Biology* [Preprint]. Available at: https://doi.org/10.1016/S0171-9335(99)80020-X.

Jo, J. *et al.* (2016) 'Midbrain-like Organoids from Human Pluripotent Stem Cells Contain Functional Dopaminergic and Neuromelanin-Producing Neurons', *Cell Stem Cell*, 19(2), pp. 248–257. Available at: https://doi.org/10.1016/j.stem.2016.07.005.

Johnson, M.B. and Walsh, C.A. (2017) 'Cerebral cortical neuron diversity and development at single-cell resolution', *Curr Opin Neurobiol*, 42, pp. 9–16. Available at: https://doi.org/10.1016/j.conb.2016.11.001.

Kadoshima, T. *et al.* (2013) 'Self-organization of axial polarity, inside-out layer pattern, and species-specific progenitor dynamics in human ES cell–derived neocortex', *Proceedings of the National Academy of Sciences*, 110(50), pp. 20284–20289. Available at: https://doi.org/10.1073/pnas.1315710110.

Kapitein, L.C. *et al.* (2005) 'The bipolar mitotic kinesin Eg5 moves on both microtubules that it crosslinks', *Nature* [Preprint]. Available at: https://doi.org/10.1038/nature03503.

Kashihara, H. *et al.* (2019) 'Cep128 associates with Odf2 to form the subdistal appendage of the centriole', *Genes to Cells*, 24(3), pp. 231–243. Available at: https://doi.org/10.1111/gtc.12668.

Kasioulis, I., Das, R.M. and Storey, K.G. (2017) 'Inter-dependent apical microtubule and actin dynamics orchestrate centrosome retention and neuronal delamination', *Elife*, 6. Available at: https://doi.org/10.7554/eLife.26215.

Keller, R. (1991) 'Chapter 5 Early Embryonic Development of Xenopus laevis', in, pp. 61–113. Available at: https://doi.org/10.1016/S0091-679X(08)60273-3.

Keller, R. *et al.* (1992) 'Planar induction of convergence and extension of the neural plate by the organizer of Xenopus.', *Developmental dynamics : an official publication of*

*the American Association of Anatomists*, 193(3), pp. 218–234. Available at: https://doi.org/10.1002/aja.1001930303.

Keller, R., Shook, D. and Skoglund, P. (2008) 'The forces that shape embryos: physical aspects of convergent extension by cell intercalation.', *Physical biology*, 5(1), p. 15007. Available at: https://doi.org/10.1088/1478-3975/5/1/015007.

Kim, K. *et al.* (2008) 'A novel function of CEP135 as a platform protein of C-NAP1 for its centriolar localization', *Experimental Cell Research* [Preprint]. Available at: https://doi.org/10.1016/j.yexcr.2008.09.016.

Kim, M. *et al.* (2016) 'Promotion and Suppression of Centriole Duplication Are Catalytically Coupled through PLK4 to Ensure Centriole Homeostasis', *Cell Reports*, 16(5), pp. 1195–1203. Available at: https://doi.org/10.1016/j.celrep.2016.06.069.

Kim, T.S. *et al.* (2013) 'Hierarchical recruitment of Plk4 and regulation of centriole biogenesis by two centrosomal scaffolds, Cep192 and Cep152', *Proceedings of the National Academy of Sciences of the United States of America*, 110(50). Available at: https://doi.org/10.1073/pnas.1319656110.

Koh, I. and Hagiwara, M. (2022) 'From Gradient to Sectioning in CUBE: Workflow for Generating and Imaging Organoid with Localized Differentiation', *bioRxiv* [Preprint]. Available at: https://www.biorxiv.org/content/early/2022/09/06/2022.09.06.506732.

Kondoh, H. and Takemoto, T. (2012) 'Axial stem cells deriving both posterior neural and mesodermal tissues during gastrulation', *Curr Opin Genet Dev*, 22(4), pp. 374–380. Available at: https://doi.org/10.1016/j.gde.2012.03.006.

Kraatz, S. *et al.* (2016) 'The Human Centriolar Protein CEP135 Contains a Two-Stranded Coiled-Coil Domain Critical for Microtubule Binding', *Structure* [Preprint]. Available at: https://doi.org/10.1016/j.str.2016.06.011.

Kubo, A. and Tsukita, S. (2003) 'Non-membranous granular organelle consisting of PCM-1: Subcellular distribution and cell-cycle-dependent assembly/disassembly', *Journal of Cell Science* [Preprint]. Available at: https://doi.org/10.1242/jcs.00282.

Lancaster, M.A. *et al.* (2013) 'Cerebral organoids model human brain development and microcephaly', *Nature*, 501(7467), pp. 373–379. Available at: https://doi.org/10.1038/nature12517.

Langman, J., Guerrant, R.L. and Freeman, B.G. (1966) 'Behavior of neuro-epithelial cells during closure of the neural tube', *J Comp Neurol*, 127(3), pp. 399–411. Available at: https://doi.org/10.1002/cne.901270308.

Lawo, S. *et al.* (2012) 'Subdiffraction imaging of centrosomes reveals higher-order organi-

zational features of pericentriolar material', *Nature Cell Biology*, 14(11), pp. 1148–1158. Available at: https://doi.org/10.1038/ncb2591.

Lawson, A. and England, M.A. (1998) *Neural Fold Fusion in the Cranial Region of the Chick Embryo*, *Dev. Dyn.*

Leck, I. (1974) 'Causation of neural tube defects: clues from epidemiology.', *British medical bulletin*, 30(2), pp. 158–163. Available at: https://doi.org/10.1093/oxfordjournals.bmb.a071187.

Lee, H. *et al.* (2007) 'Directed Differentiation and Transplantation of Human Embryonic Stem Cell-Derived Motoneurons', *Stem Cells*, 25(8), pp. 1931–1939. Available at: https://doi.org/10.1634/stemcells.2007-0097.

Lee, M. *et al.* (2017) 'PLK4 phosphorylation of CP110 is required for efficient centriole assembly', *Cell Cycle*, 16(12), pp. 1225–1234. Available at: https://doi.org/10.1080/15384101.2017.1325555.

Li, J. *et al.* (2012) 'Neurl4, a novel daughter centriole protein, prevents formation of ectopic microtubule organizing centres', *EMBO Reports*, 13(6), pp. 547–553. Available at: https://doi.org/10.1038/embor.2012.40.

Liem, K.F., Jessell, T.M. and Briscoe, J. (2000) 'Regulation of the neural patterning activity of sonic hedgehog by secreted BMP inhibitors expressed by notochord and somites', *Development*, 127(22), pp. 4855–4866. Available at: https://doi.org/10.1242/dev.127.22.4855.

Liem, K.F., Tremml, G. and Jessell, T.M. (1997) 'A role for the roof plate and its resident TGF$\beta$-related proteins in neuronal patterning in the dorsal spinal cord', *Cell*, 91(1), pp. 127–138. Available at: https://doi.org/10.1016/S0092-8674(01)80015-5.

Lin, Y.C. *et al.* (2013) 'Human microcephaly protein CEP135 binds to hSAS-6 and CPAP, and is required for centriole assembly', *EMBO Journal* [Preprint]. Available at: https://doi.org/10.1038/emboj.2013.56.

Lo, C.H. *et al.* (2019) 'Phosphorylation of CEP83 by TTBK2 is necessary for cilia initiation', *The Journal of cell biology*, 218(10), pp. 3489–3505. Available at: https://doi.org/10.1083/jcb.201811142.

Loganathan, R. *et al.* (2016) 'Extracellular matrix motion and early morphogenesis', *Development (Cambridge)*, 143(12), pp. 2056–2065. Available at: https://doi.org/10.1242/dev.127886.

Lowery, L.A. and Sive, H. (2004) 'Strategies of vertebrate neurulation and a re-evaluation of teleost neural tube formation', *Mech Dev*, 121(10), pp. 1189–1197. Available at:

https://doi.org/10.1016/j.mod.2004.04.022.

Di Lullo, E. and Kriegstein, A.R. (2017) 'The use of brain organoids to investigate neural development and disease', *Nature Reviews Neuroscience*, 18(10), pp. 573–584. Available at: https://doi.org/10.1038/nrn.2017.107.

Mahjoub, M.R., Xie, Z. and Stearns, T. (2010) 'Cep120 is asymmetrically localized to the daughter centriole and is essential for centriole assembly', *Journal of Cell Biology* [Preprint]. Available at: https://doi.org/10.1083/jcb.201003009.

Mak, L.L. (1978) *Ultrastructural Studies of Amphibian Neural Fold Fusion*, *DEVELOPMENTAL BIOLOGY*.

Malcoe, L.H. *et al.* (1999) 'The effect of congenital anomalies on mortality risk in white and black infants.', *American journal of public health*, 89(6), pp. 887–892. Available at: https://doi.org/10.2105/ajph.89.6.887.

Marshal, J.; J. *et al.* (1991) *Pattern formation in the vertebrate neural plate*, *Annu. Rev. PharmacoL Toxicol.* Plenum Press.

Marthiens, V. and Ffrench-Constant, C. (2009) 'Adherens junction domains are split by asymmetric division of embryonic neural stem cells', *EMBO Rep*, 10(5), pp. 515–520. Available at: https://doi.org/10.1038/embor.2009.36.

Martin-Belmonte, F. *et al.* (2008) 'Cell-polarity dynamics controls the mechanism of lumen formation in epithelial morphogenesis', *Curr Biol*, 18(7), pp. 507–513. Available at: https://doi.org/10.1016/j.cub.2008.02.076.

Martin, B.L. and Kimelman, D. (2008) 'Regulation of Canonical Wnt Signaling by Brachyury Is Essential for Posterior Mesoderm Formation', *Developmental Cell*, 15(1), pp. 121–133. Available at: https://doi.org/10.1016/j.devcel.2008.04.013.

Martin, B.L. and Kimelman, D. (2012) 'Canonical Wnt signaling dynamically controls multiple stem cell fate decisions during vertebrate body formation.', *Developmental cell*, 22(1), pp. 223–232. Available at: https://doi.org/10.1016/j.devcel.2011.11.001.

Mazzoni, E.O. *et al.* (2013) 'Saltatory remodeling of Hox chromatin in response to rostrocaudal patterning signals', *Nature Neuroscience*, 16(9), pp. 1191–1198. Available at: https://doi.org/10.1038/nn.3490.

Megason, S.G. and McMahon, A.P. (2002) 'A mitogen gradient of dorsal midline Wnts organizes growth in the CNS.', *Development (Cambridge, England)*, 129(9), pp. 2087–2098.

Meinhardt, A. *et al.* (2014) '3D reconstitution of the patterned neural tube from embry-

onic stem cells', *Stem Cell Reports*, 3(6), pp. 987–999. Available at: https://doi.org/10.1016/j.stemcr.2014.09.020.

Mennella, V. *et al.* (2012) 'Subdiffraction-resolution fluorescence microscopy reveals a domain of the centrosome critical for pericentriolar material organization', *Nature Cell Biology*, 14(11), pp. 1159–1168. Available at: https://doi.org/10.1038/ncb2597.

Meraldi;, P. and Nigg, E.A. (2002) 'The centrosome cycle', *FEBS Letters*, 521, pp. 9–13. Available at: https://doi.org/10.1016/S0014-5793(02)02865-X.

Metzis, V. *et al.* (2018) 'Nervous System Regionalization Entails Axial Allocation before Neural Differentiation', *Cell*, 175(4), pp. 1105-1118.e17. Available at: https://doi.org/10.1016/j.cell.2018.09.040.

Molina, A. and Pituello, F. (2017) 'Playing with the cell cycle to build the spinal cord', *Dev Biol*, 432(1), pp. 14–23. Available at: https://doi.org/10.1016/j.ydbio.2016.12.022.

Mönnich, M. *et al.* (2018) 'CEP128 Localizes to the Subdistal Appendages of the Mother Centriole and Regulates TGF-$\beta$/BMP Signaling at the Primary Cilium', *Cell Reports*, 22(10), pp. 2584–2592. Available at: https://doi.org/10.1016/j.celrep.2018.02.043.

Monzel, A.S. *et al.* (2017) 'Derivation of Human Midbrain-Specific Organoids from Neuroepithelial Stem Cells', *Stem Cell Reports*, 8(5), pp. 1144–1154. Available at: https://doi.org/10.1016/j.stemcr.2017.03.010.

Moritz, M. *et al.* (2000) 'Structure of the $\gamma$-tubulin ring complex: A template for microtubule nucleation', *Nature Cell Biology* [Preprint]. Available at: https://doi.org/10.1038/35014058.

Morris, J.K. *et al.* (2016) 'Prevention of neural tube defects in the UK: a missed opportunity', *Arch Dis Child*, 101(7), pp. 604–607. Available at: https://doi.org/10.1136/archdischild-2015-309226.

Morriss-Kay, G., Wood, H. and Chen, W.H. (1994) 'Normal neurulation in mammals.', *Ciba Foundation symposium*, 181, pp. 51–59. Available at: https://doi.org/10.1002/9780470514559.ch4.

Moss, D.K. *et al.* (2007) 'Ninein is released from the centrosome and moves bi-directionally along microtubules', *Journal of Cell Science*, 120(17), pp. 3064–3074. Available at: https://doi.org/10.1242/jcs.010322.

Moyer, T.C. *et al.* (2015) 'Binding of STIL to Plk4 activates kinase activity to promote centriole assembly', *Journal of Cell Biology*, 209(6), pp. 863–878. Available at: https:

//doi.org/10.1083/jcb.201502088.

Muguruma, K. *et al.* (2015) 'Self-Organization of Polarized Cerebellar Tissue in 3D Culture of Human Pluripotent Stem Cells', *Cell Reports*, 10(4), pp. 537–550. Available at: https://doi.org/10.1016/j.celrep.2014.12.051.

Muller, F. and O'Rahilly, R. (1987) 'The development of the human brain, the closure of the caudal neuropore, and the beginning of secondary neurulation at stage 12.', *Anatomy and embryology*, 176(4), pp. 413–430. Available at: https://doi.org/10.1007/bf00310083.

Murciano, A. *et al.* (2002) 'Interkinetic nuclear movement may provide spatial clues to the regulation of neurogenesis', *Molecular and Cellular Neuroscience*, 21(2), pp. 285–300. Available at: https://doi.org/10.1006/mcne.2002.1174.

Nakao, T. and Ishizawa, A. (1984) 'Light- and electron-microscopic observations of the tail bud of the larval lamprey (Lampetra japonica), with special reference to neural tube formation.', *The American journal of anatomy*, 170(1), pp. 55–71. Available at: https://doi.org/10.1002/aja.1001700105.

Nakatsu, T., Uwabe, C. and Shiota, K. (2000) 'Neural tube closure in humans initiates at multiple sites: evidence from human embryos and implications for the pathogenesis of neural tube defects.', *Anatomy and embryology*, 201(6), pp. 455–466. Available at: https://doi.org/10.1007/s004290050332.

Nano, M. and Basto, R. (2017) 'Consequences of Centrosome Dysfunction During Brain Development', *Adv Exp Med Biol*, 1002, pp. 19–45. Available at: https://doi.org/10.1007/978-3-319-57127-0_2.

Nardone, G. *et al.* (2017) 'YAP regulates cell mechanics by controlling focal adhesion assembly', *Nature Communications*, 8(May). Available at: https://doi.org/10.1038/ncomms15321.

Neijts, R. *et al.* (2014) 'Region-specific regulation of posterior axial elongation during vertebrate embryogenesis', *Developmental Dynamics*, 243(1), pp. 88–98. Available at: https://doi.org/10.1002/dvdy.24027.

Niederreither, K. *et al.* (1999) 'Embryonic retinoic acid synthesis is essential for early mouse post-implantation development', *Nature Genetics*, 21(4), pp. 444–448. Available at: https://doi.org/10.1038/7788.

Nievelstein, R.A. *et al.* (1993) 'Embryonic development of the mammalian caudal neural tube', *Teratology*. 1993/07/01, 48(1), pp. 21–31. Available at: https://doi.org/10.1002/tera.1420480106.

Nigg, E.A. and Stearns, T. (2011) 'The centrosome cycle: Centriole biogenesis, duplication and inherent asymmetries', *Nature Cell Biology*, 13(10), pp. 1154–1160. Available at: https://doi.org/10.1038/ncb2345.

Nordström, U. *et al.* (2006) 'An early role for Wnt signaling in specifying neural patterns of Cdx and Hox gene expression and motor neuron subtype identity', *PLoS Biology*, 4(8), pp. 1438–1452. Available at: https://doi.org/10.1371/journal.pbio.0040252.

Novitch, B.G. *et al.* (2003) 'A requirement for retinoic acid-mediated transcriptional activation in ventral neural patterning and motor neuron specification', *Neuron*, 40(1), pp. 81–95. Available at: https://doi.org/10.1016/j.neuron.2003.08.006.

O'rahilly, R. and Muller, F. (1994) *Neurulation in the normal human embryo.*

O'Rahilly, R. and Muller, F. (1994) 'Neurulation in the normal human embryo', *Ciba Found Symp.* 1994/01/01, 181, pp. 70–79.

O'Rahilly, R. and Muller, F. (2002) 'The two sites of fusion of the neural folds and the two neuropores in the human embryo', *Teratology.* 2002/04/12, 65(4), pp. 162–170. Available at: https://doi.org/10.1002/tera.10007.

Ohta, M. *et al.* (2014) 'Direct interaction of Plk4 with STIL ensures formation of a single procentriole per parental centriole', *Nature communications*, 5, p. 5267. Available at: https://doi.org/10.1038/ncomms6267.

Olivera-Martinez, I. *et al.* (2012) 'Loss of FGF-dependent mesoderm identity and rise of endogenous retinoid signalling determine cessation of body axis elongation', *PLoS Biol*, 10(10), p. e1001415. Available at: https://doi.org/10.1371/journal.pbio.1001415.

Olivera-Martinez, I. and Storey, K.G. (2007) 'Wnt signals provide a timing mechanism for the FGF-retinoid differentiation switch during vertebrate body axis extension', *Development*, 134(11), pp. 2125–2135. Available at: https://doi.org/10.1242/dev.000216.

Oughtred, R. *et al.* (2021) 'The BioGRID database: A comprehensive biomedical resource of curated protein, genetic, and chemical interactions', *Protein Science*, 30(1), pp. 187–200. Available at: https://doi.org/10.1002/pro.3978.

Panic, M. *et al.* (2015) 'The Centrosomal Linker and Microtubules Provide Dual Levels of Spatial Coordination of Centrosomes', *PLoS Genetics*, 11(5), pp. 1–22. Available at: https://doi.org/10.1371/journal.pgen.1005243.

Paridaen, J.T., Wilsch-Brauninger, M. and Huttner, W.B. (2013) 'Asymmetric inheritance of centrosome-associated primary cilium membrane directs ciliogenesis after cell division', *Cell*, 155(2), pp. 333–344. Available at: https://doi.org/10.1016/j.cell.2013.08.060.

Paridaen, J.T.M.L., Wilsch-Bräuninger, M. and Huttner, W.B. (2013) 'Asymmetric inheritance of centrosome-associated primary cilium membrane directs ciliogenesis after cell division', *Cell*, 155(2), p. 333. Available at: https://doi.org/10.1016/j.cell.2013.08.060.

Park, S.Y. *et al.* (2014) 'Molecular basis for unidirectional scaffold switching of human Plk4 in centriole biogenesis', *Nature Structural and Molecular Biology*, 21(8), pp. 696–703. Available at: https://doi.org/10.1038/nsmb.2846.

Patel, K. *et al.* (1996) *Cloning and Early Dorsal Axial Expression of Flik, a Chick Follistatin-Related Gene: Evidence for Involvement in Dorsalization/Neural Induction*, *DEVELOPMENTAL BIOLOGY*.

Patten, I. and Placzek, M. (2002) 'Opponent activities of Shh and BMP signaling during floor plate induction in vivo', *Current Biology*, 12(1), pp. 47–52. Available at: https://doi.org/10.1016/S0960-9822(01)00631-5.

Peeters, M.C. *et al.* (1998) 'Neurulation in the rabbit embryo.', *Anatomy and embryology*, 197(3), pp. 167–175. Available at: https://doi.org/10.1007/s004290050128.

Piccolo, S., Dupont, S. and Cordenonsi, M. (2014) 'The biology of YAP/TAZ: Hippo signaling and beyond', *Physiological Reviews* [Preprint]. Available at: https://doi.org/10.1152/physrev.00005.2014.

Pituello, F., Yamada, G. and Gruss, P. (1995) 'Activin A inhibits Pax-6 expression and perturbs cell differentiation in the developing spinal cord in vitro', *Proceedings of the National Academy of Sciences of the United States of America*, 92(15), pp. 6952–6956. Available at: https://doi.org/10.1073/pnas.92.15.6952.

Qian, X. *et al.* (2016) 'Brain-Region-Specific Organoids Using Mini-bioreactors for Modeling ZIKV Exposure', *Cell*, 165(5), pp. 1238–1254. Available at: https://doi.org/10.1016/j.cell.2016.04.032.

Remans, K. *et al.* (2014) 'C2 domains as protein-protein interaction modules in the ciliary transition zone', *Cell Reports*, 8(1), pp. 1–9. Available at: https://doi.org/10.1016/j.celrep.2014.05.049.

Ribes, V. *et al.* (2009) 'Early mouse caudal development relies on crosstalk between retinoic acid, Shh and Fgf signalling pathways', *Development*, 136(4), pp. 665–676. Available at: https://doi.org/10.1242/dev.016204.

Rogers, G.C. *et al.* (2009) 'The SCF Slimb ubiquitin ligase regulates Plk4/Sak levels to block centriole reduplication', *Journal of Cell Biology*, 184(2), pp. 225–229. Available at: https://doi.org/10.1083/jcb.200808049.

Saade, M. *et al.* (2013) 'Sonic hedgehog signaling switches the mode of division in the developing nervous system', *Cell Rep*, 4(3), pp. 492–503. Available at: https://doi.org/10.1016/j.celrep.2013.06.038.

Saade, M. *et al.* (2017a) 'Shh-mediated centrosomal recruitment of PKA promotes symmetric proliferative neuroepithelial cell division', *Nature Cell Biology* [Preprint]. Available at: https://doi.org/10.1038/ncb3512.

Saade, M. *et al.* (2017b) 'Shh-mediated centrosomal recruitment of PKA promotes symmetric proliferative neuroepithelial cell division', *Nature Cell Biology*, 19(5), pp. 493–503. Available at: https://doi.org/10.1038/ncb3512.

Saade, Murielle *et al.* (2018) 'A centrosomal view of cns growth', *Development (Cambridge)*, 145(21). Available at: https://doi.org/10.1242/dev.170613.

Saade, M *et al.* (2018) 'A centrosomal view of CNS growth', *Development (Cambridge, England)*, 145(21). Available at: https://doi.org/10.1242/dev.170613.

Saade, M. *et al.* (2020) 'Multimerization of Zika Virus-NS5 Causes Ciliopathy and Forces Premature Neurogenesis', *Cell Stem Cell*, 27(6), pp. 920-936.e8. Available at: https://doi.org/10.1016/j.stem.2020.10.002.

Saitsu, H. *et al.* (2004) 'Development of the posterior neural tube in human embryos', *Anat Embryol (Berl)*, 209(2), pp. 107–117. Available at: https://doi.org/10.1007/s00429-004-0421-2.

Saitsu, H. and Shiota, K. (2008) 'Involvement of the axially condensed tail bud mesenchyme in normal and abnormal human posterior neural tube development', *Congenit Anom (Kyoto)*, 48(1), pp. 1–6. Available at: https://doi.org/10.1111/j.1741-4520.2007.00178.x.

Sakaguchi, H. *et al.* (2015) 'Generation of functional hippocampal neurons from self-organizing human embryonic stem cell-derived dorsomedial telencephalic tissue', *Nature Communications*, 6(1), p. 8896. Available at: https://doi.org/10.1038/ncomms9896.

Sakai, Y. (1989) *Neurulation in the Mouse: Manner and Timing of Neural Tube Closure*, *THE ANATOMICAL RECORD*.

Sang, L. *et al.* (2011) 'Mapping the NPHP-JBTS-MKS protein network reveals ciliopathy disease genes and pathways', *Cell*, 145(4), pp. 513–528. Available at: https://doi.org/10.1016/j.cell.2011.04.019.

Sasai, Y. *et al.* (1994) 'Xenopus chordin: A novel dorsalizing factor activated by organizer-specific homeobox genes', *Cell*, 79(5), pp. 779–790. Available at: https://doi.org/10.1016/0092-8674(94)90068-X.

Satisbury, J.L. (1995) 'Centrin, centrosomes, and mitotic spindle poles', *Current Opinion in Cell Biology*, 7(1), pp. 39–45. Available at: https://doi.org/10.1016/0955-0674(95)80043-3.

Sauer, F.C. (1935) 'Mitosis in the neural tube', *The Journal of Comparative Neurology*, 62(2), pp. 377–405. Available at: https://doi.org/10.1002/cne.900620207.

Schmidt, T.I. *et al.* (2009) 'Control of Centriole Length by CPAP and CP110', *Current Biology* [Preprint]. Available at: https://doi.org/10.1016/j.cub.2009.05.016.

Schoenwolf, G.C. (1984) 'Histological and ultrastructural studies of secondary neurulation in mouse embryos', *Am J Anat*, 169(4), pp. 361–376. Available at: https://doi.org/10.1002/aja.1001690402.

Schoenwolf, G.C. and Delongo, J. (1980) 'Ultrastructure of secondary neurulation in the chick embryo', *Am J Anat*, 158(1), pp. 43–63. Available at: https://doi.org/10.1002/aja.1001580106.

Schoenwolf, G.C. and Kelley, R.O. (1980) 'Characterization of intercellular junctions in the caudal portion of the developing neural tube of the chick embryo', *Am J Anat*, 158(1), pp. 29–41. Available at: https://doi.org/10.1002/aja.1001580105.

Schroeder, T.E. (1970) 'Neurulation in Xenopus laevis. An analysis and model based upon light and electron microscopy', *Development*, 23(2), pp. 427–462. Available at: https://doi.org/10.1242/dev.23.2.427.

Schweizer, N. *et al.* (2021) 'Sub-centrosomal mapping identifies augmin-γTuRC as part of a centriole-stabilizing scaffold', *Nature Communications*, 12(1). Available at: https://doi.org/10.1038/s41467-021-26252-5.

Shao, W. *et al.* (2020) 'Centrosome anchoring regulates progenitor properties and cortical formation', *Nature*, (June 2018), pp. 1–7. Available at: https://doi.org/10.1038/s41586-020-2139-6.

Shi, X. *et al.* (2017) 'Super-resolution microscopy reveals that disruption of ciliary transition-zone architecture causes Joubert syndrome', *Nature Cell Biology*, 19(10), pp. 1178–1188. Available at: https://doi.org/10.1038/ncb3599.

Shimokita, E. and Takahashi, Y. (2011) 'Secondary neurulation: Fate-mapping and gene manipulation of the neural tube in tail bud', *Dev Growth Differ*, 53(3), pp. 401–410. Available at: https://doi.org/10.1111/j.1440-169X.2011.01260.x.

Shum, A.S.. *et al.* (1999) 'Retinoic acid induces down-regulation of Wnt-3a, apoptosis and diversion of tail bud cells to a neural fate in the mouse embryo', *Mechanisms of Development*, 84(1–2), pp. 17–30. Available at: https://doi.org/10.1016/S0925-4773(99)

00059-3.

Shum, A.S. *et al.* (2010) 'Lack of motor neuron differentiation is an intrinsic property of the mouse secondary neural tube', *Dev Dyn*, 239(12), pp. 3192–3203. Available at: https://doi.org/10.1002/dvdy.22457.

Shum, A.S. and Copp, A.J. (1996) 'Regional differences in morphogenesis of the neuroepithelium suggest multiple mechanisms of spinal neurulation in the mouse.', *Anatomy and embryology*, 194(1), pp. 65–73. Available at: https://doi.org/10.1007/bf00196316.

Sillibourne, J.E. *et al.* (2011) 'Assessing the localization of centrosomal proteins by PALM/STORM nanoscopy', *Cytoskeleton*, 68(11), pp. 619–627. Available at: https://doi.org/10.1002/cm.20536.

Sillibourne, J.E. *et al.* (2013) 'Primary ciliogenesis requires the distal appendage component Cep123', *Biology Open*, 2(6), pp. 535–545. Available at: https://doi.org/10.1242/bio.20134457.

Sirbu, I.O. and Duester, G. (2006) 'Retinoic-acid signalling in node ectoderm and posterior neural plate directs left–right patterning of somitic mesoderm', *Nature Cell Biology*, 8(3), pp. 271–277. Available at: https://doi.org/10.1038/ncb1374.

Smith, J.L. and Schoenwolf, G.C. (1989) 'Notochordal induction of cell wedging in the chick neural plate and its role in neural tube formation.', *The Journal of experimental zoology*, 250(1), pp. 49–62. Available at: https://doi.org/10.1002/jez.1402500107.

Smith, J.L. and Schoenwolf, G.C. (1991) 'Further evidence of extrinsic forces in bending of the neural plate.', *The Journal of comparative neurology*, 307(2), pp. 225–236. Available at: https://doi.org/10.1002/cne.903070206.

Smith, J.L. and Schoenwolf, G.C. (1997) 'Neurulation: coming to closure.', *Trends in neurosciences*, 20(11), pp. 510–517.

Smith, W.C. and Harland, R.M. (1992) 'Expression cloning of noggin, a new dorsalizing factor localized to the Spemann organizer in Xenopus embryos', *Cell*, 70(5), pp. 829–840. Available at: https://doi.org/10.1016/0092-8674(92)90316-5.

Spektor, A. *et al.* (2007) 'Cep97 and CP110 Suppress a Cilia Assembly Program', *Cell*, 130(4), pp. 678–690. Available at: https://doi.org/10.1016/j.cell.2007.06.027.

Staples, C.J. *et al.* (2012) 'The centriolar satellite protein Cep131 is important for genome stability', *Journal of Cell Science*, 125(20), pp. 4770–4779. Available at: https://doi.org/10.1242/jcs.104059.

Steventon, B. *et al.* (2016) 'Species-specific contribution of volumetric growth and tissue

convergence to posterior body elongation in vertebrates', *Development*, 143(10), pp. 1732 LP-- 1741. Available at: https://doi.org/10.1242/dev.126375.

Stottmann, R.W. *et al.* (2006) 'The BMP antagonist Noggin promotes cranial and spinal neurulation by distinct mechanisms.', *Developmental biology*, 295(2), pp. 647–663. Available at: https://doi.org/10.1016/j.ydbio.2006.03.051.

Suga, H. *et al.* (2011) 'Self-formation of functional adenohypophysis in three-dimensional culture', *Nature*, 480(7375), pp. 57–62. Available at: https://doi.org/10.1038/nature10637.

Takahashi, K. and Yamanaka, S. (2006) 'Induction of Pluripotent Stem Cells from Mouse Embryonic and Adult Fibroblast Cultures by Defined Factors', *Cell*, 126(4), pp. 663–676. Available at: https://doi.org/10.1016/j.cell.2006.07.024.

Takemoto, T. *et al.* (2006) 'Convergence of Wnt and FGF signals in the genesis of posterior neural plate through activation of the Sox2 enhancer N-1.', *Development (Cambridge, England)*, 133(2), pp. 297–306. Available at: https://doi.org/10.1242/dev.02196.

Tanos, B.E. *et al.* (2013) 'Centriole distal appendages promote membrane docking, leading to cilia initiation', *Genes and Development*, 27(2), pp. 163–168. Available at: https://doi.org/10.1101/gad.207043.112.

Tateishi, K. *et al.* (2013) 'Two appendages homologous between basal bodies and centrioles are formed using distinct Odf2 domains', *Journal of Cell Biology*, 203(3), pp. 417–425. Available at: https://doi.org/10.1083/jcb.201303071.

Taverna, E. and Huttner, W.B. (2010) 'Neural progenitor nuclei IN motion.', *Neuron*, 67(6), pp. 906–914. Available at: https://doi.org/10.1016/j.neuron.2010.08.027.

Thauvin-Robinet, C. *et al.* (2014) 'The oral-facial-digital syndrome gene C2CD3 encodes a positive regulator of centriole elongation', *Nature Genetics* [Preprint]. Available at: https://doi.org/10.1038/ng.3031.

Thomson, J.A. *et al.* (1998) 'Embryonic Stem Cell Lines Derived from Human Blastocysts', *Science*, 282(5391), pp. 1145–1147. Available at: https://doi.org/10.1126/science.282.5391.1145.

Tollenaere, M.A.X., Mailand, N. and Bekker-Jensen, S. (2015) 'Centriolar satellites: Key mediators of centrosome functions', *Cellular and Molecular Life Sciences*, 72(1), pp. 11–23. Available at: https://doi.org/10.1007/s00018-014-1711-3.

Tozer, S *et al.* (2017) 'Differential Routing of Mindbomb1 via Centriolar Satellites Regulates Asymmetric Divisions of Neural Progenitors', *Neuron*, 93(3), pp. 542--551 e4. Available at: https://doi.org/10.1016/j.neuron.2016.12.042.

Tozer, Samuel *et al.* (2017) 'Differential Routing of Mindbomb1 via Centriolar Satellites Regulates Asymmetric Divisions of Neural Progenitors', *Neuron*, 93(3), pp. 542-551.e4. Available at: https://doi.org/10.1016/j.neuron.2016.12.042.

Tsakiridis, A. and Wilson, V. (2015) 'Assessing the bipotency of in vitro-derived neuromesodermal progenitors.', *F1000Research*, 4, p. 100. Available at: https://doi.org/10.12688/f1000research.6345.2.

Tsou, M.F.B. and Stearns, T. (2006) 'Mechanism limiting centrosome duplication to once per cell cycle', *Nature*, 442(7105), pp. 947–951. Available at: https://doi.org/10.1038/nature04985.

Tzouanacou, E. *et al.* (2009) 'Redefining the progression of lineage segregations during mammalian embryogenesis by clonal analysis', *Dev Cell*, 17(3), pp. 365–376. Available at: https://doi.org/10.1016/j.devcel.2009.08.002.

Valenzuela, D.M. *et al.* (1995) 'Identification of mammalian noggin and its expression in the adult nervous system', *Journal of Neuroscience*, 15(9), pp. 6077–6084. Available at: https://doi.org/10.1523/jneurosci.15-09-06077.1995.

Veenvliet, J. V. *et al.* (2020) 'Mouse embryonic stem cells self-organize into trunk-like structures with neural tube and somites', *Science*, 370(6522). Available at: https://doi.org/10.1126/science.aba4937.

Veleri, S. *et al.* (2014) 'Ciliopathy-associated gene Cc2d2a promotes assembly of subdistal appendages on the mother centriole during cilia biogenesis', *Nature Communications*, 5(May). Available at: https://doi.org/10.1038/ncomms5207.

van de Ven, C. *et al.* (2011) 'Concerted involvement of Cdx/Hox genes and Wnt signaling in morphogenesis of the caudal neural tube and cloacal derivatives from the posterior growth zone.', *Development (Cambridge, England)*, 138(16), pp. 3451–3462. Available at: https://doi.org/10.1242/dev.066118.

Verrier, L. *et al.* (2018) 'Neural differentiation, selection and transcriptomic profiling of human neuromesodermal progenitor-like cells in vitro', *Development (Cambridge)*, 145(16 Special Issue). Available at: https://doi.org/10.1242/dev.166215.

Vlijm, R. *et al.* (2018) 'STED nanoscopy of the centrosome linker reveals a CEP68-organized, periodic rootletin network anchored to a C-Nap1 ring at centrioles', *Proceedings of the National Academy of Sciences of the United States of America*, 115(10), pp. E2246–E2253. Available at: https://doi.org/10.1073/pnas.1716840115.

Wang, L. *et al.* (2018) 'A distal centriolar protein network controls organelle maturation and asymmetry', *Nature Communications*, 9(1). Available at: https://doi.org/10.

1038/s41467-018-06286-y.

Wang, S. *et al.* (2018) 'Radial WNT5A-Guided Post-mitotic Filopodial Pathfinding Is Critical for Midgut Tube Elongation', *Dev Cell*, 46(2), pp. 173--188 e3. Available at: https://doi.org/10.1016/j.devcel.2018.06.011.

Wang, X. *et al.* (2009) 'Asymmetric centrosome inheritance maintains neural progenitors in the neocortex', *Nature*, 461(7266), pp. 947–955. Available at: https://doi.org/10.1038/nature08435.

Williams, C.L. *et al.* (2011) 'MKS and NPHP modules cooperate to establish basal body/transition zone membrane associations and ciliary gate function during ciliogenesis', *Journal of Cell Biology*, 192(6), pp. 1023–1041. Available at: https://doi.org/10.1083/jcb.201012116.

Wilsch-Brauninger, M., Florio, M. and Huttner, W.B. (2016) 'Neocortex expansion in development and evolution - from cell biology to single genes', *Curr Opin Neurobiol*, 39, pp. 122–132. Available at: https://doi.org/10.1016/j.conb.2016.05.004.

Wilson, L. and Maden, M. (2005) 'The mechanisms of dorsoventral patterning in the vertebrate neural tube', *Developmental Biology*, 282(1), pp. 1–13. Available at: https://doi.org/10.1016/j.ydbio.2005.02.027.

Wilson, V., Olivera-Martinez, I. and Storey, K.G. (2009) 'Stem cells, signals and vertebrate body axis extension', *Development*, 136(10), pp. 1591–1604. Available at: https://doi.org/10.1242/dev.021246.

Winey, M. and O'Toole, E. (2014) 'Centriole structure', *Philosophical Transactions of the Royal Society B: Biological Sciences*, 369(1650). Available at: https://doi.org/10.1098/rstb.2013.0457.

Woodruff, J.B., Wueseke, O. and Hyman, A.A. (2014) 'Pericentriolar material structure and dynamics', *Philosophical Transactions of the Royal Society B: Biological Sciences*, 369(1650). Available at: https://doi.org/10.1098/rstb.2013.0459.

Wymeersch, F.J. *et al.* (2016) 'Position-dependent plasticity of distinct progenitor types in the primitive streak.', *eLife*, 5, p. e10042. Available at: https://doi.org/10.7554/eLife.10042.

Yamaguchi, T.P. *et al.* (1999) 'A Wnt5a pathway underlies outgrowth of multiple structures in the vertebrate embryo.', *Development (Cambridge, England)*, 126(6), pp. 1211–1223.

Yan, X., Habedanck, R. and Nigg, E.A. (2006) 'A complex of two centrosomal proteins, CAP350 and FOP, cooperates with EB1 in microtubule anchoring.', *Molecular*

*biology of the cell*, 17(2), pp. 634–644. Available at: https://doi.org/10.1091/mbc.e05-08-0810.

Yang, H.J. *et al.* (2003) 'Neural differentiation of caudal cell mass (secondary neurulation) in chick embryos: Hamburger and Hamilton Stages 16-45', *Brain Res Dev Brain Res*, 142(1), pp. 31–36. Available at: https://www.ncbi.nlm.nih.gov/pubmed/12694942.

Yang, J., Adamian, M. and Li, T. (2006) 'Rootletin interacts with C-Nap1 and may function as a physical linker between the pair of centrioles/basal bodies in cells', *Molecular Biology of the Cell* [Preprint]. Available at: https://doi.org/10.1091/mbc.E05-10-0943.

Yang, T. *et al.* (2015) 'Superresolution pattern recognition reveals the architectural map of the ciliary transition zone', *Scientific Reports*, 5(February), pp. 1–13. Available at: https://doi.org/10.1038/srep14096.

Yang, T T *et al.* (2018) 'Super-resolution architecture of mammalian centriole distal appendages reveals distinct blade and matrix functional components', *Nat Commun*, 9(1), p. 2023. Available at: https://doi.org/10.1038/s41467-018-04469-1.

Yang, T. Tony *et al.* (2018) 'Super-resolution architecture of mammalian centriole distal appendages reveals distinct blade and matrix functional components', *Nature Communications*, 9(1). Available at: https://doi.org/10.1038/s41467-018-04469-1.

Ybot-Gonzalez, P. *et al.* (2007) 'Neural plate morhogenesis during mouse neurulation is regulated by antagonism of Bmp signalling', *Development*, 134(17), pp. 3203–3211. Available at: https://doi.org/10.1242/dev.008177.

Yoshikawa, Y. *et al.* (1997) 'Evidence That Absence ofWnt-3aSignaling Promotes Neuralization Instead of Paraxial Mesoderm Development in the Mouse', *Developmental Biology*, 183(2), pp. 234–242. Available at: https://doi.org/10.1006/DBIO.1997.8502.

Zhang, D. and Aravind, L. (2012) 'Novel transglutaminase-like peptidase and C2 domains elucidate the structure, biogenesis and evolution of the ciliary compartment', *Cell Cycle* [Preprint]. Available at: https://doi.org/10.4161/cc.22068.

Zheng, Y. *et al.* (2019) 'Dorsal-ventral patterned neural cyst from human pluripotent stem cells in a neurogenic niche', *Science Advances*, 5(12), pp. 1–14. Available at: https://doi.org/10.1126/sciadv.aax5933.

Zou, C. *et al.* (2005) 'Centrobin: A novel daughter centriole-associated protein that is required for centriole duplication', *Journal of Cell Biology*, 171(3), pp. 437–445. Available at: https://doi.org/10.1083/jcb.200506185.

9, 26, 24, 12

# Appendix 1

© 2018. Published by The Company of Biologists Ltd | Development (2018) 145, dev170613. doi:10.1242/dev.170613

REVIEW

# A centrosomal view of CNS growth

**Murielle Saade*, Jose Blanco-Ameijeiras, Elena Gonzalez-Gobartt and Elisa Martí**

## ABSTRACT

Embryonic development of the central nervous system (CNS) requires the proliferation of neural progenitor cells to be tightly regulated, allowing the formation of an organ with the right size and shape. This includes regulation of both the spatial distribution of mitosis and the mode of cell division. The centrosome, which is the main microtubule-organizing centre of animal cells, contributes to both of these processes. Here, we discuss the impact that centrosome-mediated control of cell division has on the shape of the overall growing CNS. We also review the intrinsic properties of the centrosome, both in terms of its molecular composition and its signalling capabilities, and discuss the fascinating notion that intrinsic centrosomal asymmetries in dividing neural progenitor cells are instructive for neurogenesis. Finally, we discuss the genetic links between centrosome dysfunction during development and the aetiology of microcephaly.

**KEY WORDS: Organ growth, CNS, Interkinetic nuclear migration, Asymmetric cell division, Centrosome, Growth factors, Primary microcephaly**

## Introduction

During embryonic development in higher vertebrates, the brain and anterior spinal cord are formed through primary neurulation of the embryonic neural plate, which produces a hollow neural tube (NT) that acts as the primordium of the central nervous system (CNS) (Greene and Copp, 2014). Along its entire anterior-to-posterior axis, the lumen of the NT is covered by a single type of neuroepithelial cell, termed a primary neural progenitor cell (NPC), from which all neural cell types will be generated. NPCs are specified in discrete domains with distinct transcriptional states in response to the activity of secreted proteins (Addison and Wilkinson, 2016; Cohen et al., 2013; Gupta and Sen, 2016; Le Dréau and Martí, 2012; Sousa and Fishell, 2010; Ulloa and Marti, 2010).

During development, primary NPCs proliferate in a tightly controlled manner, exhibiting distinct growth rates along the axis of the NT. The different rates of growth in the anterior and posterior NT are reflected in the enlargement of the brain chambers, which give rise to the primary anatomical structures in the brain. The main divisions initially formed in the anterior part of the CNS are the forebrain (prosencephalon), midbrain (mesencephalon) and hindbrain (rhombencephalon); these are followed caudally by the spinal cord (Fig. 1A). The forebrain comprises two telencephalic vesicles, the dorsal half of which is specified as the primordium of the cerebral cortex (Fig. 1B). At early developmental stages, key features that are important for NPC expansion are conserved along the CNS, including within the cerebral cortex and the spinal cord (Fig. 1B-D). However, later in development, NPCs in the developing cerebral cortex are organized into two germinal layers – the ventricular zone (VZ) and the subventricular zone (SVZ) – and are subject to increasing layers of complexity. These features of cortical NPCs and neurogenesis have been the subject of excellent recent reviews (Florio et al., 2017; Heide et al., 2017; Johnson and Walsh, 2017; Wilsch-Bräuninger et al., 2016) and will not be discussed further here.

Here, we aim to highlight features of primary NPCs that regulate the early growth of the embryonic CNS, de-regulation of which can cause neurodevelopmental disorders such as primary microcephaly. In particular, we discuss mechanisms involving the centrosome – the main microtubule-organizing centre (MTOC) in animal cells. We highlight how the centrosome impacts the process of interkinetic nuclear migration, which not only serves to expose dividing NPCs to the signalling-rich NT lumen environment, but also affects the shaping of the overall growing CNS. We also discuss the intrinsic properties of the centrosome and the emerging notion that centrosome asymmetries can instruct the outcome of NPC division. Moreover, based on recent findings, we highlight how growth factors, known to play a role in the generation of cell diversity during CNS development, also contribute to centrosome maturation and signalling, and thus regulate the mode of NPC division. Finally, given that many of the causative mutations for primary microcephaly affect genes encoding centrosome-related proteins (Gilmore and Walsh, 2013; Jayaraman et al., 2018), we briefly discuss how studies of the centrosome represent an interesting research direction for improving our understanding of neurodevelopmental disorders such as microcephaly.

## Centrosome-dependent interkinetic nuclear migration confines mitosis to the apical area

The NPCs that form the embryonic primordium of the CNS are organized as a pseudostratified epithelium in which elongated cells contact both the apical and basal laminae, with their nuclei adopting distinct positions along the apicobasal cell axis (Fig. 2A). During the G1 phase of the cell cycle, the nuclei of NPCs born at the apical surface of the neuroepithelium move toward the basal side. After completing S phase contacting the basal portion of the neuroepithelium, the nuclei return to the apical surface, where they undergo mitoses as their parent cells did. Collectively, these processes are referred to as interkinetic nuclear migration (INM, Fig. 2A) (Langman et al., 1966; Sauer, 1935).

In NPCs, the centrosome is anchored at the apical surface of the cell (Fig. 2B), serving as the base for the primary cilium (Dubreuil et al., 2007; Goetz and Anderson, 2010). Experimental observations indicate that the centrosome behaves as an anchor point for an apical-ward force that pulls the nucleus during G2 phase of the cell cycle. As such, the forces that drive apical nuclear migration within the VZ require the activity of centrosomal proteins, such as SAS-4 (CENPJ in mammals), Cep120, TACCs and Hook3 (Ge et al., 2010; Insolera et al., 2014; Xie et al., 2007). In parallel, and in line with the

Department of Developmental Biology, Instituto de Biología Molecular de Barcelona, Parc Científic de Barcelona, Baldiri i Reixac 20, Barcelona 08028, Spain.

*Author for correspondence (msabmc@ibmb.csic.es)

M.S., 0000-0002-3937-4291; E.M., 0000-0002-0411-0069

Development (2018) 145, dev170613. doi:10.1242/dev.170613

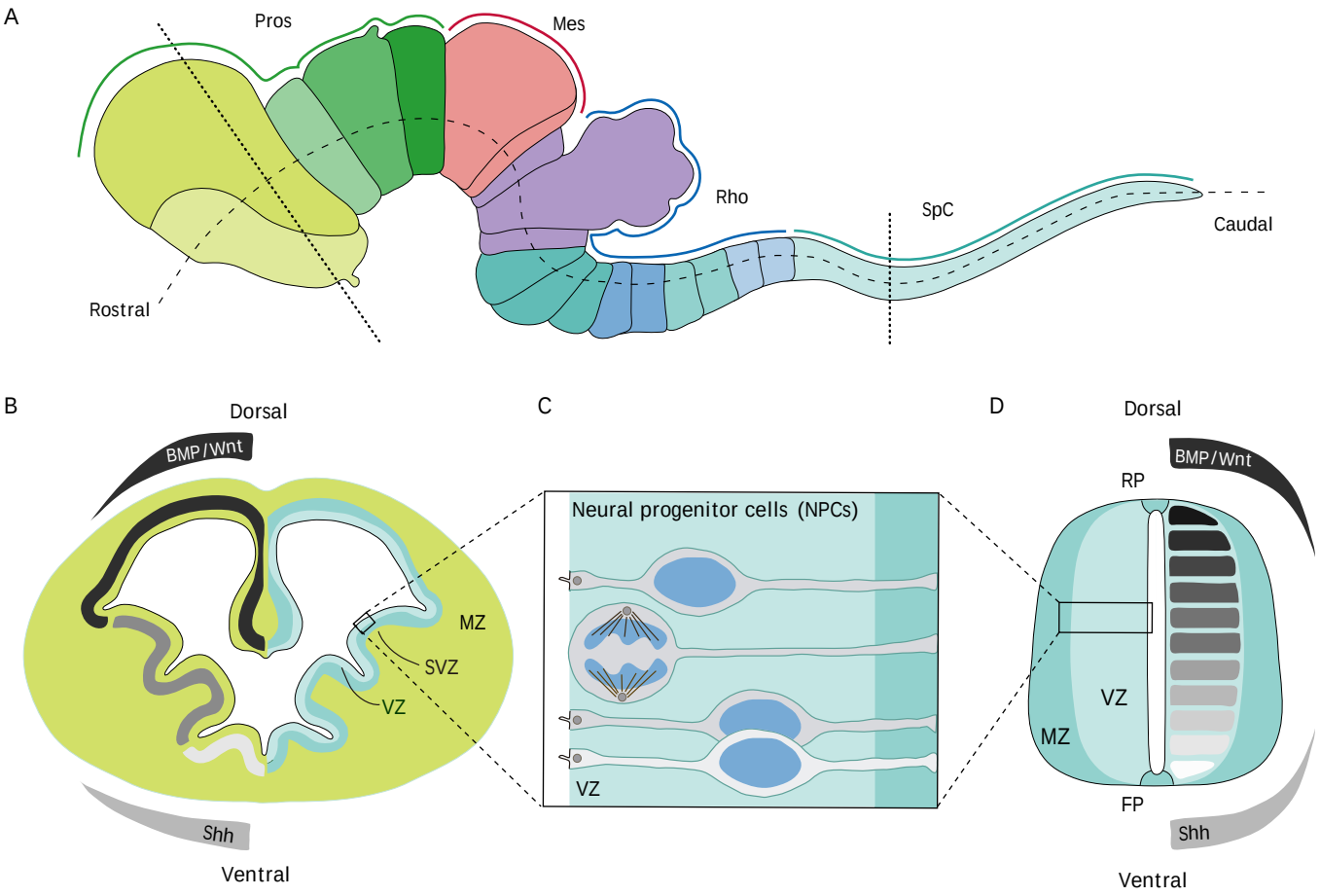


**Fig. 1. The embryonic central nervous system.** (A) Diagram of a vertebrate embryo (mouse ∼E8-10) central nervous system, showing rostral to caudal regionalization into the forebrain (prosencephalon, Pros), midbrain (mesencephalon, Mes), hindbrain (rhombencephalon, Rho), and the caudal spinal cord (SpC). (B) Diagram of a transverse section through the telencephalon. The main telencephalic subdivisions along the dorsal ventral axis are generated in response to dorsal BMP/Wnt and ventral sonic hedgehog (Shh) patterning signals. The relative position of neural progenitor cells (in the ventricular zone, VZ), intermediate progenitors (in the subventricular zone, SVZ) and post-mitotic neurons (in the mantle zone, MZ) are indicated. (C) Detailed view of dividing NPCs that occupy the VZ lining the entire neural tube lumen. NPCs are present as elongated cells that contact both the apical and basal laminae, with their nuclei adopting distinct positions along the apicobasal axis. (D) Diagram showing a transverse section through the spinal cord. The progenitor populations generated along the dorsal-ventral axis, highlighted with a greyscale on the right, are established by the conserved activity of extrinsic secreted signals (dorsal BMP/Wnt and ventral Shh). The relative position of NPCs (in the ventricular zone, VZ) and post-mitotic neurons (in the mantle zone, MZ) is shown. FP, floor plate; RP, roof plate.

role of the centrosome as a MTOC and the observation that intact microtubules are required for INM (Kosodo et al., 2011; Lee and Norden, 2013; Reinsch and Gonczy, 1998), microtubules and their associated motor proteins also contribute to the molecular machinery of INM (Tsai et al., 2010). Indeed, mutations in genes encoding dynein-interacting proteins, such as lissencephaly-1 (Lis1; also known as Pafah1b1), dynactin 1 and laminin γ1 (Lamc1), give rise to perturbed apical-ward nucleokinesis and, consequently, mitoses throughout the neuroepithelium (Del Bene et al., 2008; Feng et al., 2000; Tanaka et al., 2004; Tsuda et al., 2010). Interestingly, in shorter NPCs, such as those in the zebrafish developing retina, there must be some centrosome-independent mechanism of INM, as it appears that once apical INM is triggered a 'point of no return' is passed so that apical mitoses take place independently of centrosome position (Strzyz et al., 2015). Whether this mechanism is conserved in other neuroepithelia is not known.

The connection between the microtubule network controlling INM and the nuclear envelope is mediated by KASH-domain proteins (Syne proteins; also known as nesprin proteins), which form a complex with SUN-domain proteins in the nuclear envelope (Fig. 2B). Following the hypothesis of the centrosome as an anchor point for apical-ward INM, this microtubule network-nuclear envelope connection must be kept intact to allow such a nuclear migration. Indeed, experiments in knockout mice have revealed that the SUN-domain proteins SUN1 and SUN2 and the KASH domain proteins Syne1 and Syne2 are required for the apical migration of nuclei along microtubules toward the apical centrosome (Ge et al., 2010; Schenk et al., 2009; Xie et al., 2007; Zhang et al., 2009) (Fig. 2B).

The rationale behind the striking arrangement and dynamics of NPCs has classically been explained as a mechanism to pack more NPCs into a limited space. As such, INM serves to vary the distances of nuclei from the apical and basal surfaces, thereby allowing more NPCs to remain associated with the limited apical/basal surfaces than would be possible in a columnar epithelium. However, according to the original description of INM, 'the mitoses are confined to the region of the lumen not only because nuclei of that region divide, but because a nucleus that is about to divide moves to the region of the lumen to do so' (Sauer, 1935), indicating that it might be beneficial to send the nucleus to the apical area prior to entering mitosis. One possible advantage of sending the nucleus to the apical area during the G2 phase of the cell cycle is that it makes the centrosome available for entry into division. Supporting

Development (2018) 145, dev170613. doi:10.1242/dev.170613

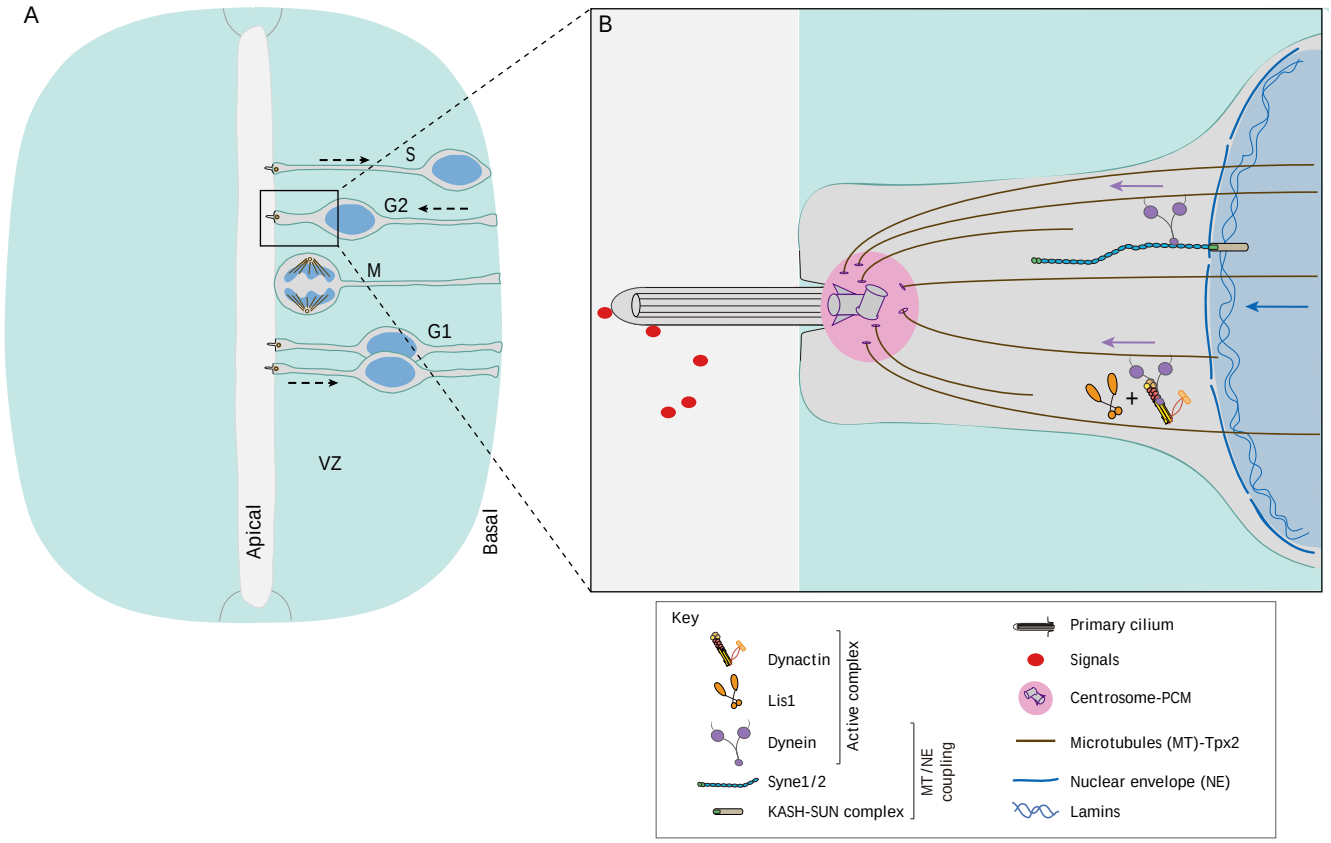


**Fig. 2. Interkinetic nuclear migration in NPCs.** (A) Diagram of a transverse section through the spinal cord. The nuclei of dividing NPCs occupy different apicobasal positions depending on the phase of the cell cycle (S, G2, M, G1). Dashed arrows indicate the direction of nuclear migration. (B) Diagram of the apical pole of an NPC in the G2 phase of the cell cycle. The primary cilium points to the NT lumen. The centrosome at the cilium base organizes microtubules to pull the nucleus apicalwards (blue arrow). A dynein complex linked to the nuclear envelope activates nuclear apical migration (purple arrows).

this idea, mitosis is in part triggered by a cascade of proteins localized to the centrosome, culminating in the activation of aurora kinase A and, subsequently, in the activation of the cyclin B/Cdk1 complex (Hirota et al., 2003; Jackman et al., 2003), which may function as a checkpoint for centrosome availability for division. The microtubule-dependent apical-ward transition of the nucleus in G2 phase might also facilitate the equal inheritance of apical attachments, thereby ensuring cohesion of the tissue despite a high proliferation rate. Additionally, increasing the exposure of NPCs to signalling pathways and molecules that function at the apical surface, such as Notch, which is known to be required for maintaining the progenitor character of NPCs (Hatakeyama et al., 2014; Ohata et al., 2011), might also be among the benefits of apical mitoses. Hence, besides affecting cell packing, INM could restrict the location of mitosis to particular regions of the NT lumen, thereby impacting the signals received by NPCs. These signals might be instructive for the outcome of cell division, as discussed below, and thus are important for CNS growth.

## Intrinsic centrosomal asymmetries in dividing neural progenitor cells are instructive for neurogenesis

Embryonic CNS growth requires a finely tuned balance between the different modes of divisions that NPCs undergo: symmetric proliferative divisions ensure expansion of the progenitor pool by generating two daughter cells with identical progenitor potential, whereas asymmetric divisions generate one daughter cell with progenitor potential and one daughter cell with a more restricted potential, which is then committed to neuronal differentiation (Fig. 3). However, cell division in general is intrinsically asymmetric as a consequence of differences in the centrosomes that are passed on to the daughter cells (Fig. 3). Before entering mitosis, the centrosome replicates in a semi-conservative manner, forming one centrosome that retains the mother centriole and another that receives the daughter centriole. As we discuss below, this centrosome asymmetry, which relates to centrosome age, structure, molecular composition, MTOC capabilities, and the recruitment of signalling components, can influence the fate of NPC divisions and, hence, the expansion of the progenitor pool.

NPCs inherit one centrosome consisting of a pair of centrioles surrounded by amorphous pericentriolar material (PCM). The two centrioles differ in their structure and function. The older ‘mother’ centriole possesses distinct sets of projections at its distal ends called subdistal and distal appendages, which bear specific proteins such as CEP164, CEP170, cenexin (also known as Odf2) and ninein that are implicated in the anchoring of microtubules, cilia formation and docking of the basal body at the plasma membrane (Graser et al., 2007; Ishikawa et al., 2005; Ou et al., 2002; Schmidt et al., 2012; Welburn and Cheeseman, 2012). In contrast to the mother centriole, the younger ‘daughter’ centriole lacks these appendages. Full acquisition of appendages by the daughter centriole is not achieved until at least one and a half cell cycles later (Hoyer-Fender, 2010; Mahen and Venkitaraman, 2012). Importantly for CNS growth, this built-in centrosome asymmetry has an impact on the fate of the daughter cells. Both in the developing mouse cortex (Paridaen et al., 2013; Wang et al., 2009) and in the chick spinal cord (Saade et al., 2017; Tozer et al., 2017) the centrosome retaining

Development (2018) 145, dev170613. doi:10.1242/dev.170613

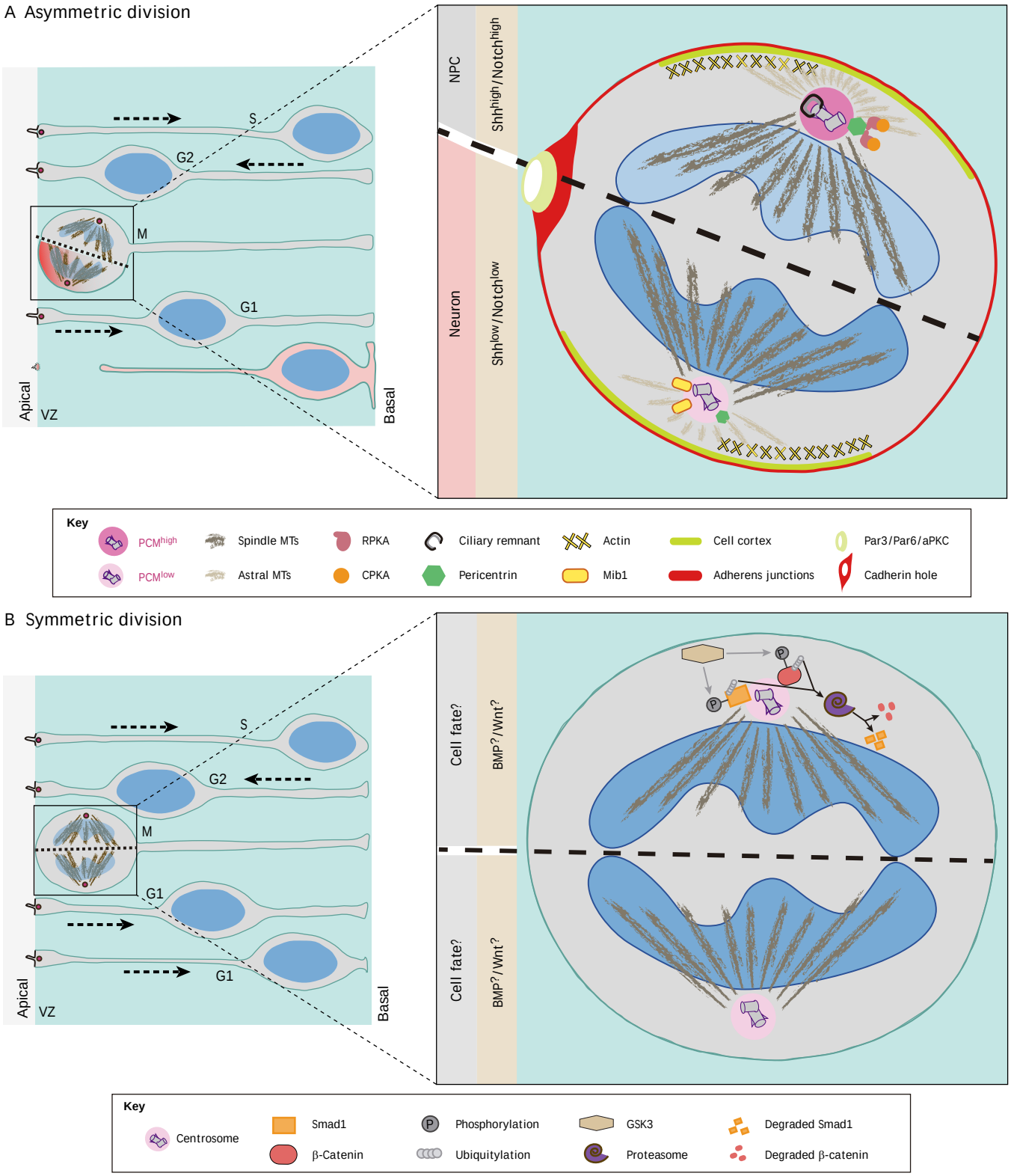


**Fig. 3. NPC modes of cell division.** (A,B) An asymmetrically dividing NPC generates one NPC and one differentiating neuron (pink, A), whereas a symmetrically dividing NPC generates two NPCs (B). (A) An asymmetrically dividing NPC shows asymmetric recruitment of PKA and Mib1 and asymmetric astral microtubule (MT) nucleation. Association of the astral MTs with the cell cortex defines the positioning of the mitotic spindle relative to the axis of polarity, favouring asymmetric inheritance of cell fate components. CPKA, protein kinase A catalytic subunit; RPKA, protein kinase A regulatory subunit; Mib1, Mind bomb-1. (B) A symmetrically dividing NPC shows centrosomal recruitment of Smad1 and β-catenin and the ubiquitin proteasome system. The final impact of this distribution of BMP and Wnt signalling components on the division mode of NPCs and the cell fate of daughter cells is still not well described. Grey arrows indicate phosphorylation; black arrows indicate proteasome-dependant degradation.

Development (2018) 145, dev170613. doi:10.1242/dev.170613

the old mother centriole is preferentially inherited by the NPC, whereas the centrosome containing the daughter (new mother) centriole is inherited by the delaminating and differentiating neuron, which leaves the VZ.

This centrosomal asymmetry has a number of downstream effects on NPC-derived cells. For instance, maturation of the daughter centriole is required for correct NPC function. The process of centrosome maturation is characterized by drastic expansion of the pericentriolar material and a robust increase in MTOC activity. During this event, proteins such as centrin and ninein are delivered to the centrosome along microtubules via a dynein/dynactin-dependent process (Dammermann and Merdes, 2002). Accordingly, the removal of mature centriole-specific proteins, including ninein (Wang et al., 2009), WDR62 and ASPM (Gai et al., 2016; Jayaraman et al., 2016), is sufficient to cause premature depletion of progenitor cells from the VZ and to impair CNS growth. Other proteins are recruited to the centrosome in a microtubule-independent manner by interacting with scaffold proteins, such as AKAP9 and pericentrin (Gillingham and Munro, 2000), which contain a localization domain (PACT domain) that targets the centrosome and serves to recruit structural and regulatory components such as γ-tubulin, microtubule binding proteins and signalling enzymes involved in microtubule nucleation (Almada et al., 2017). Supporting the relevance of centrosomal scaffold proteins in the control of the mode of NPC division, the removal of pericentrin triggers neurogenic divisions both in the chick spinal cord (Saade et al., 2017) and in the developing mouse cortex (Buchman et al., 2010). Surprisingly, pericentrin expression, together with other genes involved in centrosome maturation, appears to be regulated by the sonic hedgehog (Shh)/Gli signalling pathway (Saade et al., 2017), raising the interesting idea that classical growth factors might contribute to centrosome maturation in dividing NPCs.

Centrosome asymmetry is also reflected in notable differences in the recruitment of signalling components. One of these determinants is the Mind bomb1 (Mib1) protein, which is essential for generating functional Notch ligands (Koo et al., 2005). Mib1 is enriched at the daughter centrosome during mitosis (Fig. 3A) and gets inherited by the prospective neuron in asymmetric divisions (Tozer et al., 2017). This asymmetry is determined through the association of Mib1 with centriolar satellites (Tozer et al., 2017). Asymmetric localization of Mib1 at the daughter centrosome is accompanied by an unexpected asymmetric enrichment of the satellite markers PCM1 and AZI1 (CEP131) at the daughter centrosome (Tozer et al., 2017). Disruption of this interaction leads to symmetric Mib1 localization in mitosis, reciprocal Notch activation between sister cells, and a reduction in asymmetric NPC divisions and neurogenesis. Interestingly, centriolar satellite proteins have also been shown to assemble with microcephaly-associated proteins and promote centriole duplication (Kodani et al., 2015).

Centrosome asymmetry also impacts on the capacity to reassemble a primary cilium; the daughter cell that inherits the mother centriole reassembles a cilium and responds to external stimuli, such as Shh and other growth factors, prior to its sister cell (Anderson and Stearns, 2009). In dividing NPCs, a portion of the ciliary membrane that is preferentially attached to the mother centriole is endocytosed at the onset of mitosis, persists through mitosis at one spindle pole (Fig. 3A), and is asymmetrically inherited by one daughter cell; this cells retains progenitor character (Paridaen et al., 2013; Saade et al., 2017; Wang et al., 2009). Hence, it appears that the presence of this ciliary membrane remnant speeds up primary cilium assembly and facilitates the integration of signals, which in turn helps to maintain asymmetric NPC division.

Centrosomes, and hence centrosome asymmetry, also determine the organization and final orientation of the mitotic spindle relative to the cell cortex during cell division (Negishi et al., 2016; Rebollo et al., 2007). As discussed above, mother and daughter centrosomes differ notably in the expansion of their PCM and in their MTOC activity at mitosis entry. As such, the mother centrosome organizes a microtubule aster that is larger than that of the daughter centrosome (Fig. 3A) (Negishi et al., 2016; Rebollo et al., 2007; Yamashita et al., 2007). Astral microtubules connect to the cell cortex via the NuMA/LGN/Gai protein complex, which, by recruiting motor proteins of the dynein/dynactin complex, pulls on astral microtubules; this, in turn, drives mitotic spindle movements and orientation (Konno et al., 2008; Lesage et al., 2010; Morin et al., 2007; Saadaoui et al., 2017). In dividing NPCs, mitotic spindle orientation is associated with the partitioning of apical membrane subdomains. At the luminal surface, membrane subdomains organize to form the apical junction complex where, among other proteins, Par3/6 and atypical protein kinase C (aPKC) localize (Kosodo et al., 2004; Marthiens and ffrench-Constant, 2009). By contrast, the junctional proteins N-cadherin (Cdh2), α-catenin and β-catenin are found in the sub-apical domain (Fig. 3A) (Kosodo et al., 2004; Marthiens and ffrench-Constant, 2009; Saade et al., 2017). During interphase, the apical junction complex drives the positioning of NPCs within the epithelium. However, when NPCs divide, the components of the apical junction complex redistribute depending on the orientation of the mitotic spindle and the fate of the daughter cells. As such, a symmetric distribution of apical membrane subdomains is associated with proliferative divisions in which both daughter cells remain within the VZ as NPCs. Minor changes in spindle orientation determine whether the cleavage plane bisects or bypasses the small apical domain of dividing NPCs (Fig. 3A) and hence determine the outcome of the division (Saade et al., 2017). Importantly, it has been shown that progenitors retaining the old mother centriole reorganize a new apical polarity complex and remain within the VZ (Das and Storey, 2014). By contrast, NPCs that inherit the daughter centrosome also inherit the old apical polarity complex, which becomes disorganized upon differentiation (Das and Storey, 2014; Kasioulis et al., 2017). Together, these findings suggest that asymmetric spindle orientation is associated with a reduction in symmetric divisions, premature cell cycle exit and premature neurogenesis, potentially leading to a microcephaly phenotype (Bultje et al., 2009; Lancaster and Knoblich, 2012; Shitamukai et al., 2011; Shitamukai and Matsuzaki, 2012; Wilcock et al., 2007).

Hence, all of the findings discussed above reinforce the idea that, from a centrosomal perspective, the default outcome of any cell division should be asymmetric. Overcoming these various centrosomal, and associated, asymmetries would be required to promote symmetric proliferative divisions and embryonic CNS growth, and failure to do so might lead to neurodevelopmental defects such as microcephaly. This is an important point to note, especially as much of the effort in this field has focused on the search for signals that instruct the switch to asymmetric division, which instead appears to be the default state for NPC division (and possibly for other dividing cells).

## New roles for classic growth factors in centrosome maturation during embryonic CNS growth

In the growing CNS, the morphogenetic activity of secreted proteins that generate cell diversity (e.g. members of the Shh, Wnt and BMP families) is combined with their capacity to coordinate cell cycle progression by directly regulating discrete sets of genes that are key

Development (2018) 145, dev170613. doi:10.1242/dev.170613

components of the cell cycle machinery (Alvarez-Medina et al., 2009; Cayuso et al., 2006; Molina and Pituello, 2017; Ulloa and Briscoe, 2007). In addition to such activities that ensure the maintenance of progenitor cell proliferation, these factors appear to modulate the mode of cell division adopted by NPCs and neurons.

Shh signalling, for example, has been shown to regulate the mode of motor neuron progenitor cell division within the developing spinal cord (Saade et al., 2013). By combining experimental data with mathematical modelling, it has been shown that the cell division mode switches sharply, from proliferative divisions to neurogenic divisions, with the sudden loss of Shh activity (Saade et al., 2013). In addition, maintaining Shh signalling artificially high is sufficient to prevent this developmental switch and to maintain symmetric proliferative divisions. This observation raised the question as to whether this Shh activity might impact on centrosome biology during NPC division. As introduced above, Shh/Gli activity in NPCs is sufficient to activate the expression of a cluster of centrosomal proteins, including centriolar and pericentriolar material and centrosome-associated proteins, that might contribute to centrosomal maturation and hence overcome intrinsic centrosome asymmetries (Saade et al., 2017). Among them, pericentrin, the expression of which is activated by Shh/Gli signalling, serves to dock an equal amount of protein kinase A (PKA) to both the mother and daughter centrosomes. PKA also exerts a downstream effect on processing of the Gli transcription factors so, at early developmental stages when Shh/Gli activity is high and proliferative divisions are predominant, the centrosomal localization of PKA becomes symmetric, leading to equal Shh activity in both daughter cells. As development proceeds, however, Shh/Gli activity decreases, pericentrin expression becomes low, and PKA remains associated with only the mother centrosome, leading to asymmetric Shh activity and neurogenic divisions (Fig. 3A). Disrupting the interaction of pericentrin with the centrosome leads to PKA mislocalization in mitosis and an increase in asymmetric neurogenic divisions (Saade et al., 2017). The expression of a number of additional centrosome proteins appears to be regulated by the Shh/Gli signalling pathway. These include CEP110 (CNTRL), which colocalizes with ninein and is involved in maturation of the daughter centrosome (Ou et al., 2002); ASPM, which concentrates at NPC mitotic spindle poles and is downregulated at the switch from symmetric proliferative to asymmetric neurogenic divisions (Fish et al., 2006); and PCM1, which is a component of centriolar satellites involved in the redistribution of molecular determinants (Tozer et al., 2017). Hence, centrosome maturation and the consequent regulation of the mode of NPC division should be added to the already long list of multiple roles played by Shh/Gli signalling during CNS development (Martí and Bovolenta, 2002).

The BMP/Smad and Wnt/β-catenin signalling pathways also play major roles in regulating growth of the developing vertebrate nervous system (Le Dréau and Martí, 2012). Indeed, the mode of cell division adopted by interneurons in the developing spinal cord is dictated by different levels of activity of the canonical BMP effectors Smad1/5 (Le Dréau et al., 2014). Thus, analogous mechanisms regulating cell division, similar to those controlled by Shh, might be foreseen, particularly as signalling components of both pathways localize to centrosomes. Phosphorylated Smad1 (pSmad1), the effector of canonical BMP signalling, appears to be localized to centrosomes during cell division, although this pool of Smad1 protein (which is subjected to sequential phosphorylation by MAPK and glycogen synthase kinase 3) is targeted for degradation (Fuentealba et al., 2007). Moreover, pSmad proteins specifically targeted for proteasomal degradation are asymmetrically inherited preferentially by one daughter cell during cell division (Fig. 3B) (Fuentealba et al., 2008). Indeed, the proteasomal degradation of pSmad1 in the centrosome regulates the duration of the BMP signalling pathway, which in turn is known to maintain stem cell identity (Fuentealba et al., 2007; Le Dréau et al., 2014). This suggests that degradation mechanisms might be associated with the mother centrosome during asymmetric divisions (Fig. 3B).

Dividing NPCs in the mouse embryonic midbrain also show centrosomal localization of phosphorylated β-catenin – the effector of the canonical Wnt signalling pathway (Chilov et al., 2011) (Fig. 3B). Whether β-catenin is asymmetrically recruited to mitotic centrosomes in these cells, however, has not yet been addressed. Phosphorylated β-catenin also shows centrosomal localization in human embryonic stem cells (Fuentealba et al., 2008) and, *in vitro*, a localized Wnt signal can induce oriented cell divisions that generate distinct cell fates in embryonic stem cells (Habib et al., 2013). Moreover, in *Caenorhabditis elegans*, SYS-1/β-catenin localizes to mitotic centrosomes in mother cells and is subjected to dynamic proteasome degradation (Vora and Phillips, 2015). In this context, the centrosomal localization negatively regulates SYS-1/β-catenin levels and Wnt-dependent cell fate in daughter cells after division.

Hence, beyond age and structure, mother and daughter centrosomes appear to have different abilities to serve as hubs for the integration, duration and coordination of signalling pathways that are important for CNS growth.

## Centrosome dysfunction and microcephaly

The consequences of centrosome dysfunction during development and how they contribute to human diseases are highlighted by the study of autosomal recessive primary microcephaly (MCPH). MCPH is a genetically heterogeneous neurodevelopmental disorder characterized by a small CNS at birth and non-progressive intellectual disability. Many of the causative genes for the 20 loci mapped to date (MCPH1-MCPH20) in various populations around the globe encode centriole/centrosome or kinetochore/spindle pole proteins that are involved in centriole biogenesis, centrosome maturation, cytokinesis, centromere and kinetochore function (Table 1). This indicates that centrosome dysfunction is one of the main causes of MCPH (Jayaraman et al., 2018; Nano and Basto, 2017). Moreover, additional microcephaly phenotypes are associated with centrosome proteins, including CEP63, PCNT, NIN, POC1A (Table 1), establishing a strong genetic link between centrosome dysfunction during development and the aetiology of microcephaly. What remains to be resolved, however, is why brain size in particular is so vulnerable to centrosome mutations; centrosome dysfunction found in MCPH mostly leads to architecturally normal but smaller brains, in most cases without affecting body size. It thus appears that, compared with other organs, size regulation in the CNS might rely more on the tightly controlled mode of cell divisions that occur during developmental stages.

## Conclusions

As we have reviewed here, recent research in animal models has started to reveal the multiple roles played by centrosomes during embryonic CNS growth and neurogenesis. Centrosomes are confined to the apical pole of NPCs where they serve as a basal body for the primary cilium. As such, they regulate the exposure of cells to the growth factor signalling-rich microenvironment of the NT lumen. The subsequent integration of growth factor signals during the G1 phase of the cell cycle results in the regulated

Development (2018) 145, dev170613. doi:10.1242/dev.170613

**Table 1. The MCPH1-20 loci, their gene products and protein functions**

| Locus | Gene product | Alternative names and symbols | Protein function and localization | OMIM |
|---|---|---|---|---|
| MCPH1 | MCPH1 | Microcephalin; BRCT-repeat inhibitor of TERT expression 1; BRIT1 | Regulates chromosome condensation | 607117 |
| MCPH2 | WDR62 | WD repeat-containing protein 62 | Localizes to the centrosome and to the nucleus | 613583 |
| MCPH3 | CEP215 | Centrosomal protein, 215-kD; CDK5 regulatory subunit-associated protein; CDK5RAP2 | Localizes to the centrosome and to the spindle poles during mitosis | 608201 |
| MCPH4 | CASC5 | Kinetochore scaffold 1; KNL1 | Localizes to the kinetochore | 609173 |
| MCPH5 | ASPM | Abnormal spindle-like, microcephaly-associated | Essential for mitotic spindle assembly/function | 605481 |
| MCPH6 | CENPJ | Centromeric protein J; centrosomal P4.1-associated protein; CPAP | Localizes to the centrosome, regulates microtubule assembly and nucleation | 609279 |
| MCPH7 | STIL | SCL/TAL1-interrupting locus | Localizes to PCM, regulates centriole duplication | 181590 |
| MCPH8 | CEP135 | Centrosomal protein, 135-kD | Forms the core centriole structure, regulates early centriole assembly | 611423 |
| MCPH9 | CEP152 | Centrosomal protein, 152-kD | Core protein of the centrosome | 613529 |
| MCPH10 | ZNF335 | Zinc finger protein 335; NRC-interacting factor; NIF1 | Component of the trithorax H3K4-methylation chromatin remodelling complex | 610827 |
| MCPH11 | PHC1 | Polyhomeotic-like 1 | Component of the polycomb repressive complex-1 (PRC1) | 602978 |
| MCPH12 | CDK6 | Cyclin-dependent kinase 6 | Localizes to the centrosome, plays a role in cell cycle progression | 603368 |
| MCPH13 | CENPE | Centromeric protein E | Kinetochore-associated kinesin-like motor protein | 117143 |
| MCPH14 | SASS6 | SAS-6 centriolar assembly protein | Functions in procentriole formation | 609321 |
| MCPH15 | MFSD2A | Major facilitator superfamily domain-containing protein 2A | Sodium-dependent lysophosphatidylcholine transporter | 614397 |
| MCPH16 | ANKLE2 | Ankyrin repeat- and LEM domain-containing protein 2; LEM domain-containing protein 4; LEM4 | Regulates reassembly of the nuclear envelope at anaphase | 616062 |
| MCPH17 | CIT | Citron RHO-interacting serine/threonine kinase; serine/threonine protein kinase 21; STK21 | Essential for cytokinesis | 605629 |
| MCPH18 | WDFY3 | WD repeat- and FYVE domain-containing protein 3 | Organizes misfolded ubiquitylated proteins into bodies to be degraded by autophagy | 617485 |
| MCPH19 | COPB2 | Coatomer protein complex, subunit β2 | Subunit of the Golgi coatomer complex, necessary for retrograde intracellular trafficking | 606990 |
| MCPH20 | KIF14 | Kinesin family member 14 | Microtubule-associated motor, plays an important role in cell division | 611279 |
| SCKL6 | CEP63 | Centrosomal protein, 63-kD | Centrosomal protein | 614724 |
| SCKL7 | NIN | Ninein; GSK3B-interacting protein | Centrosomal protein, re-forms interphase centrosomal architecture after mitosis | 608684 |
| MOPD2 | PCNT | Pericentrin; kendrin; KEN | Localizes to the centrosome | 605925 |
| SOFT | POC1A | POC1 centriolar protein, chlamydomonas, homolog of, A | Localizes to centrioles, functions in centriole duplication and/or maintenance | 614783 |

OMIM, Online Mendelian Inheritance in Man

Loci beneath the line relate to other centrosome proteins with associated microcephaly phenotypes.

expression of multiple targets including genes involved in centrosome maturation. Hence, by controlling symmetric centrosomal protein assembly, growth factors can overcome the intrinsic asymmetry of the centrosome during NPC division, thereby promoting self-expanding symmetric divisions and CNS growth. Importantly, the failure to overcome such intrinsic cell division asymmetries, and thus the failure to ensure appropriate cell divisions during early CNS growth, may be responsible for neurodevelopmental disorders such as primary microcephaly.

Moving forward, we propose that we should turn our attention to the search for instructive signals that can overcome these intrinsic asymmetries in NPC divisions. As we have highlighted here, classical growth factors might be key players. For example, a role for Shh has recently been revealed and requires further investigation. It will also be important to understand how molecular components of the Wnt and BMP signalling pathways are integrated into the mitotic centrosome and whether they affect NPC modes of division. It is likely that additional regulatory mechanisms that remain to be discovered are also involved, and their characterization might expand our knowledge of how, from a centrosomal perspective, classical growth factors contribute to defining the division mode of NPCs. Do such components participate directly in the intrinsic functions of the centrosome? Does the centrosome serve as a hub for the integration, duration and distribution of these signals in NPCs after division? These key open questions need to be answered in order to fully understand CNS growth from a centrosomal point of view.

**Acknowledgements**

We apologize to colleagues whose work is not included owing to space constraints. We thank the E.M. laboratory members for useful discussions.

**Competing interests**

The authors declare no competing or financial interests.

**Funding**

The work in E.M.'s laboratory is supported by grants from Ministerio de Economía, Industria y Competitividad, Gobierno de España (BFU2016-77498-P and BFU2016-81887-REDT). E.G.-G. holds a Predoctoral Scholarship BES-2014-068589, J.B.-A. holds a Predoctoral Scholarship BES-2017-080050 from Ministerio de Economía, Industria y Competitividad, Gobierno de España.

**References**

**Addison, M. and Wilkinson, D. G.** (2016). Segment identity and cell segregation in the vertebrate hindbrain. *Curr. Top. Dev. Biol.* **117**, 581-596.

**Almada, E., Tonucci, F. M., Hidalgo, F., Ferretti, A., Ibarra, S., Pariani, A., Vena, R., Favre, C., Girardini, J., Kierbel, A. et al.** (2017). Akap350 recruits Eb1 to the spindle poles, ensuring proper spindle orientation and lumen formation in 3D epithelial cell cultures. *Sci. Rep.* **7**, 14894.

**Alvarez-Medina, R., Le Dreau, G., Ros, M. and Marti, E.** (2009). Hedgehog activation is required upstream of Wnt signalling to control neural progenitor proliferation. *Development* **136**, 3301-3309.

**Anderson, C. T. and Stearns, T.** (2009). Centriole age underlies asynchronous primary cilium growth in mammalian cells. *Curr. Biol.* **19**, 1498-1502.

**Buchman, J. J., Tseng, H.-C., Zhou, Y., Frank, C. L., Xie, Z. and Tsai, L.-H.** (2010). Cdk5rap2 interacts with pericentrin to maintain the neural progenitor pool in the developing neocortex. *Neuron* **66**, 386-402.

**Bultje, R. S., Castaneda-Castellanos, D. R., Jan, L. Y., Jan, Y.-N., Kriegstein, A. R. and Shi, S.-H.** (2009). Mammalian Par3 regulates progenitor cell asymmetric division via notch signaling in the developing neocortex. *Neuron* **63**, 189-202.

**Cayuso, J., Ulloa, F., Cox, B., Briscoe, J. and Marti, E.** (2006). The Sonic hedgehog pathway independently controls the patterning, proliferation and survival of neuroepithelial cells by regulating Gli activity. *Development* **133**, 517-528.

**Chilov, D., Sinjushina, N., Rita, H., Taketo, M. M., Mäkelä, T. P. and Partanen, J.** (2011). Phosphorylated beta-catenin localizes to centrosomes of neuronal progenitors and is required for cell polarity and neurogenesis in developing midbrain. *Dev. Biol.* **357**, 259-268.

**Cohen, M., Briscoe, J. and Blassberg, R.** (2013). Morphogen interpretation: the transcriptional logic of neural tube patterning. *Curr. Opin. Genet. Dev.* **23**, 423-428.

**Dammermann, A. and Merdes, A.** (2002). Assembly of centrosomal proteins and microtubule organization depends on PCM-1. *J. Cell Biol.* **159**, 255-266.

**Das, R. M. and Storey, K. G.** (2014). Apical abscission alters cell polarity and dismantles the primary cilium during neurogenesis. *Science* **343**, 200-204.

**Del Bene, F., Wehman, A. M., Link, B. A. and Baier, H.** (2008). Regulation of neurogenesis by interkinetic nuclear migration through an apical-basal notch gradient. *Cell* **134**, 1055-1065.

**Dubreuil, V., Marzesco, A.-M., Corbeil, D., Huttner, W. B. and Wilsch-Bräuninger, M.** (2007). Midbody and primary cilium of neural progenitors release extracellular membrane particles enriched in the stem cell marker prominin-1. *J. Cell Biol.* **176**, 483-495.

**Feng, Y., Olson, E. C., Stukenberg, P. T., Flanagan, L. A., Kirschner, M. W. and Walsh, C. A.** (2000). LIS1 regulates CNS lamination by interacting with mNudE, a central component of the centrosome. *Neuron* **28**, 665-679.

**Fish, J. L., Kosodo, Y., Enard, W., Paabo, S. and Huttner, W. B.** (2006). Aspm specifically maintains symmetric proliferative divisions of neuroepithelial cells. *Proc. Natl. Acad. Sci. USA* **103**, 10438-10443.

**Florio, M., Borrell, V. and Huttner, W. B.** (2017). Human-specific genomic signatures of neocortical expansion. *Curr. Opin. Neurobiol.* **42**, 33-44.

**Fuentealba, L. C., Eivers, E., Ikeda, A., Hurtado, C., Kuroda, H., Pera, E. M. and De Robertis, E. M.** (2007). Integrating patterning signals: Wnt/GSK3 regulates the duration of the BMP/Smad1 signal. *Cell* **131**, 980-993.

**Fuentealba, L. C., Eivers, E., Geissert, D., Taelman, V. and De Robertis, E. M.** (2008). Asymmetric mitosis: unequal segregation of proteins destined for degradation. *Proc. Natl. Acad. Sci. USA* **105**, 7732-7737.

**Gai, M., Bianchi, F. T., Vagnoni, C., Vernì, F., Bonaccorsi, S., Pasquero, S., Berto, G. E., Sgrò, F., Chiotto, A. M. A., Annaratone, L. et al.** (2016). ASPM and CITK regulate spindle orientation by affecting the dynamics of astral microtubules. *EMBO Rep.* **17**, 1396-1409.

**Ge, X., Frank, C. L., Calderon de Anda, F. and Tsai, L.-H.** (2010). Hook3 interacts with PCM1 to regulate pericentriolar material assembly and the timing of neurogenesis. *Neuron* **65**, 191-203.

**Gillingham, A. K. and Munro, S.** (2000). The PACT domain, a conserved centrosomal targeting motif in the coiled-coil proteins AKAP450 and pericentrin. *EMBO Rep.* **1**, 524-529.

**Gilmore, E. C. and Walsh, C. A.** (2013). Genetic causes of microcephaly and lessons for neuronal development. *Wiley Interdiscip. Rev. Dev. Biol.* **2**, 461-478.

**Goetz, S. C. and Anderson, K. V.** (2010). The primary cilium: a signalling centre during vertebrate development. *Nat. Rev. Genet.* **11**, 331-344.

**Graser, S., Stierhof, Y.-D., Lavoie, S. B., Gassner, O. S., Lamla, S., Le Clech, M. and Nigg, E. A.** (2007). Cep164, a novel centriole appendage protein required for primary cilium formation. *J. Cell Biol.* **179**, 321-330.

**Greene, N. D. E. and Copp, A. J.** (2014). Neural tube defects. *Annu. Rev. Neurosci.* **37**, 221-242.

**Gupta, S. and Sen, J.** (2016). Roof plate mediated morphogenesis of the forebrain: new players join the game. *Dev. Biol.* **413**, 145-152.

**Habib, S. J., Chen, B.-C., Tsai, F.-C., Anastassiadis, K., Meyer, T., Betzig, E. and Nusse, R.** (2013). A localized Wnt signal orients asymmetric stem cell division in vitro. *Science* **339**, 1445-1448.

**Hatakeyama, J., Wakamatsu, Y., Nagafuchi, A., Kageyama, R., Shigemoto, R. and Shimamura, K.** (2014). Cadherin-based adhesions in the apical endfoot are required for active Notch signaling to control neurogenesis in vertebrates. *Development* **141**, 1671-1682.

**Heide, M., Long, K. R. and Huttner, W. B.** (2017). Novel gene function and regulation in neocortex expansion. *Curr. Opin. Cell Biol.* **49**, 22-30.

**Hirota, T., Kunitoku, N., Sasayama, T., Marumoto, T., Zhang, D., Nitta, M., Hatakeyama, K. and Saya, H.** (2003). Aurora-A and an interacting activator, the LIM protein Ajuba, are required for mitotic commitment in human cells. *Cell* **114**, 585-598.

**Hoyer-Fender, S.** (2010). Centriole maturation and transformation to basal body. *Semin. Cell Dev. Biol.* **21**, 142-147.

**Insolera, R., Bazzi, H., Shao, W., Anderson, K. V. and Shi, S. H.** (2014). Cortical neurogenesis in the absence of centrioles. *Nat. Neurosci.* **17**, 1528-1535.

**Ishikawa, H., Kubo, A., Tsukita, S. and Tsukita, S.** (2005). Odf2-deficient mother centrioles lack distal/subdistal appendages and the ability to generate primary cilia. *Nat. Cell Biol.* **7**, 517-524.

**Jackman, M., Lindon, C., Nigg, E. A. and Pines, J.** (2003). Active cyclin B1-Cdk1 first appears on centrosomes in prophase. *Nat. Cell Biol.* **5**, 143-148.

**Jayaraman, D., Kodani, A., Gonzalez, D. M., Mancias, J. D., Mochida, G. H., Vagnoni, C., Johnson, J., Krogan, N., Harper, J. W., Reiter, J. F. et al.** (2016). Microcephaly proteins Wdr62 and Aspm define a mother centriole complex regulating centriole biogenesis, apical complex, and cell fate. *Neuron* **92**, 813-828.

**Jayaraman, D., Bae, B.-I. and Walsh, C. A.** (2018). The genetics of primary microcephaly. *Annu. Rev. Genomics Hum. Genet.* **19**, 177-200.

**Johnson, M. B. and Walsh, C. A.** (2017). Cerebral cortical neuron diversity and development at single-cell resolution. *Curr. Opin. Neurobiol.* **42**, 9-16.

**Kasioulis, I., Das, R. M. and Storey, K. G.** (2017). Inter-dependent apical microtubule and actin dynamics orchestrate centrosome retention and neuronal delamination. *eLife* **6**, e26215.

**Kodani, A., Yu, T. W., Johnson, J. R., Jayaraman, D., Johnson, T. L., Al-Gazali, L., Sztriha, L., Partlow, J. N., Kim, H., Krup, A. L. et al.** (2015). Centriolar satellites assemble centrosomal microcephaly proteins to recruit CDK2 and promote centriole duplication. *eLife* **4**.

**Konno, D., Shioi, G., Shitamukai, A., Mori, A., Kiyonari, H., Miyata, T. and Matsuzaki, F.** (2008). Neuroepithelial progenitors undergo LGN-dependent planar divisions to maintain self-renewability during mammalian neurogenesis. *Nat. Cell Biol.* **10**, 93-101.

**Koo, B.-K., Lim, H. S., Song, R., Yoon, M. J., Yoon, K. J., Moon, J. S., Kim, Y. W., Kwon, M. C., Yoo, K. W., Kong, M. P. et al.** (2005). Mind bomb 1 is essential for generating functional Notch ligands to activate Notch. *Development* **132**, 3459-3470.

**Kosodo, Y., Röper, K., Haubensak, W., Marzesco, A.-M., Corbeil, D. and Huttner, W. B.** (2004). Asymmetric distribution of the apical plasma membrane during neurogenic divisions of mammalian neuroepithelial cells. *EMBO J.* **23**, 2314-2324.

**Kosodo, Y., Suetsugu, T., Suda, M., Mimori-Kiyosue, Y., Toida, K., Baba, S. A., Kimura, A. and Matsuzaki, F.** (2011). Regulation of interkinetic nuclear migration by cell cycle-coupled active and passive mechanisms in the developing brain. *EMBO J.* **30**, 1690-1704.

**Lancaster, M. A. and Knoblich, J. A.** (2012). Spindle orientation in mammalian cerebral cortical development. *Curr. Opin. Neurobiol.* **22**, 737-746.

**Langman, J., Guerrant, R. L. and Freeman, B. G.** (1966). Behavior of neuro-epithelial cells during closure of the neural tube. *J. Comp. Neurol.* **127**, 399-411.

**Le Dréau, G. and Martí, E.** (2012). Dorsal-ventral patterning of the neural tube: a tale of three signals. *Dev. Neurobiol.* **72**, 1471-1481.

**Le Dréau, G., Saade, M., Gutiérrez-Vallejo, I. and Martí, E.** (2014). The strength of SMAD1/5 activity determines the mode of stem cell division in the developing spinal cord. *J. Cell Biol.* **204**, 591-605.

**Lee, H. O. and Norden, C.** (2013). Mechanisms controlling arrangements and movements of nuclei in pseudostratified epithelia. *Trends Cell Biol.* **23**, 141-150.

**Lesage, B., Gutierrez, I., Martí, E. and Gonzalez, C.** (2010). Neural stem cells: the need for a proper orientation. *Curr. Opin. Genet. Dev.* **20**, 438-442.

**Mahen, R. and Venkitaraman, A. R.** (2012). Pattern formation in centrosome assembly. *Curr. Opin. Cell Biol.* **24**, 14-23.

**Marthiens, V. and ffrench-Constant, C.** (2009). Adherens junction domains are split by asymmetric division of embryonic neural stem cells. *EMBO Rep.* **10**, 515-520.

**Martí, E. and Bovolenta, P.** (2002). Sonic hedgehog in CNS development: one signal, multiple outputs. *Trends Neurosci.* **25**, 89-96.

**Molina, A. and Pituello, F.** (2017). Playing with the cell cycle to build the spinal cord. *Dev. Biol.* **432**, 14-23.

**Morin, X., Jaouen, F. and Durbec, P.** (2007). Control of planar divisions by the G-protein regulator LGN maintains progenitors in the chick neuroepithelium. *Nat. Neurosci.* **10**, 1440-1448.

**Nano, M. and Basto, R.** (2017). Consequences of centrosome dysfunction during brain development. *Adv. Exp. Med. Biol.* **1002**, 19-45.

**Negishi, T., Miyazaki, N., Murata, K., Yasuo, H. and Ueno, N.** (2016). Physical association between a novel plasma-membrane structure and centrosome orients cell division. *eLife* **5**, e16550.

**Ohata, S., Aoki, R., Kinoshita, S., Yamaguchi, M., Tsuruoka-Kinoshita, S., Tanaka, H., Wada, H., Watabe, S., Tsuboi, T., Masai, I. et al.** (2011). Dual roles

of Notch in regulation of apically restricted mitosis and apicobasal polarity of neuroepithelial cells. *Neuron* **69**, 215-230.
**Ou, Y. Y., Mack, G. J., Zhang, M. and Rattner, J. B.** (2002). CEP110 and ninein are located in a specific domain of the centrosome associated with centrosome maturation. *J. Cell Sci.* **115**, 1825-1835.
**Paridaen, J. T. M. L., Wilsch-Bräuninger, M. and Huttner, W. B.** (2013). Asymmetric inheritance of centrosome-associated primary cilium membrane directs ciliogenesis after cell division. *Cell* **155**, 333-344.
**Rebollo, E., Sampaio, P., Januschke, J., Llamazares, S., Varmark, H. and González, C.** (2007). Functionally unequal centrosomes drive spindle orientation in asymmetrically dividing Drosophila neural stem cells. *Dev. Cell* **12**, 467-474.
**Reinsch, S. and Gonczy, P.** (1998). Mechanisms of nuclear positioning. *J. Cell Sci.* **111**, 2283-2295.
**Saadaoui, M., Konno, D., Loulier, K., Goiame, R., Jadhav, V., Mapelli, M., Matsuzaki, F. and Morin, X.** (2017). Loss of the canonical spindle orientation function in the Pins/LGN homolog AGS3. *EMBO Rep.* **18**, 1509-1520.
**Saade, M., Gutiérrez-Vallejo, I., Le Dréau, G., Rabadán, M. A., Miguez, D. G., Buceta, J. and Martí, E.** (2013). Sonic hedgehog signaling switches the mode of division in the developing nervous system. *Cell Rep.* **4**, 492-503.
**Saade, M., Gonzalez-Gobartt, E., Escalona, R., Usieto, S. and Martí, E.** (2017). Shh-mediated centrosomal recruitment of PKA promotes symmetric proliferative neuroepithelial cell division. *Nat. Cell Biol.* **19**, 493-503.
**Sauer, F. C.** (1935). Mitosis in the neural tube. *J. Comp. Neurol.* **62**, 377-405.
**Schenk, J., Wilsch-Brauninger, M., Calegari, F. and Huttner, W. B.** (2009). Myosin II is required for interkinetic nuclear migration of neural progenitors. *Proc. Natl. Acad. Sci. USA* **106**, 16487-16492.
**Schmidt, K. N., Kuhns, S., Neuner, A., Hub, B., Zentgraf, H. and Pereira, G.** (2012). Cep164 mediates vesicular docking to the mother centriole during early steps of ciliogenesis. *J. Cell Biol.* **199**, 1083-1101.
**Shitamukai, A. and Matsuzaki, F.** (2012). Control of asymmetric cell division of mammalian neural progenitors. *Dev. Growth Differ.* **54**, 277-286.
**Shitamukai, A., Konno, D. and Matsuzaki, F.** (2011). Oblique radial glial divisions in the developing mouse neocortex induce self-renewing progenitors outside the germinal zone that resemble primate outer subventricular zone progenitors. *J. Neurosci.* **31**, 3683-3695.
**Sousa, V. H. and Fishell, G.** (2010). Sonic hedgehog functions through dynamic changes in temporal competence in the developing forebrain. *Curr. Opin. Genet. Dev.* **20**, 391-399.
**Strzyz, P. J., Lee, H. O., Sidhaye, J., Weber, I. P., Leung, L. C. and Norden, C.** (2015). Interkinetic nuclear migration is centrosome independent and ensures apical cell division to maintain tissue integrity. *Dev. Cell* **32**, 203-219.
**Tanaka, T., Serneo, F. F., Higgins, C., Gambello, M. J., Wynshaw-Boris, A. and Gleeson, J. G.** (2004). Lis1 and doublecortin function with dynein to mediate coupling of the nucleus to the centrosome in neuronal migration. *J. Cell Biol.* **165**, 709-721.
**Tozer, S., Baek, C., Fischer, E., Goiame, R. and Morin, X.** (2017). Differential routing of mindbomb1 via centriolar satellites regulates asymmetric divisions of neural progenitors. *Neuron* **93**, 542-551.e544.
**Tsai, J.-W., Lian, W.-N., Kemal, S., Kriegstein, A. R. and Vallee, R. B.** (2010). Kinesin 3 and cytoplasmic dynein mediate interkinetic nuclear migration in neural stem cells. *Nat. Neurosci.* **13**, 1463-1471.
**Tsuda, S., Kitagawa, T., Takashima, S., Asakawa, S., Shimizu, N., Mitani, H., Shima, A., Tsutsumi, M., Hori, H., Naruse, K. et al.** (2010). FAK-mediated extracellular signals are essential for interkinetic nuclear migration and planar divisions in the neuroepithelium. *J. Cell Sci.* **123**, 484-496.
**Ulloa, F. and Briscoe, J.** (2007). Morphogens and the control of cell proliferation and patterning in the spinal cord. *Cell Cycle* **6**, 2640-2649.
**Ulloa, F. and Marti, E.** (2010). Wnt won the war: antagonistic role of Wnt over Shh controls dorso-ventral patterning of the vertebrate neural tube. *Dev. Dyn.* **239**, 69-76.
**Vora, S. and Phillips, B. T.** (2015). Centrosome-associated degradation limits beta-catenin inheritance by daughter cells after asymmetric division. *Curr. Biol.* **25**, 1005-1016.
**Wang, X., Tsai, J.-W., Imai, J. H., Lian, W.-N., Vallee, R. B. and Shi, S.-H.** (2009). Asymmetric centrosome inheritance maintains neural progenitors in the neocortex. *Nature* **461**, 947-955.
**Welburn, J. P. I. and Cheeseman, I. M.** (2012). The microtubule-binding protein Cep170 promotes the targeting of the kinesin-13 depolymerase Kif2b to the mitotic spindle. *Mol. Biol. Cell* **23**, 4786-4795.
**Wilcock, A. C., Swedlow, J. R. and Storey, K. G.** (2007). Mitotic spindle orientation distinguishes stem cell and terminal modes of neuron production in the early spinal cord. *Development* **134**, 1943-1954.
**Wilsch-Bräuninger, M., Florio, M. and Huttner, W. B.** (2016). Neocortex expansion in development and evolution - from cell biology to single genes. *Curr. Opin. Neurobiol.* **39**, 122-132.
**Xie, Z., Moy, L. Y., Sanada, K., Zhou, Y., Buchman, J. J. and Tsai, L.-H.** (2007). Cep120 and TACCs control interkinetic nuclear migration and the neural progenitor pool. *Neuron* **56**, 79-93.
**Yamashita, Y. M., Mahowald, A. P., Perlin, J. R. and Fuller, M. T.** (2007). Asymmetric inheritance of mother versus daughter centrosome in stem cell division. *Science* **315**, 518-521.
**Zhang, X., Lei, K., Yuan, X., Wu, X., Zhuang, Y., Xu, T., Xu, R. and Han, M.** (2009). SUN1/2 and Syne/Nesprin-1/2 complexes connect centrosome to the nucleus during neurogenesis and neuronal migration in mice. *Neuron* **64**, 173-187.

# Appendix 2

Cell Stem Cell

Article

# Multimerization of Zika Virus-NS5 Causes Ciliopathy and Forces Premature Neurogenesis

## Graphical Abstract

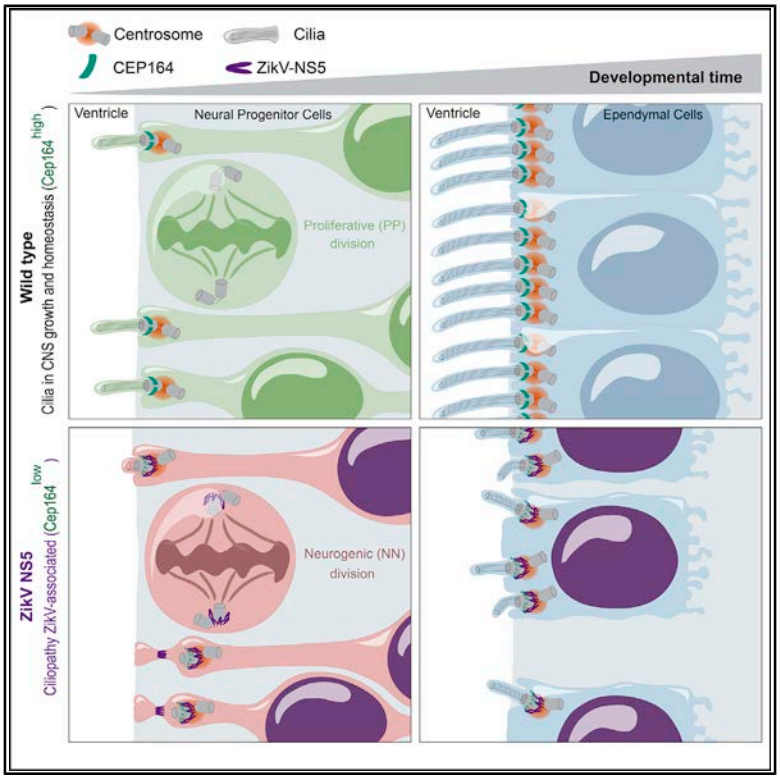


## Highlights

- ZikV-NS5 interacts with and depletes centrosome proteins at the primary cilia in NPCs
- ZikV-NS5 at the centrosome causes ciliopathy and promotes neuron delamination
- Multimeric arrangement of ZikV-NS5 is required for nuclear exit and for ciliopathy
- In human fetal brain, ZikV affects motile cilia integrity in ependymal cells

## Authors

Murielle Saade, Diego S. Ferrero, José Blanco-Ameijeiras, ..., Naiara Akizu, Nuria Verdaguer, Elisa Martí

## Correspondence

msabmc@ibmb.csic.es (M.S.), emgbmc@ibmb.csic.es (E.M.)

## In Brief

Monociliated NPC proliferation ensures normal brain growth. The NS5 protein encoded by Zika virus interacts with host proteins at the cilia base, such as CEP164; induces ciliopathy; and promotes neurogenesis. Following primary neurogenesis, NPCs differentiate into multiciliated ependymal cells in which ZikV-NS5 depletes CEP164, provoking ciliopathy and ependymal layer disorganization.

Saade et al., 2020, Cell Stem Cell *28*, 920–936
December 3, 2020 
https://doi.org/10.1016/j.stem.2020.10.002

CellPress

CellPress

Cell Stem Cell

Article

# Multimerization of Zika Virus-NS5 Causes Ciliopathy and Forces Premature Neurogenesis

Murielle Saade,[1,6,*] Diego S. Ferrero,[2,6] José Blanco-Ameijeiras,[1] Elena Gonzalez-Gobartt,[1] Marco Flores-Mendez,[3,4] Victor M. Ruiz-Arroyo,[2] Elena Martínez-Sáez,[5] Santiago Ramón y Cajal,[5] Naiara Akizu,[3,4] Nuria Verdaguer,[2] and Elisa Martí[1,7,*]

[1]Developmental Biology Department, Instituto de Biología Molecular de Barcelona (IBMB-CSIC), Parc Científic de Barcelona, C/Baldiri i Reixac 20, Barcelona 08028, Spain

[2]Structural Biology Department, Instituto de Biología Molecular de Barcelona (IBMB-CSIC), Parc Científic de Barcelona, C/Baldiri i Reixac 20, Barcelona 08028, Spain

[3]Raymond G. Perelman Center for Cellular and Molecular Therapeutics, The Children's Hospital of Philadelphia, Philadelphia, PA 19104, USA

[4]Department of Pathology and Laboratory Medicine, University of Pennsylvania, Philadelphia, PA 19104, USA

[5]Department of Pathology, Vall d'Hebron University Hospital, Translational Molecular Pathology, Vall d'Hebron Institute of Research (VHIR), Universitat Autònoma de Barcelona and Spanish Biomedical Research Network Centre in Oncology (CIBERONC), Barcelona 08035, Spain

[6]These authors contributed equally

[7]Lead Contact

*Correspondence: msabmc@ibmb.csic.es (M.S.), emgbmc@ibmb.csic.es (E.M.)

https://doi.org/10.1016/j.stem.2020.10.002

## SUMMARY

Zika virus (ZikV) is a flavivirus that infects neural tissues, causing congenital microcephaly. ZikV has evolved multiple mechanisms to restrict proliferation and enhance cell death, although the underlying cellular events involved remain unclear. Here we show that the ZikV-NS5 protein interacts with host proteins at the base of the primary cilia in neural progenitor cells, causing an atypical non-genetic ciliopathy and premature neuron delamination. Furthermore, in human microcephalic fetal brain tissue, ZikV-NS5 persists at the base of the motile cilia in ependymal cells, which also exhibit a severe ciliopathy. Although the enzymatic activity of ZikV-NS5 appears to be dispensable, the amino acids Y25, K28, and K29 that are involved in NS5 oligomerization are essential for localization and interaction with components of the cilium base, promoting ciliopathy and premature neurogenesis. These findings lay the foundation for therapies that target ZikV-NS5 multimerization and prevent the developmental malformations associated with congenital Zika syndrome.

## INTRODUCTION

Zika virus (ZikV) is a flavivirus transmitted by the bite of the *Aedes* mosquito (Pierson and Kielian, 2013). The 11 kb positive-sense, single-stranded RNA genome of ZikV encodes ten mature viral proteins: three structural (S) proteins (C, prM, and E) and seven non-structural (NS) proteins (NS1, NS2A, NS2B, NS3, NS4A, NS4B, and NS5) (Pierson and Kielian, 2013). A single amino acid substitution (S139N) in prM seems to be responsible for the change in virus tropism that provokes a dramatic increase in neonatal microcephaly (Yuan et al., 2017) and has led to this virus being declared a global threat to public health. ZikV can directly infect human neural progenitor cells (hNPCs) in both 2D and 3D *in vitro* models of the developing cerebral cortex, resulting in defects resembling congenital microcephaly (Dang et al., 2016; Gabriel et al., 2017; Garcez et al., 2016; Li et al., 2016; Nowakowski et al., 2016; Qian et al., 2016; Retallack et al., 2016; Tang et al., 2016). However, the mechanisms by which ZikV disrupts neurogenesis have not yet been fully elucidated. Macaque monkey infection provokes regional disturbances in the brain that impair postnatal neurogenesis, provoking cognitive deficits and epilepsy (Adams Waldorf et al., 2018). This vulnerability of late neurogenic regions to ZikV also persists in adult mice (Li et al., 2016). Because it is well known that human brain development extends for many years beyond birth and that adult neurogenesis influences cognitive functions, it is no longer safe to consider ZikV a transient infection in adult humans without marked long-term effects.

The limited availability of human tissue to perform histological analyses at different developmental stages (Abbott, 2011) emphasizes the need to use *in vivo* animal models to understand congenital Zika syndrome. Here we used the chick embryo neural tube (NT) to screen ZikV protein components and assess their impact on neurogenesis, particularly given that this *in vivo* model has identified fundamental processes in mammalian neural development and human disease. Through this approach, ZikV-NS5 was seen to disturb the growth of the nervous system. ZikV-NS5 is the largest NS protein (~100 kDa), and it is essential to the viral life cycle. It contains two functional domains: a N-terminal methyltransferase (MTase) domain responsible for the catalysis of 5′ mRNA capping and methylation and a RNA-dependent RNA polymerase (RdRP) domain at the C terminus

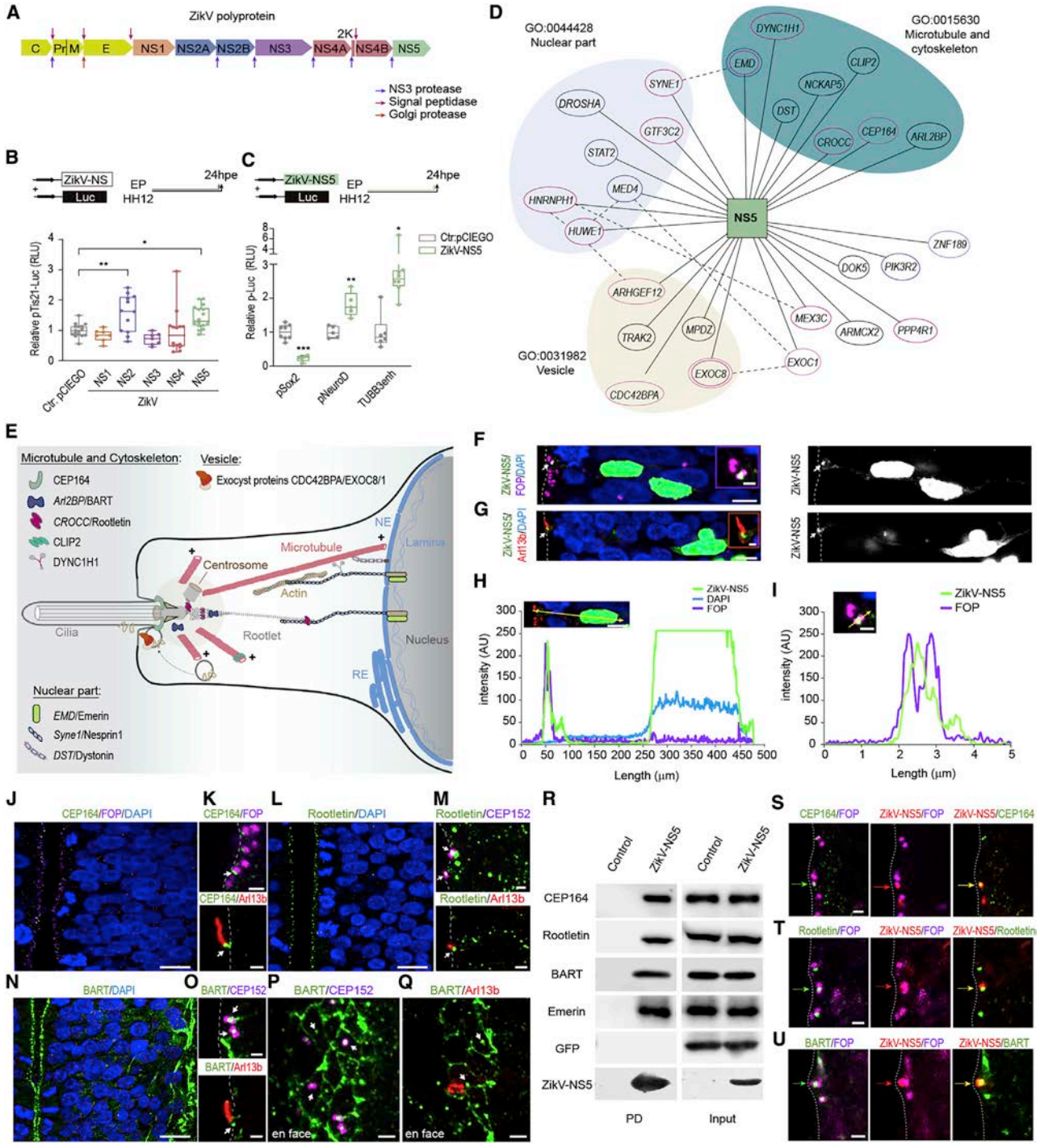


**Figure 1. ZikV-NS5 Interacts with Proteins at the Cilia Base**

(A) Scheme depicts the structural and non-structural proteins of the ZikV polyprotein. Arrows indicate proteolytic cleavage sites.

(B) Luc/Renilla activity of the pTis21-Luc reporter after electroporation (elect.) of the empty vector pCIEGO or the ZikV-NS DNAs indicated (mean ± SD, n = 6–8 embryos/condition).

(C) Luc/Renilla activity of the pSox2-Luc, pNeuroD-Luc, and Tubb3enh-Luc reporters after elect. of the empty vector pCIEGO or ZikV-NS5 (mean ± SD, n = 6–8 embryos/condition).

(D) Network representation of the ZikV-NS5-host interactome in hNPCs. NS5 is represented as a square, and the 27 interacting host proteins are represented as ellipses. The subcellular localization of the host proteins are taken from Gene Ontology. Proteins previously reported to interact with ZikV-NS5 in neural cells are in pink, and those that interact in HEK291 cells are in blue. Published physical interactions of the host proteins are indicated by dotted lines.

*(legend continued on next page)*

that drives genome replication (Duan et al., 2017; Ferrero et al., 2019; Wang et al., 2017; Zhou et al., 2007). ZikV-NS5 can form dimers and higher-order oligomers that regulate its enzymatic functions, as well as its association with other viral or host factors during infection, making it an extremely attractive anti-viral target.

To understand how ZikV-NS5 affects neurogenesis, we searched for the host ZikV-NS5 interactome in hNPCs in a yeast two-hybrid (Y2H) assay. This unbiased approach detected previously identified ZikV-NS host interactors (Coyaud et al., 2018; Scaturro et al., 2018), and it revealed that the ZikV-NS5 protein interacts with cellular components known to localize at the base of the cilium. We showed that primary cilia elongation is impaired in neural progenitor cells (NPCs) expressing ZikV-NS5 and that neural delamination is accelerated, two key events that promote premature neurogenesis and impair CNS growth. However, these effects were hindered when ZikV-NS5 multimerization was prevented by point mutations. In addition, we observed a severe ciliopathy in the ependymal cells (ECs) that line the ventricular cavities of a ZikV-infected human fetal microcephalic brain, a phenomenon that might impair the cerebrospinal fluid (CSF) flow necessary to maintain brain homeostasis and for toxin washout. Altogether, our data indicate that ZikV-NS5 causes ciliopathies—both a motile ciliopathy and a primary ciliopathy—which contribute to the collection of developmental malformations provoked in congenital Zika syndrome, such as microcephaly and ventriculomegaly.

## RESULTS

### ZikV-NS5 Interacts with Basal Ciliary Proteins in NPCs

To investigate whether individual proteins encoded by the Suriname strain (human isolate Z1106033 sequence) ZikV can directly regulate neurogenesis (Figure 1A), we monitored the expression of the anti-proliferative gene Tis21 (PC3 and BTG2) (Iacopetti et al., 1999) 24 h post-electroporation (hpe) of constructs encoding each of the ZikV structural (ZikV-S) and ZikV non-structural (ZikV-NS) proteins into Hamburger and Hamilton (HH) stage 12 chick embryo NTs (Hamburger and Hamilton, 1951) (Figure 1B; Figures S1I and S1J). The subcellular distribution of each ZikV protein was also studied in early NPCs (Figures S1A–S1H). ZikV-NS2 and ZikV-NS5 provoked an increase in luciferase activity (Figure 1B), and ZikV-NS2 has been reported to dampen NPC proliferation by directly interacting with components of the adherens junction (AJ) complex (Yoon et al., 2017). The expression of ZikV-NS5 also reduced the expression of the progenitor marker pSox2, enhancing the expression of additional pan-neural markers like pNeuroD and pTubb3 (Figure 1C; Figures S1K and S1L), without disrupting NT tissue integrity or affecting cell viability (Figures S1M–S1P). We confirm the conserved capability of ZikV-NS5 to regulate neurogenesis from several strains, such as the African strain MR766 (ZikV-NS5-AF) and the Asian strain H/PF/2013 (ZikV-NS5-AS) (Figures S2A–S2C).

We searched for the cellular proteins that might interact with ZikV-NS5 and influence neurogenesis. As such, the ZikV-NS5 (1-904)-LexA fusion protein was used as bait in a Y2H screen of a human fetal brain library (HFBR_RP1_hgx4776v1_pB29). After analyzing 99.6 million interactions and processing more than 141 colonies, 27 ZikV-NS5-host interactors were defined (Table S1), ~70% of which were common to those interactors identified previously (Coyaud et al., 2018; Scaturro et al., 2018) (Table S2). Among the host proteins detected, enrichment of the microtubule/cytoskeleton, vesicle, and nuclear compartments was revealed by Gene Ontology (GO) analysis (Figure 1D). Several of these proteins are known to localize to the base of the cilium and/or to link the nuclear envelope to the cytoskeleton (Figure 1E; Table S1).

A hallmark of NPCs is the single primary cilium at their apical surface, which is nucleated by the basal body, where the mother centriole is docked to the plasma membrane through its appendage proteins (Kim and Dynlacht, 2013) (Figure 1E). This cilium extends into the NT lumen, where it is able to detect the growth factors in the CSF that control CNS growth (Lehtinen et al., 2011). Findings from the interactome prompted us to study the subcellular distribution of ZikV-NS5 in NPCs by introducing a plasmid encoding ZikV-NS5-FLAG into the chick embryo NT. As expected given the nuclear localization signals encoded in this protein, the ZikV-NS5-FLAG protein accumulated in the nucleus

(E) Scheme depicts the apical pole of a NPC, where the primary cilium extends into the NT lumen. The centrosome at the cilium base organizes microtubules that link the nuclear envelope (NE) to the cilium base through the Rootlet. Key to proteins that interact with ZikV-NS5.
(F and G) Images show the subcellular distribution of ZikV-NS5 in elect. NPCs. (F) ZikV-NS5-FLAG visualized by anti-FLAG staining in the nucleus (DAPI) and in the centrosomes (arrow) lining the NT lumen labeled with anti-FOP. (G) ZikV-NS5-FLAG located at the base of the cilium (arrow) labeled with Arl13b-RFP.
(H and I) Plots of the fluorescence intensity (FI, in a.u.) at distances from the NT lumen (zero): purple labels centrosomes, blue labels nuclei, and green labels ZikV-NS.
(J and K) Sections showing endogenous CEP164 lining the NT lumen and arrows pointing to the distal co-localization in the mother centriole with FOP at the base of the Arl13b-RFP-labeled cilia.
(L and M) Sections showing endogenous Rootletin, in which the arrows indicate its co-localization with the centrosome marker CEP152-GFP at the base of the Arl13b-RFP-labeled cilia.
(N and O) Arrows point to endogenous BART co-localizing with CEP152-GFP at the base of the Arl13b-RFP-labeled cilia.
(P and Q) *En face* imaging of the BART-labeled apical belt of NPC endfeet, with arrows pointing to the co-localization with CEP152-labeled centrosome and at the base of Arl13b-RFP-labeled cilia.
(R) Pull-down (PD) assays show ZikV-NS5 binding to Cep164, Rootletin, BART, and Emerin in transfected HEK293 cells. Control is referred to a PD with resin in the absence of ZikV-NS5 recombinant protein, and the empty vector pCIEGO-GFP was a negative control.
(S–U) Images of ZikV-NS5-FLAG co-localization with the $FOP^{+}$ centrosome and with endogenous CEP164 (S), endogenous Rootletin (T), and endogenous BART (U) lining the NT lumen (dotted line). The proteins are indicated with colored arrows according to their fluorescence labeling.
***$p < 0.001$; **$p < 0.01$, with exact p values 0.0091 (B) and 0.0079 (C); *$p < 0.05$, with exact p values 0.0416 (B) and 0.0101 (C); ns, not significant. (B) One-way ANOVA; (c) two-sided unpaired t test. Scale bars, 5 μm (F and G), 9 μm (J, L, and N), 1 μm (F, inset; G, inset; and K, M, O, and S–U), and 2 μm (P and Q). See also Figures S1 and S2 and Tables S1 and S2.

(Ferrero et al., 2019) (Figures 1F–1H), a subcellular distribution unique among the ZikV proteins (Figures S1A–S1H). However, some ZikV-NS5 also accumulated at the base of the cilia, which was identified through the pan-cilia marker, the small guanosine triphosphatase (GTPase) ADP ribosylation factor-like 13b fused to the red fluorescent protein (Arl13b-RFP) that specifically associates with the ciliary membrane (Paridaen et al., 2013; Saade et al., 2017). ZikV-NS5 localizes to the centrosome, identified as a pair of dots at the surface of the ventricular zone (VZ), where the centrosome proteins 152K (CEP152) (Dzhindzhev et al., 2010) and FGFR1 oncogene partner (FOP) (Yan et al., 2006) were detected as pan-centrosome markers (Figures 1F–1I). As expected, ZikV-NS5-FLAG from the African and Asian strains showed conserved subcellular localization associated with the nucleus and the primary cilia base (Figures S2F–S2J). Moreover, the docking of ZikV-NS5 to the centrosomes persisted throughout mitosis in these NPCs (Figures S1Q–S1U).

To confirm that ZikV-NS5 interacts directly with components of the cilium base in a cell context, endogenous centrosome protein 164K (CEP164) was detected in NPCs by immunofluorescence, lining the NT lumen, where it co-localizes with the FOP-labeled mother centriole at the cilium base (Figures 1J and 1K). CEP164 is a mature, centriole-specific protein that localizes to the basal body distal appendages, and it is required for assembly of the primary cilium (Graser et al., 2007). ZikV-NS5 pulled down CEP164 in HEK293 cell extracts (Figure 1R; Figure S1Y), and in NPCs, ZikV-NS5 co-localized with CEP164 and with centriole markers (Figure 1S; Figure S3D). In NPCs, the endogenous rootlet coiled-coil protein (*CROCC*/Rootletin) was detected by immunofluorescence in the rootlet fibers, as well as the lining of the NT lumen, where it co-localized with centrosomal markers at the cilium base (Figures 1L and 1M). Rootletin localizes to the intercentriolar linker, and it is required for the correct positioning of the cilium basal body relative to the cell nucleus (Yang et al., 2002, 2006). ZikV-NS5 also pulled down Rootletin in HEK293 cell extracts (Figure 1R; Figure S1Y), and ZikV-NS5 co-localized with Rootletin and with centrosomal markers in NPCs (Figure 1T; Figure S3E). Moreover, immunofluorescence demonstrated the presence of the endogenous ADP ribosylation factor-like 2-binding protein (*ARL2BP*/BART) in NPCs that line the NT lumen, where it co-localized with the centrosomal marker CEP152 at the cilium base (Figures 1N–1Q). BART localizes to the basal body, and it is required for cilia elongation (Davidson et al., 2013). *En face* NT imaging revealed BART also localized to the apical belt (Figures 1P and 1Q) and the base of the primary cilium identified by Arl13b (Figure 1Q). ZikV-NS5 pulled down BART in transfected HEK293 cells (Figure 1R; Figure S1Y), and in NPCs, ZikV-NS5 co-localized with BART and with centrosomal markers (Figure 1U; Figure S4H). In addition, the Y2H screen retrieved three ZikV-NS5 protein interactors that localize to the nuclear envelope (Emerin, Nesprin, and Dystonin) (Figure 1E). ZikV-NS5 pulled down Emerin from HEK293 cells (Figure 1R), a member of the nuclear lamina-associated protein family that controls anchorage to the cytoskeleton and that links centrosomes to the nuclear envelope through an association with microtubules (Virtanen and Vartiainen, 2017; Wilson, 2000). Altogether, these data indicate the ZikV-NS5 interacts with protein components of the base of the primary cilium in NPCs.

### ZikV-NS5 Causes Ciliopathy and Premature Neuron Delamination

In dividing NPCs, cilia length shortens before entry into mitosis, and the ciliary membrane remnant is internalized along with the mother centrosome. The daughter cells that inherit the mother centrosome can reform long cilia faster and remain NPCs, whereas the differentiating daughter cells delaminate from the ventricular surface and migrate to the lateral NT (Figure 2A) (Paridaen et al., 2013; Saade et al., 2018). We assessed whether ZikV-NS5 affects cilia length, measuring the length of Arl13b-RFP-labeled cilia protruding from the two FOP-labeled centrioles at the VZ surface in NPCs. In control cells, the cilia length varied as a function of the cell-cycle phase and nuclear position (median = 2.08 ± 1.3 μm, n = 100), as in electroporated NPCs, where ZikV-NS5 is exclusively localized in the nucleus (Nu-ZikV-NS5: median = 2 ± 1.1 μm, n = 100) (Figure 2D). However, the cilia were significantly shorter in electroporated NPCs showing ZikV-NS5 localization to the centrosome at the cilia base (Cs-ZikV-NS5: median = 0.68 ± 0.3 μm, n = 60) (Figures 2B–2D; Figures S3A–S3C). Co-expressing all ZikV-associated NS proteins in NPCs did not affect the localization of NS5 to the cilia base or revert the ciliopathy (Figures S1V–S1X).

We assessed whether ZikV-NS5 from the African and the Asian strains also affects cilia length according to the subcellular localization in electroporated NPCs. In electroporated NPCs, where ZikV-NS5-AF and ZikV-NS5-AS are exclusively localized in the nucleus (Nu-ZikV-NS5-AF: median = 2.2 ± 1.3 μm, n = 65; Nu-ZikV-NS5-AS: median = 2.1 ± 1 μm, n = 45) (Figures S2D–S2F and S2I), cilia length varied as in controls cells (Figures S2D and S2E). However, the cilia were significantly shorter in electroporated NPCs showing ZikV-NS5-AF and ZikV-NS5-AS localization to the centrosome at the cilia base (Cs-ZikV-NS5-AF: median = 0.7 ± 0.74 μm, n = 36; Cs-ZikV-NS5-AS: median = 0.7 ± 0.36 μm, n = 32) (Figures S2D, S2E, and S2G–S2J).

To show the conservation of defects caused by ZikV-NS5 protein, we cultured human induced pluripotent stem cells (iPSCs) following a standard neural induction protocol (Akizu et al., 2013). Like the phenotype that we described in the chick embryo NT, hNPCs after transfection with ZikV-NS5 increased the expression of the anti-proliferative gene Tis21 (Figures 3A–3D). Moreover, ZikV-NS5 pulled down endogenous CEP164, Rootletin, and BART in hNPCs (Figure 3E) and localized at the base of Arl13b-labeled primary cilia in Nestin-positive hNPCs, and this subcellular localization caused cilia shortening (Figures 3F–3L).

To search for the mechanism by which ZikV-NS5 mediates cilia shortening, we quantified the endogenous target proteins in NPCs relative to the subcellular localization of ZikV-NS5. Compared with electroporated NPCs with ZikV-NS5-exclusive localization in the nucleus, there was a significant reduction in CEP164 protein when ZikV-NS5 localized to the centrosome at the cilia base (Nu-ZikV-NS5: median = 0.85 ± 0.05 a.u., n = 54; Cs-ZikV-NS5: median = 0.32 ± 0.05 a.u., n = 43) (Figures 2E and 2H; Figures S3D and S3F). Interestingly, less CEP164 was reported previously in ZikV-infected NPCs forming brain organoids (Gabriel et al., 2017). In addition, there was less endogenous centrosomal Rootletin and BART in NPCs upon ZikV-NS5 localization to the centrosome at the cilia base (Rootletin: Nu-ZikV-NS5 median = 0.9 ± 0.05 a.u., n = 80; Cs-ZikV-NS5 median = 0.3 ± 0.04 a.u., n = 52; BART: Nu-ZikV-NS5

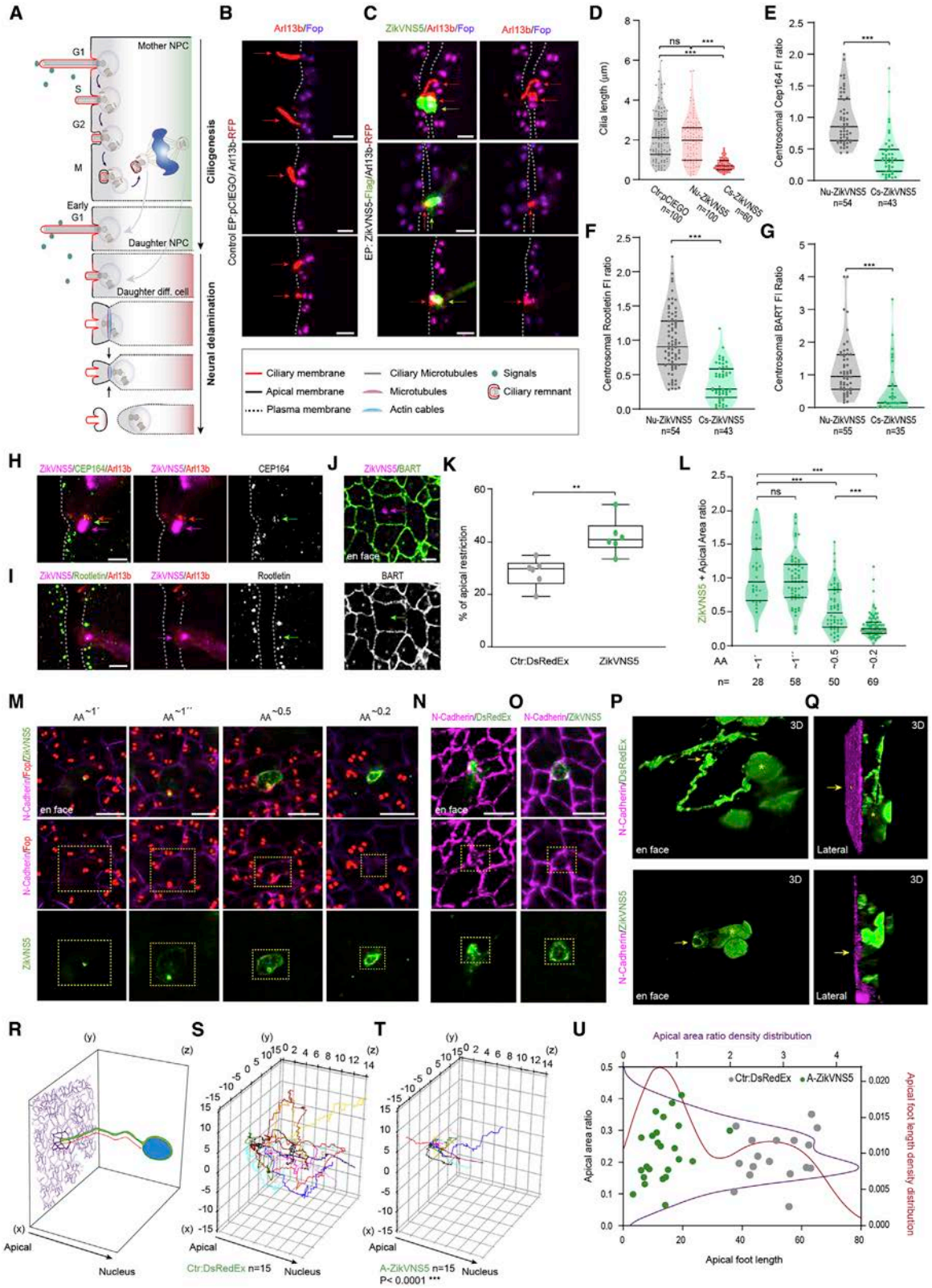


**Figure 2. ZikV-NS5 Localization to the Cilium Base Impairs Cilia Elongation and Promotes Neural Delamination**

(A) Scheme depicts the variation in cilia length during the cell cycle in a dividing NPC. The daughter cell remaining as a NPC regrows a primary cilium, whereas the daughter cell entering differentiation delaminates from the epithelium.

*(legend continued on next page)*

median = 0.95 ± 0.1 a.u., n = 55; Cs-ZikV-NS5 median = 0.15 ± 0.1 a.u., n = 35) (Figures 2F, 2G, 2I, and 2J; Figures S3E and S3G). Hence, the reduction in the endogenous CEP164, Rootletin, and BART protein at the centrosome of cells expressing ZikV-NS5 correlated with the impaired cilia elongation in NPCs. In turn, cilia shortening might impair the reception of extracellular growth signals, such as those provided by Sonic Hedgehog (Shh), an important regulator of proliferation (Goetz and Anderson, 2010; Saade et al., 2018).

In NPCs, apical centrosomes organize a microtubule ring that, when aligned with the actin cables, plays an active role in reducing their apical surface and withdrawing their apical endfoot from the ventricular surface (Figure 2A) (Baek et al., 2018; Kasioulis et al., 2017). We evaluated whether ZikV-NS5 might influence neural delamination, because BART localizes to this apical belt (Figures 1P, 1Q, and 2J; Figures S3H, S3J, and S3K). We measured the apical area (AA) of electroporated cells surrounded by non-electroporated neighbors in *en face* images of the NT, with the latter used as a reference for AA restriction. The proportion of NPCs with a smaller AA is higher following ZikV-NS5 electroporation (control ratio = 28.32 ± 5.13; ZikV-NS5 ratio = 41.90 ± 6.7; control median = 0.7 ± 0.53 a.u., n = 163; ZikV-NS5 median = 0.51 ± 0.46 a.u., n = 213) (Figure 2K; Figure S3L). The AA was delimitated by the AJ-associated protein N-cadherin, and the centrosome was defined by FOP (Figure 2M). In the non-restricted AA, ZikV-NS5 localizes to either the central or the lateral centrosome, a feature that precedes neural delamination (AA∼1′ ratio = 0.92 ± 0.46; AA∼1″ ratio = 0.92 ± 0.39) (Figures 2L and 2M; Figure S3I) (Wilsch-Bräuninger et al., 2012). However, the localization of ZikV-NS5 to the apical belt was correlated with a reduction in the AA (AA∼0.5 ratio = 0.46 ± 0.35; AA∼0.2 ratio = 0.23 ± 0.19) (Figures 2L and 2M; Figure S3L), coinciding with early apical-to-basal migration of the centrosome (Figure 2M; Figures S3I, S3M, and S3N; Video S1). Moreover, a reduction in the AA at the ventricular surface is preceded by the basal migration of the newborn delaminating neuronal cell body (Kasioulis et al., 2017). Confocal images of DsRedEx or ZikV-NS5 electroporated cells were used to generate 3D reconstructions and to track the cell processes that extend from the restricted apical endfoot surface to the nucleus (Figures 2N–2R). ZikV-NS5 electroporated cells have a short apical foot length (control length = 51.5 ± 9.85 μm, n = 17; ZikV-NS5 length = 13 ± 7 μm, n = 25) (Figures 2O–2Q, 2T, and 2U; Videos S2 and S3) compared with control (Figures 2N, 2P, 2Q, 2S, and 2U; Video S4), indicating that ZikV-NS5 promotes apical endfoot restriction at the ventricular surface before the basal migration of the newborn delaminating neuronal cell body is completed.

Finally, when we assessed the expression of Tis21 to determine whether these cellular events promote terminal neurogenesis, reporter activation was associated with the localization of ZikV-NS5 to the cilium base (Figure S3O). Quantification of pTis21-RFP$^+$ NPCs at 16 hpe (n = 5 embryos) showed that 93% ± 7% of the NPCs expressed pTis21-RFP when ZikV-NS5 was localized to the cilium base, as opposed to 25% ± 10% of NPCs in which ZikV-NS5 localized to the nucleus (n = 5 embryos) or 25% ± 3% of the control NPCs (n = 6 embryos) (Figure S3P). Altogether, these data indicate that primary cilia elongation is impaired and apical endfoot restriction is accelerated in NPCs exposed to ZikV-NS5 protein, two key events that promote neural delamination. These results prompted us to study how the ZikV-NS5 protein affects primary neurogenesis and embryonic CNS growth.

## The Multimeric Arrangement of ZikV-NS5 Is Required to Promote Terminal Neurogenic Divisions

Normal growth of the CNS requires a fine balance of the different modes of NPC division, and a premature switch to

(B and C) Images show the Arl13b-RFP-labeled cilia (arrows) and FOP-stained centrosomes lining the NT lumen (dotted line) in (B) control and (C) ZikV-NS5 elect. (green arrows) NPCs.
(D) Cilia length in elect. NPCs with empty vector (control); in elect. NPCs with ZikV-NS5, in which the protein remains localized within the nucleus (Nu-ZikV-NS5); and in elect. NPCs with ZikV-NS5, in which the protein is localized to the centrosome at the cilia base (Cs-ZikV-NS5).
(E–G) Average pixel FI of the indicated endogenous proteins at the centrosome of NPCs in which ZikV-NS5 remains localized within the nucleus (Nu-ZikV-NS5) compared with NPCs in which the ZikV-NS5 localized to the centrosome at the cilia base (Cs-ZikV-NS5). The ratio of FI was obtained dividing by the mean of FI of the indicated endogenous in four of the non-elect. neighbor NPCs (spaced by one cell distance from the ZikV-NS5 elect. NPCs).
(H and I) Images of ZikV-NS5-FLAG (purple arrow) co-localization with Arl13b (red arrows) and endogenous CEP164 (H) or endogenous Rootletin (I) (green arrows).
(J) *En face* images of the endogenous BART-labeled apical ring and its absence from the centrosome, where ZikV-NS5-FLAG is located (purple arrow).
(K) Plots of the proportion of cells with apically restricted areas in DsRedEx-control and ZikV-NS5 elect. NTs (n = 6 embryos; median ± SD).
(L) Plots of apical areas (AAs) in relation to ZikV-NS5 positioning. The non-restricted areas (~1) correspond to ZikV-NS5 co-localization at the centrosome, and the restricted areas ($\leq$0.5) correspond to ZikV-NS5 localization at the apical belt.
(M) *En face* images of N-cadherin-labeled AJs, FOP-labeled centrosomes, and ZikV-NS5-FLAG subcellular localization according to the AA.
(N and O) *En face* images of N-cadherin showing restricted AAs in DsRedEx-control (N) and ZikV-NS5-FLAG elect. NPCs (O).
(P and Q) 3D reconstructions of the apical foot in DsRedEx-control or ZikV-NS5-FLAG transfected NPCs. Arrows point to the apical endfoot area facing the NT lumen (N-cadherin, purple; asterisks correspond to nuclei).
(R) Scheme depicts the apical foot length (red line) as the distance between the restricted apical endfoot area facing the NT lumen (purple) and the basal nucleus (blue) in NPCs.
(S and T) 3D Python plots of apical foot length in NPCs expressing DsRedEx (S) (control) in comparison to NPCs presenting an apical belt distribution of ZikV-NS5 (T) (A-ZikV-NS5). Both conditions show similar apical endfoot area restriction ($0 < AA \geq 0.5$), as shown in (U).
(U) Plots of the apical foot length relative to the apical endfoot area restriction in DsRedEx-control (gray dots) and apical belt ZikV-NS5-expressing NPCs (green dots). The density distribution of the apical endfoot area restriction presents a Gaussian distribution (purple), whereas the density distribution of the apical foot length presents a bimodal distribution (red).
In violin plots, the upper and lower lines indicate the interquartile range and the middle line indicates the median. ***$p < 0.001$; **$p < 0.01$, with exact p value 0.0043 (K); *$p < 0.05$; ns, not significant. (D–K) Mann-Whitney U test; (L) Kruskal-Wallis test. Scale bars, 2 μm (B, C, and H–J) and 4 μm (M–O). See also Figures S1–S3 and Videos S1, S2, S3, and S4.

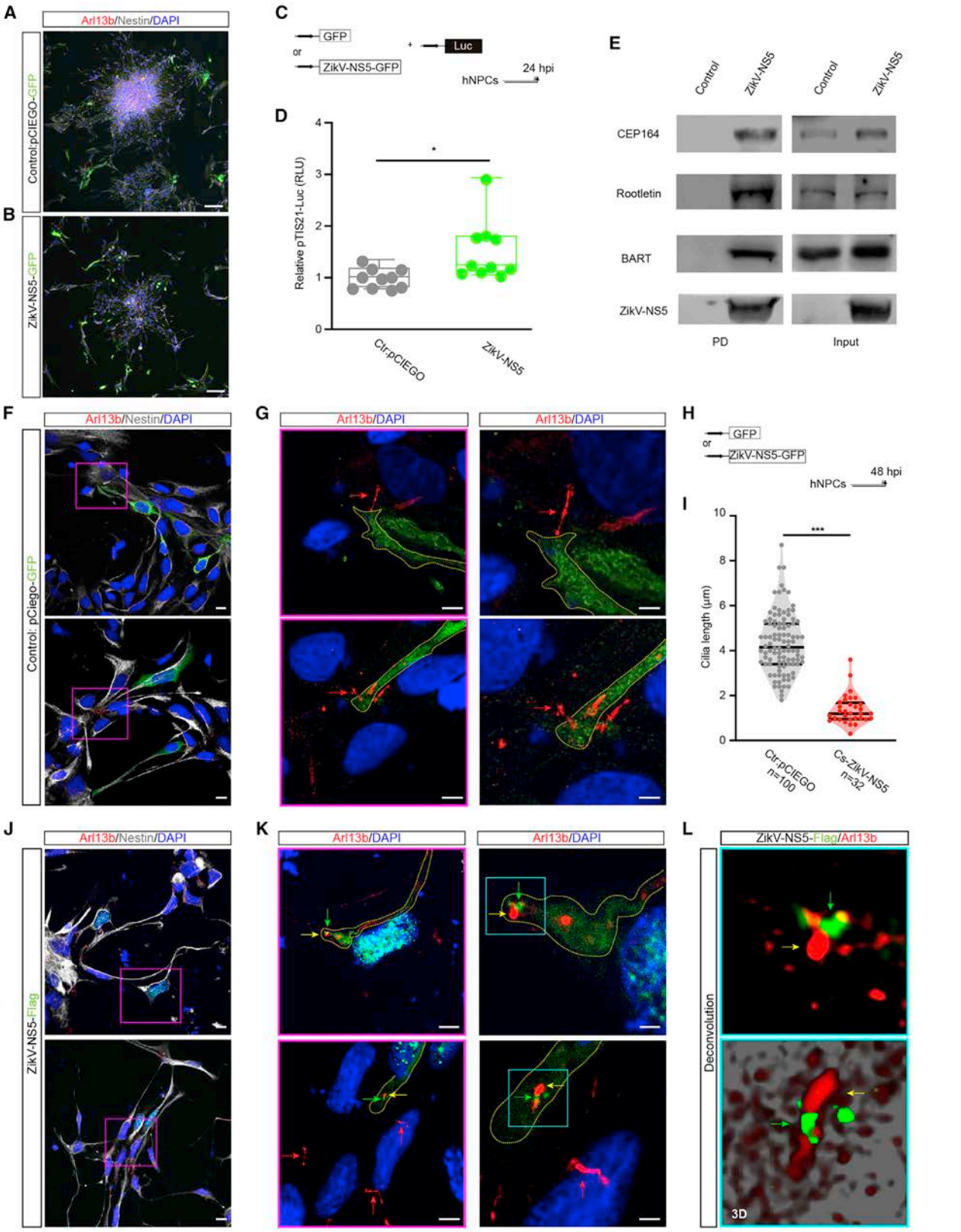


*(legend on next page)*

neuron-generating divisions may cause microcephaly (Saade et al., 2018). Symmetric proliferative divisions that leave two NPC daughter cells (PP) can be monitored *in vivo* with the pSox2-EGFP construct, whereas pSox2-EGFP and the neurogenic pTis21-RFP reporter are co-expressed in asymmetric divisions that produce one NPC and one differentiating neuron (PN). By contrast, symmetric neurogenic divisions generating two neurons (NN) that detach from the VZ can be monitored by the expression of the pTis21-RFP reporter (Figure 4A) (Le Dréau et al., 2014; Saade et al., 2013, 2017). To determine whether ZikV-NS5 affects the mode of NPC division, stage HH10/12 embryos were co-electroporated with ZikV-NS5, together with the pSox2-EGFP/pTis21-RFP reporters (Figure 4B). When the embryos were analyzed at 24 hpe through fluorescent-activated cell sorting (FACS), the rate of PP divisions (pSox2-EGFP$^+$ cells) was seen to decrease significantly in ZikV-NS5 embryos (from 51% ± 2% in controls to 30% ± 2.8% in ZikV-NS5 embryos). This reduction in PP divisions took place at the expense of an increase in neurogenic divisions (from 18% ± 1.6% in controls to 46.4% ± 5.6% in ZikV-NS5 embryos) (Figure 4C). Similarly, when electroporated embryos were immunostained at 24 hpe, there was again a clear decrease in the rate of PP divisions (in pH3$^+$ cells) in ZikV-NS5 embryos (from 32% ± 3.4% in controls to 16% ± 6.5% in ZikV-NS5-EP embryos), which was compensated by an increase in NN divisions (from 13% ± 3.4% in controls to 33% ± 6.4% in ZikV-NS5-EP embryos) (Figures 4D–4F). Altogether, these data suggest that by preventing cilia elongation, the ZikV-encoded NS5 protein alone is sufficient to switch the mode of NPC division and to promote neural delamination. Thus, ZikV-NS5 drives the exhaustion of the neural progenitor pool.

To better define the neurogenic effects of ZikV-NS5, we monitored the expression of Tis21 after co-electroporation of the reporter and the ZikV-NS5 N-terminal (NTerm) domain (residues 1–262; MTase) or ZikV-NS5 C-terminal (CTerm) domain (residues 267–903; RdRP) into the chick embryo NT (Figures S4A and S4B). In contrast to the ZikV-NS5-CTerm domain, the ZikV-NS5-NTerm domain alone was sufficient to enhance pTis21-Luciferase reporter activity (Figure S4B). Moreover, the ZikV-NS5-NTerm domain drove an increase in the rate of NN divisions in the embryos, as witnessed in immunostained embryos (pH3$^+$ cells; Figures S4C–S4E) and by -encoded analysis (Figures S4C and S4F). Altogether, these data suggest that the neurogenic capacity of the ZikV-NS5 protein resides in its N-terminal domain, which prompted us to assess whether enzymatic activity was required to promote neurogenesis.

The MTase domain of the NS5 flavivirus protein mediates the addition of a guanine cap to the 5′ end of the RNA genome, and the sequential methylation of guanine N-7 and ribose 2′-O to form a type 1 cap structure ($^{m7N}$GpppA$^{2'Om}$). This activity is essential to evade the host's immune response and for replication, increasing the viral polyprotein translation efficiency. The ZikV MTase active site contains residues K61, D146, K182, and E218, which are in close contact with the S-adenosylmethionine (SAM) co-factor, the methyl group donor for the reaction (Figure 4G). However, a single amino acid substitution (D146A) was sufficient to abolish MTase activity (Zhou et al., 2007) (MTDead). To assess whether this enzymatic activity is required for the neurogenic capacity of ZikV-NS5, we co-electroporated the pTis21-Luciferase reporter, together with the ZikV-NS5-MTDead construct. Consequently, the luciferase activity of the reporter increased in response to mutant ZikV-NS5 MTase in a similar manner to that produced by the ZikV-NS5 protein (Figure 4I). Indeed, the ZikV-NS5-MTDead construct also provoked an increase in the rate of NN divisions in embryos when analyzed by FACS (13% ± 3% in controls, 42.5% ± 4.5% in ZikV-NS5, and 40.5% ± 3% in ZikV-NS5-D146A embryos) (Figure 4J).

We recently characterized the supramolecular arrangement of the full-length ZikV-NS5, highlighting the assembly of NS5 monomers into dimeric structures, as well as the interactions of dimers to form higher-order fibrillar structures (Ferrero et al., 2019). The main interface for dimer formation involves MTase-MTase contacts, connecting amino acids Y25, K28, and K29 in one ZikV-NS5 molecule with residues K45 and D46 of the second ZikV-NS5 subunit (Ferrero et al., 2019) (Figure 4H). To test whether the multimeric arrangement of ZikV-NS5 is required to promote premature neurogenesis, we used the ZikV-NS5-Y25A/K28S/K29A mutant that fails to form dimers (MultimDead) (Ferrero et al., 2019). This MultimDead mutant protein did not induce premature differentiation of NPCs (Figure 4I), and in embryos analyzed by FACS at 24 hpe, dimerization was required for ZikV-NS5 to promote the neurogenic mode of NPC division (25% ± 2% NN divisions in ZikV-NS5-MultimDead embryos) (Figure 4J). These data indicate that although the enzymatic activity of NS5 is dispensable, ZIKV-NS5 oligomerization is required for this protein to promote neurogenesis.

To define the cellular mechanisms altered by the ZikV-NS5 protein variants, we followed their subcellular distribution in

**Figure 3. ZikV-NS5 Localization to the Cilium Base Impairs Cilia Elongation in hNPCs**

(A and B) Selected images show hNPCs positive for Nestin and transfected with the GFP control vector (A) or ZikV-NS5-GFP (B).

(C) DNA transfection for luciferase assay.

(D) Luc/Renilla activity of the pTis21-Luc reporter 24 h after transfection of the empty vector GFP or the ZikV-NS5 DNA (mean ± SD, n = 10).

(E) hNPC endogenous protein extracts were analyzed by western blot. PD assays show ZikV-NS5 binding to endogenous Cep164, Rootletin, and BART. Control is referred to a PD with resin in the absence of ZikV-NS5 recombinant protein.

(F and G) Images show Arl13b-labeled cilia in Nestin-positive hNPCs transfected with the control vector encoding for GFP. Different inset magnifications of (F) (purple squares) show selected GFP-positive hNPCs (dashed yellow line) with a normal Arl13b-labeled cilia (red arrow; G).

(H) DNA transfection for the cilia length measurement using Arl13b as a pan-cilia marker. (I) Cilia length in hNPCs transfected with the control vector encoding GFP and in hNPCs transfected with ZikV-NS5 in which the protein is localized to the centrosome at the cilia base (Cs-ZikV-NS5).

(J–L) Images show Arl13b-labeled cilia in Nestin-positive hNPCs transfected with ZikV-NS5 (J). Different inset magnifications of (J) (purple squares) show ZikV-NS5 localization close to the cilia (green arrow) and Arl13b-labeled defected cilia (yellow arrow; K). Normal cilia are shown with red arrows (K). Different inset magnifications of (K) (blue squares) show deconvolution images of ciliopathy (yellow arrow) associated with apical ZikV-NS5 (green arrow; L).

In violin plots, the upper and lower lines indicate the interquartile range and the middle line indicates the median. ***$p < 0.001$; **$p < 0.01$; *$p < 0.05$; ns, not significant. Mann-Whitney U test (D and G). Scale bars, 75 μm (A and B), 10 μm (F and J), 5 μm (G and K), and 2 μm (F, insets; J; and K, insets).

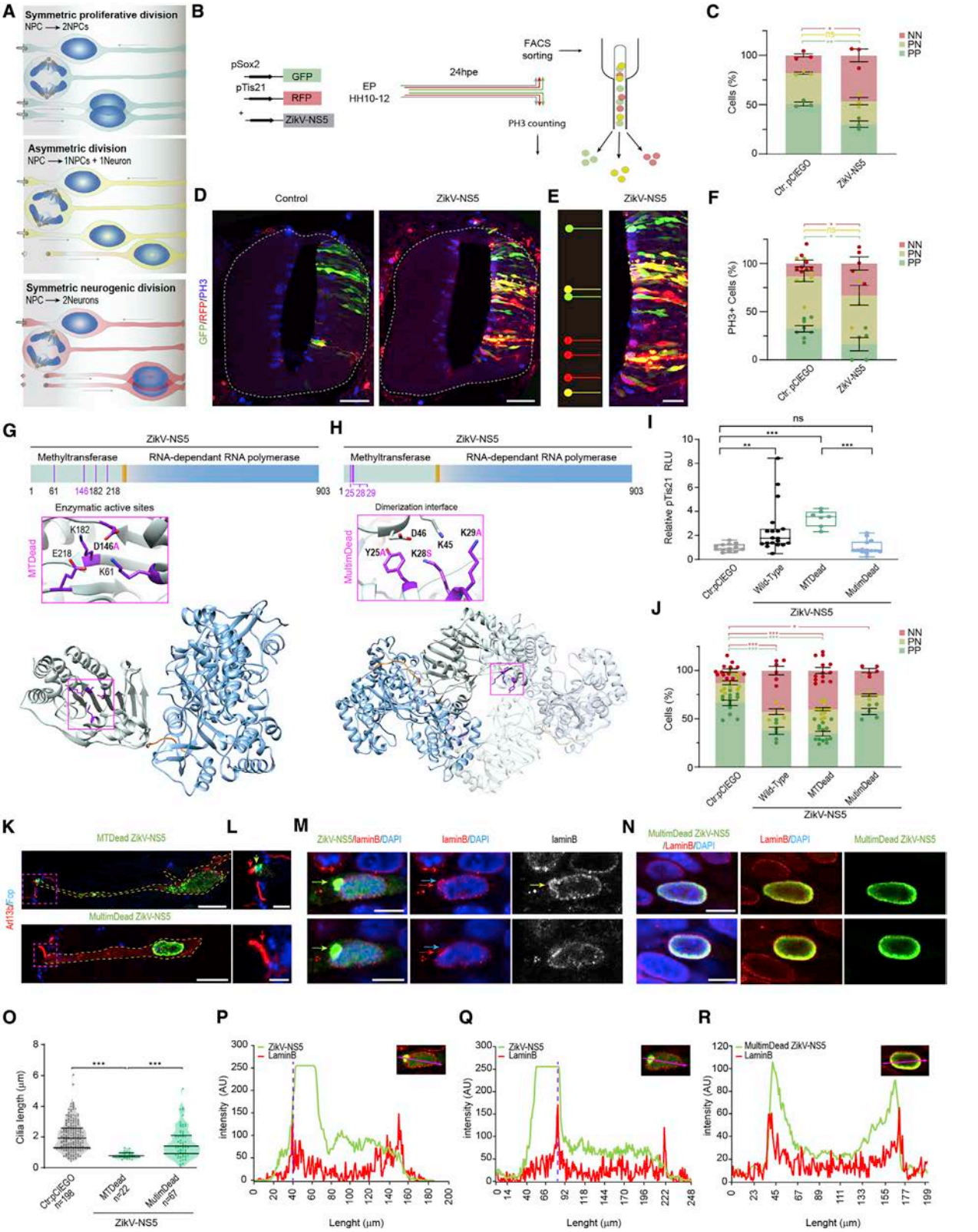


*(legend on next page)*

chick embryo NPCs. The ZikV-NS5-MTDead protein was detected in the nucleus and at the cilium base, like the wild-type protein, whereas the MultimDead protein variant was retained within the nucleus, concentrating near the nuclear envelope (Figures 4K–4N). Moreover, the multimerization of ZikV-NS5 contributes to the formation of ring-like nuclear aggregates that exit the nucleus toward the apical foot and localize at the centrosome forming the cilia base (Figure S4G). Furthermore, the nuclear exit of multimerized ZikV-NS5 is associated with the transient disruption of the nuclear envelope, evident as lamin B blebs and protruding chromatin (Figures 4M, 4N, and 4P–4R). This transient loss of nuclear integrity has already been reported in ZikV infection (Onorati et al., 2016), as well as in other viral infections (Hatch and Hetzer, 2014). Nuclear retention of the ZikV-NS5-MultimDead protein, might rely on its reduced capacity to bind the nuclear envelope components such as Emerin (Figures S4J and S4K). Hence, the trafficking of ZikV-NS5 to the cilia base appears to depend on its capacity to form multimers.

The retention of ZikV-NS5 within the nucleus was sufficient to prevent the ciliopathy, as evident by the length of the Arl13b-RFP-labeled cilia in NPCs (control median = 1.98 ± 0.97 μm, n = 198; ZikV-NS5-MTDead median = 0.82 ± 0.2 μm, n = 22; ZikV-NS5-MultimDead median = 1.44 ± 1 μm, n = 67) (Figure 4O). Even though the ZikV-NS5-MultimDead protein variant has a reduced capacity to bind to the nuclear envelope protein Emerin and to the centrosome protein CEP164 (Figures S4J and S4K), a high concentration of this protein can pass through the nuclear envelope (Figures S4L, S4M, S4Q, and S4R), translocate to the cilia base, and induce ciliopathy (Figures S4N–S4P), ultimately promoting the neurogenic responses of the pTis21-Luc reporter as the non-mutated ZikV-NS5 (Figures S4S and S4T).

## Microcephaly in a Human Post-mortem ZikV-Infected Fetal Brain Is Accompanied by Ciliopathy in ECs

To support our hypothesis that the ciliopathy caused by ZikV-NS5 results in a microcephaly phenotype, we examined the post-mortem tissue of a reported ZikV-infected microcephalic fetus from a ZikV-infected mother. The pregnant woman reported possible exposure to the *Aedes* mosquito until the 12$^{th}$ gestational week (GW), and ZikV RNA was detected in GW22. After ultrasound and MRI, the fetus was diagnosed with severe microcephaly and the pregnancy was terminated in GW22+6. A severe developmental delay was evident in forebrain coronal sections, with almost complete cortical plate (CP) agyria when compared with the control sections of a non-pathological GW21 fetal brain. A thinner CP, intermediate zone (IZ), and subventricular zone (SVZ) were also detected (Figures 5A and 5B). We examined the layered organization of neurons in two CP areas, which not only showed a dramatic reduction in neuron numbers in the ZikV-infected fetal brain compared with the control GW21 brain (Figure 5C; Figures S5A–S5E) but also showed an aberrant neuronal distribution. In the ZikV-infected brain, both Satb2+ upper-layer neurons (Figures 5D and 5E; Figures S5F and S5G) and Ctip2+ lower-layer neurons (Figures 5F and 5G; Figures S5H and S5I), were distributed throughout the CP. Moreover, cortical neurons ectopically localized in the IZ in the ZikV-infected brain (Figures S5C and S5D) were similar to cortical abnormalities caused by cilia deficiencies, such as in Arl13b mutant radial glial cells (Higginbotham et al., 2013).

During development and upon termination of primary neurogenesis, monociliated NPCs differentiate into multiciliated ECs (Spassky et al., 2005). To test whether the ciliopathy described in the chick embryo NPCs might persist in the ECs of the ZikV-infected human fetal brain, we first assessed the distribution of the viral NS5 protein (Retallack et al., 2016) in the ZikV-infected

**Figure 4. Multimeric Arrangement of ZikV-NS5 Is Required for Its Localization to the Cilia Base and the Promotion of Terminal Neurogenic Divisions**

(A) Scheme showing the three modes of NPC division.

(B) Scheme representing the reporter co-elect. experiments, harvested at 24 hpe, either for FACS or for PH3 immunostaining.

(C) Quantification of the cells expressing the reporters corresponding to each division: PP (green), PN (yellow), and NN (red). The data represent mean ± SEM.

(D and E) Images show pSox2 (green) and pTis21 (red) NPCs and pH3-stained mitoses (blue) in control or ZikV-NS5 (E) elect. NTs. Green, yellow, and red lines in (E) indicate mitotic PP, PN, and NN divisions, respectively.

(F) Quantification of reporter-expressing pH3$^+$ dividing cells in each condition. The data represent mean ± SEM.

(G) Scheme depicts the MTase and RdRP domains in the ZikV-NS5 protein. A 3D representation of one NS5 monomer is shown in an orientation from the top of RdRP, with the MTase domain shown in gray and the RdRP finger, palm, and thumb subdomains in blue. The inset shows the amino acids involved in the enzymatic activity, with the amino acid substitution highlighted in purple.

(H) Scheme depicts the ZikV-NS5 protein and a 3D representation of one ZikV-NS5 dimer. The inset shows the amino acids involved in dimerization, highlighting the amino acid substitution in purple.

(I) Luc/Renilla activity of the pTis21-Luc reporter after elect. of the DNAs indicated (mean ± SD, n = 6–8 embryos/condition).

(J) Quantification of reporter-expressing FACS cells in each condition: PP (pSox2$^+$/pTis21$^-$, green), PN (pSox2$^+$/pTis21$^+$, yellow) and NN (pSox2$^-$/pTis21$^+$, red). The data represent mean ± SEM.

(K and L) Images of Arl13b at cilia, the FOP-labeled centrosomes at the cilia base, and the localization of the ZikV-NS5 variants: ZikV-NS5-MTDead at the cilium base (green arrow in L) and ZikV-NS5-MultimDead excluded from the cilium base (red arrows point to cilia in L).

(M and N) Images of nuclear ZikV-NS5-FLAG in two separate z stacks. The upper image shows nuclear aggregates (green arrow) causing disruption of the NE. The lower image shows the ZikV-NS5-FLAG aggregates (green arrow) exit from the NE. NE disruption is highlighted by lamin B (red arrow) and DAPI (blue arrow). ZikV-NS5-MultimDead, shown in two separate cells in (N), localizes near the NE.

(O) Cilia length in control NPCs and those elect. with the mutant ZikV-NS5 constructs (upper and lower lines indicate the interquartile range, and the middle line indicates the median).

(P and Q) Plots of the FI (in a.u.) of green-labeled ZikV-NS5 relative to red lamin B labeling at the two separate z stacks shown in (M). The purple dotted line depicts NE disruption.

(R) Plots of the FI (in a.u.) of green-labeled ZikV-NS5-MultimDead with the same intensity profile as the red-labeled lamin B.

***$p < 0.001$; **$p < 0.01$, with exact p values 0.0054 (C) and 0.0034 (I); *$p < 0.05$, with exact p values 0.0129 (C), 0.0151 (NN) and 0.0398 (PP) (F), and 0.0225 (J); ns, not significant. (C) and (F) Two-sided unpaired t test; (I and J) one-way ANOVA; (O) Kruskal-Wallis test. Scale bars, 30 μm (D), 15 μm (E), 7 μm (K), 2 μm (L), and 5 μm (M and N). See also Figures S3 and S4.

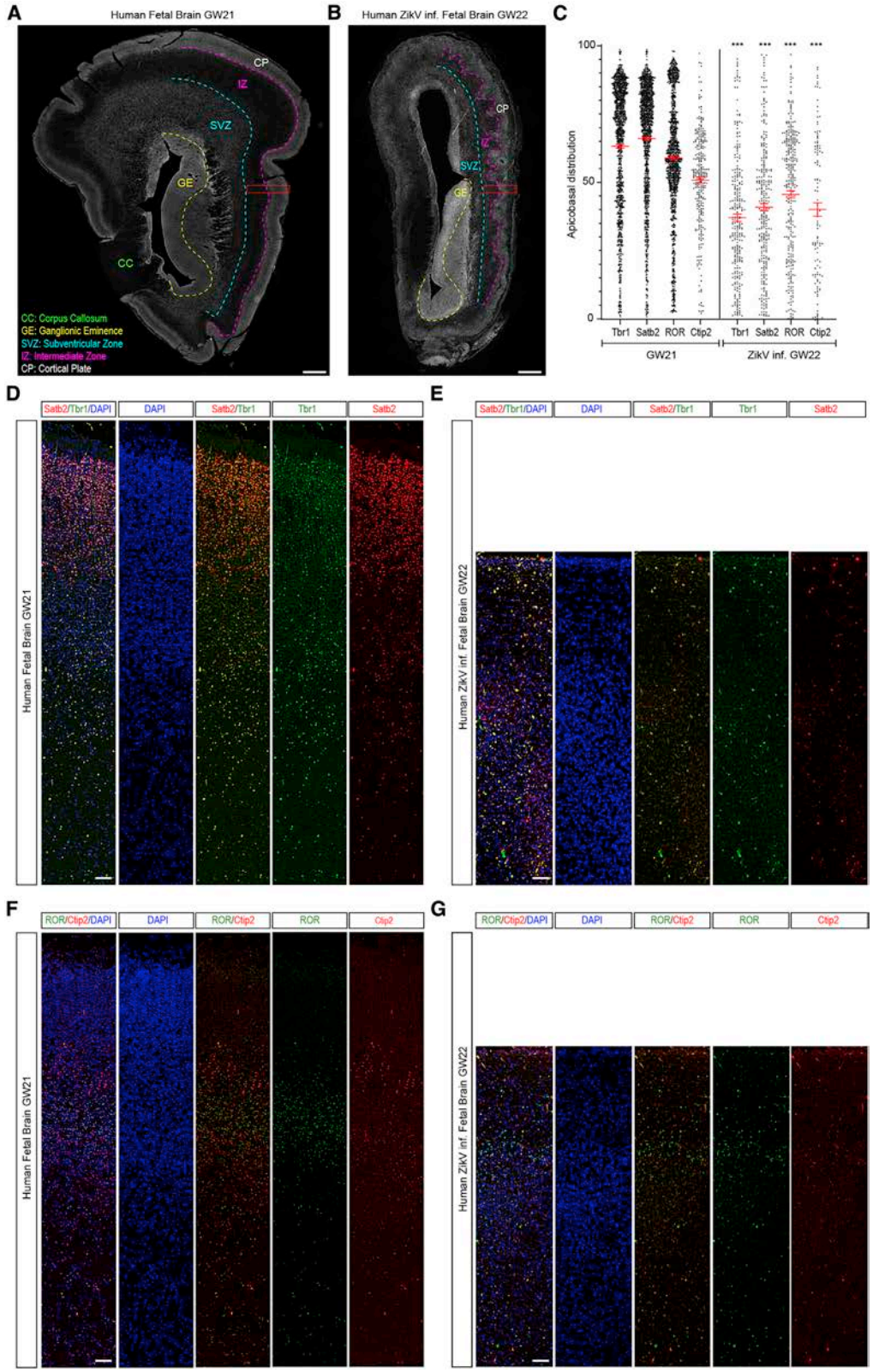


**Figure 5. Microcephaly in ZikV-Infected Human Fetal Brain Is Accompanied by Severe Disorganization of the Cortical Plate**

(A) Representative image of control GW21 forebrain coronal sections indicating the different forebrain areas. The red inset highlights the area quantified in (C) and the images shown in (D) and (F).

*(legend continued on next page)*

brain. Consistent with the viral infection early in gestation, the NS5 protein spread from the ependymal layer to the SVZ and CP (Figure 6A). Moreover, the viral NS5 protein was detected in sub-ECs (Figure 6B) and in ECs, co-localizing with the acetylated α-tubulin-labeled cilia shaft (Figures 6C and 6D), cilia that are shorter than in the control GW21 ECs (Figure 6E).

In addition, we observed a severe disorganization of the S100β$^+$ ECs lining the ventricle (Figures 6F and 6G), as reported in ZikV-infected macaque tissues (Adams Waldorf et al., 2018), with differentiating ECs expanding their apical surface and assembling multiple motile cilia (Mahuzier et al., 2018). To next investigate whether ZikV infection affected ciliogenesis, the length of the acetylated α-tubulin cilia shafts protruding from the VZ surface was measured in the ~2.5 mm ependymal layer facing the ganglionic eminence (GE) in ZikV-infected ECs, comparing these values to those in control ECs in the GW21 and GW23 (Figures 6H–6K). Although control tissue showed an increase in cilia length associated with EC maturation (GW21: median = 6.3 ± 1.57 μm, n = 281; GW23: median = 7.8 ± 1.77 μm, n = 225), the EC multicilia were significantly shorter and more disorganized in ZikV-infected tissue (median = 3.86 ± 1.14 μm, n = 422) (Figures 6L–6N).

Multiciliated EC differentiation involves the assembly of numerous centrioles that migrate apically and anchor to the plasma membrane. In the case of these cilia, Cep164 localizes to the distal appendages and Rootletin extends from the proximal end of the centrioles to their rootlets (Mahuzier et al., 2018) (Figure 6O). 3D imaging highlighted the disturbed CEP164 distribution at the apical surface of ZikV-infected ECs relative to controls (Figures 6P and 6Q). To search for the mechanisms underlying the ZikV-mediated ciliopathy in human tissue, we quantified the endogenous Cep164 protein in ECs relative to the centriole marker Pericentrin. ZikV-infected ECs had significantly less CEP164 protein than control ECs, which is itself required for motile cilia assembly (Siller et al., 2017) (control mean = 0.47 ± 0.15, n = 26; ZikV-infected mean = 0.18 ± 0.06, n = 24) (Figure 6R). Altogether, our analysis revealed that ZikV infection of human fetal brain tissue not only compromises primary neurogenesis, resulting in a severe microcephalic brain, but also disrupts EC differentiation and provokes ciliopathy in these cells. This ciliopathy is likely to impair the flux of CSF elements necessary for brain homeostasis in these cells, as well as for toxin washout, further contributing to the developmental malformations associated with congenital Zika syndrome, such as microcephaly and ventriculomegaly.

## DISCUSSION

ZikV has evolved multiple mechanisms to exploit or perturb fundamental cellular processes in NPCs (Scaturro et al., 2018). Previous data showed that NS4AB interferes with the mTOR pathway in NPCs, reducing proliferation and inducing autophagy (Liang et al., 2016), and that NS2A interacts with AJs while disrupting the integrity of the developing neuroepithelium and again perturbing NPC proliferation (Yoon et al., 2017). The NS2B3 heterodimer was also shown to disturb the cell cycle, because it affects the host protein Septin-2 that is involved in NPC cytokinesis (Li et al., 2019). To date, NS5 has only been shown to counteract host antiviral mechanisms by targeting the interferon pathway (Grant et al., 2016). Here we describe a toxic effect of NS5 on NPCs by showing its capacity to interact with multiple host proteins at the cilium base, consequently promoting ciliopathy and premature NPC differentiation.

Primary and motile cilia differ in their structure, composition, and function. In the developing brain, primary cilia are non-motile signaling organelles present on NPCs that help integrate growth signals. Multiple motile cilia are found on the surface of the ECs lining all brain ventricles, where they contribute to the flow of CSF. During brain development, monociliated NPCs differentiate into multiciliated ECs, providing an ideal system to study the impact of pathogen infection on these two developmental stages. The primary cilium has a microtubule-based core and an axoneme that extends from a specialized centriole at the base of the cilium, the site where Cep164, Rootletin, and Bart are located (Figure 1E). Differentiation of ECs involves the assembly of numerous centrioles that migrate apically and anchor to the plasma membrane (Mahuzier et al., 2018). Here we show that in NPCs, ZikV-NS5 binds directly to the ciliary basal body, impairing the normal development of this organelle and resulting in cilia shortening (Figures 1 and 2). We hypothesize that NS5 interaction with CEP164, Rootletin, and BART might target these proteins for ubiquitination and degradation (Grant et al., 2016) at the cilia basal body, perturbing cilia assembly. Failure to elongate a primary cilium after mitosis diminishes the responses to external stimuli like Shh and to other growth factors that promote symmetric NPC division and CNS growth (Goetz and Anderson, 2010; Saade et al., 2018). Remarkably, reduced levels of CEP164 and centriole damage were previously associated with ZikV infection (Gabriel et al., 2017). In addition, dysregulation of neurogenesis through the Notch pathway, a modulator of NPC response to Shh ligand, was also reported in ZikV infections (Ferraris et al., 2019). Hence, the primary ciliopathy provoked by ZikV-NS5 seems to be responsible for the microcephaly induced by ZikV. We found that in human post-mortem tissue of a presumed ZikV-infected microcephalic fetus from a ZikV-infected mother, ECs exhibited a severe ciliopathy that might prevent the flow of the CSF necessary to maintain brain homeostasis and toxin washout (Figures 5 and 6). The distinction between a motile ciliopathy and a primary ciliopathy seems to be unclear, because hydrocephalus may also be

(B) Representative image of ZikV-infected GW22 forebrain coronal sections. The red box highlights the area quantified in (C) and the images shown in (E) and (G).
(C) Relative apicobasal position of Tbr1+, Satb2+, ROR+, or Ctip2+ neurons at GW21 and ZikV-infected (ZikikV inf.) GW22. Values represent median ± SEM. Total number of neurons counted, GW21: Tbr1+ n = 1.304, Satb2+ n = 1.303, ROR+ n = 1.329, Ctip2+ n = 293; ZIKV inf. GW22: Tbr1+ n = 283, Satb2+ n = 290, ROR + n = 320, Ctip2+ n = 120.
(D and E) Representative images of the generating cortical plate and intermediate zone at GW21 (D) and ZikV inf. GW2 (E), immunostained for markers of postmitotic neuron Tbr1+ and upper-layer neuron Satb2.
(F and G) Representative images of the generating cortical plate and intermediate zone at GW21 (F) and ZikV inf. GW2 (G), immunostained for markers of deep-layer neurons ROR and Ctip2.
All figures were digitally stitched by the appropriate image software as described in STAR Methods. ***p < 0.001; **p < 0.01; *p < 0.05. (C) Mann-Whitney U test. Scale bars, 1.5 mm (A and B) and 100 μm (D–G). See also Figure S5.

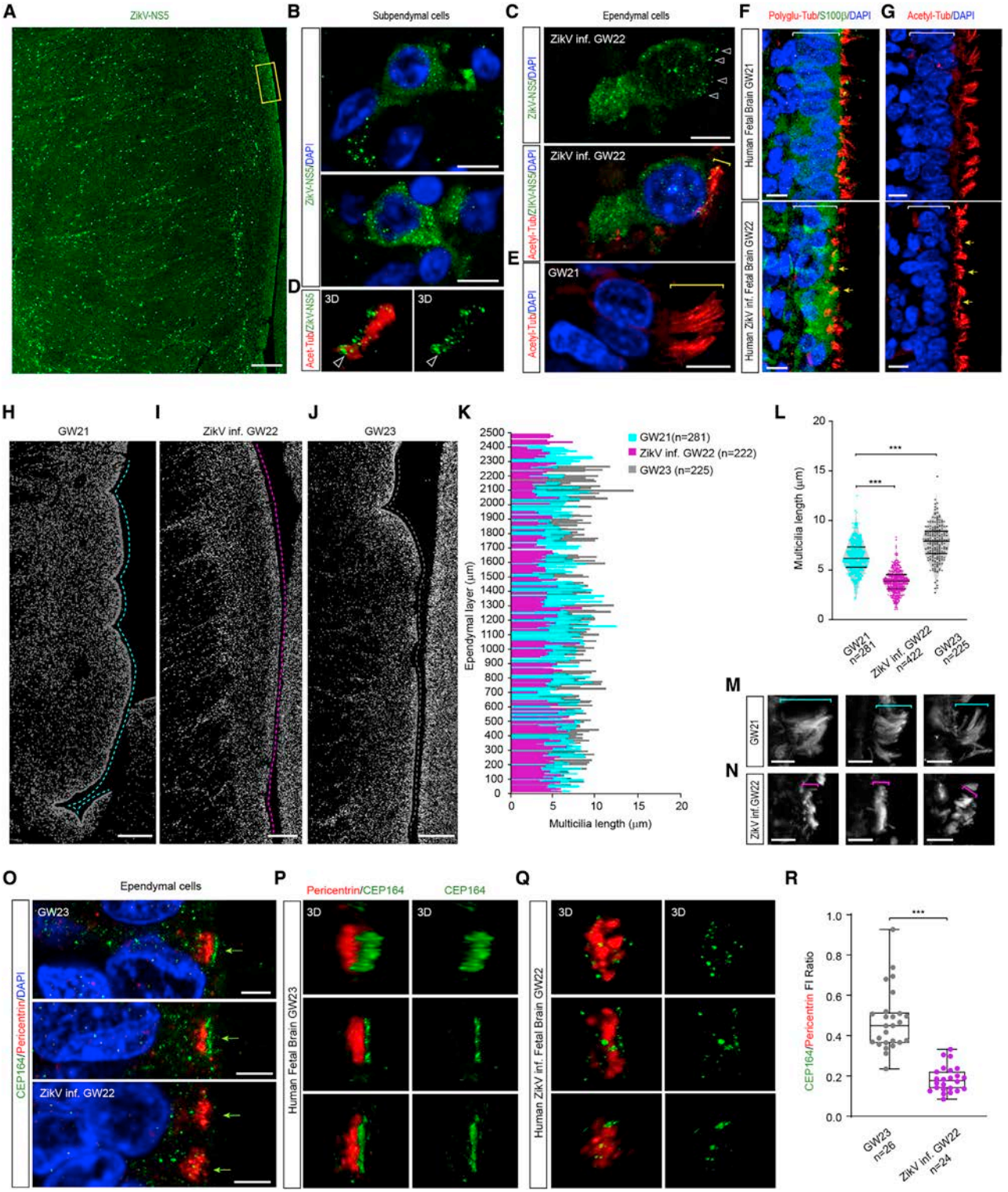


**Figure 6. Microcephaly in ZikV-Infected Human Fetal Brain Is Accompanied by Ciliopathy in ECs**

(A) Immunostaining for the viral NS5 protein in ZikV-infected GW22 coronal forebrain sections.

(B) Selected images from (C) (inset, yellow square) showing the viral ZikV-NS5 protein in sub-ECs with DAPI-stained nuclei.

(C) Images show acetylated tubulin-labeled multicilia in ZikV-NS5-infected ECs with DAPI-stained nuclei. Arrowheads point to the ZikV-NS5 protein, and the bracket indicates the cilia length.

(D) 3D image of ZikV-NS5 (arrowhead) localized to the basal acetylated tubulin-labeled multicilia. Arrowheads clearly show the green dots at the base of cilia.

*(legend continued on next page)*

observed in several primary cilia disorders (Valente et al., 2014). Here we show that a single pathogen can cause both types of ciliopathy, depending on the cell targeted.

We have also demonstrated that both the ciliopathy and the imbalance in the mode of division produced by ZikV-NS5 strongly depend on its quaternary structure. The recently reported X-ray structures of the full-length ZikV-NS5 revealed a dimer-based helicoidal arrangement of the protein that is mediated by MTase-MTase interactions, involving residues Y25, K28, and K29 (Figure 4H) (Ferrero et al., 2019). Here we show that the monomeric ZikV-NS5 Y25A/K28S/K28A variant is retained within the cell nucleus, forming a diffuse pattern. These data suggest that nuclear multimerization of NS5 is required to escape from this cellular compartment and travel to the basal body. Our results show that the capacity of ZikV-NS5 to form multimers contributes to its interference with components of the cilium base, a fundamental mechanism underlying the distinct developmental malformations attributed to congenital Zika syndrome. These findings suggest alternative routes that could be followed to discover potential antiviral agents that target the intermolecular interfaces involved in dimer/oligomer formation.

### Limitations of Study

In this study, we recognize the limitations associated with the ZikV-NS5 strategy for passing the nuclear envelope barrier. The key mechanisms at the nuclear envelope and how ZikV-NS5 multimerization capacity favors nuclear egress are still debated. Testing nuclear export inhibitors such as leptomycin B on infected NPCs could help in deciphering whether active export via the pathway of nuclear pore complexes is involved in this process. We should also consider that the exit of ZikV-NS5 from the nucleus is clearly accompanied by lamin B blebbing and disorganization (Figure 4M). This lets us suggest that ZikV-NS5 nuclear egression could involve structural and mechanical aberrations of the nuclear lamina, a mechanism already reported in several viral infections (Stiekema et al., 2020).

## STAR★METHODS

Detailed methods are provided in the online version of this paper and include the following:

- KEY RESOURCES TABLE
- RESOURCE AVAILABILITY
  - Lead Contact
  - Materials Availability
  - Data and Code Availability
- EXPERIMENTAL MODEL AND SUBJECT DETAILS
  - Tissue Procurement
  - Chick embryos
  - Human NPC culture
- METHOD DETAILS
  - DNA Constructs
  - Yeast Two-Hybrid Analysis
  - Cell culture transfection and Pull-down assays
  - Western Blot
  - Immunohistochemistry and microscopy
  - Flow cytometry
  - Luciferase reporter assay
  - Quantification of ciliary length
  - Measurement of fluorescence intensities and area
  - Apical foot length measurement
  - GO Analysis
  - Sequence alignments
  - ZikV-NS5 Structure Cartoons
- QUANTIFICATION AND STATISTICAL ANALYSIS

## SUPPLEMENTAL INFORMATION

Supplemental Information can be found online at https://doi.org/10.1016/j.stem.2020.10.002.

## ACKNOWLEDGMENTS

We thank Dr. Elena Rebollo and Jaume Boix for their technical assistance at the AFMU Facility (IBMB) and Leica Microsystems for supporting and collaborating with the AFMU Facility. We are grateful to researchers who provided DNAs and antibodies. The work in E.M.'s laboratory was supported by grants BFU2016-77498-P, BFU2016-77498-P, and La Maratò de TV3 foundation 201833-10. M.S. holds a Ramón Y Cajal fellowship (RYC2018-025379-I). J.B.-A is a recipient of a BES-2017-080050 PhD scholarship. The work in N.V.'s laboratory was supported by grants BIO2017-83906-P, Maria de Maeztu Unit of Excellence MDM-2014-0435 (MCIU), and La Maratò de TV3 foundation 201833-10. The work in N.A.'s laboratory was supported by NIH/NINDS R00NS089859 and IDDRC-NPDA (CHOP/Penn).

## AUTHOR CONTRIBUTIONS

M.S. conceived and performed the experiments, analyzed data, discussed results, and revised the manuscript. D.S.F. conceived and performed the structural and biochemical experiments with the help of V.M.R.-A., analyzed data, discussed results, and revised the manuscript. J.B.-A. and E.G.-G. contributed to experiments, image acquisition, image analysis and quantification, and statistics and revised the manuscript. E.M.-S. and S.R.C. provided human tissues. M.F.-M. performed experiments in hNPCs, analyzed data, discussed

(E) Images showing acetylated tubulin-labeled multicilia in control GW21 ECs with DAPI-stained nuclei, in which the bracket indicates the cilia length.
(F) Images of poly-glutamylated tubulin-stained multicilia in S100$\beta^+$ ECs of control GW21 fetal brain and ZikV GW22 fetal brain.
(G) Images of acetylated tubulin-stained multicilia in control GW21 and ZikV GW22 ECs, in which the yellow arrows indicate multicilia shortening.
(H–J) Images depicting the 2.5 mm ependymal areas (dotted lines) used to measure cilia length in control GW21, ZikV-infected GW22, and control GW23 forebrain sections.
(K) Plots of the cilia length along the ependymal layer at the developmental stages indicated.
(L) Plots of the cilia length in ECs of control GW21, ZikV-infected GW22, and control GW23 forebrain sections (upper and lower lines indicate the interquartile range, and the middle line indicates the median).
(M and N) Images of acetylated tubulin-stained multicilia in control GW21 (M) and in ZikV-infected GW22 (N) ECs, in which brackets indicate the cilia length.
(O) Images of PCNT-stained multiple centrosomes and the CEP164-stained multicilia base in control GW21 and ZikV-infected GW22 ECs.
(P and Q) 3D image showing Pericentrin and CEP164 localization to the base of multicilia in control GW23 (P) and ZikV-infected GW22 (Q) ECs.
(R) Boxplot of the CEP164/Pericentrin FI ratio, showing reduced expression of CEP164 in the multiple centrosomes of ZikV-infected ECs (mean ± SD).
(A) and (H)–(J) were digitally stitched by the appropriate image software as described in STAR Methods. ***$p < 0.001$; **$p < 0.01$; *$p < 0.05$. (N) Kruskal-Wallis test; (R) Mann-Whitney U test. Scale bars, 200 μm (A and H–J), 6 μm (B, C, E–G, M, and N), and 3 μm (O).

results, and revised the manuscript. N.A. conceived experiments in hNPCs, discussed results, and revised the manuscript. N.V. conceived structural experiments, discussed results, and revised the manuscript. E.M. conceived experiments, analyzed the data, discussed results, and drafted the manuscript.

## DECLARATION OF INTERESTS

The authors declare no competing interests.

Received: March 25, 2020
Revised: August 16, 2020
Accepted: October 8, 2020
Published: November 3, 2020

## REFERENCES

Abbott, A. (2011). Tissue-bank shortage: Brain child. Nature *478*, 442–443.

Adams Waldorf, K.M., Nelson, B.R., Stencel-Baerenwald, J.E., Studholme, C., Kapur, R.P., Armistead, B., Walker, C.L., Merillat, S., Vornhagen, J., Tisoncik-Go, J., et al. (2018). Congenital Zika virus infection as a silent pathology with loss of neurogenic output in the fetal brain. Nat. Med. *24*, 368–374.

Akizu, N., Cantagrel, V., Schroth, J., Cai, N., Vaux, K., McCloskey, D., Naviaux, R.K., Van Vleet, J., Fenstermaker, A.G., Silhavy, J.L., et al. (2013). AMPD2 regulates GTP synthesis and is mutated in a potentially treatable neurodegenerative brainstem disorder. Cell *154*, 505–517.

Alonso-López, D., Gutiérrez, M.A., Lopes, K.P., Prieto, C., Santamaría, R., and De Las Rivas, J. (2016). APID interactomes: providing proteome-based interactomes with controlled quality for multiple species and derived networks. Nucleic Acids Res. *44* (W1), W529–W535.

Baek, C., Freem, L., Goïame, R., Sang, H., Morin, X., and Tozer, S. (2018). Mib1 prevents Notch Cis-inhibition to defer differentiation and preserve neuroepithelial integrity during neural delamination. PLoS Biol. *16*, e2004162.

Baronti, C., Piorkowski, G., Charrel, R.N., Boubis, L., Leparc-Goffart, I., and de Lamballerie, X. (2014). Complete coding sequence of zika virus from a French polynesia outbreak in 2013. Genome Announc *2*, e00500–e00514.

Bartel, P.L., Chien, C.-T., Sternglanz, R., and Fields, S. (1993). Using the two-hybrid system to detect protein-protein interactions. In Cellular Interactions in Development: A Practical Approach, D.A. Hartley, ed. (Oxford University Press), pp. 153–179.

Béranger, F., Aresta, S., de Gunzburg, J., and Camonis, J. (1997). Getting more from the two-hybrid system: N-terminal fusions to LexA are efficient and sensitive baits for two-hybrid studies. Nucleic Acids Res. *25*, 2035–2036.

Bergsland, M., Ramsköld, D., Zaouter, C., Klum, S., Sandberg, R., and Muhr, J. (2011). Sequentially acting Sox transcription factors in neural lineage development. Genes Dev. *25*, 2453–2464.

Caspary, T., Larkins, C.E., and Anderson, K.V. (2007). The graded response to Sonic Hedgehog depends on cilia architecture. Dev. Cell *12*, 767–778.

Castro, D.S., Skowronska-Krawczyk, D., Armant, O., Donaldson, I.J., Parras, C., Hunt, C., Critchley, J.A., Nguyen, L., Gossler, A., Göttgens, B., et al. (2006). Proneural bHLH and Brn proteins coregulate a neurogenic program through cooperative binding to a conserved DNA motif. Dev. Cell *11*, 831–844.

Coyaud, E., Ranadheera, C., Cheng, D., Gonçalves, J., Dyakov, B.J.A., Laurent, E.M.N., St-Germain, J., Pelletier, L., Gingras, A.C., Brumell, J.H., et al. (2018). Global Interactomics Uncovers Extensive Organellar Targeting by Zika Virus. Mol. Cell. Proteomics *17*, 2242–2255.

Dang, J., Tiwari, S.K., Lichinchi, G., Qin, Y., Patil, V.S., Eroshkin, A.M., and Rana, T.M. (2016). Zika Virus Depletes Neural Progenitors in Human Cerebral Organoids through Activation of the Innate Immune Receptor TLR3. Cell Stem Cell *19*, 258–265.

Davidson, A.E., Schwarz, N., Zelinger, L., Stern-Schneider, G., Shoemark, A., Spitzbarth, B., Gross, M., Laxer, U., Sosna, J., Sergouniotis, P.I., et al. (2013). Mutations in ARL2BP, encoding ADP-ribosylation-factor-like 2 binding protein, cause autosomal-recessive retinitis pigmentosa. Am. J. Hum. Genet. *93*, 321–329.

Duan, W., Song, H., Wang, H., Chai, Y., Su, C., Qi, J., Shi, Y., and Gao, G.F. (2017). The crystal structure of Zika virus NS5 reveals conserved drug targets. EMBO J. *36*, 919–933.

Dzhindzhev, N.S., Yu, Q.D., Weiskopf, K., Tzolovsky, G., Cunha-Ferreira, I., Riparbelli, M., Rodrigues-Martins, A., Bettencourt-Dias, M., Callaini, G., and Glover, D.M. (2010). Asterless is a scaffold for the onset of centriole assembly. Nature *467*, 714–718.

Enfissi, A., Codrington, J., Roosblad, J., Kazanji, M., and Rousset, D. (2016). Zika virus genome from the Americas. Lancet *387*, 227–228.

Ferraris, P., Cochet, M., Hamel, R., Gladwyn-Ng, I., Alfano, C., Diop, F., Garcia, D., Talignani, L., Montero-Menei, C.N., Nougairède, A., et al. (2019). Zika virus differentially infects human neural progenitor cells according to their state of differentiation and dysregulates neurogenesis through the Notch pathway. Emerg. Microbes Infect. *8*, 1003–1016.

Ferrero, D.S., Ruiz-Arroyo, V.M., Soler, N., Usón, I., Guarné, A., and Verdaguer, N. (2019). Supramolecular arrangement of the full-length Zika virus NS5. PLoS Pathog. *15*, e1007656.

Formstecher, E., Aresta, S., Collura, V., Hamburger, A., Meil, A., Trehin, A., Reverdy, C., Betin, V., Maire, S., Brun, C., et al. (2005). Protein interaction mapping: a *Drosophila* case study. Genome Res. *15*, 376–384.

Frangi, A.F., Niessen, W.J., Vincken, K.L., and Viergever, M.A. (1998). Multiscale vessel enhancement filtering. In Medical Image Computing and Computer-Assisted Intervention—MICCAI'98, W.M. Wells, A. Colchester, and S. Delp, eds. (Springer), pp. 130–137.

Fromont-Racine, M., Rain, J.C., and Legrain, P. (1997). Toward a functional analysis of the yeast genome through exhaustive two-hybrid screens. Nat. Genet. *16*, 277–282.

Gabriel, E., Ramani, A., Karow, U., Gottardo, M., Natarajan, K., Gooi, L.M., Goranci-Buzhala, G., Krut, O., Peters, F., Nikolic, M., et al. (2017). Recent Zika Virus Isolates Induce Premature Differentiation of Neural Progenitors in Human Brain Organoids. Cell Stem Cell *20*, 397–406.e5.

Garcez, P.P., Loiola, E.C., Madeiro da Costa, R., Higa, L.M., Trindade, P., Delvecchio, R., Nascimento, J.M., Brindeiro, R., Tanuri, A., and Rehen, S.K. (2016). Zika virus impairs growth in human neurospheres and brain organoids. Science *352*, 816–818.

Goetz, S.C., and Anderson, K.V. (2010). The primary cilium: a signalling centre during vertebrate development. Nat. Rev. Genet. *11*, 331–344.

Grant, A., Ponia, S.S., Tripathi, S., Balasubramaniam, V., Miorin, L., Sourisseau, M., Schwarz, M.C., Sánchez-Seco, M.P., Evans, M.J., Best, S.M., and García-Sastre, A. (2016). Zika Virus Targets Human STAT2 to Inhibit Type I Interferon Signaling. Cell Host Microbe *19*, 882–890.

Grard, G., Moureau, G., Charrel, R.N., Holmes, E.C., Gould, E.A., and de Lamballerie, X. (2010). Genomics and evolution of Aedes-borne flaviviruses. J Gen Virol *91*, 87–94.

Graser, S., Stierhof, Y.D., Lavoie, S.B., Gassner, O.S., Lamla, S., Le Clech, M., and Nigg, E.A. (2007). Cep164, a novel centriole appendage protein required for primary cilium formation. J. Cell Biol. *179*, 321–330.

Hamburger, V., and Hamilton, H.L. (1951). A series of normal stages in the development of the chick embryo. J. Morphol. *88*, 49–92.

Hatch, E., and Hetzer, M. (2014). Breaching the nuclear envelope in development and disease. J. Cell Biol. *205*, 133–141.

Higginbotham, H., Guo, J., Yokota, Y., Umberger, N.L., Su, C.Y., Li, J., Verma, N., Hirt, J., Ghukasyan, V., Caspary, T., and Anton, E.S. (2013). Arl13b-regulated cilia activities are essential for polarized radial glial scaffold formation. Nat. Neurosci. *16*, 1000–1007.

Iacopetti, P., Michelini, M., Stuckmann, I., Oback, B., Aaku-Saraste, E., and Huttner, W.B. (1999). Expression of the antiproliferative gene TIS21 at the onset of neurogenesis identifies single neuroepithelial cells that switch from proliferative to neuron-generating division. Proc. Natl. Acad. Sci. USA *96*, 4639–4644.

Kasioulis, I., Das, R.M., and Storey, K.G. (2017). Inter-dependent apical microtubule and actin dynamics orchestrate centrosome retention and neuronal delamination. eLife *6*, e26215.

Kim, S., and Dynlacht, B.D. (2013). Assembling a primary cilium. Curr. Opin. Cell Biol. *25*, 506–511.

Le Dréau, G., Escalona, R., Fueyo, R., Herrera, A., Martínez, J.D., Usieto, S., Menendez, A., Pons, S., Martinez-Balbas, M.A., and Marti, E. (2018). E proteins sharpen neurogenesis by modulating proneural bHLH transcription factors' activity in an E-box-dependent manner. eLife *7*, e37267.

Le Dréau, G., Saade, M., Gutiérrez-Vallejo, I., and Martí, E. (2014). The strength of SMAD1/5 activity determines the mode of stem cell division in the developing spinal cord. J. Cell Biol. *204*, 591–605.

Lehtinen, M.K., Zappaterra, M.W., Chen, X., Yang, Y.J., Hill, A.D., Lun, M., Maynard, T., Gonzalez, D., Kim, S., Ye, P., et al. (2011). The cerebrospinal fluid provides a proliferative niche for neural progenitor cells. Neuron *69*, 893–905.

Li, H., Saucedo-Cuevas, L., Regla-Nava, J.A., Chai, G., Sheets, N., Tang, W., Terskikh, A.V., Shresta, S., and Gleeson, J.G. (2016). Zika Virus Infects Neural Progenitors in the Adult Mouse Brain and Alters Proliferation. Cell Stem Cell *19*, 593–598.

Li, H., Saucedo-Cuevas, L., Yuan, L., Ross, D., Johansen, A., Sands, D., Stanley, V., Guemez-Gamboa, A., Gregor, A., Evans, T., et al. (2019). Zika Virus Protease Cleavage of Host Protein Septin-2 Mediates Mitotic Defects in Neural Progenitors. Neuron *101*, 1089–1098.e4.

Liang, Q., Luo, Z., Zeng, J., Chen, W., Foo, S.S., Lee, S.A., Ge, J., Wang, S., Goldman, S.A., Zlokovic, B.V., et al. (2016). Zika Virus NS4A and NS4B Proteins Deregulate Akt-mTOR Signaling in Human Fetal Neural Stem Cells to Inhibit Neurogenesis and Induce Autophagy. Cell Stem Cell *19*, 663–671.

Longair, M.H., Baker, D.A., and Armstrong, J.D. (2011). Simple Neurite Tracer: open source software for reconstruction, visualization and analysis of neuronal processes. Bioinformatics *27*, 2453–2454.

Madeira, F., Park, Y.M., Lee, J., Buso, N., Gur, T., Madhusoodanan, N., Basutkar, P., Tivey, A.R.N., Potter, S.C., Finn, R.D., et al. (2019). The EMBL-EBI search and sequence analysis tools APIs in 2019. Nucleic Acids Res. *47*, W636–W641.

Mahuzier, A., Shihavuddin, A., Fournier, C., Lansade, P., Faucourt, M., Menezes, N., Meunier, A., Garfa-Traoré, M., Carlier, M.F., Voituriez, R., et al. (2018). Ependymal cilia beating induces an actin network to protect centrioles against shear stress. Nat. Commun. *9*, 2279.

Mi, H., Muruganujan, A., and Thomas, P.D. (2013). PANTHER in 2013: modeling the evolution of gene function, and other gene attributes, in the context of phylogenetic trees. Nucleic Acids Res. *41*, D377–D386.

Nowakowski, T.J., Pollen, A.A., Di Lullo, E., Sandoval-Espinosa, C., Bershteyn, M., and Kriegstein, A.R. (2016). Expression Analysis Highlights AXL as a Candidate Zika Virus Entry Receptor in Neural Stem Cells. Cell Stem Cell *18*, 591–596.

Onorati, M., Li, Z., Liu, F., Sousa, A.M.M., Nakagawa, N., Li, M., Dell'Anno, M.T., Gulden, F.O., Pochareddy, S., Tebbenkamp, A.T.N., et al. (2016). Zika Virus Disrupts Phospho-TBK1 Localization and Mitosis in Human Neuroepithelial Stem Cells and Radial Glia. Cell Rep. *16*, 2576–2592.

Paridaen, J.T., Wilsch-Bräuninger, M., and Huttner, W.B. (2013). Asymmetric inheritance of centrosome-associated primary cilium membrane directs ciliogenesis after cell division. Cell *155*, 333–344.

Pettersen, E.F., Goddard, T.D., Huang, C.C., Couch, G.S., Greenblatt, D.M., Meng, E.C., and Ferrin, T.E. (2004). UCSF Chimera—a visualization system for exploratory research and analysis. J. Comput. Chem. *25*, 1605–1612.

Pierson, T.C., and Kielian, M. (2013). Flaviviruses: braking the entering. Curr. Opin. Virol. *3*, 3–12.

Pool, M., Thiemann, J., Bar-Or, A., and Fournier, A.E. (2008). NeuriteTracer: a novel ImageJ plugin for automated quantification of neurite outgrowth. J. Neurosci. Methods *168*, 134–139.

Potter, C., Zhu, W., Razafsky, D., Ruzycki, P., Kolesnikov, A.V., Doggett, T., Kefalov, V.J., Betleja, E., Mahjoub, M.R., and Hodzic, D. (2017). Multiple Isoforms of Nesprin1 Are Integral Components of Ciliary Rootlets. Curr. Biol. *27*, 2014–2022.

Qian, X., Nguyen, H.N., Song, M.M., Hadiono, C., Ogden, S.C., Hammack, C., Yao, B., Hamersky, G.R., Jacob, F., Zhong, C., et al. (2016). Brain-Region-Specific Organoids Using Mini-bioreactors for Modeling ZIKV Exposure. Cell *165*, 1238–1254.

Rain, J.C., Selig, L., De Reuse, H., Battaglia, V., Reverdy, C., Simon, S., Lenzen, G., Petel, F., Wojcik, J., Schächter, V., et al. (2001). The protein-protein interaction map of *Helicobacter pylori*. Nature *409*, 211–215.

Retallack, H., Di Lullo, E., Arias, C., Knopp, K.A., Laurie, M.T., Sandoval-Espinosa, C., Mancia Leon, W.R., Krencik, R., Ullian, E.M., Spatazza, J., et al. (2016). Zika virus cell tropism in thse developing human brain and inhibition by azithromycin. Proc. Natl. Acad. Sci. USA *113*, 14408–14413.

Robert, X., and Gouet, P. (2014). Deciphering key features in protein structures with the new ENDscript server. Nucleic Acids Res. *42*, W320–W324.

Saade, M., Gutiérrez-Vallejo, I., Le Dréau, G., Rabadán, M.A., Miguez, D.G., Buceta, J., and Martí, E. (2013). Sonic hedgehog signaling switches the mode of division in the developing nervous system. Cell Rep. *4*, 492–503.

Saade, M., Gonzalez-Gobartt, E., Escalona, R., Usieto, S., and Martí, E. (2017). Shh-mediated centrosomal recruitment of PKA promotes symmetric proliferative neuroepithelial cell division. Nat. Cell Biol. *19*, 493–503.

Saade, M., Blanco-Ameijeiras, J., Gonzalez-Gobartt, E., and Martí, E. (2018). A centrosomal view of CNS growth. Development *145*, dev170613.

Scaturro, P., Stukalov, A., Haas, D.A., Cortese, M., Draganova, K., Płaszczyca, A., Bartenschlager, R., Götz, M., and Pichlmair, A. (2018). An orthogonal proteomic survey uncovers novel Zika virus host factors. Nature *561*, 253–257.

Schneider, C.A., Rasband, W.S., and Eliceiri, K.W. (2012). NIH Image to ImageJ: 25 years of image analysis. Nature methods *9*, 671–675.

Siller, S.S., Sharma, H., Li, S., Yang, J., Zhang, Y., Holtzman, M.J., Winuthayanon, W., Colognato, H., Holdener, B.C., Li, F.Q., and Takemaru, K.I. (2017). Conditional knockout mice for the distal appendage protein CEP164 reveal its essential roles in airway multiciliated cell differentiation. PLoS Genet. *13*, e1007128.

Spassky, N., Merkle, F.T., Flames, N., Tramontin, A.D., García-Verdugo, J.M., and Alvarez-Buylla, A. (2005). Adult ependymal cells are postmitotic and are derived from radial glial cells during embryogenesis. J. Neurosci. *25*, 10–18.

Stiekema, M., van Zandvoort, M.A.M.J., Ramaekers, F.C.S., and Broers, J.L.V. (2020). Structural and Mechanical Aberrations of the Nuclear Lamina in Disease. Cells *9*, 1884.

Tang, H., Hammack, C., Ogden, S.C., Wen, Z., Qian, X., Li, Y., Yao, B., Shin, J., Zhang, F., Lee, E.M., et al. (2016). Zika Virus Infects Human Cortical Neural Progenitors and Attenuates Their Growth. Cell Stem Cell *18*, 587–590.

Valente, E.M., Rosti, R.O., Gibbs, E., and Gleeson, J.G. (2014). Primary cilia in neurodevelopmental disorders. Nat. Rev. Neurol. *10*, 27–36.

Virtanen, J.A., and Vartiainen, M.K. (2017). Diverse functions for different forms of nuclear actin. Curr. Opin. Cell Biol. *46*, 33–38.

Vojtek, A.B., and Hollenberg, S.M. (1995). Ras-Raf interaction: two-hybrid analysis. Methods Enzymol. *255*, 331–342.

Wang, X., Tsai, J.W., Imai, J.H., Lian, W.N., Vallee, R.B., and Shi, S.H. (2009). Asymmetric centrosome inheritance maintains neural progenitors in the neocortex. Nature *461*, 947–955.

Wang, B., Tan, X.F., Thurmond, S., Zhang, Z.M., Lin, A., Hai, R., and Song, J. (2017). The structure of Zika virus NS5 reveals a conserved domain conformation. Nat. Commun. *8*, 14763.

Wilsch-Bräuninger, M., Peters, J., Paridaen, J.T., and Huttner, W.B. (2012). Basolateral rather than apical primary cilia on neuroepithelial cells committed to delamination. Development *139*, 95–105.

Wilson, K.L. (2000). The nuclear envelope, muscular dystrophy and gene expression. Trends Cell Biol. *10*, 125–129.

Wojcik, J., Boneca, I.G., and Legrain, P. (2002). Prediction, assessment and validation of protein interaction maps in bacteria. J. Mol. Biol. *323*, 763–770.

Yan, X., Habedanck, R., and Nigg, E.A. (2006). A complex of two centrosomal proteins, CAP350 and FOP, cooperates with EB1 in microtubule anchoring. Mol. Biol. Cell *17*, 634–644.

Yang, J., Liu, X., Yue, G., Adamian, M., Bulgakov, O., and Li, T. (2002). Rootletin, a novel coiled-coil protein, is a structural component of the ciliary rootlet. J. Cell Biol. *159*, 431–440.

Yang, J., Adamian, M., and Li, T. (2006). Rootletin interacts with C-Nap1 and may function as a physical linker between the pair of centrioles/basal bodies in cells. Mol. Biol. Cell *17*, 1033–1040.

Yoon, K.J., Song, G., Qian, X., Pan, J., Xu, D., Rho, H.S., Kim, N.S., Habela, C., Zheng, L., Jacob, F., et al. (2017). Zika-Virus-Encoded NS2A Disrupts Mammalian Cortical Neurogenesis by Degrading Adherens Junction Proteins. Cell Stem Cell *21*, 349–358.e6.

Yuan, L., Huang, X.Y., Liu, Z.Y., Zhang, F., Zhu, X.L., Yu, J.Y., Ji, X., Xu, Y.P., Li, G., Li, C., et al. (2017). A single mutation in the prM protein of Zika virus contributes to fetal microcephaly. Science *358*, 933–936.

Zhou, Y., Ray, D., Zhao, Y., Dong, H., Ren, S., Li, Z., Guo, Y., Bernard, K.A., Shi, P.Y., and Li, H. (2007). Structure and function of flavivirus NS5 methyltransferase. J. Virol. *81*, 3891–3903.

## STAR★METHODS

### KEY RESOURCES TABLE

| REAGENT or RESOURCE | SOURCE | IDENTIFIER |
|---|---|---|
| Antibodies | | |
| BART | Dr. Richard Khan (EMORY) | N/A |
| CEP164 | Dr. Cyaran Morisson (NUI) | N/A |
| FOP | Dr. Olivier Rosnet (IBDM) | N/A |
| Rootletin | Abcam | Cat#ab121653; RRID:AB_11129547 |
| Pericentrin | Abcam | Cat#ab4448; RRID:AB_304461 |
| Flag | Our Lab; Saade et al., 2017 | N/A |
| GFP | Our Lab; Saade et al., 2017 | N/A |
| Penta.HIS | QIAGEN | Cat#34660; RRID:AB_2619735 |
| Myc | ProSci | Cat# 51-118; RRID:AB_1947601 |
| Anti-Rabbit IgG-Peroxidase | Sigma | Cat# A0545; RRID:AB_257896 |
| Anti-Mouse IgG-Peroxidase | Thermo Fisher Scientific | Cat# A16011; RRID:AB_2534685 |
| RFP | Our Lab; Saade et al., 2017 | N/A |
| Acetylated tubulin | Sigma | Cat# T6793; RRID:AB_477585 |
| Polyglutamylated-tubulin | Enzo Life Sciences | Cat# AG-20B-0020; RRID:AB_2335608 |
| N-Cadherin | Thermo Fisher Scientific | Cat# 13-2100; RRID:AB_2533007 |
| Lamin B1 | Thermo Fisher Scientific | Cat# 33-2000; RRID:AB_2533106 |
| PH3 | Millipore | Cat# Ser-10; RRID:AB_2315135 |
| ROR | R and D Systems | Cat# PP-H3925-00; RRID:AB_2254092 |
| Ctip2 | Abcam | Cat# ab18465; RRID:AB_2064130 |
| Satb2 | Abcam | Cat# ab51502; RRID:AB_882455 |
| Tbr1 | Abcam | Cat# ab183032 |
| Caspase 3 | BD Biosciences | Cat# 550821; RRID:AB_393906 |
| HUC/D | Molecular Probes | Cat# A-21271; RRID:AB_221448 |
| NS5 | Novus Biologicals | Cat# NBP2-42900 |
| S100β | Agilent | Cat# Z0311; RRID:AB_10013383 |
| Alexa Fluor 488 donkey anti-rabbit IgG (H+L) | Thermo Fisher Scientific | Cat #: A-21206; RRID: AB_2535792 |
| Alexa Fluor 488 donkey anti-mouse IgG (H+L) | Thermo Fisher Scientific | Cat #: A-21202; RRID: AB_141607 |
| Alexa Fluor 555 donkey anti-rabbit IgG (H+L) | Thermo Fisher Scientific | Cat #: A-31572; RRID: AB_162543 |
| Alexa Fluor 555 donkey anti-mouse IgG (H+L) | Thermo Fisher Scientific | Cat #: A-31570; RRID:AB_2536180 |
| Alexa Fluor 633 donkey anti-mouse IgG (H+L) | Thermo Fisher Scientific | Cat #: A-21050; RRID:AB_141431 |
| Alexa Fluor 633 donkey anti-rat IgG (H+L) | Thermo Fisher Scientific | Cat #: A-21094; RRID:AB_141553 |
| Biological Samples | | |
| Postmortem GW21 human brain sections | Neuropathology laboratory, Pathology Department, H. U. Vall d'Hebron-PR(AG) 129/201, Barcelona, Spain. | N/A |
| Postmortem GW23 human brain sections | Neuropathology laboratory, Pathology Department, H. U. Vall d'Hebron-PR(AG) 129/201, Barcelona, Spain. | N/A |

(*Continued on next page*)

*Continued*

| REAGENT or RESOURCE | SOURCE | IDENTIFIER |
|---|---|---|
| ZikV Infected Postmortem GW22 human brain sections | Neuropathology laboratory, Pathology Department, H. U. Vall d'Hebron-PR(AG) 129/201, Barcelona, Spain. | N/A |
| Chemicals, Peptides, and Recombinant Proteins | | |
| C-terminal His tagged ZikV-NS5 protein | Our Lab; Ferrero et al., 2019 | N/A |
| Dulbecco's Modification of Eagle's Medium (DMEM) | Sigma-Aldrich | Cat# D5796 |
| Fetal Bovine Serum (FBS) | Sigma-Aldrich | Cat# 12103C |
| Non-essential Amino acids | Sigma-Aldrich | Cat# M7145 |
| penicilin and streptomicin | Sigma-Aldrich | Cat# P4333 |
| Amphotericin B | GIBCO | Cat# 15290-18 |
| Lipofectamine 2000 reagent | Invitrogen | Cat# 11668019 |
| Phusion DNA polymerase | Thermo Fisher Scientific | Cat# F530S |
| Complete ULTRA Tablets, Mini, EDTA-free, EASYpack Protease Inhibitor Cocktail | Roche | Cat# 05892791001 |
| His-trap TALON resin | Takara | Cat# 635503 |
| ECL kit | BIO-RAD | Cat# 170-5061 |
| DAPI | Sigma-Aldrich | Cat# D9542 |
| Mowiol | Sigma-Aldrich | Cat# 81381 |
| Trypsin-EDTA | Sigma-Aldrich | Cat# T3924 |
| Accutase | ThermoFisher | Cat# 1110501 |
| Lipofectamine Stem | ThermoFisher | Cat# STEM00001 |
| Critical Commercial Assays | | |
| GeneArt Site-Directed Mutagenesis PLUS System | Agilent | Cat# A14604 |
| Dual Luciferase Reporter Assay System | Promega | Cat# E1910 |
| NucleoSpin Plasmid, Mini kit for plasmid DNA | Macherey-Nagel | Cat# 740588.50 |
| Deposited Data | | |
| ZikV-NS5 structure | Ferrero et al., 2019 | N/A |
| Experimental Models: Cell Lines | | |
| Human cell line 293T (or HEK293T) | ATCC | Cat# CRL-3216; RRID:CVCL_0063 |
| H9 Human Embryonic Stem Cell (WA09) | WiCell | RRID:CVCL_9773 |
| Experimental Models: Organisms/Strains | | |
| White Leghor chick embryos (Stages 12 to 24 somites) | Granja Gibert | N/A |
| ZikV Suriname strain, human isolate sequence Z1106033 | Enfissi et al., 2016 | GeneBank: KU312312.1 |
| ZikV African strain MR766 | Grard et al., 2010 | GeneBank : DQ859059 |
| ZikV Asian strain H/PF/2013 | Baronti et al., 2014 | GenBank : KJ776791 |
| Oligonucleotides | | |
| Primers for pCIEGO-Flag, See Table S3 | Our Lab; Saade et al., 2017 | N/A |
| Primers for pCIEGO- ZikV Structural genes (C, Pre-M, E) from Suriname strain, See Table S3 | This paper | N/A |
| Primers for pCIEGO- ZikV Non Structural (NS1-NS5) genes from Suriname strain, See Table S3 | This paper | N/A |
| Primers for pCIEGO- ZikV-NS5 truncations and mutations, See Table S3 | This paper | N/A |

(*Continued on next page*)

*Continued*

| REAGENT or RESOURCE | SOURCE | IDENTIFIER |
|---|---|---|
| Primers for pCIEGO- ZikV-NS5 African strain, See Table S3 | This paper | N/A |
| Primers for pCIEGO- ZikV-NS5 Asian strain, See Table S3 | This paper | N/A |
| Primers for pEGFP Rootletin (1-1462), See Table S3 | This paper | N/A |
| Primers for pEGFP-BART1, See Table S3 | This paper | N/A |
| Recombinant DNA | | |
| pCAGGS without florescent marker (pCIEGO) | Our Lab; Saade et al., 2017 | N/A |
| pCAGGS_ires_H2B: GFP (pCIG) | Our Lab; Saade et al., 2017 | N/A |
| pCS2_H2B-GFP | Our Lab; Saade et al., 2017 | N/A |
| pEGFP-C1 | Clontech | Cat #6084-1 |
| Human Cep164 cDNA | Dr. Eric Nigg (Biozentrum), | RRID:Addgene_41149 |
| Full length Rootletin in pEGFP | Addgene | RRID:Addgene_41166 |
| BART-1 cDNA | Dr. Michael Cheetham (UCL) | |
| pEGFP-C1 Emerin | Addgene | RRID:Addgene_61993 |
| DsRedex | Dr. Roger Tsien (UCSD) | N/A |
| CEP152-GFP | OriGene | CAT#: RG211581 |
| Arl13b-RFP, Arl13b-GFP | Dr. Magdalena Götz (LMU) | N/A |
| pSox2:GFP | Our Lab; Saade et al., 2013 | N/A |
| pTis21:RFP | Our Lab; Saade et al., 2013 | N/A |
| pSox2:luc | Our Lab; Saade et al., 2017 | N/A |
| pTis21:luc | Our Lab; Saade et al., 2017 | N/A |
| pNeuroD:luc | Dr. François Guillemot (The Francis Crick Institute) | N/A |
| pTubb3:luc | Our Lab; Le Dréau et al., 2018 | N/A |
| Software and Algorithms | | |
| Fiji/ImageJ (2.0) | ImageJ; Schneider et al., 2012 | https://imagej.nih.gov/ij/; RRID:SCR_003070 |
| Agile Protein Interactomes DataServer (APID) | Alonso-López et al., 2016 | http://apid.dep.usal.es; RRID:SCR_008871 |
| (PANTHER) classification system version 14.0 | Mi et al., 2013 | http://pantherdb.org; RRID:SCR_004869 |
| Clustal Omega | | https://www.ebi.ac.uk/Tools/msa/clustalo/; RRID:SCR_001591 |
| ESPript 3.0. Structure protein | | http://espript.ibcp.fr/ESPript/ESPript/; RRID:SCR_006587 |
| Chimera software | UCSF Chimera; Pettersen et al., 2004 | https://www.cgl.ucsf.edu/chimera/; RRID:Addgene_15601 |
| BD FACSDiva Software v. 6.1.3 | BD Biosciences | RRID:SCR_001456 |
| Flowjo (10.2) software | FlowJo | RRID:SCR_008520 |
| Volocity v.6.2 software | Perkinelmer | RRID:SCR_002668 |
| LSM Software ZEN 2.1 | Zeiss | RRID:SCR_013672 |
| Leica LAS X software -Thunder imaging system software | Leica Microsystems | RRID:SCR_013673 |
| GenBank public database | NCBI | https://www.ncbi.nlm.nih.gov/genbank/; RRID:SCR_002760 |
| Ensembl public database | Ensembl | https://uswest.ensembl.org/info/data/index.html; RRID:SCR_002344 |

(*Continued on next page*)

*Continued*

| REAGENT or RESOURCE | SOURCE | IDENTIFIER |
|---|---|---|
| GraphPad Prism (8.02) | GraphPad | http://cicblade.dep.usal.es:8080/APID/init.action; RRID:SCR_002798 |
| Python (7.04) | Python | https://wingware.com/news/2019-07-11; RRID:SCR_008394 |
| Macro for measuring Multicilia length in Human Ependymal cells | This paper; Github | https://github.com/MolecularImagingPlatformIBMB/MeasureMultiCilia |

## RESOURCE AVAILABILITY

### Lead Contact

Further information and requests for resources and reagents should be directed to and will be fulfilled by the Lead Contact, Elisa Marti (emgbmc@ibmb.csic.es).

### Materials Availability

All plasmids generated in this study are available from the Lead Contact with a completed Materials Transfer Agreement.

### Data and Code Availability

The macro generated during this study to measure the length and positioning of the multiciliated patches along the ependymal cell layer in human brain has been deposited on GitHub (https://github.com/MolecularImagingPlatformIBMB/MeasureMultiCilia).

## EXPERIMENTAL MODEL AND SUBJECT DETAILS

### Tissue Procurement

All work was performed according to EU guidelines for the acquisition and distribution of human tissue for bio-medical research purposes and with approval by the human Investigation Committees and Institutional Ethics Committees of CSIC-007/2019 and VHIR. De-identified postmortem human brain specimens were obtained from tissue collection at the Neuropathology laboratory, Pathology Department, H. U. Vall d'Hebron-PR(AG)129/201. Appropriate informed consent was obtained and all available non-identifying information was recorded for each specimen. Tissue was handled in accordance with ethical guidelines and regulations for the research use of human brain tissue set forth by the WMA Declaration of Helsinki.

### Chick embryos

Eggs from white Leghorn chickens were staged according to the method of Hamburger and Hamilton (1951). *In ovo* electroporation was performed at stage HH10-12 (36 hours post fertilization -hpf-, 12 somite stage) and the embryos were recovered at 24 hpf. Embryos were electroporated with Clontech purified plasmid DNA (0,05-1 μg/ml in H2O) with Fast Green (50 ng/ml). Briefly, the plasmid DNA was injected into the NT lumen and electrodes were placed either side of the embryo to perform electroporation using an Intracel Dual Pulse (TSS10) electroporator, delivering five 50 ms pulses of 20-30V.

### Human NPC culture

Human neural progenitor cells (hNPCs, WiCell) were obtained as previously described (Akizu et al., 2013). Briefly, embryoid bodies (EBs) were formed by mechanical dissociation of H9 human embryonic stem cell clusters, plated in suspension in neural induction media (DMEM F12, 1x N2, 1x B27, 1 μM LDN and 1 μM SB431542) for 9 days with daily media replacement. Resultant EBs were then plated on poly-ornithine/laminin coated dishes in NBF medium (DMEM F12, 1x N2, 1x B27, 20 ng/ml bFGF, 1x Penicillin-Streptomycin). Neural rosettes, visible after 3-5 days, were dissociated with Accutase (ThermoFisher) to obtain hNPCs. hNPCs were expanded and all experiments performed between passage 3 and 6.

hNPCs were cultured in 24-well plates ($1.8x10^5$ cells/well) and transfected with 1 μg of pCIG or pCIEGO-ZikVNS5-GFP using lipofectamine stem (ThermoFisher) in NBF media following manufacturer's instructions. 48h after transfection cells were washed once with PBS and fixed with cold methanol for 10 minutes at −20C. Fixed cells were permeabilized/blocked with blocking solution (2% fetal serum bovine plus 0.1% Tween 20 in PBS) for 2h. Cells were incubated with primary antibodies in blocking solution overnight at 4°C. After 3 washes with 0.1% Tween 20-PBS, cells were incubated with fluorescently labeled secondary antibodies for 2 h at room temperature. Fluorescence signal was detected using Leica confocal microscope and images were processed with ImageJ (ImageJ).

## METHOD DETAILS

### DNA Constructs

All oligonucleotides designed to generate the following DNA constructs are listed in Table S3. DNA constructs used for control conditions are the pCAGGS without florescent marker (pCIEGO) and pCAGGS_ires_H2B: GFP (pCIG). Tagged ZikV proteins were expressed with pCIEGO-EGFP and/or its modified version pCIEGO-FLAG, constructed ligating a short dsDNA sequence codifying for FLAG followed by a stop codon in EcoRI multiple cloning site of pCIEGO-EGFP vector. The dsDNA was formed annealing an equimolar mixture of two oligos that generate cohesive ends compatible with EcoRI site. Polyprotein ORF codifying for ZikV structural proteins (C, Pr-M, E) and ZikV non-structural proteins (NS1-NS5) were chemically synthetized (GeneArt, ThermoFisher) based on the Suriname strain, human isolate sequence Z1106033 (GenBank: KU312312.1) introducing some silence mutations to eliminate restriction sites naturally present. Polyprotein ORF codifying for ZikV-NS5s were chemically synthetized (GeneArt, ThermoFisher) based on the African strain MR766 (GenBank: DQ859059) and the Asian H/PF/2013 strain (GenBank: KJ776791). This sequence was employed as a template to obtain ZikV-NS proteins ORFs by PCR using Phusion DNA polymerase (Thermo Fisher, F530S) and specific DNA primers with restriction sites and following the standard protocol provided by manufacturers.

MTDead ZikV-NS5-D146A and MultimDead Y25A/K28S/K29A punctual mutants in pCIEGO-FLAG vector were generated by PCR using pCIEGO-ZikV-NS5-FLAG vector as template and QuickChange site directed mutagenesis kit (Agilent) according to manufacturer's instructions. DNA fragments codifying for ZikV-NS5 residues ranging from 1-262 and 267-903 were obtained by PCR using the proper primers and Phusion DNA polymerase (ThermoFisher), subsequently digested with restriction enzymes, purified from agarose gel and cloned in pCIEGO-FLAG as described above.

Human Cep164 cDNA was kindly received from Pr. Eric Nigg (Graser et al., 2007) (Biozentrum, University of Basel, Switzerland) cloned into pCJW206 vector to produce a C-terminal myc tagged CEP164 protein. Full length Rootletin in pEGFP vector was purchased from Addgene. R1463 codon was replaced by stop codon to express a more soluble protein with the construct pEGFP-Rootletin (1-1462) as previously reported (Potter et al., 2017). Punctual mutagenesis was introduced using specific primers and QuickChange mutagenesis kit following the manufacturer's protocol (Agilent). BART-1 gene was kindly provided by Pr. Michael Cheetham (UCL, London). The ORF was amplified by PCR using specific primers flanked by restriction sites and Phusion DNA polymerase following the standard protocol provided by manufacturers (ThermoFisher). The DNA fragment was digested with proper enzymes, purified and cloned into previously digested pEGFP-C1 vector (Clontech) to generate pEGFP-BART-1 construct. pEGFP-C1 Emerin (637) construct was obtained from Addgene and was transfected to produce the fusion protein EGFP-Emerin (637).

pCS2_H2B-GFP was electroporated to label the nucleus. DsRedex (kindley provided by Pr. Roger Tsien, UCSD, USA) encodes DsRedexpress, a red fluorescent protein that diffuses throughout neuroepithelial cells and thereby reveals their morphology (Wang et al., 2009). CEP152-GFP (50 ng/ul: Origene), encoding a centriolar component required for centriole duplication, was electroporated to label the centrosome (Dzhindzhev et al., 2010; Saade et al., 2017). Arl13b-RFP and Arl13b-GFP (Kindly provided by Pr. Magdalena Götz, LMU, Germany), encoding the ciliary membrane component Arl13b (Caspary et al., 2007; Saade et al., 2017) (50ng/ul) was electroporated to label the primary cilia membrane. The pSox2:GFP and pTis21:RFP reporters used to assess the modes of divisions undergone by NPCs were previously described in details (Saade et al., 2013). For luciferase assays, The pSox2:luc and pTis21: RFP were derived from the pSox2:GFP and pTis21: RFP, respectively (Saade et al., 2013, 2017). The pNeuroD:luc was kindly provided by Pr. François Guillemot (The Francis Crick Institute, UK) (Castro et al., 2006). The pTubb3:luc reporter was obtained by subcloning the Tubb3 enhancer region present in the pTubb3enh:GFP plasmid (Bergsland et al., 2011) (kindly provided by Jonas Muhr, Karolinska Institute, Sweden) into the pGL3:luc vector (Promega).

### Yeast Two-Hybrid Analysis

Yeast two-hybrid screening was performed by Hybrigenics Services, S.A.S., Paris, France (http://www.hybrigenics-services.com). The coding sequence of ZikV-NS5 protein from Zika virus was PCR-amplified and cloned into pB29 as an N-terminal fusion to LexA (ZikV-NS5-LexA). The construct was checked by sequencing the entire insert and used as a bait to screen a random-primed human Fetal Brain cDNA library constructed into pP6. pB29 and pP6 derive from the original pBTM116 (Béranger et al., 1997; Vojtek and Hollenberg, 1995) and pGADGH (Bartel et al., 1993) plasmids, respectively.

99 million clones (9-fold the complexity of the library) were screened using a mating approach with YHGX13 (Y187 *ade2-101*::*loxP-kanMX-loxP*, *MAT*$\alpha$) and L40$\Delta$*Gal4* (*MAT*a) yeast strains as previously described (Fromont-Racine et al., 1997). 141 $His^+$ colonies were selected on a medium lacking tryptophan, leucine and histidine. The prey fragments of the positive clones were amplified by PCR and sequenced at their 5′ and 3′ junctions. The resulting sequences were used to identify the corresponding interacting proteins in the GenBank database (NCBI) using a fully automated procedure.

The exact codes of the algorithm used to analyze the Y2H data and to calculate the confidence score for each interaction, PBS (predicted biological score), are described in detail in the following publications (Formstecher et al., 2005; Rain et al., 2001). Briefly, the description of the confidence score, the Predicted Biological Score (PBS) relies on two different levels of analysis. First, a local score takes into account the redundancy and independency of prey fragments, as well as the distribution of reading frames and stop codons in overlapping fragments. Second, a global score takes into account the interactions found in all the screens performed at Hybrigenics using the same library. The scores were divided into four categories, from A (highest confidence) to D (lowest confidence). A fifth category (E) specifically flags interactions involving highly connected prey domains previously found several times in screens performed on libraries derived from the same organism. Finally, several of these highly connected domains have been

confirmed as false-positives of the technique and are now tagged as F. The PBS scores have been shown to positively correlate with the biological significance of interactions (Rain et al., 2001; Wojcik et al., 2002).

### Cell culture transfection and Pull-down assays

293T cells (ATCC) were cultured in 100 mm dishes (Corning) with standard cell culture conditions at 37°C in DMEM suplemented with 10% FBS (SIGMA), 1% Non-essential Amino acids (SIGMA), 1% penicilin and streptomicin (SIGMA), 0.5 μg/ml Amphotericin B (GIBCO). Plasmids containing human ZikV-NS5 interacting proteins (pEGFP-BART-1, pEGFP-Rootletin, pCJW206-CEP164 and pEGFP-Emerin) and empty pEGFP-C1 (to express GFP) vector were purified by miniprep kit (Macherey-Nagel) and were independently transfected into 293T cells in 10 mm culture dishes using Lipofectamine 2000 reagent (Invitrogen) following manufacturer's instructions. 48 hs post transfection cells were washed twice with PBS, harvested and centrifuged at 1500 rpm for 5 min. The cellular pellets were individually re-suspended in 1 mL lysis buffer (20 mM Tris pH8, 120 mM NaCl, 1% Triton X-100, 0.05% SDS, 10% glycerol) supplemented with protease inhibitors (Complete Mini EDTA Free, Roche). Cell extracts were clarified by centrifugation at 13.000 rpm for 10 min. Recombinant purified c-terminal His tagged ZikV-NS5 protein (Ferrero et al., 2019) (5 μg) was added to each supernatant tube and incubated for 4 hs at 4°C. 10 μL of His-trap TALON resin (Takara) was added to each tube and incubated for additional 2 hs. Resin was pull-down by centrifugation at 1500 rpm at 4°C during 5 min and washed twice with lysis buffer and 1 mM imidazole. Proteins were finally eluted washing TALON resin with 500 mM imidazole in PBS. Comparative pull-down assay between WT ZikV-NS5 and MultimDead Y25A/K28S/K29A mutant was performed identically using 2.5 μg of each protein.

For Pull-down assays of endogenous proteins, hNPC were cultured in 100 mm dishes, harvested, centrifuged and cell pellet stored in dry ice. The cellular pellets from 2 dishes were re-suspended in 600 μl lysis buffer (20 mM Tris pH8, 120 mM NaCl, 1% Triton X-100, 0.05% SDS, 10% glycerol) supplemented with protease inhibitors (Complete Mini EDTA Free, Roche). Cell extracts were clarified by centrifugation at 13.000 rpm for 10 min. Supernatant was recovered and equally divided in two Eppendorf. Recombinant purified c-terminal His tagged ZikV-NS5 protein (Ferrero et al., 2019) (5 μg) was added only to one supernatant tube and incubated for 4 hs at 4°C. After that, 10 μL of His-trap TALON resin (Takara) was added to each tube and incubated for additional 2 hs. Resin was pull-down by centrifugation at 1500 rpm at 4°C during 5 min and washed twice with lysis buffer and 1 mM imidazole. Proteins were finally eluted washing TALON resin with 500 mM imidazole in PBS.

### Western Blot

Proteins from pull down eluted samples were separated in a 10% SDS-PAGE and transferred onto nitrocellulose membranes (Amersham) by wet electroblotting (50V, 150 mA, ON) in 25 mM Tris-HCl pH 8.3, 192 mM glycine, 20% (v:v) methanol buffer. Membranes were blocked with 5% non-fat milk in PBST (0.5% Tween 20 in PBS) during 2 hours at RT, followed by incubation with primary antibody anti-GFP (Saade et al., 2017), or anti-His (QIAGEN) during 1 hours at RT in blocking buffer, two washes with PBST and a final incubation with secondary antibody anti-Mouse IgG-HRP, diluted 1:2000 (Thermo Fisher Scientific). Immunoreactive signals were detected with ECL kit (BIO-RAD) and visualized by Odyssey Fc imaging system (LI-COR). Western Blot quantifications were performed using ImageJ/ Fiji softwares.

Western Blot from pull down of endogenous hNPC proteins, were performed identically. The primary antibodies diluted in blocking buffer were anti-Cep164 (1:500, provided by Dr. Cyaran Morisson-NUI), anti-Rootletin (1:1000,Abcam) and anti-Bart (1:2000, provided by Richard Khan-EMORY). Secondary antibody was replaced for anti-Rabbit-HRP antibody (1:2000) for Rootletin and BART detection.

### Immunohistochemistry and microscopy

Human tissues were fixed in 4% PFA or Bouins solution overnight, paraffin embedded and sectioned following standard procedures. For markers of cortical layers and ZikV-NS5 stainings, heat-induced antigen retrieval was performed in 10 mM sodium citrate buffer (pH 6) at 95°C for 20 min after deparafination, as described before (Retallack et al., 2016). Chick embryos were fixed in 4% PFA for 2 h at 4°C, and immunostaining was performed on vibratome sections (40 μm) following standard procedures. For centrosome staining, Chick embryos were fixed in pre-chilled (−20°C) 100% methanol overnight at −20°C. For *en-face* imaging, the neural tube of (HH16-18) chick embryos was open sagittally (dorsoventrally) at the lumen along the ventricle. Notochord and somites were discarded to allow a better whole mounting of the neural tube. After washing in PBS-0.1% Triton, the sections were incubated overnight at 4C with the appropriate primary antibodies diluted in a solution of PBS-0.1% Triton supplemented with 10% bovine serum albumin or sheep serum. After washing in PBS-0.1% Triton, sections were incubated for 2 hr at room temperature with the appropriate secondary antibodies diluted in a solution of PBS-0.1% Triton supplemented with 10% bovine serum albumin or sheep serum. Alexa488-, Alexa555- and Alexa633- antibodies were obtained from Thermo Fisher Scientific. Sections were finally stained with 1 μg/ml DAPI (Sigma) and mounted in Mowiol (Sigma). Images were acquired at room temperature on a Zeiss LSM780 confocal microscope system using 25 × (Plan-Apochromat 25x/0.8 Imm Korr DIC), 40 × (Plan-Apochromat 40x/1.3 Oil DIC M27) or 63 × (Plan-Apochromat 63x/1.4 Oil DIC M27) lenses. Human sections were acquired using the Thunder Imager 3D Live Cell from Leica microsystems, equipped with the objectives Plan Fluotar 10x/0.32, Plan Fluotar 25x/0.8 MultiImmersion and Plan-Apochromat 100x/1.4 Oil. Human forebrain coronal sections, cortical and ependymal layers were built with mosaic merge using the Thunder Imager. Tiled images were digitally stitched by Leica LAS X software (Leica) to generate full scan images shown. For image processing and data analysis,

we used the ImageJ /FIJI. Three-dimensional (3D) reconstruction of whole neuroepithelial cells from an *en-face* view were built from z stacks using the Volocity v.6.2 software (PerkinElmer). This software was also used to 3D reconstruct NP mitotic cells and the multi-centrosome/cilia of human ependymal cells.

### Flow cytometry

Chicken embryos were recovered 24 hr after co-electroporation of the pSox2:eGFP and pTis21:RFP reporters together with the indicated encoding plasmids. Cell suspensions were obtained from pools of 6–8 dissected neural tubes after digestion with Trypsin-EDTA (Sigma) for 10–15 min, and further processed on a FACS Aria III cell sorter (BD Biosciences) for measurement of eGFP and RFP fluorescences. At least 5000 cells for each progenitor population (PP, PN and NN) were analyzed per sample.

### Luciferase reporter assay

The activity of pTis21, pNeuroD, Tubb3enh, and pSox2 were assessed in the neural tube using the corresponding Luciferase vectors. Reporters were co-electroporated with a Renilla luciferase reporter construct carrying the cytomegalovirus immediate early enhancer promoter for normalization (Promega). NTs obtained at 24 hpe were processed following the Dual Luciferase Reporter Assay protocol (Promega), as described previously (Saade et al., 2013). The data are presented as the mean ± s.e.m. from 6-8 embryos per experimental condition (biological replicates).

### Quantification of ciliary length

In NPCs, primary cilia length was assessed from Arl13b and polyglutamylated tubulin signals. Pictures were taken at the confocal microscope and the maximum intensity projection in the z axis (0.5 μm spaced optical sections) was used for the measurement of cilia length and assessment of morphology using ImageJ /Fiji software. Arl13b signal was used to measure the length of the cilia in μm from the cilia tip to the basal body as stained with FOP antibody (provided by Dr. Olivier Rosnet, IBDM). Since microtubules constitute the core structure of primary cilia, the fluorescence average pixel intensity of tubulin polyglutamylation (Enzo Life Sciences) has been measured. To measure the length of multicilia in human forebrain ependymal cells, we used the 3D Live Cell Thunder Imager that allowed for fast and precise multidimensional image acquisition of a large (~2.5 mm) ependymal layer that faces the ganglionic eminence in coronal sections; a Plan-Apochromat 100x/1.4 Oil lens was used to avoid resolution loss. The whole area of interest was acquired as a mosaic of Z stacks (0.5 μm spacing). The image dataset was first Z-projected, using as criterion the maximum intensity of acetylated-tubulin signal (Sigma), and then merged to a single mosaic image. The length and positioning of the multiciliated patches was measured along the ependymal cell layer using the following macro (https://github.com/MolecularImagingPlatformIBMB/MeasureMultiCilia).

### Measurement of fluorescence intensities and area

All measurements of fluorescent intensities were carried out using ImageJ/ FIJI softwares. The fluorescence average pixel intensity of CEP164 and Rootletin was measured at the centrosome level ($FOP^+$) in electroporated NPCs showing a cilia base localization of ZikV-NS5 and ciliopathy ($Arl13b^+$). For controls, the fluorescence average pixel intensity of centrosomal CEP164 and Rootletin was measured in the surrounding electroporated NPCs where ZikV-NS5 is not localized in the cilia base and where the cilia structure is normal. The fluorescence average pixel intensity of BART was measured at the centrosome level in *en-face* view of NPCs showing a ZikV-NS5 centrosomal localization. The control was defined by measuring the fluorescence average pixel intensity of centrosomal BART in the apical area of the non-transfected close neighbor cells. BART distribution in the apical cell border and Rootletin linking the rootlet fiber were excluded from these quantifications. Centrosomal proteins mean intensity were measured in the sum projection of the 6 z stacks encompassing CEP164, Rootletin and BART stainings (0.5 μm spaced optical sections). In human ependymal cells, the fluorescence average pixel intensity of CEP164 and Pericentrin (Abcam,) was measured and presented as a ratio. N-cadherin staining was used to define the size of apical area. The apical area ratio was obtained by dividing the apical area of an electroporated NPC by the mean apical area of four of its non-electroporated neighbor cells (spaced by one cell row from the electroporated cell). To characterize the differentiation state of NPCs according to the subcellular localization of the ZikV-NS5, the level of electroporation was first defined by measuring the mean intensity of ZikV-NS5-flag or the control vector H2B-GFP in the nucleus. NPCs with the same level of electroporation (same nuclear mean intensity of FLAG or GFP staining) were considered for pTis21-RFP quantification. In human forebrain, the average number of cells positive for Tbr1 (Abcam), Satb2

(Abcam,), ROR (R and D Systems,) and Ctip2 (Abcam,) per field and along the apico-basal axis was counted using ImageJ/ FIJI softwares ImageJ.

### Apical foot length measurement

For cell 3D reconstruction from *en-face* neural tube, electroporated NPCs showing apical endfoot restriction (ratio of apical area < 0.5 μm) have been acquired with a z stack encompassing ~70 μm for the control dsRedex staining from the most apical endfoot to the nucleus (0.5 μm spaced optical sections). ZikV-$NS5^+$ NPCs have been acquired with a z stack encompassing ZikV-NS5 distribution from the most apical endfoot to the nucleus with a ranging from 6 to 36 μm. 3D reconstructions were built from z stacks using the Volocity v.6.2 software (PerkinElmer) and ImageJ/Fiji softwares. The reconstruction and measurement of the apical foot length was performed using the Simple Neural Tracer framework from ImageJ (Frangi et al., 1998; Longair et al., 2011; Pool et al., 2008).

Briefly, a semi-automatic tracing was performed from the endfoot to the nucleus through 3D image stacks taking into consideration the tube-like structure of the apical foot. Details of the traces were exported as CSV and SWC files for a 3D Python plotting (7.04) using the Matplotlib library (Python).

### GO Analysis

The ZikV-NS5 target proteins were *in silico* analyzed to identify protein-protein interactions experimentally reported among them using the Agile Protein Interactomes DataServer (APID) (Alonso-López et al., 2016). Moreover, in order to identify the main cell compartments where ZikV-NS5 belongs, a Gene Ontology (GO) analysis was performed using the Protein ANalysis THrough Evolutionary Relationships (PANTHER) classification system version 14.0 (Mi et al., 2013).

### Sequence alignments

Human Cep164, Rootletin and BART protein sequences were obtained from Sanger sequenced constructs that are identical to Genebank:NP_055771.4, NP_055490.4, AAH03087.1 sequences, respectively. Chicken (Gallus gallus) CEP164, Rootletin and BART-1 protein sequences were obtained from NCBI (Genebank : XP_024999041.1, XP_015152501.1, NP_001007971.1, respectively). Protein sequences alignments were performed using Clustal Omega program (Madeira et al., 2019) and colored using ESPript 3.0 program (Robert and Gouet, 2014). For CEP164 and Rootletin, only ZikV-NS5 interacting domain sequences identified by Y2H assay were employed for sequence alignment.

### ZikV-NS5 Structure Cartoons

ZikV-NS5 structure cartoons were generated by Chimera software (UCSF Chimera), a visualization system for exploratory research and analysis (Pettersen et al., 2004) using the crystal structure coordinates deposited at PDB (PDB: 6I7P) and specifically colored to enhance protein features like domains or residues.

## QUANTIFICATION AND STATISTICAL ANALYSIS

No statistical method was used to predetermine sample size. The experiments were not randomized. The investigators were not blinded to allocation during experiments or outcome assessment. Statistical analyses were performed using the GraphPad Prism 8.0.2 software (GraphPad Software, Inc.). For apical foot length measurement, Kernel density plots have been applied to represent the dataset distribution corresponding to the ratio of the apical area versus the apical foot length of electroporated NPCs

Quantitative data are expressed as mean ± sem or mean ± stdev except for violin plots that present median with quartile range. The n values are indicated in figures or the corresponding legends. The normal distribution of the values was assessed by the Shapiro-Wilk normality test. Significance was then assessed with a two-sided unpaired t test, one-way ANOVA + Tukey's test or two-way ANOVA + Sidak's or +Dunnettś test for data presenting a normal distribution, or alternatively with non-parametric Mann–Whitney or Kruskal-Wallis +Dunn's multiple comparisons' tests for non-normally distributed data. n.s: non-significant; *$p < 0.05$ or less, as indicated in individual figures.

# Appendix 3

Article

Developmental Cell

# Cell intercalation driven by SMAD3 underlies secondary neural tube formation

## Graphical abstract

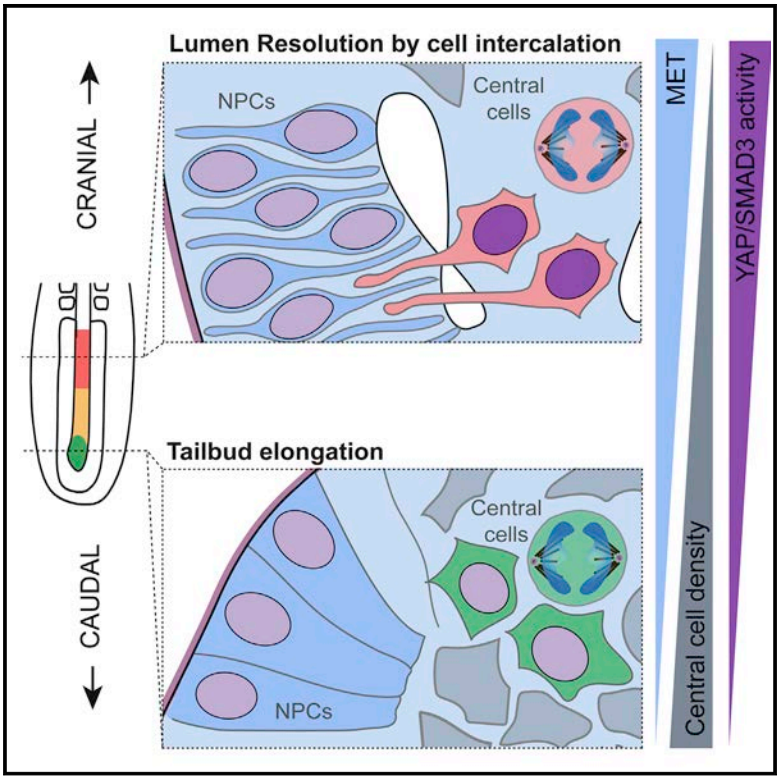


## Authors

Elena Gonzalez-Gobartt, José Blanco-Ameijeiras, Susana Usieto, Guillaume Allio, Bertrand Benazeraf, Elisa Martí

## Correspondence

emgbmc@ibmb.csic.es

## In brief

Gonzalez-Gobartt et al. show, during secondary neural tube formation, that the resolution of a single continuous lumen requires the intercalation of central cells, under the control of the TGF-β signaling effector SMAD3. These findings have implications toward understanding the development of caudal skin-covered neural tube defects.

## Highlights

- Lumen initiation follows the acquisition of neural identity and epithelial polarization
- Programmed cell death does not correlate with lumen resolution
- SMAD3 regulates the motility of central intercalating cells
- Resolution of a single central lumen requires SMAD3/YAP-mediated cell intercalation

Gonzalez-Gobartt et al., 2021, Developmental Cell *56*, 1147–1163
April 19, 2021 
https://doi.org/10.1016/j.devcel.2021.03.023

CellPress

Developmental Cell

CellPress

Article

# Cell intercalation driven by SMAD3 underlies secondary neural tube formation

Elena Gonzalez-Gobartt,[1] José Blanco-Ameijeiras,[1] Susana Usieto,[1] Guillaume Allio,[2] Bertrand Benazeraf,[2] and Elisa Martí[1,3,*]

[1]Instituto de Biología Molecular de Barcelona, CSIC, Parc Científic de Barcelona, C/Baldiri i Reixac 20, Barcelona 08028, Spain
[2]Centre de Biologie du Développement (CBD), Centre de Biologie Intégrative (CBI), Université de Toulouse, CNRS, UPS, Toulouse, France
[3]Lead contact
*Correspondence: emgbmc@ibmb.csic.es
https://doi.org/10.1016/j.devcel.2021.03.023

## SUMMARY

Body axis elongation is a hallmark of the vertebrate embryo, involving the architectural remodeling of the tail bud. Although it is clear how neuromesodermal progenitors (NMPs) contribute to embryo elongation, the dynamic events that lead to *de novo* lumen formation and that culminate in the formation of a 3-dimensional, neural tube from NMPs, are poorly understood. Here, we used *in vivo* imaging of the chicken embryo to show that cell intercalation downstream of TGF-β/SMAD3 signaling is required for secondary neural tube formation. Our analysis describes the events in embryo elongation including lineage restriction, the epithelial-to-mesenchymal transition of NMPs, and the initiation of lumen formation. We show that the resolution of a single, centrally positioned lumen, which occurs through the intercalation of central cells, requires SMAD3/Yes-associated protein (YAP) activity. We anticipate that these findings will be relevant to understand caudal, skin-covered neural tube defects, among the most frequent birth defects detected in humans.

## INTRODUCTION

A proliferative cell population at the posterior end of the vertebrate embryo, known as neuromesodermal progenitors (NMPs), sustained body axis elongation in vertebrates (Cambray and Wilson, 2007; Tzouanacou et al., 2009; Henrique et al., 2015). These cells produce both the neural tissue that makes up the caudal spinal cord and mesodermal tissues like muscle and bone (Kölliker, 1884; Cambray and Wilson, 2007; McGrew et al., 2008; Henrique et al., 2015). NMPs can be generated *in vitro* from human pluripotent stem cells (Gouti et al., 2014). This advance has not only allowed the regulatory gene networks that determined NMP fate specification and lineage restriction to be deciphered (Gouti et al., 2017; Metzis et al., 2018), but it has also provided a new experimental paradigm to study the cellular and molecular basis of caudal spinal cord generation. However, despite their relevance to understand caudal skin-covered neural tube defects (NTDs) (Saitsu and Shiota, 2008; Greene and Copp, 2014; Morris et al., 2016), the signaling pathways and cellular events required to shape the secondary neural tube (SNT) from NMPs are poorly understood.

Morphogenesis of the SNT involves the mesenchymal-to-epithelial transition (MET) of NMPs, which is concomitant to the lineage restriction and the confinement of these cells within a medullary cord, surrounded by a growing basement membrane (BM). The subsequent cavitation of this cord is required to form the SNT (Griffith et al., 1992; Catala et al., 1995; Colas and Schoenwolf, 2001; Shimokita and Takahashi, 2011).

Here, we have used the chick embryo to examine the signaling pathways that control the cellular rearrangements shaping the SNT. We found transforming growth factor β (TGF-β) signaling to be active during SNT formation. We show that the initial events in SNT formation, involving the lineage restriction of NMPs, the MET, and full epithelialization of caudal neural progenitor cells appear to be largely independent of SMAD3 activity. However, establishing a single, centrally positioned continuous lumen occurs through the intercalation of central cells and this requires a SMAD3/Yes-associated protein (YAP) signaling module. Together, we describe here an activity for TGF-β/SMAD3 that may be relevant to the development of human caudal skin-covered NTDs.

## RESULTS

### SNT formation in the chick embryo requires TGF-β-mediated Smad3 activity

During vertebrate development, NMPs are recruited to elongate the caudal body axis and to drive the elongation of the neural tube (NT). These bipotential cells will generate neural progenitor cells (NPCs) of the caudal medullary cord by undergoing a MET, forming the SNT. The process is completed by the formation of a lumen in the medullary cord, and it can be followed along the rostro-caudal axis of a HH15 chick embryo (Hamburger and Hamilton, 1951), 50–55 h post-fertilization (Figures 1A–1E). The first cells to epithelialize are confined to the periphery of the medullary cord, while the central cells remain mesenchymal until the

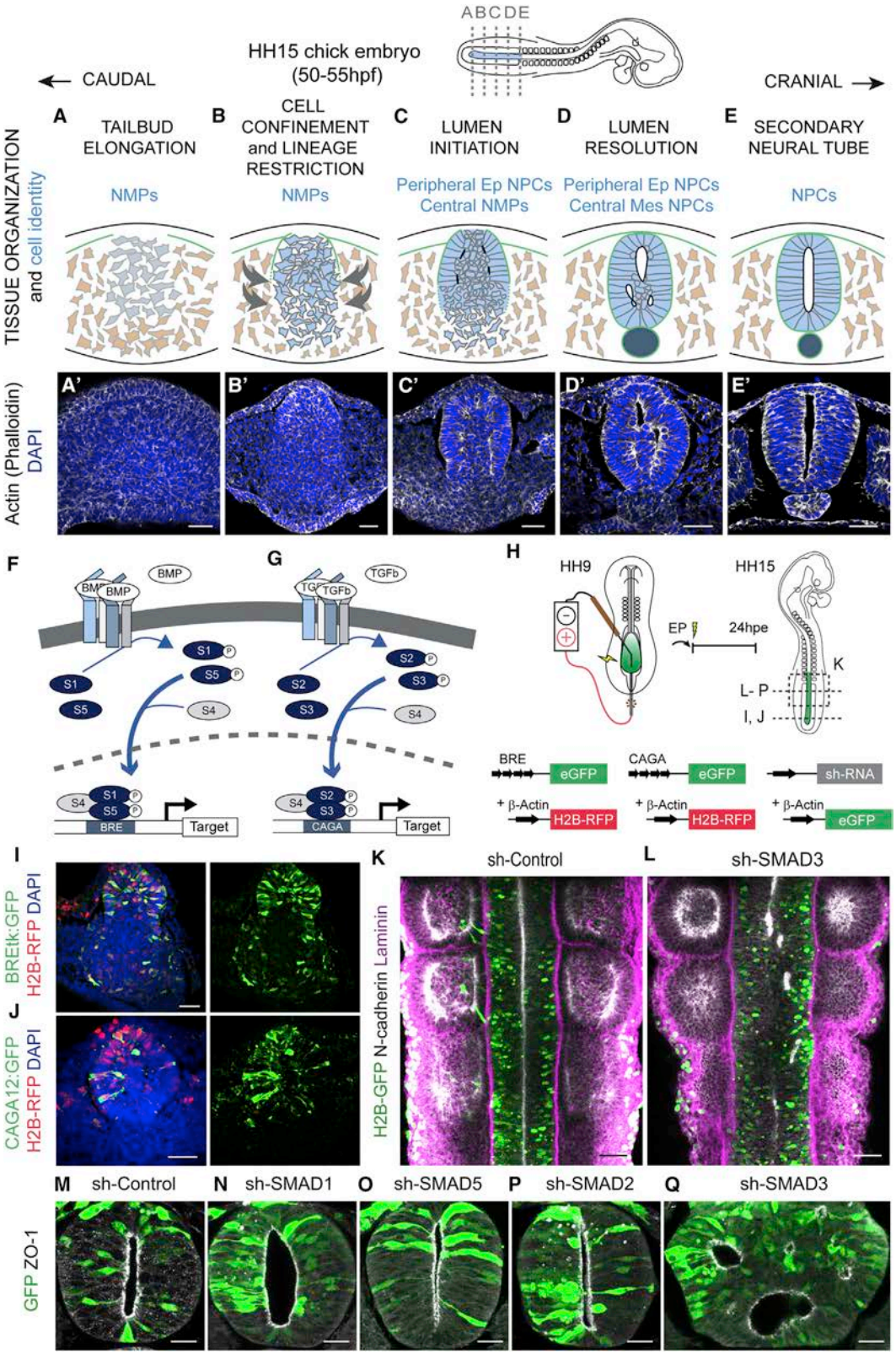


**Figure 1. SNT formation in the chick embryos requires TGF-β-mediated SMAD3 activity**

(A–E) Scheme showing a stage-HH15 chick embryo, and the cellular processes occurring along the caudal to rostral axis during secondary neural tube (SNT) formation: (A) Taildbud elongation, (B) Cell confinement and lineage restriction, (C) Lumen initiation, (D) Lumen resolution, and the fully formed (E) secondary neural tube. SNT cells are shown in light blue, the mesoderm is in brown and the notochord appears in dark blue.

*(legend continued on next page)*

very end of the process. Small cavities of varied size form between these two cell populations, later resolving to form a single central lumen (Figures 1A′–1E′) (Schoenwolf and Delongo, 1980; Schoenwolf and Kelley, 1980).

Members of the WNT and FGF signaling pathways play relevant roles in the control of NMP growth and maintenance and their differentiation into neural or mesodermal lineages (Turner et al., 2014), although very little is known about signals that instruct the 3D shaping of the caudal NT. Here we analyzed the expression of ligands of the main developmental pathways in the tail bud of stage HH15 chick embryos. Whole-mount *in situ* hybridization and transverse sections through these same embryos revealed that the expression of BMP2 and TGF-β1 may potentially be associated with SNT formation (Figures S1A–S1L). Interestingly, the TGF-β/BMP pathways are known to play key roles in rostral NT formation (reviewed in Le Dréau and Martí, 2012; Ulloa and Briscoe, 2007), yet their roles in SNT formation are less well understood. Canonical TGF-β/BMP signaling is in general linear, with ligands binding to a defined receptor complex composed of two transmembrane serine/threonine kinases that in turn propagate the signal through the SMAD family of transcription factors (Figures 1F and 1G). *In situ* hybridization experiments to study the distribution of *SMAD* mRNA revealed strong SMAD3 expression in polarizing NMPs at the dorsal periphery of the cord, later spreading to the entire developing SNT (Figures S2A–S2I).

We next assessed the endogenous activity of the TGF-β/BMP pathways *in vivo* by electroporating a BMP (BRE:eGFP: Le Dréau et al., 2014, 2012) or a TGF-β-responsive (CAGA12-GFP; Míguez et al., 2013) fluorescent reporter construct, together with a control H2B-RFP vector (Figure 1H). Both the TGF-β and BMP pathways were active in the elongating chick embryo tail bud at 24 h post-electroporation (hpe) (Figures 1I, 1J, and S3A). Electroporation of the TGF-β-responsive CAGA12:GFP fluorescent reporter that is specific to SMAD3 activity (Míguez et al., 2013), together with the control H2B-RFP vector, showed strong activity in the caudal and SNT region at 24 hpe, whereas control H2B-RFP+ cells were found along the whole rostro-caudal axis (Figure S3A).

To test the contribution of canonical TGF-β/BMP signaling to SNT formation, we analyzed the consequence of SMAD inhibition through the electroporation of short-hairpin (sh)RNA targeting specific chick *SMAD* transcripts. BMP signaling appeared to be dispensable for the correct morphogenesis of the SNT, since inhibition of SMAD1/5 resulted in the formation of a normal SNT (Figures 1M–1O). Similarly, while electroporation of sh-SMAD2 efficiently inhibited endogenous SMAD2 expression (Míguez et al., 2013), it was insufficient to perturb SNT formation (Figure 1P). However, inhibition of the TGF-β effector SMAD3 produced an aberrant SNT that contained multiple small lumens distributed along the rostro-caudal (Figures 1K and 1L) and the dorsoventral axes (Figure 1Q). While sh-SMAD3 electroporation efficiently diminished the endogenous SMAD3 (Figures S3B and S3C), it did not compromise either tissue or NMP viability, as assessed by the rate of apoptosis and of cell proliferation of the SMAD3 deficient or the sh-Control cells (Figures S3D–S3H). Moreover, 24 hpe of a dominant-negative form of SMAD3 (SMAD3S/A; García-Campmany and Martí 2007) resulted in a multi-lumen phenotype (Figure S3I). This aberrant SNT was specifically rescued by co-electroporation of a dominant active form of SMAD3 (SMAD3S/D; García-Campmany and Martí 2007) together with the sh-SMAD3 (Figure S3I). These observations indicated that inhibition of SMAD3 produced an aberrant SNT and prompted us to search for the precise cellular events regulated by TGF-β/SMAD3 signaling that might drive SNT formation.

## Confinement of NMPs and lineage restriction to NPCs are independent of SMAD3 activity

Co-expression of the T/Brachyury (T/BRA) and SOX2 transcription factors characterizes NMPs, while NPCs emerging from dual-fated NMPs downregulate T/Bra but maintain strong SOX2 expression (Kondoh and Takemoto, 2012; Olivera-Martinez et al., 2012; Gouti et al., 2014; Tsakiridis and Wilson, 2015; Wymeersch et al., 2016). Complete neural lineage restriction can be followed in stage HH15 chick embryos by analyzing T/BRA$^+$ and SOX2$^+$ expression at different axial levels, from the posterior elongating tail bud to the level of the last formed somite (Figures 2A–2E). At initial stages, T/Bra was expressed widely in the tail bud, even in the lateral mesoderm that was excluded from the quantifications here. Later in development, T/BRA was downregulated along the SN axis and finally, it became restricted to the notochord (Figures 2A′–2E′). Weak SOX2 expression initially appeared in the dorsal and central areas of the early tail bud (Figure 2A″), and this propagated ventrally (Figure 2B″) before eventually becoming confined to the NT (Figure 2E″). Hence, the differentiation of NPCs in the medullary cord apparently advances in a dorsoventral direction.

Quantification of endogenous T/BRA and SOX2 within the region undergoing secondary neurulation not only revealed a strong reduction in T/BRA as this axis is established (median ± IQR $\log_{10}$ of T/BRA corrected total cell fluorescence (CTCF) axis elongation = 3.6 ± 0.2; cell confinement = 3.3 ± 0.5; lumen initiation = 3.0 ± 0.3; lumen resolution = 2.3 ± 0.4;

(A′–E′) Transverse sections at different rostro-caudal levels showing the distribution of actin (white), with DAPI (blue) staining the cell nuclei. Scale bars, 40 μm. NMPs, neuromesodermal progenitors; NPCs, neural progenitors; Ep, epithelial; Mes, mesenchymal.

(F and G) Scheme summarizing the BMP and TGF-β signaling components. Once phosphorylated, R-SMADs form a trimeric complex with SMAD4 (S4), consisting of two R-SMADs molecules and one SMAD4. This complex binds to BMP-responsive elements (BREs) or TGF-β-responsive elements (CAGA) found in target genes promoters and modulate the expression of target genes.

(H) Scheme showing the method and timing of chick embryo electroporation, and the DNA constructs used. HH, Hamburger & Hamilton stage; EP, electroporation; hpe, hours post-electroporation.

(I) The BMP reporter is active in NMPs 24 hpe of BRE:GFP (green) and control H2B-RFP (red). DAPI (blue) stains the nuclei. Scale bar, 40 μm.

(J) The TGF-β reporter is active in NMPs 24 hpe of CAGA12:GFP (green) and control H2B-RFP (red). DAPI (blue) stains the nuclei. Scale bar, 40 μm.

(K and L) Dorsal views of sh-Control H2B-GFP (green) or sh-SMAD3 (green) electroporated NTs. N-cadherin (white) lines the NT lumen and laminin (pink) stains the basement membrane and somites. Scale bars, 40 μm.

(M–Q) Selected images of transverse sections 24 hpe of the indicated DNAs (green), ZO-1 staining (white) lines the NT lumen. Electroporation of sh-SMAD3 results in multiple lumens (L). Scale bar, 20 μm.

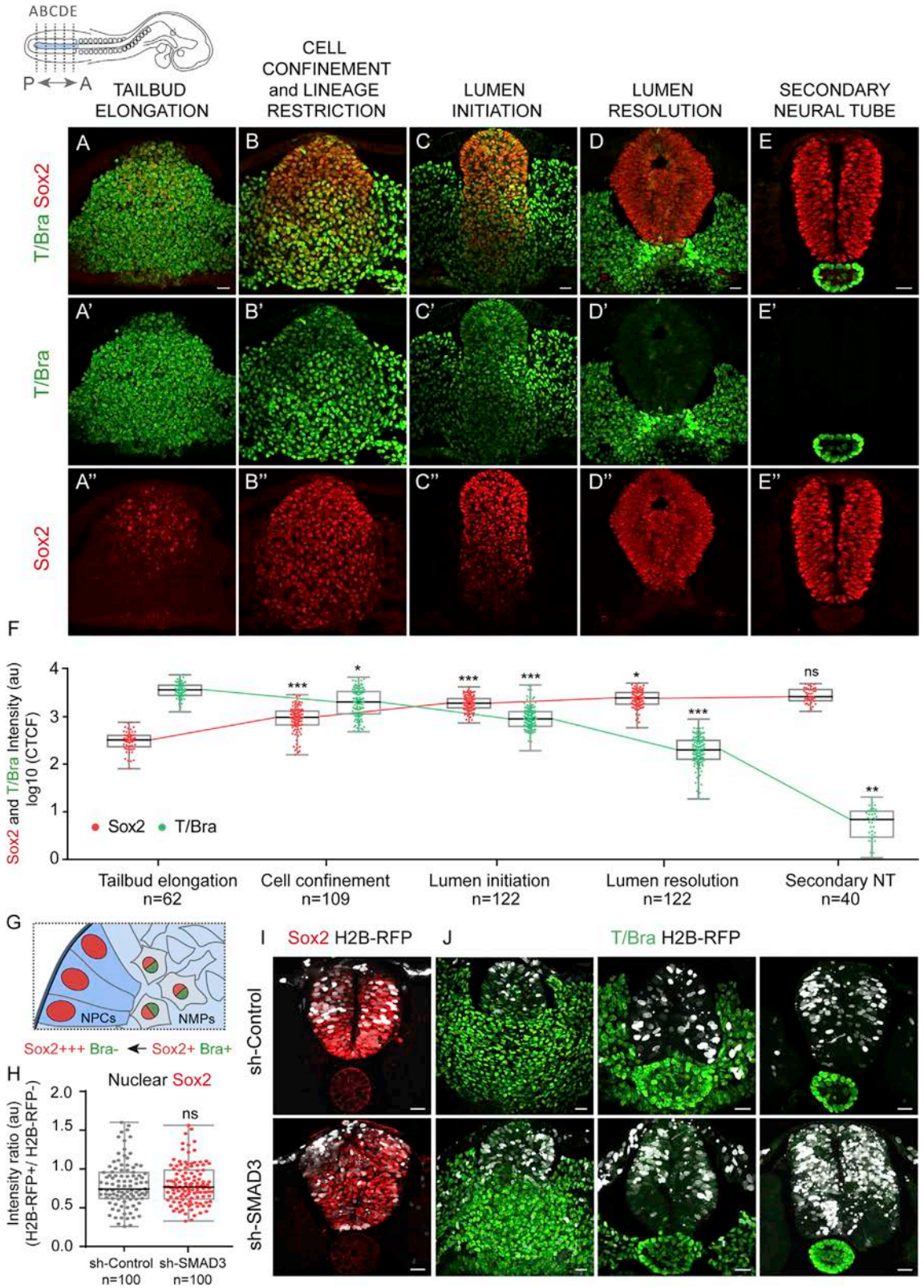


**Figure 2. Confinement of NMPs and lineage restriction into NPCs are both independent of SMAD3 activity**

(A–E) Selected images of transverse sections stained for T/Bra (green) and Sox2 (red) at the level of: (A) Taildbud elongation, (B) Cell confinement and lineage restriction, (C) Lumen initiation, (D) Lumen resolution, and the fully formed (E) secondary neural tube. Scale bars, 20 μm.

*(legend continued on next page)*

SNT = 0.8 ± 0.5: Figure 2F) but also an increase in SOX2 (median ± IQR $log_{10}$ of SOX2 CTCF axis elongation = 2.5 ± 0.2; cell confinement = 3.0 ± 0.3; lumen initiation = 3.3 ± 0.2; lumen resolution = 3.4 ± 0.2; SNT = 3.4 ± 0.2: Figure 2F), coincident with the progressive generation of NPCs. The expression of T/BRA and SOX2 shifted gradually as the SNT developed, suggesting the existence of a transitional state in the path from NMPs to NPCs. We also found a positive correlation between T/BRA expression and the distance from the BM and conversely, a negative correlation between SOX2 expression and its distance from the BM (Figures S4A and S4B). Moreover, during cell confinement, lumen initiation and lumen resolution, SOX2 was more strongly expressed by peripheral cells than central cells (Figure S4C). Conversely, T/BRA expression was stronger in central cells than in peripheral cells (Figure S4D). In summary, bipotential NMPs convert into NPCs by downregulating T/BRA and upregulating SOX2, which occurs concomitantly with cell confinement by the BM (Figure 2G).

To test the possible role of canonical TGF-β signaling in NMP lineage restriction, we further examined T/BRA and SOX2 expression 24 hpe of the sh-SMAD3 construct (Figures 2H–2J). T/BRA expression was normally downregulated by NMPs electroporated with sh-SMAD3, although it was still expressed strongly by the surrounding lateral mesoderm cells, as well as by the axial notochord cells (Figure 2J). The expression of SOX2 in NPCs electroporated with sh-SMAD3 was comparable with that in the surrounding non-electroporated cells (median ± IQR SOX2 intensity ratio sh-Control = 0.7 ± 0.3 versus sh-SMAD3 = 0.8 ± 0.4; Figures 2H and 2I), and these $SOX2^+$ cells became progressively restricted to the SNT (Figure S4E). These observations indicate that SMAD3 activity is largely dispensable for the initial cell confinement and neural lineage restriction events.

## Lumen initiation occurs at a one-cell distance from the BM, and it is independent of SMAD3 activity

Concomitant with the neural lineage restriction of NMPs, these cells epithelialize as the SNT undergoes morphogenesis, a process that can be traced along the rostro-caudal axis of stage-HH15 chick embryos. The first cells to acquire epithelial polarity are those in contact with the forming BM, those located dorsally and at the periphery of the cord (Figures 3A–3D), and those undergoing epithelialization similar to that of MDCK cells growing in 3D culture (Martín-Belmonte et al., 2008; Bryant et al., 2014) and in the early mouse embryo (Bedzhov and Zernicka-Goetz, 2014).

To characterize the subcellular events that accompany NMP epithelialization, we analyzed cell shape, the centrosome position, the Golgi distribution, and the distribution of polarized proteins at the early stages of the MET (Figures 3E–3L and S5A–S5D). During MET in the SNT, the shape of the cells shifted from polygonal to elongated (median ± IQR circularity central cells = 0.8 ± 0.1 versus peripheral cells = 0.3 ± 0.2), concomitant with a basal translocation of the nucleus (Figures 3E–3I). The perinuclear centrosome relocated apically, as witnessed by its distance of the $FOP^+$ labeled centrosomes (Yan et al., 2006) from the nucleus (median ± IQR distance central cells = 0.9 ± 0.5 μm versus peripheral cells = 9.7 ± 10.3 μm: Figures 3E and 3J). The wide variation in the peripheral cell centrosome-to-nucleus distance is related to the onset of interkinetic nuclear migration, which separates or brings together the centrosome and the nucleus depending on the phase of the cell cycle. In addition, the Golgi elongated and became confined to the apical cellular process (median ± IQR distance central cells = 3.3 ± 1.6 μm versus peripheral cells = 9.9 ± 6.8 μm: Figures 3F and 3K), as determined by labeling with the *cis*-Golgi matrix protein GM130 (Nakamura et al., 1995) and as observed for NPCs in the developing cerebral cortex (Taverna et al., 2016). Finally, cell epithelialization involves the reorganization of the apical membrane into discrete microdomains where N-cadherin and the ZO-1/occludin complex occupy internal positions, whereas aPKC concentrates in the most apical domain (Aaku-Saraste et al., 1996; Chenn et al., 1998; Afonso and Henrique, 2006; Marthiens and Ffrench-Constant, 2009). Indeed, apical proteins such as N-cadherin or ZO-1 accumulated at the apical pole of the cell (Figures 3G, 3H, and 3L). To establish the sequence of apical polarization and the possible correlation with lumen initiation, we analyzed the subcellular localization of FOP, N-cadherin, and aPKC during the initial stages of MET (Figures S5E–S5M). While all the cells analyzed already had an apically localized centrosome, several also presented apical N-cadherin and a few accumulated apical aPKC. Neither N-cadherin nor aPKC were distributed apically prior to apical centrosome positioning and similarly, apical aPKC was never detected prior to the apical accumulation of N-cadherin (Figures S5E–S5I). Moreover, co-staining of FOP, N-cadherin, and ZO-1 revealed that N-cadherin and ZO-1 co-localized apically at the same time, and again, never before FOP appeared apically (Figures S5E–S5I). Finally, in peripheral cells β1-integrin was distributed basal before FOP accumulated apically, and no cells were found with only one of these two elements apicobasally polarized, which suggests that apical and basal polarity is organized concomitantly (Figures S5H and S5J). In summary, we found that the subcellular events that lead to apicobasal polarization of NPCs are sequential, whereby apical centrosome positioning and basal β1-integrin localization is followed by N-cadherin/ZO-1 apical membrane accumulation, and finally, the apical membrane localization of aPKC (Figure 3L).

(F) Plots nuclear fluorescence intensity of T/Bra and Sox2 during the indicated tissue remodeling events (horizontal bold lines show the median cell number from 10 embryos: n = 62, 109, 122, 122, 40): *p < 0.05, **p < 0.01, ***p < 0.001 Kruskal-Wallis test.

(G) Scheme showing the developing SNT and lineage restriction of NMPs into NPCs. Cells contacting the basement membrane (purple) are the first to downregulate T/Bra and upregulate Sox2.

(H) Plots ratio of Sox2 fluorescence intensity in sh-Control and sh-SMAD3-electroporated cells (bold horizontal lines show the median; n = 100, 100 cells from 10 embryos/condition): p > 0.05 Mann-Whitney test.

(I) Selected transverse sections of sh-Control and sh-SMAD3 electroporated cells (white) showing the SNT stained for Sox2 (red). Scale bars, 20 μm.

(J) Selected transverse sections of sh-Control and sh-SMAD3 electroporated cells (white) showing the developing SNT stained for T/Bra (green). Scale bars, 20 μm.

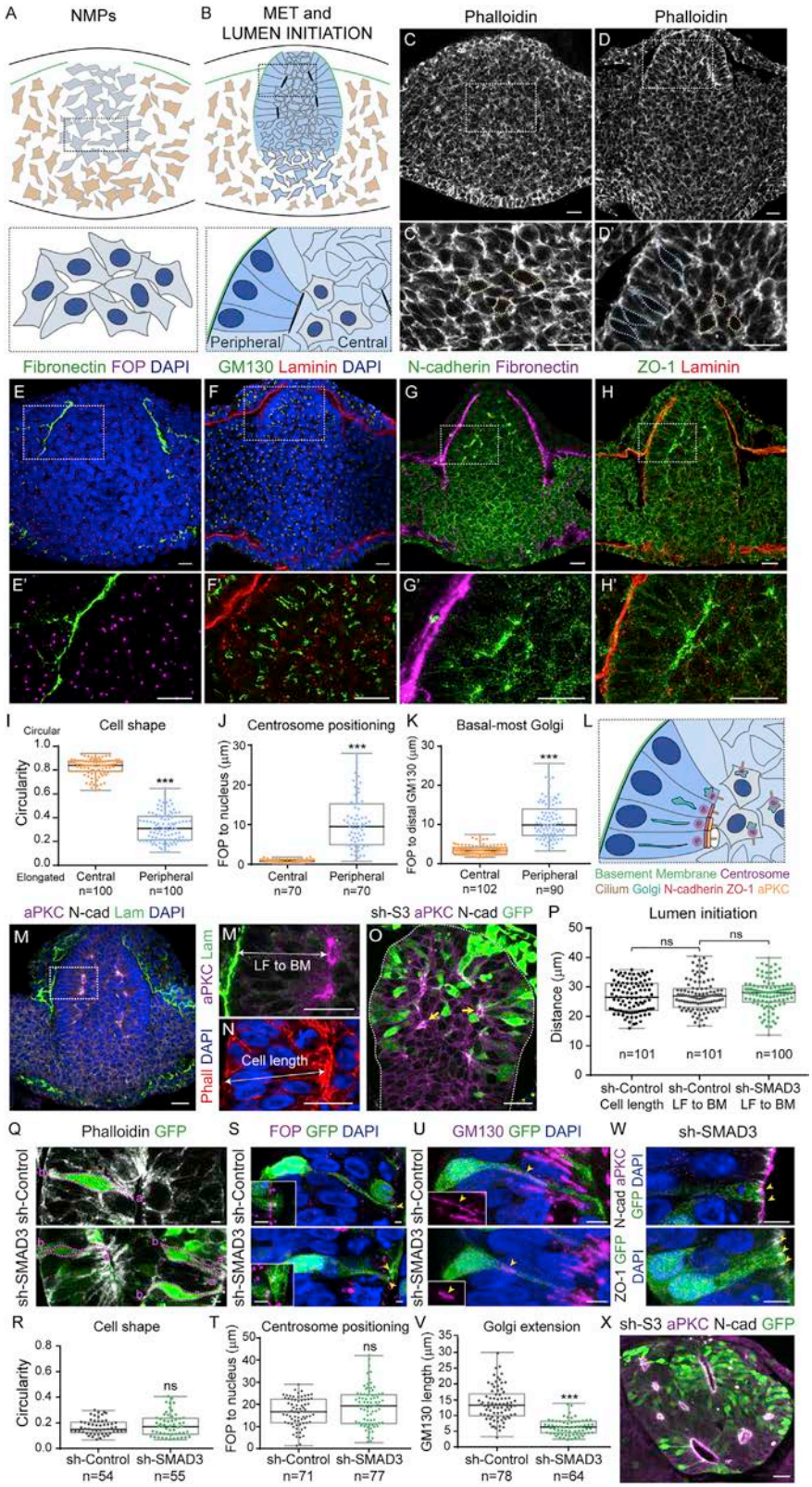


**Figure 3. Lumen initiation occurs at an equivalent distance of one cell from the basement membrane, and it is independent of SMAD3 activity**

(A and B) Schemes representing the cellular processes occurring during MET of the NMPs (MET, mesenchymal-to-epithelial transition; NMPs, neuromesodermal progenitors).

*(legend continued on next page)*

As NMPs transformed into fully epithelialized NPCs, we observed multiple small lumens emerging at the interface between the peripheral epithelial and central mesenchymal cell populations (Figures 3L and 3M). These small lumens always formed at a distance equivalent to one cell from the BM (median ± IQR cell length = 26.5 ± 9.2 μm versus lumen foci [LF] to BM distance = 26.8 ± 6.4 μm: Figures 3M–3P). We tested whether canonical TGF-β signaling might be required to trigger MET and to initiate lumen formation. At 24 hpe, sh-SMAD3 cells correctly restricted N-cadherin and aPKC to their apical pole, and multiple small lumens were established at one-cell distance from the BM (median ± IQR LF to BM distance sh-Control = 26.8 ± 6.4 μm versus sh-SMAD3 = 28.0 ± 5.5 μm: Figure 3P). Hence, SMAD3 activity appears to be dispensable for the subcellular processes involved in triggering the MET and in the initial formation of LF, which prompted us to search for defects in late stages of MET and SNT lumen resolution.

We tested whether canonical TGF-β signaling might be implicated in the final NPC epithelialization. To this end, we analyzed cell shape, centrosome positioning, Golgi elongation, and polar protein distribution in sh-SMAD3 electroporated cells in the SNT at the rostro-caudal levels where the morphogenesis of the neighboring somites and underlying notochord had been completed. At 24 hpe, sh-SMAD3 cells of the SNT had properly elongated (median ± IQR circularity sh-Control = 0.1 ± 0.1 versus sh-SMAD3 = 0.2 ± 0.1: Figures 3Q and 3R), and their centrosomes were situated apically, similar to sh-Control electroporated cells (median ± IQR FOP to nucleus distance sh-Control = 16.6 ± 10.6 μm versus sh-SMAD3 = 19.3 ± 13.0 μm: Figures 3S and 3T). Although sh-SMAD3 electroporated cells failed to elongate their Golgi apparatus (median ± IQR GM130 length sh-Control = 13.3 ± 6.9 μm versus sh-SMAD3 = 6.3 ± 3.7 μm: Figures 3U and 3V), these cells establish apical membrane microdomains containing N-cadherin, ZO-1, and aPKC like sh-Control electroporated cells (Figure 3W). Although, apicobasal polarity is correctly organized in NPCs, sh-SMAD3-electroporated embryos developed multiple lumens in the SNT, in which initial small lumens formed correctly, but they failed to coalesce into a single central cavity (Figure 3X). Together, these results indicated that SMAD3 activity was largely dispensable for the subcellular processes involved in cell epithelialization, yet it appeared to be required to establish a centrally positioned single lumen during SNT formation.

## SMAD3 activity is required for cell intercalation and the resolution of a single central lumen in the SNT

Formation of a single and continuous lumen in the SNT requires distinct cellular rearrangements and 3D tissue remodeling. 3D images of the lumen from ZO-1 *in-toto*-immunostained HH15 chick embryos were generated by Imaris reconstruction (Figures 4A–4F) to analyze their size and shape. Accordingly, the small caudal focal lumens were seen to first coalesce into three enlarged lumens (one dorsal-central and two ventral-lateral), which finally fused into a single central cavity in the more rostral domains (Figures 4A–4F; Videos S1 and S2). We also found a population of cells that remained in between the lumens until they finally coalesced. Lumen resolution therefore required the clearance of this central cell population to generate a SNT

(C and D) Selected images of transverse sections stained for actin (white). Higher magnifications of the boxed regions are shown in (C′ and D′) and the dotted lines in (D′) define the central (orange) and peripheral (blue) cell shapes. Scale bars, 20 μm.
(E–H) Selected images of transverse sections showing: (E, E') Fibronectin and FOP staining. (F, F') GM130 and Laminin staining, (G, G') N-cadherin and Fibronectin staining, and (H, H') ZO-1 and Laminin staining. A higher magnification of the boxed regions is shown in (E′–H′). Scale bars, 20 μm.
(I) Circularity plots of central and peripheral cord cells (bold horizontal lines show the median; n = 100, 100 cells from 10 embryos): ***p < 0.001 Mann-Whitney test.
(J) Plots the distance from centrosomes (FOP staining) to the nucleus (DAPI) in central and peripheral cord cells (bold horizontal lines show the median; n = 70, 70 cells from 10 embryos): ***p < 0.001 Mann-Whitney test.
(K) Plots the distance from centrosomes (FOP staining) to the basal-most part of the Golgi apparatus (distal GM130) in central and peripheral cord cells (bold horizontal lines show the median; n = 102 and 90 cells from 10 embryos): ***p < 0.001 Mann-Whitney test.
(L) Scheme of the progressive epithelialization of NPCs from mesenchymal NMPs. The centrosome is the first organelle to be apically localized, followed by the Golgi apparatus and N-cadherin/ZO-1, and finally aPKC. The BM (green) confines the cells undergoing epithelialization.
(M) Selected transverse section at the stage of lumen initiation stained for aPKC (green), N-cadherin (red) and laminin (purple). A higher magnification of the boxed region appears in (M′) to show the distance from LF to the BM. Scale bars, 20 μm.
(N) Selected transverse section at the lumen initiation stage where cell length is visualized by actin (red) and nuclear (DAPI, blue) staining. Scale bar, 20 μm.
(O) Selected image of transverse sections 24 hpe of sh-SMAD3 electroporation (green) at the lumen initiation stage, showing N-cadherin (white) and aPKC distribution (purple). Yellow arrows indicate two LF. Scale bar, 20 μm.
(P) Plots cell length and distance from LF to the BM in sh-Control and sh-SMAD3 embryos at the lumen initiation stage (bold horizontal lines show the median; n = 101, 101, and 100 cells from 10 embryos/condition): p > 0.05 Kruskal-Wallis test.
(Q) Selected images of 24 hpe sh-Control and sh-SMAD3 electroporated cells (green) showing the actin cytoskeleton (white). Dotted pink lines delineate the cell shape, and the apical (A) and basal (B) surfaces are indicated for each cell. Scale bars, 5 μm.
(R) Plots cell shape/circularity in 24 hpe sh-Control and sh-SMAD3 electroporated embryos (bold horizontal lines show the median; n = 54 and 55 cells from 10 embryos/condition): p > 0.05 Mann-Whitney test.
(S) Selected images of 24-hpe sh-Control and sh-SMAD3-electroporated cells (green) showing the apically localized centrosomes (purple; yellow arrows). Higher magnifications are shown bottom left. Scale bars, 2.5 μm.
(T) Plots the distance from the apical FOP to the nucleus in 24-hpe sh-Control and sh-SMAD3-electroporated embryos (bold horizontal lines show the median; n = 71 and 77 cells from 10 embryos/condition); p > 0.05, Mann-Whitney test.
(U) Selected images of 24 hpe sh-Control and sh-SMAD3 electroporated cells (green) showing the *cis*-Golgi organization (purple; yellow arrows). Scale bars, 5 μm.
(V) Plots of Golgi extension determined by GM130 staining of 24-hpe sh-Control and sh-SMAD3-electroporated embryos (bold horizontal lines show the median; n = 71 and 77 cells from 10 embryos/condition); ***p < 0.001, Mann-Whitney test.
(W) Selected images of sh-SMAD3 electroporated cells (green) stained for the indicated apical polarity proteins (yellow arrows). Scale bars, 5 μm.
(X) Selected image of transverse sections 24 hpe of sh-SMAD3 (green). N-cadherin (white) and aPKC (purple) line the small multiple lumens apically. Scale bar, 20 μm.

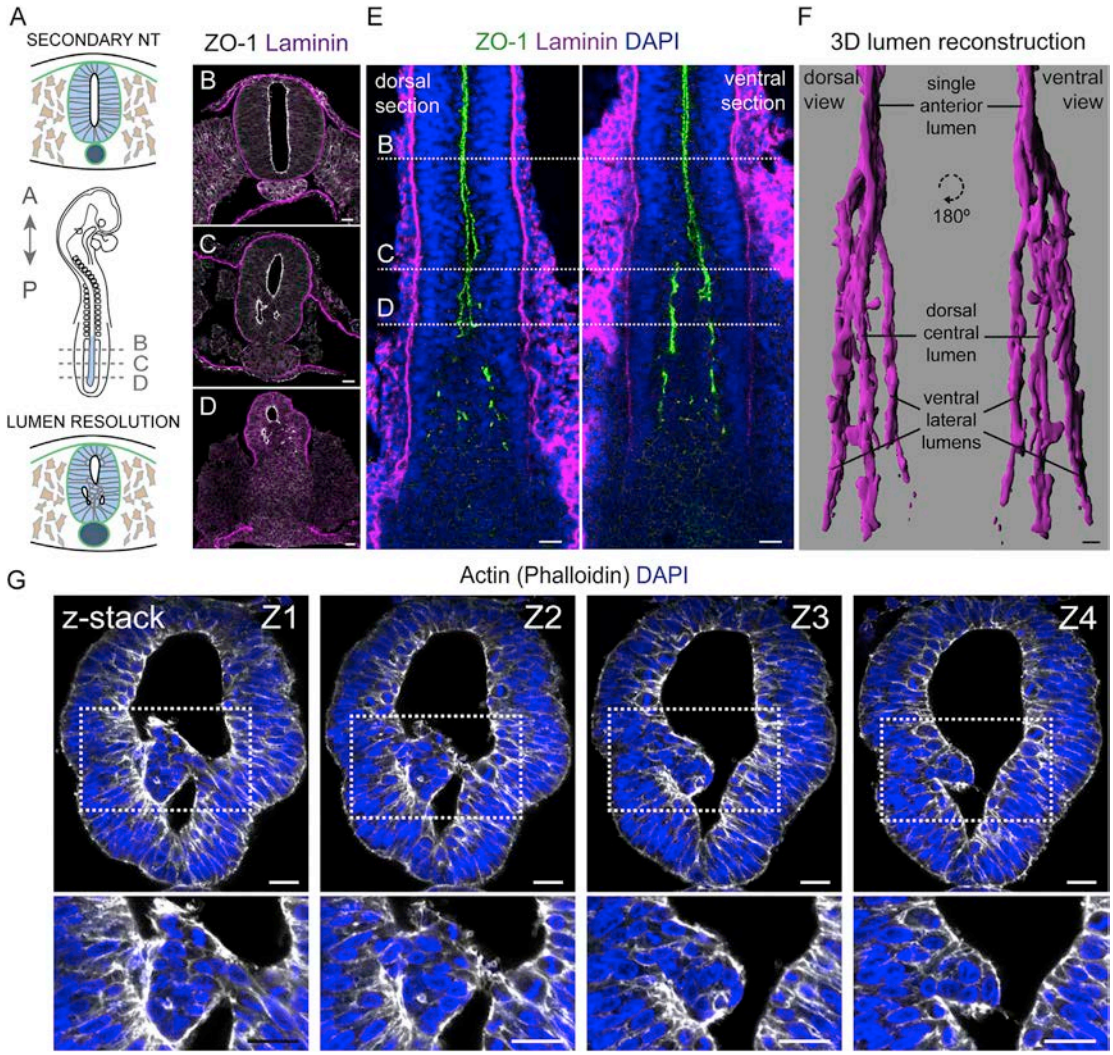


**Figure 4. SMAD3 activity is required for cell intercalation and the resolution of a single central lumen in the *SNT***

(A) Drawing of a stage HH15 chick embryo and the cellular processes that occur during secondary lumen resolution to give rise to a SNT with a single central lumen.

(B–D) Selected transverse sections at (B) rostral, (C) medial, and (D) caudal levels in (A), showing the localization of the apical protein ZO-1 (white) and the BM (laminin, purple). Scale bars, 20 μm.

(E) Dorsal views at two different dorsoventral levels of the SN region of a stage HH15 chick embryo stained for ZO-1 (green) and laminin (purple). DAPI (blue) stains cell nuclei and the dotted lines show the rostro-caudal levels in (B–D). Scale bars, 20 μm.

(F) Dorsal and ventral views of 3D reconstructions of the secondary lumen in a stage-HH15 chick embryo. The single rostral lumen caudally splits into one dorsal-central lumen and two ventral-lateral lumens (n = 5 embryos). Scale bar, 20 μm.

(G) Consecutive sections of a transverse z stack (Z1–Z4) at the lumen resolution phase with the actin (white) and nuclei (DAPI, blue) stained. Higher magnifications of the boxed regions are shown in Z1′–Z4′. The inner mass of central cells initially contacts the two lateral walls of the neuroepithelium (yellow arrows in Z1′). Eventually, it detaches from the right side of the SNT (yellow arrows in Z2′ and Z3′), and cells move toward the left to intercalate (orange arrows in Z3′ and Z4′). Scale bars, 20 μm.

composed of NPCs arranged around a single central cavity (Figures S6A–S6L).

The analysis of these central cells revealed that even though they had already lost T/Bra expression (Figures S6A and S6B) and were therefore referred to as central NPCs, they retained certain mesenchymal characteristics. Central NPCs remained round at a point when peripheral NPCs at that stage of lumen resolution had already lost their circularity and were heading toward full elongation in the formed SNT (Figures S6C and S6F). The centrosome of these central NPCs remained close to their nucleus (Figures S6D, S6E, and S6G), and they retained a pericentrosomal Golgi apparatus (Figures S6D, S6E, and S6H). Some apical polarity components were detected, although not organized as in the peripheral NPCs (Figure S6E).

Resolution into a single continuous lumen in the SNT requires the clearance of the central mesenchymal NPCs. To test whether cell death is implicated in this lumen resolution, cleaved caspase-3 and TUNEL staining was performed on stage-HH15

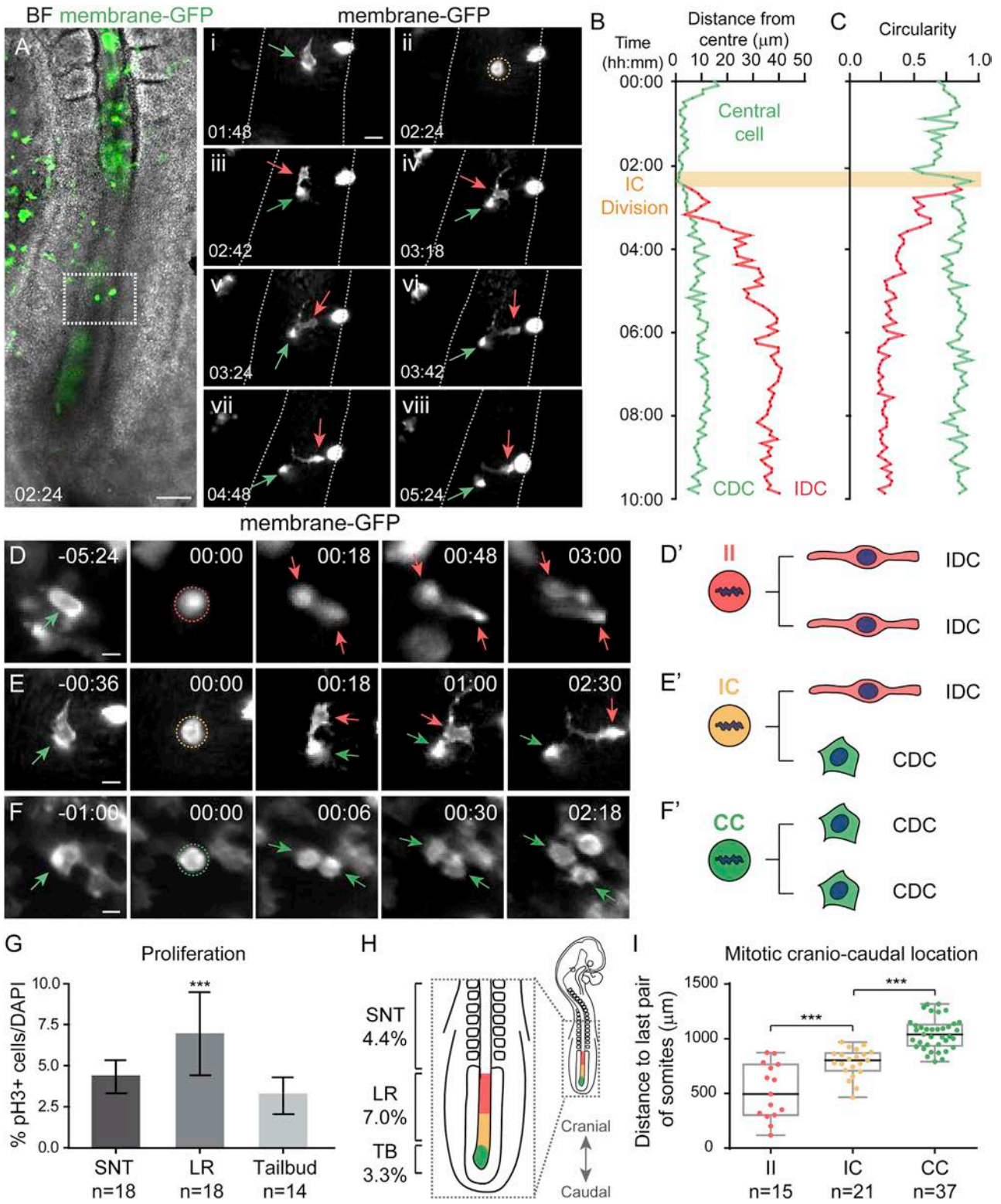


**Figure 5. Three different outcomes after cell division coexist in the central intercalating cells of the developing *SNT*, but at different rostro-caudal levels**

(A) Selected frames of membrane-GFP-electroporated embryos time-lapse movies showing a representative mitosis. A central mesenchymal cell (Ai, green arrow) divides (Aii, orange dotted circle) and generates one IDC (Aiii–Aviii, red arrow) and one CDC (Aiii–Aviii, green arrow). Scale bars, 100 and 20 μm.

*(legend continued on next page)*

chick embryo sections at various rostro-caudal levels. While a variable number of apoptotic cells were detected in the dorsal NT and dorsal non-neural ectoderm, such cells were almost virtually absent from the forming SNT, or even from the inner cell mass surrounded by forming lumens, indicating that cell death does not contribute to lumen resolution in the SNT (Figures S6M–S6O). However, the population of centrally located NPCs appeared to intercalate among the epithelialized NPCs of the developing SNT, as observed in transverse sections in which actin was stained with phalloidin (Figure 4G). Interestingly, this process of lumen resolution by cell intercalation appeared to require SMAD3 activity, since at 24 hpe, sh-SMAD3 electroporation led to the formation of centrally located NPCs at lumen resolution stages that did not undergo apoptosis and die (Figures S6M–S6O).

To directly test this hypothesis, we electroporated stage HH9 chick embryos to analyze the process *in vivo*, which were later cultured and imaged under an upright wide-field microscope. This system allows chick embryos to elongate and to develop at the approximate same rate as they do *in ovo* (Bénazéraf et al., 2010; Gonzalez-Gobartt et al., 2021; Rupp et al., 2003). It also permits fluorescently labeled electroporated cells in the elongating SNT to be tracked over time. These cells are highly motile, with a high rate of cell division, and they undergo important cell mixing. Analysis of membrane-GFP-electroporated cells revealed round mesenchymal cells situated centrally in the elongating SNT (green arrows in Figure 5Ai and first time point in Figures 5D–5F). We consistently observed central cell intercalation into the lateral walls of the neuroepithelium, perceived as a lateral cell movement away from the center of the tissue, and this was accompanied by an elongation of the cells (Figures 5A–5C and S7A–S7C; Video S3). Notably, intercalating cells were highly protrusive (Figures 5D–5F), and their intercalation always occurred just after cell division (dotted circles in Figures 5D–5F). Indeed, the proportion of mitotic cells in fixed sections of stage HH15 embryos was significantly higher in the area where the single lumen is resolving than in the formed SNT or the caudal tail bud (mean ± SD% pH3 cells SNT = 4.4 ± 1.0 μm versus lumen resolution [LR] = 7.0 ± 2.5 μm versus tail bud = 3.3 ± 1.1 μm; Figure 5G).

We quantified the distance of central mitotic membrane-GFP$^+$ cells from the center, their circularity, and rostro-caudal location (relative to the last pair of somites formed) over time and that of their daughter cells. The outcome of central cell division varied along the rostro-caudal axis (Figures 5D–5F). At the rostral SNT (median ± IQR distance to the last pair of somites = 494.8 ± 464.0 μm), central cells divided before both daughter cells elongated and migrated laterally to intercalate among the epithelialized NPCs (Figures 5D, 5H, and 5I; Video S4). We referred to this mode of division as II, as it produced two intercalating daughter cells (IDCs; Figure 5D′). This process resembles the stereotyped cell divisions named c-divisions occurring during zebrafish NT formation, in which NPCs located on one side of the embryo contribute to descendant daughter cells lying on the two sides of the forming NT (Tawk et al., 2007). However, cell tracking experiments showed that central cells intercalation occur at either one or the two sides of the forming SNT randomly. In the intermediate regions (median ± IQR distance to the last pair of somites = 803.2 ± 163.2 μm), central cells division resulted in one daughter cell remaining mesenchymal and centrally located, while the other cell elongated and migrated laterally to intercalate among epithelialized NPCs forming the SNT (Figures 5E, 5H, and 5I; Video S3). We termed this mode of division as IC, as it gave rise to one IDC and a central daughter cell (CDC; Figure 5E′). At the caudal tail bud (median ± IQR distance to the last pair of somites = 1,040.0 ± 193.1 μm) central mesenchymal cells divided, such that both daughter cells remain round and centrally located (Figures 5F, 5H, 5I, and S7D–S7F; Video S5). We termed this mode of division as CC, as it generates two central cells (Figure 5F′).

To test whether canonical TGF-β signaling influenced cell intercalation and LR during SNT formation, stage HH9 chick embryos were electroporated with a sh-SMAD3 or sh-Control SOX2p:GFP vector (Uchikawa et al., 2003; Saade et al., 2013) to track the fluorescently labeled cells over time (Figures 6A–6D, S7G, and S7H). Each of the three different outcome of cell division were evident at the corresponding rostro-caudal levels in SOX2p:GFP sh-Control embryos (median ± IQR distance to the last pair of somites sh-Control II = 732 ± 378.8 μm, IC = 843 ± 123 μm, CC = 1,008 ± 163 μm: Figure 6E) and daughter cells intercalated normally (Figures S7J, S7K, S7G, and S7H; Video S6). Although sh-SMAD3 electroporated central cells divided in a similar ratio as the sh-Control electroporated cells (Figures S3G and S3H), most divisions generated two cells that remained centrally located in sh-SMAD3 electroporated embryos. These daughter cells failed to intercalate into the lateral epithelialized SNT (Figures 6A–6E; Videos S7 and S8), regardless of their rostro-caudal location (median ± IQR distance to the last pair of somites sh-SMAD3 IC = 718.8 ± 503.5 μm, CC = 831.9 ± 445.8 μm; Figure 6E). Faulty cell intercalation in sh-

(B) Distance from the center of the cells in (D) during the time-lapse movie (10 h). One daughter cell remains in the center (green) while the other moves away and intercalates into the lateral wall of the SNT (red).

(C) Circularity of the cells in (D) during the time-lapse movie (10 h). One daughter cell maintains the high circularity of the mother cell (green) while the other elongates (red).

(D–F) Selected frames of time-lapse movies of membrane-GFP-electroporated embryos showing representative mitosis and the different outcomes after cell division. The parental central cell (green arrow) generates two IDCs (red arrows) in (A); one CDC (green arrow) and one IDC (red arrow) in (B); and two CDCs (green arrows) in (C). Scale bars, 10 μm.

(D′–F′) Schemes of the three different outcomes of central cell division that coexist during SNT formation.

(G) Plots of the mitotic pH3$^+$ cells once SNT is formed, in the lumen resolution stage (LR) and in the early elongating tail bud (TB) (mean ± SD, n = 18, 18, and 14 sections from 10 embryos): $^{**}p < 0.01$,$^{***}p < 0.001$ one-way ANOVA.

(H) Scheme of a stage-HH15 chick embryo showing a higher magnification of its caudal region. The mean mitotic indexes in (D) are indicated for each region (left). The approximate rostro-caudal location of each mode of division is also shown (II, red; IC, yellow; CC, green).

(I) Plots of the rostro-caudal distribution of each of the three different outcomes of central cell division, represented as the distance of each division to the last formed pair of somites (bold horizontal lines show the median; n = 15, 21, and 37 divisions from 13 time-lapse movies): $^{***}p < 0.001$ one-way ANOVA.

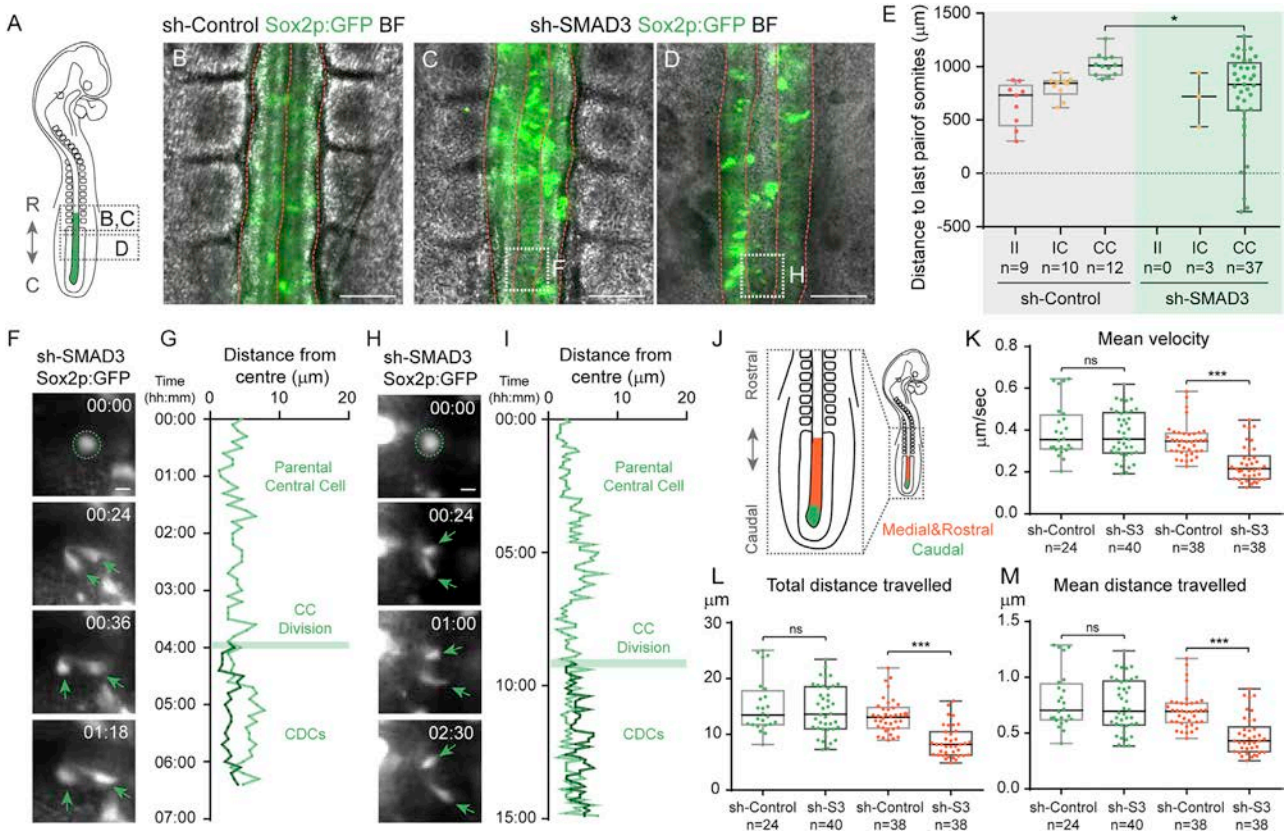


**Figure 6. sh-SMAD3 electroporated cells fail to intercalate into the lateral walls of the forming *SNT***

(A) Drawing of an electroporated HH15 chick embryo showing the rostro-caudal levels of (B–D).

(B) Selected frame of time-lapse movies of sh-Control Sox2p:GFP-electroporated embryos at the rostro-caudal level indicated in (A). Red dotted lines define the apicobasal surfaces of the SNT. Scale bar, 100 μm.

(C and D) Selected frames of time-lapse movies of sh-SMAD3 Sox2p:GFP-electroporated embryos at the rostro-caudal levels indicated in (A). Red dotted lines define the apicobasal surfaces of the SNT. Note the abnormal accumulation of cells in the center of the SNT. Frames are the last time points of the mitotic sequences in (F and H), as indicated by the boxed regions. Scale bars, 100 μm.

(E) Plots of the rostro-caudal distribution of each of the three different outcomes of central cell division, as the distance to the last formed pair of somites in both Sox2p:GFP+sh-Control and sh-SMAD3 electroporated embryos. Almost all sh-SMAD3 divisions generate two CDCs (CC divisions) regardless of the rostro-caudal position (bold horizontal lines show the median; n = 9/10/12 divisions from 5 Sox2p:GFP sh-Control and n = 0/3/37 divisions from 6 sh-SMAD3 time-lapse movies): *p < 0.05 Kruskal-Wallis test.

(F and H) Selected frames of sh-SMAD3 Sox2p:GFP movies showing two different cell divisions at the rostro-caudal positions indicated in (C and D). The dotted circles indicate the mitosis (CC divisions, green), the green arrows point to CDCs. Scale bars, 10 μm.

(G and I) Plots cell distance from the center along the time-lapse movie of sh-SMAD3 Sox2p:GFP cells in (F and H). All daughter cells remain close to the center (both dark and light green). CDC, central daughter cell.

(J) Schematic drawing of a stage HH15 chick embryo showing a higher magnification of its caudal region. The approximate rostro-caudal location for each of the tracked cells is also shown (green, caudal; orange, medial/rostral).

(K) Plots mean velocity of sh-Control and sh-SMAD3 daughter cells tracked along 20 time points after mitosis (2 h) from caudal (green) and medial/rostral (orange) locations (bold horizontal lines show the median; n = 24 and 38 divisions from 5 Sox2p:GFP sh-Control and n = 40 and 38 divisions from 6 sh-SMAD3 time-lapse movies): ***p < 0.001 Kruskal-Wallis test.

(L and M) Plots of the total distance and the mean distance traveled of sh-Control and sh-SMAD3 daughter cells tracked along 20 time points after mitosis (2 h) from caudal (green) and medial/rostral (orange) locations (bold horizontal lines show the median; n = 24 and 38 divisions from 5 Sox2p:GFP sh-Control and n = 40 and 38 divisions from 6 sh-SMAD3 time-lapse movies): ***p < 0.001 Kruskal-Wallis test.).

SMAD3-electroporated embryos resulted in the abnormal persistence of central cells at rostral levels (Figures 6C and 6D) that eventually elongated at these central positions (last time points in Figures 6F–6I).

Next, we measured daughter cell motility in sh-Control and sh-SMAD3 cells, using the SOX2p:GFP reporter for time-lapse movies, during the 2 h that followed the mitosis (Figure 6J). According to their locations, caudal central cells moved with similar speed and to comparable distances, irrespective of the loss of SMAD3 activity (mitosis at >900 μM from last pair of somites) (median ± IQR mean velocity sh-Control = 0.36 ± 0.16 μm/s versus sh-SMAD3 = 0.36 ± 0.19 μm/s; median ± IQR total distance sh-Control = 13.5 ± 6.1 μm versus sh-SMAD3 = 13.6 ± 7.5 μm; median ± IQR mean distance sh-Control = 0.71 ± 0.32 μm versus sh-SMAD3 = 0.7 ± 039 μm; Figures 6K–6M), indicating that SMAD3 activity was dispensable for tail bud

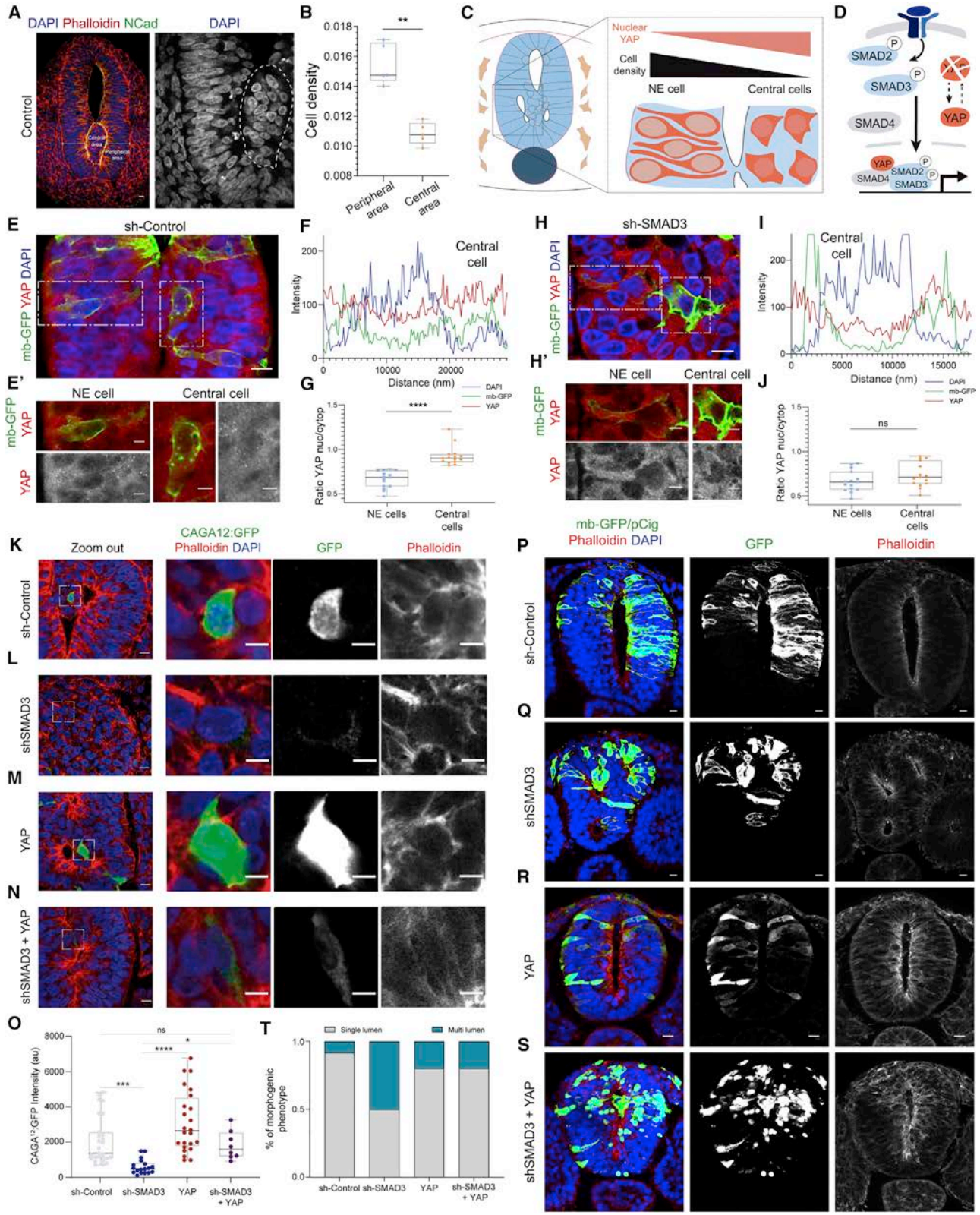


**Figure 7. SMAD/YAP interaction mediates central cells intercalation into the lateral walls of the forming *SNT***

(A) Selected section at the stage of lumen resolution stained for N-cadherin (green) and phalloidin (red). DAPI (blue) stains the cell nuclei. A higher magnification of the central region shows the area quantified in (B). Scale bars, 10 μm.

*(legend continued on next page)*

elongation. However, sh-SMAD3-electroporated medial and rostral cells (mitosis at <900 μm from last pair of somites) moved significantly slower than sh-Control cells, and to shorted distances (median ± IQR mean velocity sh-Control = 0.35 ± 0.09 μm/s versus sh-SMAD3 = 0.21 ± 0.11 μm/s; median ± IQR total distance sh-Control = 13.1 ± 3.7 μm versus sh-SMAD3 = 8.2 ± 4.2 μm; median ± IQR mean distance sh-Control = 0.69 ± 0.17 μm versus sh-SMAD3 = 0.43 ± 0.22 μm; Figures 6K–6M). Although this impaired cell motility disturbed central cells entering the neural epithelium, the reorganization of cytoskeletal structures appeared to be independent on SMAD3 activity. At 24 hpe sh-SMAD3 electroporated central cells generate membrane protrusions (Figures S7I–S7L).

Remarkably, we noted that during cell intercalation in the SNT, the density of the cells shifted from low in the central areas to high cell density in the peripheral NPCs (median ± IQR nuclei density central areas = 0.011 ± 0.001 nuclei/μm versus peripheral areas = 0.015 ± 0.003 nuclei/μm; Figures 7A and 7B). Cell density directly regulates the activity of the Hippo pathway and its downstream effector the YAP (Varelas et al., 2008, 2010; Elosegui-Artola et al., 2017; Nardone et al., 2017) (Figures 7C and 7D); hence, we next tested the endogenous YAP protein in the SNT at the rostro-caudal levels where the clearance of the central mesenchymal cells takes place. Immunostaining for the endogenous YAP protein revealed that the active YAP (nuclear/cytoplasm ratio) was high in the central intercalating cells compared with the peripheral NPCs (median ± IQR ratio YAP nuclear/cytoplasm central cells = 0.900 ± 0.088 versus peripheral cells = 0.685 ± 0.175; Figures 7E–7G). Interestingly, previous findings established that YAP can physically interact with SMAD proteins and that its activity is required for optimal SMAD transcriptional responses in several cellular contexts, including the early mouse embryo, the *Drosophila* wing imaginal disc and the progenitor cells of the developing cerebral cortex (Alarcón et al., 2009; Varelas et al., 2010; Najas et al., 2020) (Figure 7D). Our analyses show that the nuclear/cytoplasm YAP ratio was significantly reduced in sh-SMAD3-electroporated central cells, compared with the peripheral NPCs and to sh-Control central cells (median ± IQR ratio YAP nuclear/cytoplasm sh-SMAD3 central cells = 0.713 ± 0.260 versus sh-Control central cells = 0.900 ± 0.088 versus sh-SMAD3 peripheral cells = 0.656 ± 0.197; Figures 7H–7J).

Moreover, the reduction in TGF-β transcriptional responses caused by electroporation of sh-SMAD3 was significantly rescued by the co-eletroporation of a wild-type form of YAP (median ± IQR sh-Control = 1,361.0 ± 1,475.0 au versus sh-SMAD3 = 494 ± 532.8 au versus YAP = 2,617 ± 2725au versus sh-SMAD3 + YAP = 1,566 ± 1,319 au; Figures 7K–7O) indicating that YAP might participate together with SMAD3 in controlling TGF-β mediated central cell intercalation. Finally, we tested whether increasing YAP activity could compensate for the multi-lumen phenotype in SNT formation, caused by SMAD3 inhibition. *In ovo* co-electroporation of YAP was sufficient for the resolution of a single centrally positioned developing lumen and rescued the multi-lumen phenotype driven by sh-SMAD3 electroporation, generating a SNT in which the lumen is largely unique and centrally positioned (Figures 7P–7T). Altogether, our results show that a SMAD3/YAP signaling module is required for the cell intercalation driving SNT formation and that impaired cell intercalation disturbed the resolution of the developing lumen and ultimately led to NTDs involving a multi-lumen phenotype.

## DISCUSSION

In this study, we provide a description of the morphogenetic events through which the SNT is generated in the chick embryo, knowledge that will be crucial to unravel the causes of caudal NTDs, among the most common birth defects in humans. We found that the final resolution of the central NT lumen involves

(B) Plots of the cell density in peripheral versus central areas; n = 5; **p < 0.01 Mann-Whitney test.
(C) Schemes representing the processes occurring during cell intercalation into the NE (neuroeptithelial) cells. The nuclear YAP is inversely proportional to the cell density.
(D) Scheme summarizing the TGF-β signaling interaction with the YAP transcriptional co-factor. Transmembrane receptors phosphorylate transcription factors SMAD2/3 that form a complex with SMAD4. This complex binds to the transcriptional co-factor YAP to modulate the expression of target genes.
(E) Selected sections 24 hpe of sh-Control electroporation (green) at the lumen resolution stage, showing endogenous YAP (red/white) and nuclear DAPI (blue) Scale bars, 10 μm. Higher magnification of the boxed regions appeared in (E′) to show the YAP distribution (red/white) in neuroepithelial (NE) cell and in the central cells. Scale bars, 5 μm.
(F) Plots of the fluorescence intensity (AU) of red-labeled YAP relative to the blue DAPI nuclear labeling, in the sh-Control-electroporated central cell shown in (E). The green line depicts the electroporated central cell.
(G) Plots of the nuclear/cytoplasmic YAP immunostaining in peripheral neuroepithelial versus central sh-Control electroporated cells; n = 15; ****p < 0.0001, Mann-Whitney test.
(H) Selected image of transverse sections 24 hpe of sh-SMAd3 electroporation (green), showing endogenous YAP (red/white) and nuclear DAPI (blue) Scale bars, 10 μm. Higher magnification of the boxed regions appeared in (H′) to show the YAP distribution (red/white) in NE cell and in central cells. Scale bars, 5 μm.
(I) Plots of the fluorescence intensity (AU) of red-labeled YAP relative to the blue DAPI nuclear labeling, in the sh-SMAD3 electroporated central cell shown in (H). The green line depicts the electroporated central cell.
(J) Plots of the nuclear/cytoplasmic YAP immunostaining in peripheral neuroepithelial versus central sh-SMAD3 electroporated cells;; n = 15; ns p > 0.1, Mann-Whitney test.
(K–N) Selected images of transverse sections 24 hpe of the CAGA12:GFP reporter (green/white), together with sh-Control (K), sh-SMAD3 (L), YAP (M), and sh-SMAD3 + YAP (N) at the lumen resolution stage, showing phalloidin (red/white) and DAPI (blue). Scale bars, 10 μm. Higher magnification of the boxed regions appeared in (K–N) to show the GFP expression in central cells. Scale bars, 5 μm.
(O) Plots the fluorescence intensity (AU) of green labeled CAGA12:GFP in the electroporated central cells shown in (K–N); n = 15, Mann-Whitney test.
(P–S) Selected image of transverse sections 24 hpe of sh-Control (P), sh-SMAD3 (Q), YAP (R), and sh-SMAD3 + YAP (T) showing phalloidin (red) and DAPI (blue). White shows GFP the distribution of electroporated cells. Phalloidin shows the multi-lumen phenotype. Scale bars, 5 μm.
(T) Plots of the proportion of unique (gray) versus multiple (blue) lumens in the electroporated SNT. n = 27 cells from sh-control, n = 18 cells from sh-SMAD3, n = 24 cells from YAP and n = 8 cells from sh-SMAD3 + YAP; *p < 0.05, ***p < 0.001, ****p < 0.0001, Kruskal-Wallis test.

cell intercalation into the lateral walls of the neuroepithelium (Schoenwolf and Delongo, 1980). We also show that defective SMAD3 activity during the formation of the SNT leads to caudal NTDs characterized by the presence of multiple small lumens. This phenotype is not due to changes in cell viability, cell identity, lumen initiation, or apicobasal polarity disruption, but rather, it arises from a failure in central cell intercalation during LR. Finally, we found that SMAD3 activity is required for the motility of intercalating cells, through a YAP-mediated transcriptional mechanisms.

We studied the process of secondary neurulation starting from the stage when mesenchymal NMPs drive caudal body axis elongation to the complete formation of the SNT, in which epithelial NPCs surround a single central lumen. Based on our findings, we divided the morphogenesis of the SNT into three fundamental steps: (1) confinement of NMPs and neural lineage restriction, (2) MET and *de novo* formation of multiple lumens, and (3) LR into a single central cavity. SNT formation involves two related cell events, a change in cell identity from NMPs to NPCs and subsequently, the polarization of mesenchymal (front-rear) into epithelial (apicobasal) cells. Both transformations are temporarily associated with the growth of the BM. Concomitant to these cellular changes, the SNT lumen forms *de novo* in between cells, with small lumens opening up at the equivalent of a one-cell distance from the BM. The formation of these lumens is associated with the isolation of a central mesenchymal cell population. The possibility of central cell intercalation into the lateral walls of the neuroepithelium has been contemplated (Schoenwolf and Delongo, 1980), although not experimentally tested. By performing *in vivo* time-lapse imaging in electroporated chick embryos, we were able to follow central NPCs over time, showing that central cells intercalate into the lateral walls of the neuroepithelium. The result of this process is that a hollow SNT is formed, composed of epithelial NPCs encompassing a single central lumen.

The molecular signals driving SNT formation remain largely unknown. WNT and FGF signaling play important roles in the maintenance and expansion of NMPs (Yamaguchi et al., 1999; Takemoto et al., 2006; Garriock et al., 2015; Wymeersch et al., 2016), and in the induction of the mesodermal or neural lineage of NMP derivatives (Yoshikawa et al., 1997; Diez del Corral et al., 2002; Martin and Kimelman, 2012; Nowotschin et al., 2012; Gouti et al., 2017). Here, we show that both TGF-β and BMP signaling pathways are active during SNT formation, supporting the results obtained from our analysis of gene expression. Depletion of TGF-β SMAD3 but not SMAD2 generates an NTD characterized by a multi-lumen phenotype. We cannot completely rule out a role for BMP in this process, as the negative results obtained with BMP sh-SMAD electroporation could reflect a requirement for the inhibition of the BMP pathway for the SNT to form. The different outcomes following the inhibition of two TGF-β SMADs might reside in the fact that SMAD3 and SMAD2 can either co-operate or antagonize each other to regulate their transcriptional targets (Míguez et al., 2013). Phosphorylated R-SMAD proteins form heterotrimeric complexes with SMAD4 that enter the nucleus, where they recruit various co-factors and bind to DNA in order to regulate target gene expression (Moustakas et al., 2001; Moustakas and Heldin, 2002; Shi and Massagué, 2003; Brown et al., 2007). We found that the TGF-β pathway is active, and SMAD3 is expressed strongly by central cells at the stage of LR. We hypothesize that TGF-β signaling, through SMAD3, could replace the lost T/BRA activity in central NPCs and ensure that they retain their mesenchymal features. The mesenchymal capacities retained confer high cell motility and invasive properties to central cells, permitting their intercalation into the lateral walls of the developing neuroepithelium. Indeed, TGF-β activity controls actin polymerization and actomyosin contractility during lumen expansion in the *Ciona intestinalis* notochord (Denker et al., 2015). Both actin polymerization and actomyosin contractility are essential for mesenchymal cell migration (Ridley et al., 2003; Chi et al., 2014). However, here, we found that central intercalating cells maintain their capability to generate cell protrusions regardless of the loss of SMAD3, pointing toward the implication of canonical transcriptional responses.

Among the transcriptional co-factors that directly interact with SMAD proteins are the Yes-associated proteins (YAP/TAZ), components of the Hippo pathway, the main censors of cell density (Piccolo et al., 2014). We found the endogenous levels of nuclear (active) YAP to be varied between central intercalating and neuroepthelial cells, in association to the variations in cell density, and depending on the presence of SMAD3. This nuclear YAP protein appears to be capable of modulating TGF-β transcriptional activity in central intercalating cells. Moreover, *in vivo* functional experiments proved these transcriptional responses to be functionally relevant for central cell behavior, since overexpression of YAP was sufficient to rescue the multi-lumen phenotype generated by the absence of SMAD3. Together, we propose here a model in which central cells require SMAD3/YAP-mediated motility properties to intercalate into the densely packed neuroepithelium and that defective SMAD3 transcriptional activity during the formation of the SNT leads to caudal NTDs.

### Limitations of the study

In this study, we recognize the limitations associated with the fact that sh-SMAD3-electroporated cells lay next to wild-type cells, since the chick embryo *in ovo* electroporation technique generates a mosaic tissue. Based on this limitation, we believe that the described defects in secondary neurulation would resemble a hypomorphic genotype more than a null genotype. The fact that depletion of SMAD3 activity resulted in properly epithelialized cells with correct apicobasal polarity, which organized around multiple lumens, as opposed to the absence of polarization and the complete inexistence of a lumen, points to a role of this pathway in the last steps of SNT lumen formation, the resolution of a single lumen by the intercalation of central cells, although we cannot completely exclude the possibility of SMAD3 contributing in earlier steps of secondary neurulation.

## STAR★METHODS

Detailed methods are provided in the online version of this paper and include the following:

- KEY RESOURCES TABLE
- RESOURCE AVAILABILITY
  - Lead contact
  - Materials availability

## SUPPLEMENTAL INFORMATION

Supplemental information can be found online at https://doi.org/10.1016/j.devcel.2021.03.023.

## ACKNOWLEDGMENTS

The authors are indebted to Dr Elena Rebollo for her invaluable technical assistance at the AFMU Facility (IBMB); We thank Leica Microsystems for supporting and collaborating with the AFMU Facility (IBMB). We are grateful to researchers that kindly provided DNAs and antibodies, as indicated in the reporting summary. The work in EM's laboratory was supported by grants BFU2016-77498-P and RED2018-102553-T. EGG was recipient of a BES-2014-068589 PhD scholarship. JBA is a recipient of a BES-2017-080050 PhD scholarship.

## AUTHOR CONTRIBUTIONS

Conceptualization, E.G.-G. and J.B.-A.; formal analysis, E.G.-G. and J.B.-A.; investigation, E.G.-G., J.B.-A., G.A., and B.B.; validation and visualization, E.G.-G., J.B.-A., G.A., B.B., and E.M.; writing – original draft, E.G.-G. and E.M.; review & editing, J.B.-A., G.A., B.B., and E.M.; resources, S.U.; supervision, E.M.; funding acquisition, E.M.

## DECLARATION OF INTERESTS

The authors declare no competing interests.

Received: February 15, 2020
Revised: January 7, 2021
Accepted: March 19, 2021
Published: April 19, 2021

## REFERENCES

Aaku-Saraste, E., Hellwig, A., and Huttner, W.B. (1996). Loss of occludin and functional tight junctions, but not ZO-1, during neural tube closure–remodeling of the neuroepithelium prior to neurogenesis. Dev. Biol. *180*, 664–679.

Afonso, C., and Henrique, D. (2006). PAR3 acts as a molecular organizer to define the apical domain of chick neuroepithelial cells. J. Cell Sci. *119*, 4293–4304.

Alarcón, C., Zaromytidou, A.I., Xi, Q., Gao, S., Yu, J., Fujisawa, S., Barlas, A., Miller, A.N., Manova-Todorova, K., Macias, M.J., et al. (2009). Nuclear CDKs drive Smad transcriptional activation and turnover in BMP and TGF-β pathways. Cell *139*, 757–769.

Attardo, A., Calegari, F., Haubensak, W., Wilsch-Brauninger, M., and Huttner, W.B. (2008). Live imaging at the onset of cortical neurogenesis reveals differential appearance of the neuronal phenotype in apical versus basal progenitor progeny. PLoS One *3*, e2388.

Bedzhov, I., and Zernicka-Goetz, M. (2014). Self-organizing properties of mouse pluripotent cells initiate morphogenesis upon implantation. Cell *156*, 1032–1044.

Bénazéraf, B., Francois, P., Baker, R.E., Denans, N., Little, C.D., and Pourquié, O. (2010). A random cell motility gradient downstream of FGF controls elongation of an amniote embryo. Nature *466*, 248–252.

Brown, K.A., Pietenpol, J.A., and Moses, H.L. (2007). A tale of two proteins: differential roles and regulation of Smad2 and Smad3 in TGF-beta signaling. J. Cell. Biochem. *101*, 9–33.

Bryant, D.M., Roignot, J., Datta, A., Overeem, A.W., Kim, M., Yu, W., Peng, X., Eastburn, D.J., Ewald, A.J., Werb, Z., and Mostov, K.E. (2014). A molecular switch for the orientation of epithelial cell polarization. Dev. Cell *31*, 171–187.

Cambray, N., and Wilson, V. (2007). Two distinct sources for a population of maturing axial progenitors. Development *134*, 2829–2840.

Caspary, T., Larkins, C.E., and Anderson, K.V. (2007). The graded response to Sonic Hedgehog depends on cilia architecture. Dev. Cell. *12*, 767–778.

Catala, M., Teillet, M.A., and Le Douarin, N.M. (1995). Organization and development of the tail bud analyzed with the quail-chick chimaera system. Mech. Dev. *51*, 51–65. https://www.ncbi.nlm.nih.gov/pubmed/7669693.

Chenn, A., Zhang, Y.A., Chang, B.T., and McConnell, S.K. (1998). Intrinsic polarity of mammalian neuroepithelial cells. Mol. Cell. Neurosci. *11*, 183–193.

Chi, Q., Yin, T., Gregersen, H., Deng, X., Fan, Y., Zhao, J., Liao, D., and Wang, G. (2014). Rear actomyosin contractility-driven directional cell migration in three-dimensional matrices: a mechano-chemical coupling mechanism. J. R. Soc. Interface *11*, 20131072.

Colas, J.F., and Schoenwolf, G.C. (2001). Towards a cellular and molecular understanding of neurulation. Dev. Dyn. *221*, 117–145, https://doi.org/10.1002/dvdy.1144.

Denker, E., Sehring, I.M., Dong, B., Audisso, J., Mathiesen, B., and Jiang, D. (2015). Regulation by a TGFbeta-ROCK-actomyosin axis secures a non-linear lumen expansion that is essential for tubulogenesis. Development *142*, 1639–1650.

Dennler, S., Itoh, S., Vivien, D., DijkeTen, P., Huet, S., and Gauthier, J.M. (1998). Direct binding of Smad3 and Smad4 to critical TGFβ-inducible elements in the promoter of human plasminogen activator inhibitor-type 1 gene. EMBO J *17*, 3091–3100.

Diez del Corral, R., Breitkreuz, D.N., and Storey, K.G. (2002). Onset of neuronal differentiation is regulated by paraxial mesoderm and requires attenuation of FGF signalling. Development *129*, 1681–1691.

Dzhindzhev, N.S., Yu, Q.D., Weiskopf, K., Tzolovsky, G., Cunha-Ferreira, I., Riparbelli, M., Rodrigues-Martins, A., Bettencourt-Dias, M., Callaini, G., and Glover, D.M. (2010). Asterless is a scaffold for the onset of centriole assembly. Nature *467*, 714–718.

Elosegui-Artola, A., Andreu, I., Beedle, A.E.M., Lezamiz, A., Uroz, M., Kosmalska, A.J., Oria, R., Kechagia, J.Z., Rico-Lastres, P., Le Roux, A.L., et al. (2017). Force triggers YAP nuclear entry by regulating transport across nuclear pores. Cell, 1397–1410.e14.

García-Campmany, L., and Martí, E. (2007). The TGFbeta intracellular effector Smad3 regulates neuronal differentiation and cell fate specification in the developing spinal cord. Development *134*, 65–75.

Garriock, R.J., Chalamalasetty, R.B., Kennedy, M.W., Canizales, L.C., Lewandoski, M., and Yamaguchi, T.P. (2015). Lineage tracing of neuromesodermal progenitors reveals novel Wnt-dependent roles in trunk progenitor cell maintenance and differentiation. Development *142*, 1628–1638.

Gonzalez-Gobartt, E., Allio, G., Bénazéraf, B., and Martí, E. (2021). In vivo analysis of the Mesenchymal-to-Epithelial transition during chick secondary neurulation. Methods Mol. Biol. *2179*, 183–197.

Gouti, M., Delile, J., Stamataki, D., Wymeersch, F.J., Huang, Y., Kleinjung, J., Wilson, V., and Briscoe, J. (2017). A gene regulatory network balances neural and mesoderm specification during vertebrate trunk development. Dev. Cell *41*, 243–261.e7.

Gouti, M., Tsakiridis, A., Wymeersch, F.J., Huang, Y., Kleinjung, J., Wilson, V., and Briscoe, J. (2014). In vitro generation of neuromesodermal progenitors reveals distinct roles for wnt signalling in the specification of spinal cord and paraxial mesoderm identity. PLoS Biol. *12*, e1001937.

Greene, N.D., and Copp, A.J. (2014). Neural tube defects. Annu. Rev. Neurosci. *37*, 221–242.

Griffith, C.M., Wiley, M.J., and Sanders, E.J. (1992). The vertebrate tail bud: three germ layers from one tissue. Anat. Embryol. (Berl) *185*, 101–113.

Hamburger, V., and Hamilton, H.L. (1951). A series of normal stages in the development of the chick embryo. J. Morphol. *88*, 49–92.

Henrique, D., Abranches, E., Verrier, L., and Storey, K.G. (2015). Neuromesodermal progenitors and the making of the spinal cord. Development *142*, 2864–2875.

Kojima, S., Vignjevic, D., and Borisy, G.G. (2004). Improved silencing vector co-expressing GFP and small hairpin RNA. Biotechniques *36*, 74–79.

Kölliker, A. (1884). Die embryonalen Keimblä tter und die Gewebe. Z. Wiss. Zool. *40*, 179–213.

Kondoh, H., and Takemoto, T. (2012). Axial stem cells deriving both posterior neural and mesodermal tissues during gastrulation. Curr. Opin. Genet. Dev. *22*, 374–380.

Korchynskyi, O., and Ten Dijke, P. (2002). Identification and functional characterization of distinct critically important bone morphogenetic protein-specific response elements in the Id1 promoter. J. Biol. Chem. *277*, 4883–4891.

Le Dréau, G., Garcia-Campmany, L., Rabadán, M.A., Ferronha, T., Tozer, S., Briscoe, J., and Martí, E. (2012). Canonical BMP7 activity is required for the generation of discrete neuronal populations in the dorsal spinal cord. Development *139*, 259–268.

Le Dréau, G., and Martí, E. (2012). Dorsal-ventral patterning of the neural tube: a tale of three signals. Dev. Neurobiol. *72*, 1471–1481.

Le Dréau, G., Saade, M., Gutiérrez-Vallejo, I., and Martí, E. (2014). The strength of SMAD1/5 activity determines the mode of stem cell division in the developing spinal cord. J. Cell Biol. *204*, 591–605.

Levy, D., Adamovich, Y., Reuven, N., and Shaul, Y. (2008). Yap1 phosphorylation by c-Abl is a critical step in selective activation of proapoptotic genes in response to DNA damage. Mol. Cell. *29*, 350–361.

Marthiens, V., and Ffrench-Constant, C. (2009). Adherens junction domains are split by asymmetric division of embryonic neural stem cells. EMBO Rep. *10*, 515–520.

Martin, B.L., and Kimelman, D. (2012). Canonical Wnt signaling dynamically controls multiple stem cell fate decisions during vertebrate body formation. Dev. Cell *22*, 223–232.

Martín-Belmonte, F., Yu, W., Rodríguez-Fraticelli, A.E., Ewald, A.J., Werb, Z., Alonso, M.A., and Mostov, K. (2008). Cell-polarity dynamics controls the mechanism of lumen formation in epithelial morphogenesis. Curr. Biol. *18*, 507–513.

McGrew, M.J., Sherman, A., Lillico, S.G., Ellard, F.M., Radcliffe, P.A., Gilhooley, H.J., Mitrophanous, K.A., Cambray, N., Wilson, V., and Sang, H. (2008). Localised axial progenitor cell populations in the avian tail bud are not committed to a posterior Hox identity. Development *135*, 2289–2299.

Megason, S.G., and McMahon, A.P. (2002). A mitogen gradient of dorsal midline Wnts organizes growth in the CNS. Development *129*, 2087–2098.

Metzis, V., Steinhauser, S., Pakanavicius, E., Gouti, M., Stamataki, D., Ivanovitch, K., Watson, T., Rayon, T., Mousavy Gharavy, S.N., Lovell-Badge, R., et al. (2018). Nervous system regionalization entails axial allocation before neural differentiation. Cell *175*, 1105–1118.e17.

Míguez, D.G., Gil-Guiñón, E., Pons, S., and Martí, E. (2013). Smad2 and Smad3 cooperate and antagonize simultaneously in vertebrate neurogenesis. J. Cell Sci. *126*, 5335–5343.

Morris, J.K., Rankin, J., Draper, E.S., Kurinczuk, J.J., Springett, A., Tucker, D., Wellesley, D., Wreyford, B., and Wald, N.J. (2016). Prevention of neural tube defects in the UK: a missed opportunity. Arch. Dis. Child. *101*, 604–607.

Moustakas, A., and Heldin, C.H. (2002). From mono- to oligo-Smads: the heart of the matter in TGF-beta signal transduction. Genes Dev. *16*, 1867–1871.

Moustakas, A., Souchelnytskyi, S., and Heldin, C.H. (2001). Smad regulation in TGF-beta signal transduction. J. Cell Sci. *114*, 4359–4369.

Najas, S., Pijuan, I., Esteve-Codina, A., Usieto, S., Martinez, J.D., Zwijsen, A., Arbonés, M.L., Martí, E., and Le Dréau, G. (2020). A SMAD1/5-YAP signalling module drives radial glia self-amplification and growth of the developing cerebral cortex. Development *147*.

Nakamura, N., Rabouille, C., Watson, R., Nilsson, T., Hui, N., Slusarewicz, P., Kreis, T.E., and Warren, G. (1995). Characterization of a cis-Golgi matrix protein, GM130. J. Cell Biol. *131*, 1715–1726, https://doi.org/10.1083/jcb.131.6.1715.

Nardone, G., Oliver-De La Cruz, J., Vrbsky, J., Martini, C., Pribyl, J., Skládal, P., Pešl, M., Caluori, G., Pagliari, S., Martino, F., et al. (2017). YAP regulates cell mechanics by controlling focal adhesion assembly. Nat. Commun. *8*, 15321.

Nowotschin, S., Ferrer-Vaquer, A., Concepcion, D., Papaioannou, V.E., and Hadjantonakis, A.K. (2012). Interaction of Wnt3a, Msgn1 and Tbx6 in neural versus paraxial mesoderm lineage commitment and paraxial mesoderm differentiation in the mouse embryo. Dev. Biol. *367*, 1–14.

Olivera-Martinez, I., Harada, H., Halley, P.A., and Storey, K.G. (2012). Loss of FGF-dependent mesoderm identity and rise of endogenous retinoid signalling determine cessation of body axis elongation. PLoS Biol. *10*, e1001415.

Piccolo, S., Dupont, S., and Cordenonsi, M. (2014). The biology of YAP/TAZ: Hippo signaling and beyond. Physiol. Rev. *94*, 1287–1312.

Ridley, A.J., Schwartz, M.A., Burridge, K., Firtel, R.A., Ginsberg, M.H., Borisy, G., Parsons, J.T., and Horwitz, A.R. (2003). Cell migration: integrating signals from front to back. Science *302*, 1704–1709.

Rupp, P.A., Rongish, B.J., Czirok, A., and Little, C.D. (2003). Culturing of avian embryos for time-lapse imaging. BioTechniques *34*, 274–278.

Saade, M., Gonzalez-Gobartt, E., Escalona, R., Usieto, S., and Martí, E. (2017). Shh-mediated centrosomal recruitment of PKA promotes symmetric proliferative neuroepithelial cell division. Nat. Cell Biol. *19*, 493–503.

Saade, M., Gutiérrez-Vallejo, I., Le Dréau, G., Rabadán, M.A., Miguez, D.G., Buceta, J., and Martí, E. (2013). Sonic hedgehog signaling switches the mode of division in the developing nervous system. Cell Rep. *4*, 492–503.

Saitsu, H., and Shiota, K. (2008). Involvement of the axially condensed tail bud mesenchyme in normal and abnormal human posterior neural tube development. Congenit. Anom. (Kyoto) *48*, 1–6.

Schneider, C.A., Rasband, W.S., and Eliceiri, K.W. (2012). NIH Image to ImageJ: 25 years of image analysis. Nat. Methods. *9*, 671–675.

Schoenwolf, G.C., and Delongo, J. (1980). Ultrastructure of secondary neurulation in the chick embryo. Am. J. Anat. *158*, 43–63.

Schoenwolf, G.C., and Kelley, R.O. (1980). Characterization of intercellular junctions in the caudal portion of the developing neural tube of the chick embryo. Am. J. Anat. *158*, 29–41.

Shi, Y., and Massagué, J. (2003). Mechanisms of TGF-beta signaling from cell membrane to the nucleus. Cell *113*, 685–700.

Shimokita, E., and Takahashi, Y. (2011). Secondary neurulation: fate-mapping and gene manipulation of the neural tube in tail bud. Dev. Growth Differ. *53*, 401–410.

Takemoto, T., Uchikawa, M., Kamachi, Y., and Kondoh, H. (2006). Convergence of Wnt and FGF signals in the genesis of posterior neural plate through activation of the Sox2 enhancer N-1. Development *133*, 297–306.

Taverna, E., Mora-Bermúdez, F., Strzyz, P.J., Florio, M., Icha, J., Haffner, C., Norden, C., Wilsch-Bräuninger, M., and Huttner, W.B. (2016). Non-canonical features of the Golgi apparatus in bipolar epithelial neural stem cells. Sci. Rep. *6*, 21206.

Tawk, M., Araya, C., Lyons, D.A., Reugels, A.M., Girdler, G.C., Bayley, P.R., Hyde, D.R., Tada, M., and Clarke, J.D. (2007). A mirror-symmetric cell division that orchestrates neuroepithelial morphogenesis. Nature *446*, 797–800.

Tsakiridis, A., and Wilson, V. (2015). Assessing the bipotency of in vitro-derived neuromesodermal progenitors. F1000Res *4*, 100.

Turner, D.A., Hayward, P.C., Baillie-Johnson, P., Rué, P., Broome, R., Faunes, F., and Martinez Arias, A. (2014). Wnt/beta-catenin and FGF signalling direct the specification and maintenance of a neuromesodermal axial progenitor in ensembles of mouse embryonic stem cells. Development *141*, 4243–4253.

Tzouanacou, E., Wegener, A., Wymeersch, F.J., Wilson, V., and Nicolas, J.F. (2009). Redefining the progression of lineage segregations during mammalian embryogenesis by clonal analysis. Dev. Cell *17*, 365–376.

Uchikawa, M., Ishida, Y., Takemoto, T., Kamachi, Y., and Kondoh, H. (2003). Functional analysis of chicken Sox2 enhancers highlights an array of diverse regulatory elements that are conserved in mammals. Dev. Cell *4*, 509–519. https://www.ncbi.nlm.nih.gov/pubmed/12689590.

Ulloa, F., and Briscoe, J. (2007). Morphogens and the control of cell proliferation and patterning in the spinal cord. Cell Cycle *6*, 2640–2649.

Varelas, X., Sakuma, R., Samavarchi-Tehrani, P., Peerani, R., Rao, B.M., Dembowy, J., Yaffe, M.B., Zandstra, P.W., and Wrana, J.L. (2008). TAZ controls Smad nucleocytoplasmic shuttling and regulates human embryonic stem-cell self-renewal. Nat. Cell Biol. *10*, 837–848.

Varelas, X., Samavarchi-Tehrani, P., Narimatsu, M., Weiss, A., Cockburn, K., Larsen, B.G., Rossant, J., and Wrana, J.L. (2010). The crumbs complex couples cell density sensing to hippo-dependent control of the TGF-β-SMAD pathway. Dev. Cell *19*, 831–844.

Wymeersch, F.J., Huang, Y., Blin, G., Cambray, N., Wilkie, R., Wong, F.C., and Wilson, V. (2016). Position-dependent plasticity of distinct progenitor types in the primitive streak. eLife *5*, e10042.

Yamaguchi, T.P., Bradley, A., McMahon, A.P., and Jones, S. (1999). A Wnt5a pathway underlies outgrowth of multiple structures in the vertebrate embryo. Development *126*, 1211–1223.

Yan, X., Habedanck, R., and Nigg, E.A. (2006). A complex of two centrosomal proteins, CAP350 and FOP, cooperates with EB1 in microtubule anchoring. Mol. Biol. Cell *17*, 634–644.

Yoshikawa, Y., Fujimori, T., McMahon, A.P., and Takada, S. (1997). Evidence that absence ofWnt-3aSignaling promotes neuralization instead of paraxial mesoderm development in the mouse. Dev. Biol. *183*, 234–242.

## STAR★METHODS

### KEY RESOURCES TABLE

| REAGENT or RESOURCE | SOURCE | IDENTIFIER |
|---|---|---|
| **Antibodies** | | |
| Acetylated Tubulin | Sigma | RRID: AB_477585 |
| Apkc | Santa Cruz | RRID: AB_628148 |
| c-Caspase3 | BD Biosciences | RRID: AB_397274 |
| Fibronectin | DSHB | RRID: AB_2105970 |
| FOP (FGFR1OP) | Olivier Rosnet | |
| GM130 | BD Biosciences | RRID: AB_398141 |
| Integrinα6 | DSHB | RRID: AB_528301 |
| Integrinβ1 | DSHB | RRID: AB_2128055 |
| N-cadherin | ZYMED | RRID: AB_2533007 |
| Laminin-111 | Sigma | RRID: AB_477163 |
| phospho-Histone3 | Upstate | RRID: AB_310177 |
| phospho-Histone3 | Sigma | RRID: AB_260096 |
| phospho-SMAD2/3 | Santa Cruz | RRID: AB_2193189 |
| Polyglutamilated Tubulin | Adipogen | RRID: AB_2490210 |
| SMAD2 | Cell signalling | RRID: AB_10626777 |
| SMAD3 | Abcam | RRID: AB_2192903 |
| Sox2 | Abcam | RRID: AB_2341193 |
| T/Bra | R&D | RRID: AB_2200235 |
| YAP | Santa Cruz | RRID: AB_1131430 |
| ZO-1 | Invitrogen | RRID: AB_2533147 |
| **Chemicals, Peptides, and Recombinant Proteins** | | |
| TRITC conjugated phalloidin | Sigma-Aldrich | P1951 |
| **Critical Commercial Assays** | | |
| In situ cell death detection kit POD | Roche | Cat. No. 11 684 817 910 |
| **Experimental Models: Organisms/Strains** | | |
| Fertilized eggs from the White-Leghorn strain of chickens | Granja Gilbert | N/A |
| **Recombinant DNA** | | |
| Plasmid: ARL13B-RFP | (Caspary et al., 2007; Saade et al., 2017) | N/A |
| Plasmid: BRE:GFP | (Korchynskyi and Ten Dijke, 2002; Le Dréau et al., 2012) | N/A |
| Plasmid: CAGA12:GFP | (Dennler et al., 1998; Míguez et al., 2013) | N/A |
| Plasmid: CEP152-GFP | (Dzhindzhev et al., 2010; Saade et al., 2017) | N/A |
| Plasmid: pCAGGS_Flag-YAP1_ires_GFP | (Najas et al., 2020) | N/A |
| Plasmid: pCAGGS:_ires_GFP | (Megason and McMahon, 2002) | N/A |
| Plasmid: pCDNA:Flag-YAP1 | (Levy et al., 2008) | N/A |
| Plasmid: pCS2:H2B-GFP | (Le Dréau et al., 2014) | N/A |
| Plasmid: pCS2:H2B-RFP | (Le Dréau et al., 2014) | N/A |
| Plasmid: pCS2:membrane-GFP | (Attardo et al., 2008) | N/A |
| Plasmid: pSHIN | (Kojima et al., 2004) | N/A |
| Plasmid: pSUPER | Oligoengine (cat# VEC-pBS-0002) | N/A |
| Plasmid: SMAD3-3S/D | (García-Campmany and Martí 2007) | N/A |
| Plasmid: SMAD3-3S/A | (García-Campmany and Martí 2007) | N/A |
| Plasmid: Sox2p:GFP | (Saade et al., 2013; Uchikawa et al., 2003) | N/A |
| Plasmid: pSHIN-sh-SMAD1 | (Le Dréau and Martí, 2012) | N/A |

(*Continued on next page*)

*Continued*

| REAGENT or RESOURCE | SOURCE | IDENTIFIER |
|---|---|---|
| Plasmid: pSHIN- sh-SMAD5 | (Le Dréau and Martí, 2012) | N/A |
| Plasmid: pSHIN-sh-SMAD2 | (Míguez et al., 2013) | N/A |
| Plasmid: pSHIN- sh-SMAD3 | (García-Campmany and Martí 2007) | N/A |
| Plasmid: pSUPER-sh-SMAD1 | (Le Dréau and Martí, 2012) | N/A |
| Plasmid: pSUPER- sh-SMAD5 | (Le Dréau and Martí, 2012) | N/A |
| cDNA for ISH probes (See Table S1) | N/A | N/A |
| Software and Algorithms | | |
| ImageJ | (Schneider et al., 2012) | SCR_003070 |
| ZEN software | Zeiss | SCR_013672 |
| Adobe Photoshop CS5 | Adobe | SCR_014199 |
| Imaris software | Bitplane | SCR_007370 |
| Adobe Illustrator CS5 | Adobe | SCR_014199 |
| GraphPad Prism 6 | GraphPad Software | SCR_002798 |

## RESOURCE AVAILABILITY

### Lead contact

Further information and requests for resources and reagents should be directed to and will be fulfilled by the Lead Contact, Elisa. Martí. emgbmc@ibmb.csic.es

### Materials availability

This study did not generate new unique reagents.

### Data and code availability

This study did not generate/analyze any datasets/code.

## EXPERIMENTAL MODEL AND SUBJECT DETAILS

### Chick embryos

Fertilized eggs from the White-Leghorn strain of chickens were incubated horizontally at 38.5°C in an atmosphere of 70% humidity. Embryos were staged following morphological criteria (Hamburger and Hamilton, 1951). Embryos sex cannot be reported due to technical limitations associated with the early developmental stages used in this study.

## METHOD DETAILS

### Chick in ovo electroporation

An Intracel Dual Pulse (TSS-20 Ovodyne) electroporator equipped with a footswitch was used to generate electric pulses. We separated a pair of platinum commercial electrodes (CUY610P1.5-1, Nepagene) and only used one side as the positive electrode. We incorporated a sharpened and bent 90° tungsten needle (Fine Science Tools) into a holder and used it as the negative 'microelectrode'

Eggs were horizontally incubated at 38.5°C in an atmosphere of 70% humidity until HH9 stage. DNA plasmids were diluted at 0.05-2μg/μl in 60% sucrose in sigma H2O (Sigma-Aldrich, W4502) with 50 ng/ml of Fast Green FCF (Sigma-Aldrich, F7258). Before manipulation, 5ml of albumen was removed from the egg with a syringe and a window was opened at the top of the shell to visualize the embryo. Thin forceps were used to open a small hole in the posterior region of the area opaca, just outside of the area pellucida 200ml of 1% Penicillin/Streptomycin (P/S) (Gibco, 15070063) were poured on top of the embryo to improve electrode conductivity. DNA solution was then injected onto the epiblast with a glass capillary by blowing air through an aspirator tube (Sigma-Aldrich, A5177-5EA). DNA was introduced with a glass capillary needle (GD-1, Narishige; made with Narishige PC-10 glass capillary puller) into the small concave region at their posterior end of the stage HH9 embryo, where the neural tube is still open. The platinum electrode connected to the positive lead (+) was carefully inserted below the embryo through the hole made previously, parallel to its antero-posterior axis. The tungsten microelectrode connected to the negative lead (-) was then positioned on top of the embryo, also in parallel to its antero-posterior axis. Five 50 ms square pulses of 5V at intervals of 50 ms were delivered. The window in the shell was finally sealed with plastic tape and embryos were incubated until the desired stage.

### Chick embryo culture mounting for in vivo imaging

Filter paper rings were prepared from 2 x 2 cm squares of Whatman grade 1 filter paper (Sigma-Aldrich, WHA1001325) in which a clover-leaf shaped hole was made in the centre with a paper punch, cutting the corners so that they fit in the round imaging plates. Imaging plates were also prepared in advanced by bedding several Millicell cell culture plate inserts (0.4 mm: Millipore, PICMORG50) with an Agar/Albumen mix.

The tape-sealed window in the egg was reopened and the thick albumen surrounding and covering the embryo carefully removed with a soft tissue. A paper ring was placed on top of the vitelline membrane so that the embryo located in the center of the clover-shaped hole, the vitelline membrane was cut through and around the whole perimeter of the filter paper ring and finally the filter with the embryo attached was pulled away from the yolk. Embryos with the best overall morphology and the greatest level of transgene expression were selected for imaging and transferred ventral side up to the imaging plates.

Imaging was performed inside a culture chamber created from a Corning ® Costar ® polystyrene 6-well plate (Sigma, CLS3736). To favour the optics, the plastic in the lid was replaced with glass. Each well of the culture chamber was filled with 1.5 mL of a solution of 5 ml thin albumen and 5 ml of 123 mM NaCl, the embryos in the imaging plates were transferred to the wells of the culture chamber and 1xPBS was added in between wells to maintain a moist environment inside the culture chamber. The culture chamber was finally sealed with electrical insulation tape.

### In vivo time-lapse imaging

Embryos were visualised under an upright wide-field microscope Axio Imager 2 (Zeiss) equipped with a motorized stage and an incubation chamber. The temperature was set to 39.5 °C so that the temperature at the level of the embryo was around 37.5 °C. The Experiment designer module of version 2.3 blue edition of the ZEN software (Zeiss) (RRID: SCR_013672) was used to set up the acquisition. For 5x objective, 10 z images every 10 minutes for 100 loops were acquired with a resolution of 1024x1024 binning 4x4. For 20x objective, 10 z images every 6 minutes for 150 loops were acquired with a resolution of 1024x1024 binning 4x4. The images of each embryo acquired were first time-stitched with the ZEN software (Zeiss) and then exported to Image J/Fiji software for image processing and analysis.

### Whole-mount immunohistochemistry

In toto embryo immunostaining procedure was carried out as follows: Chick embryos were removed from the egg at stage HH15 and fixed in 5ml 4% paraformaldehyde (PFA) (Sigma-Aldrich, 16005) in 1xPhosphate Buffered Saline (PBS) for 2 hours at room temperature (RT) or overnight at 4°C. Embryos were transferred to a 2ml tube, using a Pasteur pipette with the end cut off. Embryos were washed 3 x 30 min in 0.5% Triton-X-100 (Sigma-Aldrich, X100) in PBS (PBT).

Embryos were incubated in blocking solution consisting of 0.5% PBT + 1% Albumin from Bovine Serum (BSA, Sigma-Aldrich, 9048-46-8), 0.2% sodium azide (Sigma-Aldrich, S2002) for 1h at RT. Embryos were incubated in blocking solution with primary antibody for 2 to 3 days at 4°C with gentle shaking. Following incubation, embryos were washed 3 x 1h in 0.5% PBT. Embryos were then incubated in blocking solution with secondary antibodies for 2 days at 4°C with gentle shaking. After washing, embryos were incubated overnight at 4oC with DAPI (1:1000) (Sigma) in 0.5% PBT. Finally, embryos were initially washed 3 x 10 min in PBT, followed by 3 longer 30 min washes, transferred to PBS and stocked at 4°C. A full list of antibodies used in this study can be found in the Key Resources Table.

### Free-floating sections immunohistochemistry

Immunostaining of transversal vibratome sections was carried out as follows: Chick embryos were removed from the egg at stage HH15 and fixed in 4% PFA in 1xPBS for 2 hours at RT or 4 h at 4°C. Embryos were embedded in plastic moulds with a warm 5% agarose - 10% sucrose matrix and cooled down to solidify. Agarose embryo-blocks were sectioned at 50-100μm thickness in a Leica Vibratome (VT1000S), obtaining free-floating transversal sections. Sections were washed 3 x 5 min in PBT (PBS + 0.1% Triton-X-100). Sections were incubated in blocking solution (10% BSA in PBT) for at least 30min at RT. Sections were incubated in antibody solution (1% BSA in PBT) with primary antibody overnight at 4°C with gentle shaking. Following incubation, sections were washed 3 x 10 min in PBT. Sections were then incubated in secondary antibodies in antibody solution for 2 hours at room temperature. Finally, embryos were initially washed 3 x 10 min in PBT washes and transferred to water for glass-slide mounting, and covered by Mowiol (Sigma-Aldrich, 81381) and a glass-coverslip.

Counter-stains were added during incubation with secondary antibody. DAPI (1:5000) was used to visualise nuclei (Sigma-Aldrich, D9542). TRITC conjugated phalloidin (1:1000) was used to visualize F-actin/tissue structure (Sigma-Aldrich, P1951). A full list of antibodies used in this study can be found in the Key Resources Table.

### In situ hybridization

Embryos were removed from the egg at stage HH15 and fixed overnight at 4°C in 4% PFA diluted in 1xPBS. The next day embryos were dehydrated with a series of increasing methanol concentration solutions (25%, 50%, 75% and 100% methanol). Embryos were then stored at -20°C for at least overnight. Whole-mount in situ hybridisation was performed following standard procedures with the InsituPro VSi robot (Intavis). Each condition was replicated in two wells with 3-4 embryos each. Probes from the chicken EST project (http://www.chick.manchester.ac.uk/) were used at 1:200. Sonic hedgehog probe was always used as positive control. Hybridized embryos were post-fixed in 4% PFA, rinsed in PBT and embedded in plastic moulds with a warm 5% agarose - 10% sucrose matrix

and cooled down to solidify. Agarose embryo-blocks were sectioned at 50μm thickness in a Leica Vibratome, obtaining free-floating transversal sections. Finally, sections were transferred to water for glass-slide mounting, and covered by Mowiol and a glass-coverslip. A full list of probes used in this study can be found in the Key Resources Table.

### TUNEL staining in free-floating sections

The deoxynucleotidyl transferase–mediated deoxyuridinetriphosphate nick end labelling (TUNEL) assay was used to detect programmed cell death by apoptosis. The TUNEL assay was performed using the In situ cell death detection kit POD (Roche, 11 684 817 910) following the manufacturer instructions with some modifications. Embryos were removed from the egg at stage HH15 and fixed overnight at 4°C in 4% PFA diluted in 1xPBS. The next day embryos were dehydrated with a series of solutions with increasing methanol concentration (25%, 50%, 75% and 100% methanol). Embryos were stored at -20 °C for at least overnight and up to six months. Embryos were rehydrated and embedded in plastic moulds with a warm 5% agarose - 10% sucrose matrix and cooled down to solidify. Agarose embryo-blocks were sectioned at 50μm thickness in a Leica Vibratome, obtaining free-floating transversal sections. TUNEL staining was then performed and the most posterior sections were used as positive controls. Colour was developed using DAB substrate in a solution containing 0.3% H2O2, prepared following the manufacturer instructions (Sigma-Aldrich, 7411-49-6). DAB reaction was stopped by washing a few times in PBS pH=7. Finally, TUNEL stained sections were transferred to water for glass-slide mounting, and covered by Mowiol and a glass-coverslip.

## QUANTIFICATION AND STATISTICAL ANALYSIS

### 3D lumen reconstruction

Raw whole-mount confocal data was exported to the Imaris software (Bitplane) (RRID:SCR_007370). The secondary forming lumen was reconstructed using the Contour Surface tool. The 3D structure was extracted by manually drawing the lumen contour, visible with ZO-1 immunostaining, on consecutive 2D z-slices.

### General Image Analysis

Raw confocal data was exported to ImageJ/FiJi (http://rsbweb.nih.gov/ij/)(RRID: SCR_003070) to be processed and analysed (Rueden et al., 2017; Schindelin et al., 2012). Projections of z-stacks are maximum projections unless otherwise indicated. Figures and schemes were generated using Adobe Illustrator CS5 (RRID: SCR_014199).

### Nuclear SMAD3 intensity

Sh-SMAD3 and pSUPER control vectors were co-electroporated with H2B-RFP and stained with an antibody against endogenous SMAD3. Images from both conditions were acquired with the same laser and gain parameters. The polygon selection tool of ImageJ was used to delineate H2B-RFP+ cell nuclei and the integrated density was measured. Results are presented in GraphPad Prism 6 box & whisker plots.

### Cell death

Cleaved-Caspase3 (c-Caspase3) antibody was used to detect apoptosis in fixed transversal sections of stage HH15 chick embryos. For WT quantifications, we counted both the number of c-Capase3+ cells and the number of total DAPI cells. For electroporated embryos, we counted c-Caspase3+ cells, H2B-RFP+ cells and total cells (DAPI). Percentages were then calculated and presented in GraphPad Prism 6 bar graphs.

### Proliferation

Phospho-histone 3 (pH3) antibody was used to detect mitotic cells in fixed transversal sections of stage HH15 chick embryos. For WT quantifications, we counted both the number of pH3+ cells and the number of total DAPI cells. For electroporated embryos, we counted pH3+ cells, H2B-RFP+ cells and total cells (DAPI). Percentages were then calculated and presented in GraphPad Prism 6 bar graphs.

### Sox2 and T/Bra nuclear intensities

Images from fixed transversal sections of stage HH15 chick embryos stained for Sox2 and T/Bra antibodies were acquired with the same gain and laser parameters. The area, integrated density and mean grey value were measured for each nucleus and for three neighbouring selections with no fluorescence (background measurements). The level of fluorescence in the nucleus was then determined with the corrected total cell fluorescence (CTCF). CTCF is calculated with the formula CTCF= Integrated nuclear density – (Area of selected nucleus x Mean fluorescence of background readings). $Log_{10}$ (CTCF) was finally calculated and represented in GraphPad Prism 6 box & whisker plots.

Images from fixed stage HH15 transversal sections stained for Sox2, T/Bra and Fibronectin were used to correlate nuclear intensities (CTCF) with cell distance from the basement membrane (BM). A straight line was drawn with the ImageJ command from the centre of the nucleus to the closest Fibronectin staining and distance was measured. Results are presented in GraphPad Prism 6 linear regression plots. We considered peripheral cells those in contact with the BM and central cells those located further than 40μM from BM.

Sh-SMAD3 and H2B-RFP control vectors were electroporated and stained with an antibody against Sox2. Images were acquired with the same parameters and analysed. The polygon selection tool of ImageJ was used to delineate electroporated cell nuclei and the integrated density of Sox2 nuclear staining was measured. For each selected H2B-RFP+ positive nucleus, three nucleus of non-electroporated neighbouring cells (negative for H2B-RFP) were also delimited and their Sox2 integrated density measured. The following ratio was then calculated: integrated density of nuclear Sox2 H2B-RFP + cell/mean integrated density of three H2B-RFP- neighbouring cells. Results are presented in GraphPad Prism 6 box & whisker plots.

### Cell shape

Actin staining (Phalloidin) was used to visualize cell shape in WT, pSUPER control and sh-SMAD3 transversal sections. Cells were delimited with the polygon selection tool and cell shape was quantified by measuring cell circularity, a parameter included in ImageJ Shape descriptors. Circularity is calculated with the formula $4\pi\times$[Area]/[Perimeter]2, with a value of 1.0 indicating a perfect circle. As the value approaches 0.0, it indicates an increasingly elongated shape. Results are presented in GraphPad Prism 6 box & whisker plots.

### Centrosome positioning

The centrosomes were visualized with FOP antibody and DAPI was used to stain the nucleus in WT, pSUPER control and sh-SMAD3 transversal sections. The straight-line tool of ImageJ was used to draw a line from the centrosomes to the edge of the nucleus and the distance was measured. Results are presented in GraphPad Prism 6 box & whisker plots.

### Golgi measurements; Basal-most Golgi

The centrosomes and the Golgi apparatus were visualized with FOP and GM130 antibodies, respectively, in HH15 WT transversal sections. The straight-line tool of ImageJ was used to draw a line from the centrosomes to the distal end of GM130 staining and the distance was measured. Results are presented in GraphPad Prism 6 box & whisker plots showing all points, median and inter-quartile range.

### Golgi extension

The Golgi apparatus was visualized with GM130 antibody in pSUPER control and sh-SMAD3 transversal sections. The straight-line tool of ImageJ was used to draw a line from the apical to the basal limit of GM130 staining and its length was measured. Results are presented in GraphPad Prism 6 box & whisker plots.

### Sequence of protein polarisation

Fixed transversal confocal images of FOP, N-cadherin, ZO-1, aPKC and β1 Integrin in the polarising medullary cord were used to define the sequence of epithelial polarity acquisition. Co-stainings were used to analyse the presence or absence of the mentioned components in each cell. We calculated the percentage of cells with: i. only the centrosome localised apically; ii. apically localised centrosome and apical N-cadherin; iii. apical centrosome, apical N-cadherin and apical ZO-1; iv. apical centrosome, apical N-cadherin and apical aPKC; v. apical centrosome and basal β1 integrin and vi. apical centrosome, basal β1 integrin and apical N-cadherin. Results are represented in GraphPad Prism 6 stacked bar graphs.

### Cell length and distance from lumen foci to basement membrane

Actin staining (phalloidin) and DAPI were used to visualize cell shape and cell nuclei in transversal control sections at the lumen initiation stage. The straight-line tool of ImageJ was used to draw a line along the length of the cell and its distance was measured. aPKC and Laminin were used to visualise the small lumen foci and the basal lamina, respectively, in control and sh-SMAD3 transversal sections at the lumen initiation stage. A straight line was drawn from the lumen foci to the closest laminin staining with the ImageJ command. Results are presented in GraphPad Prism 6 box & whisker plots.

### SMAD apico-basal intensity profiles

CEP152-GFP was electroporated in order to detect the two centrioles in chick neuroepithelial cells. CEP152-GFP electroporated embryos were co-stained with polyglutamilated tubulin, to visualize the primary cilium, and SMAD3, phSMAD2/3 and SMAD2 antibodies to study their localisation. Intensity profiles were generated with the Plot profile ImageJ command by drawing a straight line from the apical tip of the primary cilium to the basal daughter centriole. Intensity for the stained proteins was then measured along the drawn line.

### Quantifications in time-lapse movies; Distance to last pair of somites

The distance to the last pair of somites was measured in the generated movies (membrane-GFP or sh-SMAD3 and pSUPER control co-electroporated with Sox2p:GFP). Cell divisions of mesenchymal cells in the centre of the tissue were spotted and the first time point where mitotic rounding was detected was analysed. A straight line was drawn from the mitosis to the level of the last pair of somites, visible in bright-field images, with the ImageJ straight-line tool. Distance was measured and presented in GraphPad Prism 6 box & whisker plots.

### Distance from centre

A straight line was drawn in the centre of the neural tube by following the lumen in all movie time points. membrane-GFP+, sh-SMAD3 Sox2p:GFP + or pSUPER control Sox2p:GFP + mitosis were spotted and tracked back until the beginning of the movie. The distance from the drawn midline to the analysed cell and their daughter cells was measured in each time point with the ImageJ straight-line tool. Results along time are presented in GraphPad Prism 6 linear regression graphs.

### Circularity

membrane-GFP+, sh-SMAD3 Sox2p:GFP + or pSUPER control Sox2p:GFP + cell divisions were spotted in time-lapse movies and tracked back until the beginning of the movie. Cells were delimited with the polygon selection tool of Image J and cell shape was quantified by measuring cell circularity in each time point. Circularity is calculated with the formula $4\pi\times$[Area]/[Perimeter]2, with a value of 1.0 indicating a perfect circle. As the value approaches 0.0, it indicates an increasingly elongated shape. Results along time are presented in GraphPad Prism 6 linear regression graphs.

### Cell motion analysis

sh-SMAD3 Sox2p:GFP+ or pSUPER control Sox2p:GFP+ cell divisions of mesenchymal cells in the centre of the tissue were spotted and daughter cells were tracked with the Manual Tracking plugin in ImageJ/FiJi (Fabrice P. Cordelières -https://imagej.nih.gov/ij/plugins/track/track.html), starting at the end of mitosis (t=0) and for 20 time points of the time-lapse movie. Velocity and distance were obtained from the track results for each time point. Mean velocity, mean distance and total distance were calculated and are presented in GraphPad Prism 6 box & whisker plots.

### Quantification of central cell protrusions

membrane-GFP was co-electroporated with pSuper or sh-SMAD3 in chicken embryos NT in order to draw the cell shape of central cells during secondary neurulation. The number of protrusions was quantified in central cells at the rostro-caudal level of lumen resolution. This quantification was done by hand with the Cell Counter plugin in ImageJ/Fiji (Kurt De Vos - https://imagej.nih.gov/ij/plugins/cell-counter.html). Moreover, the protrusions length was delimitated by hand and measured in ImageJ/Fiji. Both protrusions number and length was presented in GraphPad Prism 6 violin plots.

### Quantification of YAP nuclear/cytoplasmic ratio

membrane-GFP was electroporated in order to draw the cell shape in chick neuroepithelial cells. DAPI staining was used to detect the nucleus. YAP was stained using a YAP antibody to assess protein levels. YAP activity was inferred from the ratio of nuclear over the cytoplasmic YAP protein levels. Nuclear regions were delimitated by hand in the ImageJ using DAPI staining as reference. Cytoplasmic region was estimated subtracting the nuclear area to the total cell area delimitated by hand in the ImageJ using the GFP staining as reference. YAP protein levels were assessed in the already defined nuclear and cytoplasmic areas through the ratio of RawIntDensity over the area extension using ImageJ/Fiji. Distance was presented in GraphPad Prism 6 box & whisker plots.

### Quantification of CAGA12 reporter activity in central cells

pSUPER, sh-SMAD3, YAP-FLAG and YAP-FLAG + sh-SMAD3 were co-electroporated with the reporter CAGA$^{12}$:GFP in chick embryos NT to assess the role of these proteins controlling TGF$\beta$ transcriptional activity. Central cells area was delimitated by hand using Phalloidin staining as reference. In the delimitated central cell, CAGA$^{12}$ activation was assessed through the ratio of GFP RawIntDensity over the cell area extension using ImageJ/Fiji. CAGA$^{12}$:GFP intensity was presented in GraphPad Prism 6 box & whisker plots.

### Multi-lumen phenotype assessment

membrane-GFP, sh-SMAD3, SMAD3 S/A, SMAD3 S/D, YAP-FLAG, SMAD3 S/D + sh-SMAD3 and YAP-FLAG + sh-SMAD3 were electroporated in chick embryos NT to assess the role of these proteins in secondary neurulation. In order to evaluate the proper formation of a single lumen in the secondary neurulation area, the ventricle/s shape was analysed using Phalloidin or DAPI staining. NTs were analysed at rostrocaudal level of the last pair of somites. Embryos were considered to present multi-lumen phenotype when the Phalliodin staining presents more than a single lumen per section. Distance was presented in GraphPad Prism 6 stacked bar plots.

### Statistical analysis

Quantitative data is expressed as mean±sem/SD or as median±IQR. Statistical analysis was performed using the GraphPad Prism 6 (RRID: SCR_002798). Significance was assessed by performing the Mann-Whitney test when comparing two populations or the Kruskal-Wallis when comparing more than two. In this later case, Dunn's multiple comparisons test was also run. In the few cases were data followed a normal distribution, assessed with the D'Agostino Pearson omnibus normality test, one-way ANOVA was performed. In this later case, Tukey's multiple comparisons test was also run (*$p<0.05$, **$p<0.01$, and ***$p<0.001$). The statistical details of experiments can be found in the figure legends.

# Appendix 4

© 2022. Published by The Company of Biologists Ltd | Journal of Cell Science (2022) 135, jcs259395. doi:10.1242/jcs.259395

REVIEW

SUBJECT COLLECTION: CILIA AND FLAGELLA

# Centrosome maturation – in tune with the cell cycle

**Jose Blanco-Ameijeiras, Pilar Lozano-Fernández and Elisa Martí***

## ABSTRACT

Centrosomes are the main microtubule-organizing centres, playing essential roles in the organization of the cytoskeleton during interphase, and in the mitotic spindle, which controls chromosome segregation, during cell division. Centrosomes also act as the basal body of cilia, regulating cilium length and affecting extracellular signal reception as well as the integration of intracellular signalling pathways. Centrosomes are self-replicative and duplicate once every cell cycle to generate two centrosomes. The core support structure of the centrosome consists of two molecularly distinct centrioles. The mother (mature) centriole exhibits accessory appendages and is surrounded by both pericentriolar material and centriolar satellites, structures that the daughter (immature) centriole lacks. In this Review, we discuss what is currently known about centrosome duplication, its dialogue with the cell cycle and the sequential acquisition of specific components during centriole maturation. We also describe our current understanding of the mature centriolar structures that are required to build a cilium. Altogether, the built-in centrosome asymmetries that stem from the two centrosomes inheriting molecularly different centrioles sets the foundation for cell division being an intrinsically asymmetric process.

**KEY WORDS: Cell division, Centrosome asymmetries, Primary cilium, Centrosome maturation**

## Introduction

The centrosome is a small, non-membranous organelle capable of self-replication. Centrosomes perform several critical functions in animal cells, which include serving as the main microtubule-organizing centre (MTOC), the basal body of cilia and a platform for intracellular signalling, as well as organizing the mitotic spindle during cell division (Arquint et al., 2014). The centrosome was first identified at the end of the 19th century, and at the time described as a moderately and uniformly stained sphere interspersed with a filamentous scaffold (Boveri, 1900). More recently, genomics and proteomics has helped us better define the components and understand the biology of the centrosome, and some of the diseases associated with centrosome dysfunction. In addition, in the past decade, technological breakthroughs, which include super-resolution microscopy, have helped researchers to characterize the composition and 3D organization of the centrosome at the molecular level. Here, we provide an up-to-date view of the 3D organization of the centrosome and the asymmetries between mother and daughter centrioles, as well as discuss how centrosome replication is coordinated with the cell cycle. We will also highlight the dynamics of centriole maturation, involving the recruitment of proteins required for appendage assembly, as well as centriole 'dematuration', which involves the partial disassembly of the appendages. Finally, we will discuss the organization of the basal body and transition zone of cilia. Many key findings in the field come from studies in model organisms such as *Drosophila* or *C. elegans* (Marthiens and Basto, 2020; Schwarz et al., 2018), but in this Review we will mostly refer to the human (mammalian) system. We aim to highlight the orchestration of centriolar protein recruitment and removal during the cell cycle, which results in two molecularly distinct centrosomes. Remarkably, the built-in centrosome asymmetries that stem from the two centrosomes inheriting different centrioles are the underlying basis for spindle positioning and cell division being intrinsically asymmetric.

## A pair of molecularly distinct centrioles form the core support structure of the centrosome

### Centrioles and appendages

Centrioles are cylindrical structures that are ∼500 nm long and have a diameter of 250 nm in vertebrate cells (Winey and O'Toole, 2014). They are composed of triplets of microtubules (MTs) organized around a central cartwheel with an evolutionarily conserved nine-fold symmetry (Azimzadeh and Marshall, 2010) (Fig. 1). Typically, two centrioles are joined perpendicularly by their proximal ends, a connection that is sustained by the proteinaceous centrosome linker in conjunction with MT forces (Panic et al., 2015). Of these two centrioles, only one is fully mature, exhibiting two characteristic accessory structures, the distal appendages (DAs) and the subdistal appendages (SDAs); this centriole is termed the mother centriole. Both DAs and SDAs can be visualized by electron microscopy (EM) and are observed as electron-dense ring-like structures with a head that attaches to the centriole MTs through a stem, which in turn connects with two MT triplets (Bowler et al., 2019; Bystrevskaya et al., 1988; Paintrand et al., 1992). The classical view is that the DAs and SDAs have a similar centriolar distribution, shape and size, yet this now appears to be only partially true. In most cases, both appendages show the nine-fold symmetry of the centriole wall, with the head-like structures radially disposed around the MT triplets (Bowler et al., 2019; Ibrahim et al., 2009). However, although mother centrioles always have nine DAs around their walls (Uzbekov and Alieva, 2018), the number of SDAs can vary between different cell types (Bystrevskaya et al., 1988, 1992; Komesli et al., 1989). The heads of both the DA and SDA are ∼40 nm in length and extend for ∼100 nm from the centriole wall (Fig. 1) (Bowler et al., 2019; Ibrahim et al., 2009). In cilia, DAs (also known here as transition fibres) are the platform that allows a transition zone (TZ) to be established, which contains a ring-like protein structure that extends for ∼120 nm along the ciliary axis with a nine-fold symmetry, and which connects MTs with the ciliary membrane (Shi et al., 2017). The daughter centriole, the younger of the two centrioles, is less mature and lacks SDAs and DAs; however, it has several daughter centriolar proteins (DCPs) that are recruited to nascent centrioles in order to regulate their elongation and homeostasis (Li et al., 2012; Mahjoub et al., 2010; Zou et al., 2005).

Instituto de Biología Molecular de Barcelona, Parc Científic de Barcelona, Baldiri i Reixac 20, Barcelona 08028, Spain.

*Author for correspondence (emgbmc@ibmb.csic.es)

E.M., 0000-0001-5839-7133

Journal of Cell Science (2022) 135, jcs259395. doi:10.1242/jcs.259395

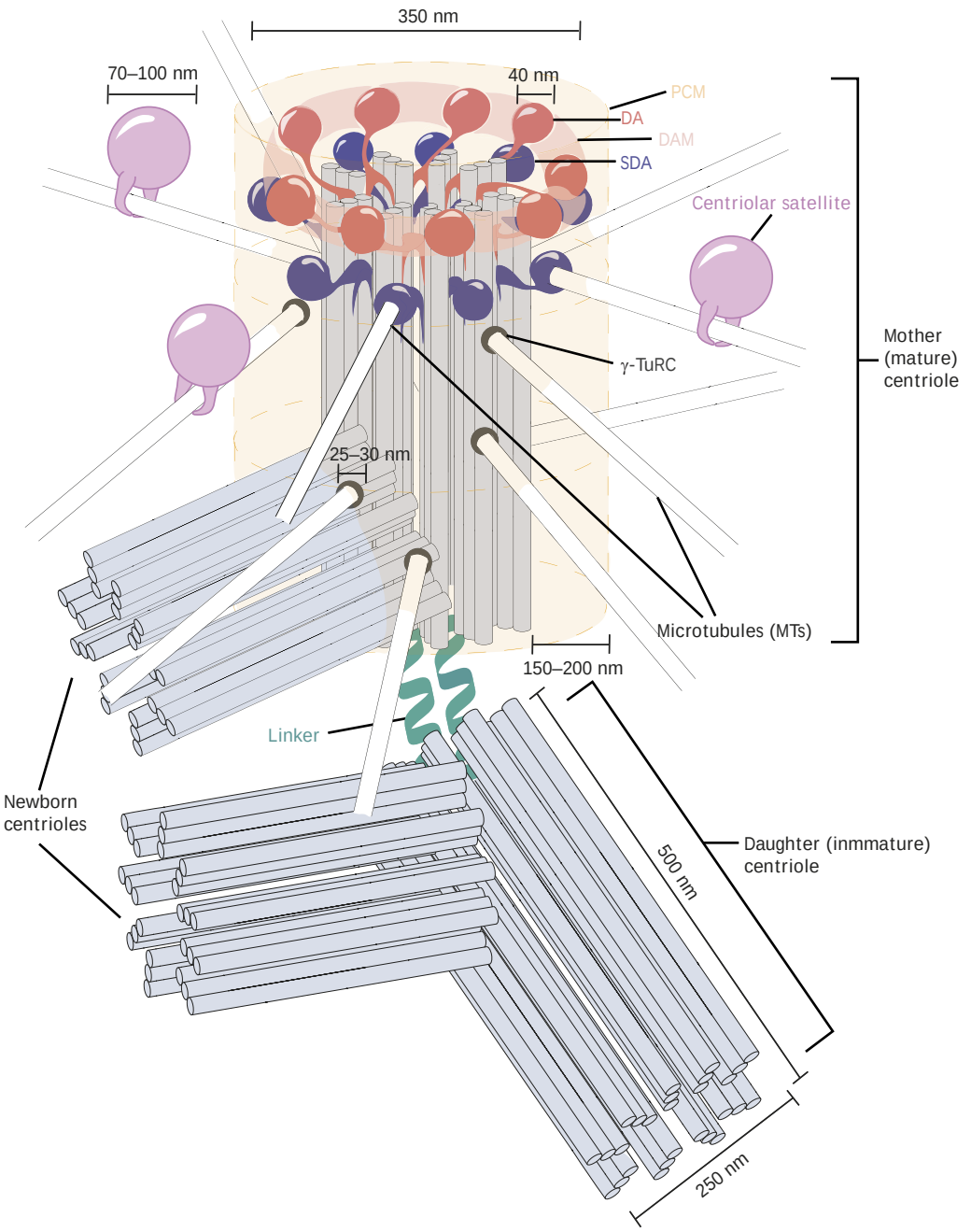


**Fig. 1. 3D reconstruction of a mature centrosome in the $G_2$ phase of the cell cycle.** The mother (mature) centriole is decorated with distal (DA, terracotta) and subdistal appendages (SDA, purple), as well as pericentriolar material (PCM, pale yellow). Proteins filling the space between DA constitute the distal appendage matrix (DAM, pale terracotta). Centriolar triplet microtubules are illustrated in grey-blue. Mother and daughter centrioles are connected through a proteinacous linker (green), and newborn centrioles emerge from each pre-existing centriole. Microtubules (MTs) nucleated by the mature centriole emerge from the γ-tubulin ring complex (γ-TuRC, dark grey) and centriolar satellites (lavender) travel along the MTs.

### Pericentriolar material and centriolar satellites

The pericentriolar material (PCM), a proteinaceous material surrounding the mother centriole, forms a cylindrical structure devoid of MTs that assembles around the centriole and is the focal point of MT nucleation (Jana, 2021). Initially, the PCM was considered to be a disorganized proteinaceous matrix, and indeed, in the earliest examples of electron micrographs of centrosomes it is described as an amorphous pericentriolar halo arising from the highly structured centrioles (Robbins et al., 1968). However, super-resolution microscopy has revealed that the PCM is a highly organized structure located in the vicinity of the mother centriole (Fu and Glover, 2012; Lawo et al., 2012; Mennella et al., 2012; Sonnen et al., 2012). The PCM is organized into concentric protein layers that attach to the mother centriole via pericentrin, a large protein that forms fibrils orientated with its C-terminal domain adjacent to the centriole wall and its N-terminus extending outwards into the PCM (Lawo et al., 2012; Mennella et al., 2012; Woodruff et al., 2014). These PCM protein layers accommodate the γ-tubulin ring complex (γ-TuRC) (Moritz et al., 2000), which is ∼25–30 nm in diameter and the origin of MT nucleation (Conduit et al., 2015) (Fig. 1). The size of the PCM varies widely as it undergoes dynamic changes, with the proximal layer extending ∼150–200 nm from the centriole wall as cells proceed through the cell cycle (Fry et al., 2017a).

How protein exchange and replacement occur between the centrosome and the cytoplasm has long remained unclear. However, it now appears that centriolar satellites (CSs) (Fig. 1), spherical granular structures of ∼70–100 nm in diameter (Tollenaere et al., 2015), are responsible for centrosomal protein transport (Bärenz et al., 2011). These CSs travel towards the centrosome along the MTs and are thought to play important regulatory roles in centrosome biology (Bärenz et al., 2011; Prosser and

Pelletier, 2020). Indeed, CS depletion alters the composition of the PCM (Dammermann and Merdes, 2002; Hames et al., 2005) and basal body (Kim et al., 2008a; Sillibourne et al., 2013).

## The centrosome replicates in coordination with the cell cycle

Centrosomes possess a self-replicative capacity that, like DNA replication, is coordinated with the cell cycle. In order to guarantee that there is a constant number of centrosomes in the cell, cycling cells establish two layers of control: (1) cell cycle control, whereby each centriole duplicates exactly once per cell cycle, and (2) copy number control, whereby only one new centriole forms alongside each pre-existing one (Nigg and Stearns, 2011). In most cells, centrosomes can form *de novo*, unless this is blocked by the pre-existing centrosomes (Heath et al., 1986; Khodjakov et al., 2002; Marshall, 2009). Here, we summarize the main events of canonical centrosome duplication during the cell cycle: procentriole formation during $G_1$, elongation of the procentriole during S phase, centrosome maturation during $G_2$, and centrosome separation as the cell enters mitosis. However, we note that there are some examples of non-canonical centrosome biogenesis where cells assemble *de novo* centrosomes without previous centriolar structures present in the cell (e.g. during the amoeba-to-flagellate transition in *Naegleria gruberi*, in parthenogenetic insect eggs and during oogenesis in most animal cells) (Nabais et al., 2017).

### The procentriole forms during the $G_1$ phase of the cell cycle

As the structural backbone of the organelle, the centriole wall is the principal checkpoint for centrosome duplication. Upon duplication, the newborn centrioles, elongating from procentrioles, remain engaged with the pre-existing ones until the end of mitosis, preventing them from acting as a template for re-duplication and thereby guaranteeing cell cycle control (Tsou and Stearns, 2006). During $G_1$, the centrosomal proteins CEP192 and CEP152 make up the inner components of the PCM and are sequentially recruited to the wall of the daughter centriole, while in the case of the mother centriole, both proteins are inherited from the previous cell cycle (Fig. 2A). CEP192 is distributed in a barrel shape all along the proximo-distal axis, whereas CEP152 is restricted to the proximal end of the centriole (Sonnen et al., 2013). CEP192 promotes the recruitment of CEP152 and the Polo kinase PLK4 (Kim et al., 2013), and once at the centriole, CEP152 competes with CEP192 to restrict PLK4 to the CEP152-containing proximal end of the centriole (Park et al., 2014) (Fig. 2A). The activity of PLK4 controls the number of centrioles arising from each mother centriole, thereby regulating centriole copy number (Bettencourt-Dias et al., 2005; Habedanck et al., 2005).

At the $G_1$/S transition, exactly one procentriole is formed for each pre-existing centriole (Fig. 2B). The temporal restriction of this process depends on the availability of the protein STIL, which is controlled by the CDK1–cyclin-B complex (Zitouni et al., 2016) and proteolysis mediated by the anaphase-promoting complex/cyclosome containing FZR1 (Cdh1 in yeast) or CDC20 (APC/$C^{FZR1}$ or APC/$C^{CDC20}$) (Arquint et al., 2012). PLK4 undergoes trans-autophosphorylation, and is thereby targeted for proteasomal degradation unless it binds to STIL (Cunha-Ferreira et al., 2009, 2013; Rogers et al., 2009). STIL is phosphorylated upon interaction with PLK4, allowing the centriolar loading of the coiled-coil protein SAS6 (encoded by *SASS6*) for cartwheel assembly (Moyer et al., 2015). Subsequently, the formation of a STIL–SAS6 complex establishes a negative-feedback loop by restricting PLK4 stabilization to a single focus, guaranteeing copy number control (Kim et al., 2016; Ohta et al., 2014). Moreover, STIL oligomerization could also contribute to the restriction of PLK4 to a single focal point (Banterle and Gönczy, 2017). SAS6 forms homodimers in the cytoplasm that, upon centriolar loading, undergo higher-order oligomerization to form a ring-like structure of nine homodimeric units (Keller et al., 2014). These ring-like oligomers then stack on top of each other to form the cartwheel structure (Fig. 2A).

### The procentriole elongates during the S phase of the cell cycle

The cartwheel structure serves as a template for centriole elongation. Although this process is less well studied than procentriole formation, MT nucleation and its stabilization in the nine-fold symmetry requires the cartwheel–MT connection to be established, ensuring that elongation can occur during the S phase of the cell cycle. This connection probably takes place through CEP135, which can bind to SAS6 (Lin et al., 2013a) and to MTs (Kraatz et al., 2016) (Fig. 2B). Moreover, CEP135 recruits CPAP (also known as CENPJ), a protein implicated in MT stability, to the centriole wall (Lin et al., 2013a). In turn, CPAP will recruit CEP120, which allows CCDC52 (also known as SPICE1) to be incorporated into the complex (Comartin et al., 2013). Although CEP135 lies upstream of the other members of the complex in the recruitment hierarchy, some kind of positive feedback must exist between the different members of the complex, as depletion of CPAP, CEP120 or SPICE1 reduces CEP135 recruitment, ultimately impairing centriole elongation (Comartin et al., 2013). Centriole length is positively regulated by CPAP and CEP120 (Keller et al., 2009; Lin et al., 2013b; Schmidt et al., 2009) and negatively regulated by CCP110 and CEP97, which cap the distal end of centrioles (Schmidt et al., 2009; Spektor et al., 2007). The timely restriction of elongation is at least in part controlled through CPAP availability, which is regulated throughout the cell cycle by both APC/$C^{FZR1}$-driven proteolysis and degradation mediated by poly-ADP-ribosylation (PARsylation) (Kim et al., 2012; Tang et al., 2009).

### Centrosome maturation takes place during the $G_2$ phase of the cell cycle

During late $G_2$ and the mitotic prophase, the centrosome increases in size from ∼500 nm in diameter during interphase to several micrometres at mitosis (Woodruff et al., 2017). This is mainly due to the recruitment of PCM components that enhance its MT-nucleating capacity to guarantee correct spindle pole formation during mitosis (Meraldi and Nigg, 2002). In addition to PCM recruitment, DAs and SDAs are assembled at the G2 phase of the cell cycle. This maturation process initiates the breaking of the intrinsic centrosome molecular asymmetries (Figs 2C and 3C).

Up until the $G_2$/M transition, centrosome separation is prevented by a flexible proteinaceous linker that bridges the centriole walls via CEP135 (Fig. 2B) (Lin et al., 2013a). Besides binding to the MT triplets of the centriole wall and the SAS6 cartwheel structure, CEP135 interacts with the linker protein CNAP1 (also known as CEP250) (Kim et al., 2008b). CNAP1 segregates into two pools at the proximal ends of the maternal and daughter centriole (Fry et al., 1998), which operate as anchor points for CROCC (also known as rootletin), a filamentous protein that forms the rootlet fibres that join the centrioles (Bahe et al., 2005; Yang et al., 2006). A further component of the proteinaceous linker is CEP68, which is a filament modulator that regulates the thickness of the rootlet fibres (Vlijm et al., 2018). Although CNAP1, CROCC and CEP68 are the best studied components of the linker, LRRC45 and CNTLN are also associated with this structure (Fang et al., 2014; He et al., 2013).

Journal of Cell Science (2022) 135, jcs259395. doi:10.1242/jcs.259395

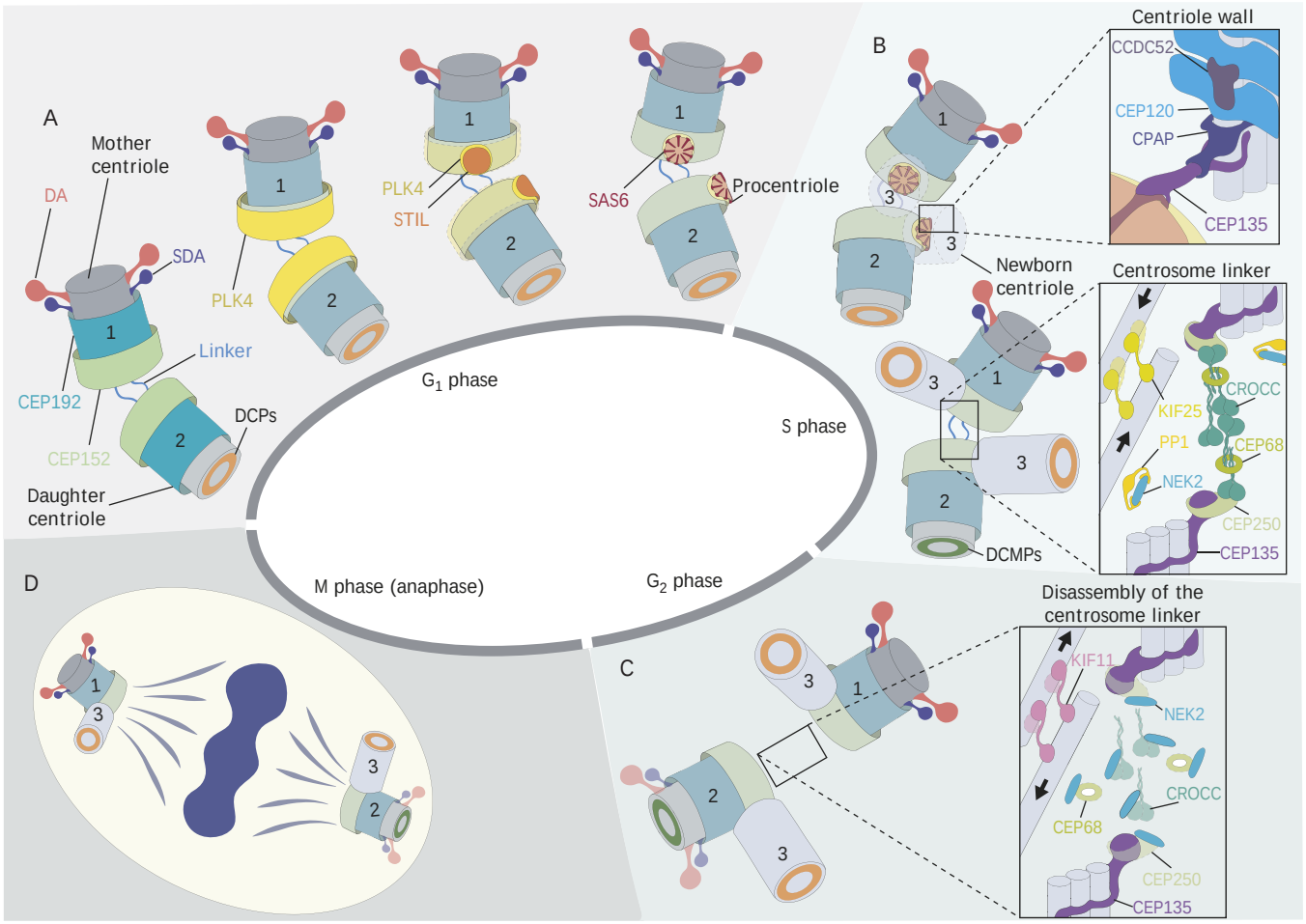


**Fig. 2. Self-replication and maturation of the centrosome during the cell cycle.** (A) In the mature centrosome, mother and daughter centrioles are connected through a proteinacous linker (mid-blue). The mother centriole (1) is decorated with distal (DA, terracotta) and subdistal appendages (SDA, dark-blue). Upon entering the cell cycle, CEP192 and CEP152 (inner components of the PCM), are recruited to the daughter centriole (2). On the daughter centriole, DCPs (orange ring) regulate centriole elongation. Restriction of PLK4 and STIL to a single focus ensures that only one procentriole cartwheel forms from a pre-existing centriole in $G_1$ phase. (B) Elongation of the newborn centriole (3) during S phase. The centriole wall expanded view shows proteins contributing to cartwheel–MT stabilization. Newborn centriole elongation terminates in S phase with the addition of DCPs. The transition from daughter to new mother centriole includes the loss of DCPs and the recruitment of new daughter centriole maturation proteins (DCMP, green ring). The expanded view shows proteins in the centrosome linker connecting centriolar MTs. (C) Daughter centriole maturation into a new 'mother' by the assembly of DAs and SDAs occurs during the $G_2$ phase of the cell cycle. Centrosome separation, caused by the disassembly of the linker (see expanded view) occurs at the end of $G_2$. (D) Two molecularly distinct centrosomes nucleate the mitotic spindle. Centriolar MTs and PCM are not shown for clarity.

In addition to the proteinaceous linker, MT fibres are also involved in preventing centrosome separation. As such, sliding of anti-parallel MTs is induced through the activity of the bipolar minus-end-directed kinesin KIF25, generating forces that tether the centrosomes together until mitosis (Decarreau et al., 2017; Jean et al., 1999).

#### Duplicated centrosomes separate on entering mitosis

At the end of $G_2$, the proteinaceous linker is disrupted to allow the two centrosomes to separate and polarize at mitosis (Fig. 2C,D). The stability of the proteinaceous linker is mainly regulated by the kinase NEK2 and the phosphatase PP1 (Helps et al., 2000). The balance between NEK2 and PP1 activities is determined by activation of the Polo kinase PLK1, which in turn relies on cyclinA2–Cdk activity that is mediated by Aurora kinase A (AURKA) (Gheghiani et al., 2017). Upon its activation, NEK2 phosphorylates CNAP1 (Fry et al., 1998; Hardy et al., 2014) and CROCC (Bahe et al., 2005), inducing their displacement from the proteinaceous linker and ultimately triggering its dissolution (Fig. 2C) (Agircan et al., 2014; Fry et al., 2017b). Besides the dissolution of the proteinaceous linker, mechanical forces exerted by the MTs contribute to centrosome separation. KIF11 (also known as EG5), a member of the kinesin-5 subfamily of motor proteins, generates outward forces that antagonize KIF25 activity and so induce the sliding of anti-parallel MTs of the centrosome linker in opposing directions (Kapitein et al., 2005). The two separated centrosomes nucleate the mitotic spindle (Fig. 2D). From centriole duplication until anaphase, centrioles remain tightly engaged such that the proximal end of the newborn centriole lies in opposition to the lateral portion of the proximal end of the pre-existing centriole. During anaphase, the protease separase is activated in order to guarantee sister chromatid separation, and it also acts on centrosomes, leading to centriole disengagement (Tsou and Stearns, 2006).

### Centriole remodelling in cycling cells

As mentioned above, mature centrioles can be differentiated from immature (newborn and daughter) centrioles by the presence of their

Journal of Cell Science (2022) 135, jcs259395. doi:10.1242/jcs.259395

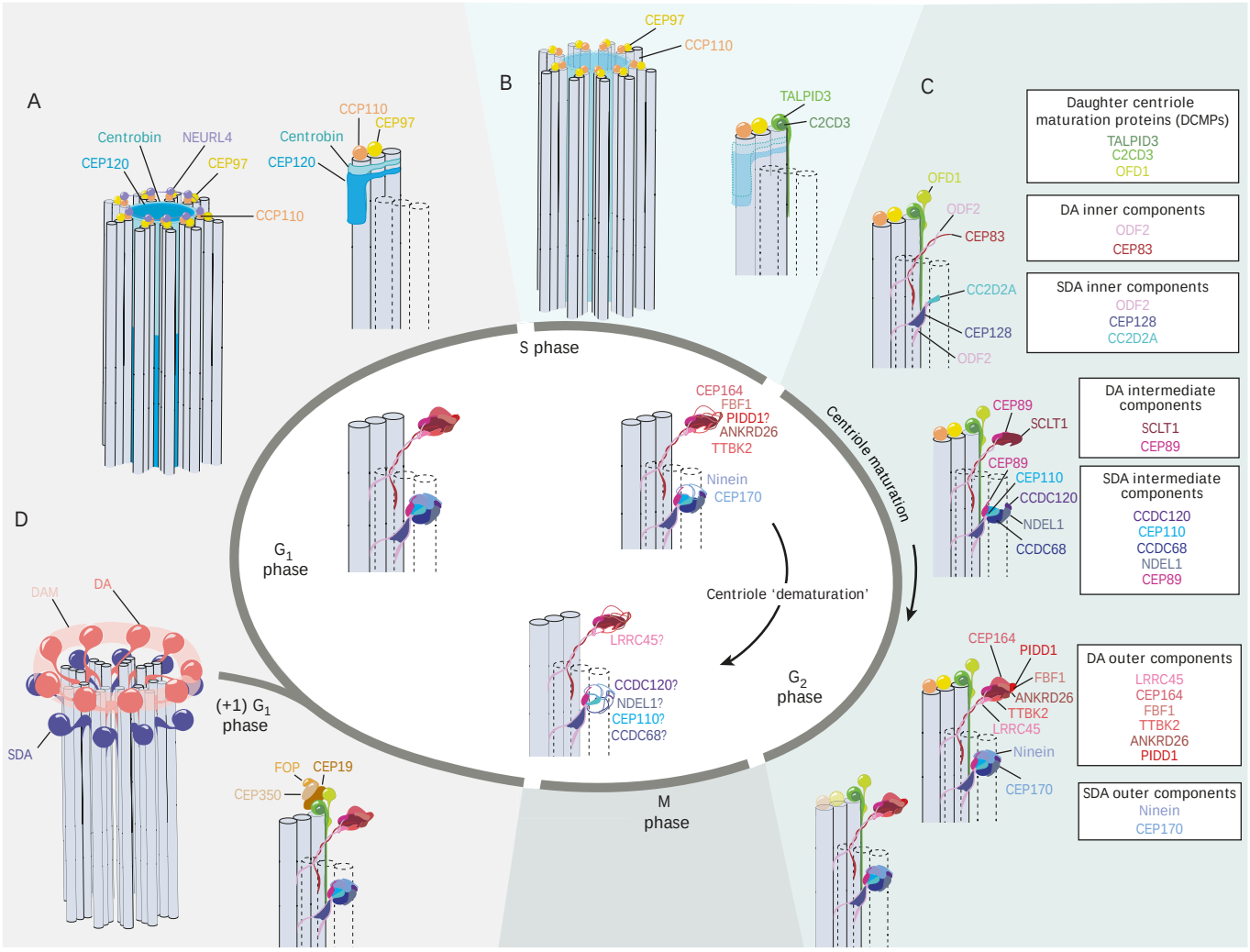


**Fig. 3. Assembly and disassembly of protein complexes contributing to centriole maturation during the cell cycle.** The assembly of protein complexes are depicted in the outer part of the circle. (A) MT triplets of the daughter centriole with proteins involved in centriole elongation (CEP120 and centrobin) and decorated with specific distal end capping proteins (CCP110, CEP97 and NEURL4). The scheme on the right illustrates a single MT triplet (grey) accommodating daughter centriole-specific proteins. (B) Daughter centriole maturation initiates at the end of S phase, with the removal of CEP120 and centrobin (pale blue), and the recruitment of daughter centriole maturation proteins (DCMPs) TALPID3 and C2CD3. (C) Daughter centriole maturation into a new mother centriole includes the sequential assembly of DAs and SDAs during the G2 phase of the cell cycle, and the disassembly of DCPs (CCP110, CEP97; spheres shown with transparency at the end of the G2). The text boxes indicate the specific proteins that are sequentially assembled within each indicated compartment. Partial disassembly of DAs and SDAs occurs as illustrated in the inner part of the circle (centriole 'dematuration'). During G2, proteins including CEP164, FBF1, ANKRD26 and TTBK2, disassemble from the DAs, while ninein and CEP170 disassemble from the SDAs. Proteins whose disassembly is predicted but has not been experimentally demonstrated are indicated with question marks. (D) After M phase, recruitment of the CEP350–FOP–CEP19 protein complex to the mature centriole contributes to its capacity to transform into a ciliary basal body, which contains DAs, SDAs and DAM.

appendages (DA and SDA) and the PCM (Fig. 1). These intrinsic centriole asymmetries are already present in the zygote, transmitted from the spermatozoan centrioles, since the oocyte does not have a functional centrosome (Avidor-Reiss and Fishman, 2019). Establishment of some of the best-understood molecular asymmetries of centrioles is co-ordinated with the cell cycle and generated by the recruitment and removal of relevant non-mature centriole proteins, as well as by appendage assembly and disassembly (Fig. 3).

### Specific DCPs contribute to centriole elongation

Although non-mature centrioles lack SDAs and DAs, they are enriched in DCPs that are sequentially incorporated into the growing centriole (Fig. 3A). CEP120, a member of the MT-stabilization complex, is thought to be the first newborn centriole-associated protein to be incorporated into the elongating centrioles (Comartin et al., 2013). The presence of CEP120 in the centriole allows centrobin to become incorporated, which will interact with and prevent the degradation of CPAP, another member of the MT stabilization complex that is active during centriole elongation (Figs 2B and 3A) (Gudi et al., 2015; Wang and Dynlacht, 2018; Zou et al., 2005). As is the case for CEP120, centrobin follows the dynamics of the cell cycle and, during the $G_1$/S transition, is enriched at newborn centrioles. The longitudinal distribution of centrobin appears to be specifically enriched in the distal half of the centriole walls (Wang and Dynlacht, 2018; Zou et al., 2005), and the presence of both CEP120 and centrobin suppresses DA and SDA assembly (Fig. 3A) (Wang et al., 2018).

Subsequent to CEP120 and centrobin incorporation, NEURL4 localizes to the distal end of the daughter centrioles. NEURL4 is an

E3 ubiquitin ligase cofactor that interacts with CCP110 and thereby regulates its distal accumulation (Li et al., 2012; Loukil et al., 2017). CCP110 is a distal end-capping protein that contributes to centriole elongation and centrosome separation (Kim and Dynlacht, 2013; Schmidt et al., 2009; Spektor et al., 2007; Yadav et al., 2016). CCP110 interacts directly with CEP97 to form a DCP complex (Fig. 3A), which needs to be removed from the distal end of the daughter centriole before the final phase of centriole maturation (Spektor et al., 2007). Recent findings indicate that CEP97 not only acts as a recruitment factor for CCP110 (Spektor et al., 2007), but also contributes to the control of centriole length by regulating microtubule acetylation (Dobbelaere et al., 2020).

In addition to CCP110 and NEURL4, the poly(ADP-ribose) polymerase PARP3, which marks single-strand DNA breaks (Shall and de Murcia, 2000), preferentially interacts with the newborn centriole at its N-terminal domain (Augustin et al., 2003). Whether PARP3 is merely acting as part of a DNA-integrity checkpoint that controls the cell cycle, or whether it fulfils an additional role in centriole biogenesis and/or maturation remains to be elucidated. At the end of centriole elongation, the transition from newborn to daughter centriole is induced by the loss of specific newborn proteins, and the subsequent recruitment of new assembling proteins (Lin et al., 2013b; Mahjoub et al., 2010). Here, TALPID3 (also known as KIAA0586), which interacts with CCP110 (Kobayashi et al., 2014) and the distal part of CEP120, recruits C2CD3 and thus facilitates the removal of CEP120 and centrobin (Wu et al., 2014). C2CD3 also controls centriole elongation (Thauvin-Robinet et al., 2014) (Fig. 3B).

#### The assembly of DAs initiates maturation of the daughter centriole into a new mother centriole

The removal of specific newborn centriolar proteins allows OFD1, a centrosomal protein that modulates centriole length and the formation of distal appendages (Alfieri et al., 2020), to localize to the distal end of the daughter centriole (Fig. 3C); this is mediated by CEP90 and MNR (also known as PIBF1 and KIAA0753, respectively), protein components of the CSs (Kumar et al., 2021). OFD1 recruitment triggers DA formation, leading to the gradual maturation of the daughter centriole and it becoming a mother centriole in the next cell cycle (Wang et al., 2018). Components of DAs are assembled in a hierarchical manner, with first the inner, then the intermediate, and finally the outer components recruited to form a fully mature DA (Fig. 3C). OFD1 recruits the inner DA component CEP83 through a yet to be defined mechanism. This likely elicits events that lead to the incorporation of intermediate DA components, such as SCLT1 and CEP89 (Yang et al., 2018). The incorporation of SCLT1 subsequently triggers the recruitment of outer DA components, such as LRRC45 and probably CEP164; this in turn contributes to FBF1 recruitment, while CEP164 also recruits Tau tubulin kinase 2 (TTBK2) (Čajánek and Nigg, 2014; Kurtulmus et al., 2018; Tanos et al., 2013; Ye et al., 2014).

When fully mature, DAs adopt a pinwheel-like structure with a spherical head that connects through a thin stem to two MT triplets of the centriole wall (Wang et al., 2018). The connection with the centriole wall is thought to be established through ODF2, a SDA-associated protein that was also recently characterized as a proximal DA component (Chong et al., 2020; Huang et al., 2017; Kashihara et al., 2019; Tateishi et al., 2013), and through CEP83 (Yang et al., 2018). CEP83 is required for the recruitment of CEP89, SCLT1, FBF1 and CEP164 to appendages, without affecting the distribution of ODF2 (Tanos et al., 2013). Thus, ODF2 and CEP83 likely form the stem that joins the DA heads to the centriole wall (Figs 3C and 4C). CEP89, SCLT1, LRRC45, FBF1, CEP164, TTBK2 and the recently characterized centrosome protein ANKRD26, as well as PIDD1, are all known components of the DA head (Figs 3C and 4C) (Bowler et al., 2019; Burigotto et al., 2021; Evans et al., 2021; Lo et al., 2019; Tanos et al., 2013; Yang et al., 2018). In addition, super-resolution imaging of DAs has shown that there are also proteins filling the space between each pinwheel blade, constituting a new ultrastructural element, the distal appendage matrix (DAM) (Yang et al., 2018) (Fig. 4A). The correct localization of CEP164 and LRRC45 in the DA are required for DAM formation (Yang et al., 2018). Owing to its outer localization at the DA, ANKRD26 might also contribute to forming the DAM (Bowler et al., 2019).

#### The assembly of SDAs follows DA formation

Protein components of the SDA are also recruited gradually in a hierarchical manner; inner, intermediate and outer components are recruited to form fully mature SDAs with a spherical head that connects to two MT triplets of the centriole wall through a conical structure (Figs 3C and 4C). C2CD3 initiates the recruitment of ODF2 and likely a few additional inner SDA components (Thauvin-Robinet et al., 2014; Wang et al., 2018). However, it remains unknown whether this recruitment is mediated by direct interactions or through indirect mediators. The base of the conical SDA is formed by CC2D2A, ODF2 and CEP128, which form the inner SDA layer (Ishikawa et al., 2005; Kashihara et al., 2019; Tateishi et al., 2013; Veleri et al., 2014). Subsequently, CCDC120, CEP110 (also known as CNTRL), CCDC68 and NDEL1 interact with ODF2 and CEP128, establishing an intermediate layer (Chong et al., 2020; Huang et al., 2017; Kashihara et al., 2019; Tateishi et al., 2013). Interestingly, CEP89 is a DA protein implicated in ciliogenesis (Sillibourne et al., 2011; Tanos et al., 2013) and is also present in SDAs (Chong et al., 2020), highlighting that there is some overlap between DA and SDA composition. Finally, ninein and CEP170 form an outer layer, which interacts with at least CCDC120 and CCDC68 (Figs 3C and 4C) (Huang et al., 2017).

Some SDA proteins, such as CCDC68, CCDC120, ninein and CEP170, have also been detected at a second location, the proximal end of the centriole (Chong et al., 2020; Huang et al., 2017). Although the biological relevance of this dual distribution of some SDA components is not clear, we hypothesize that this secondary proximal site might serve as a rapid-access reservoir of factors, which would accelerate the maturation of the daughter centriole. As such, a delay owing to protein translation would be at least partially by-passed.

#### The assembly of the CEP350–FOP–CEP19 protein complex further contributes to centriole maturation and asymmetries

A protein complex formed by FOP (also known as CEP43), CEP350 and CEP19 has recently been reported to assemble in-between DAs and SDAs (Kanie et al., 2017; Mojarad et al., 2017; Nishijima et al., 2017) (Fig. 3D). C2CD3 contributes to the recruitment of CEP350 and FOP (Mojarad et al., 2017), while C2CD3, TALPID3 and OFD1 contribute to the specific localization of CEP19 during centriole maturation (Wang et al., 2018). Moreover, the recruitment of CEP19 appears to be linked to the removal of newborn centriole proteins, including CCP110, and contributes to the early steps of ciliary basal body formation through the recruitment of ciliary vesicles (Kanie et al., 2017; Mojarad et al., 2017; Wang et al., 2018). In summary, it appears that TALPID3 and C2CD3 are two main triggers of maturation, promoting assembly of the DA, SDA and the CEP350-FOP-CEP19 protein complex.

Journal of Cell Science (2022) 135, jcs259395. doi:10.1242/jcs.259395

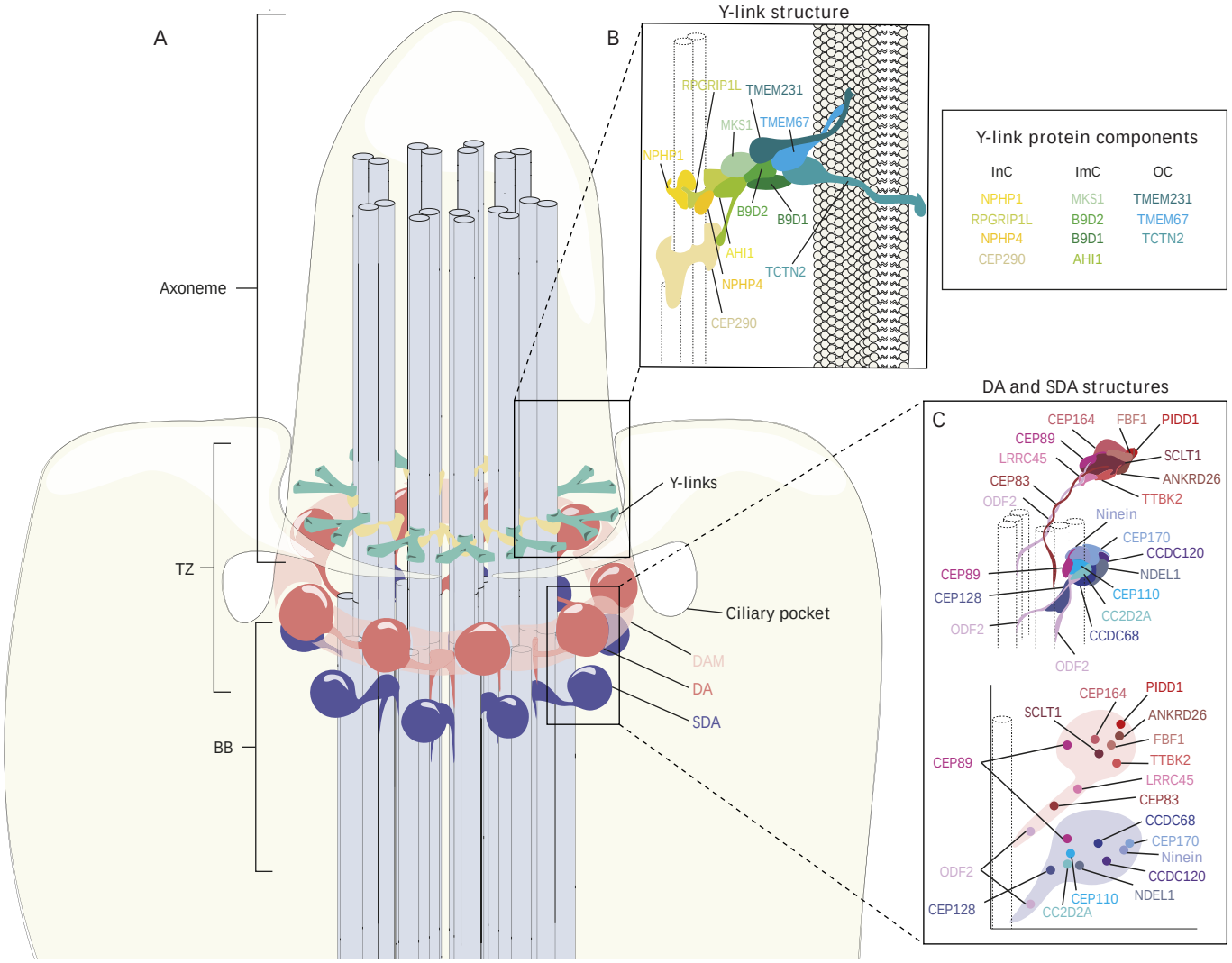


**Fig. 4. Mature centriole organization at the basal body of the cilium.** (A) Microtubule triplets of the basal body (BB) extend as doublets into the axoneme. This transition from triplets to doublets occurs at the transition zone (TZ), where Y-links connect microtubules to the extracellular membrane. (B) The relative position of protein complexes forming the Y-links that connect microtubule doublets to the plasma membrane. Proteins identified in the Y-link inner components (InC, in yellow/beige), the intermediate components (ImC, in greens), and the outer components (OC, in blues) are listed. (C) The relative positioning of DA (red) and SDA (blue) protein complexes as they associate to centriolar microtubule triplets.

Indeed, the recruitment of these proteins to the daughter centriole at the $G_1$/S transition represents the onset of the maturation process. Intriguingly, TALPID3 and C2CD3 are also present in the newborn centrioles, together with the CCP110 cap (Tsai et al., 2019), although they do not induce centriole maturation in growing newborn centrioles.

### Centriole appendages partially disassemble on entering mitosis

CEP164 is displaced from the centriole just before mitosis (Schmidt et al., 2012), which suggests that, in part at least, mature centriole appendages are disassembled prior to entering division. EM data indicates that fewer DAs exist during mitosis and that there is a reduction in the head density due to transient displacement of the outer DA components FBF1, CEP164, ANKRD26 and TTBK2 (Bowler et al., 2019). However, inner components, such as CEP83 and SCLT1, maintain the nine-fold association with the mother centriole during mitosis (Bowler et al., 2019). Interestingly, SDAs retain this nine-fold symmetry but, as occurs in DAs, their head density is significantly reduced (Vorobjev and Chentsov, 1982). Moreover, it has been reported that both CEP170 and ninein association with the centrosome is reduced during division (Brunet et al., 2004; Chen et al., 2003); therefore, SDAs may undergo a similar transient remodelling during mitosis to that undertaken by their outer components. Further studies are needed to confirm such a SDA partial disassembly and to better characterize this process in DAs by assessing the behaviour of other components. The biological significance of the transient remodelling of the outer elements of DAs and SDAs is not yet clear, although it has been proposed that it might be a mechanism to equalize the age gap between the two mother centrioles of sister cells when DAs and SDAs re-assemble. Owing to the spatiotemporal correlation between the transient disassembly of DAs and SDAs on the older mother centriole and the maturation of the younger mother centriole (Bowler et al., 2019; Nakagawa et al., 2001; Piel et al., 2000), we propose that this process serves as a mechanism to transfer the maturation state. We hypothesize that the disassembled DA and SDA elements from the older mother centrioles could be distributed evenly between both daughter cells at mitosis, and that this could be

one of the mechanisms contributing to balancing out the built-in centrosome asymmetries in order to generate two daughter cells with identical fate and behaviour.

## Cilia formation, a task for the mother centriole

One key function of centrosomes is to assemble cilia, MT-based organelles that protrude from the cell surface and can either be motile or non-motile. Motile cilia are required for cell locomotion and the propulsion of extracellular fluids, while non-motile primary cilia play critical roles in integrating signalling pathways (Mitchison and Valente, 2017). Particular attention has been paid recently to the role played by the primary cilium in the integration of growth factor signalling during neural development (Saade et al., 2018). Cilium assembly requires the transformation of the mother centriole into a basal body, which provides a template with nine-fold symmetry on which the axonemal structure of the cilium can be built (Fig. 4A). The basal body also dictates the position and orientation of the forming cilium. At the basal body, the centrosomal DA is involved in cilium assembly, while the SDA acts as a MT-anchoring point (Bornens, 2012; Clare et al., 2014). The TZ is situated just above the ciliary basal body and comprises the most proximal region of the cilium that separates the basal body from the axoneme. In functional cilia, the transport of molecules to the axoneme and ciliary membrane is tightly controlled, with the TZ acting as a ciliary gate that controls molecular access (Garcia-Gonzalo and Reiter, 2017).

### Cilia are templated by mature centriolar structures

Like DAs and SDAs, the TZ adopts a ring-like protein structure composed of repetitive units, the Y-links, which bind to ciliary MT doublets and connect them to the ciliary membrane (Gilula and Satir, 1972). Y-links are organized in three layers: an inner layer of proteins located close to the MT doublets of the axoneme, an outer layer of transmembrane proteins in the ciliary membrane, and an intermediate layer of proteins in-between (Fig. 4B). In addition to these layers, CEP290 provides the base upon which Y-link components assemble by occupying the space between the axoneme and the plasma membrane (Yang et al., 2015). In the absence of CEP290, the distance between the MTs and ciliary membrane increases and the Y-link structure is lost (Craige et al., 2010) (Fig. 4B).

The inner components of the Y-links identified to date are RPGRIP1L (also known as NPHP8) and NPHP1 (Sang et al., 2011; Shi et al., 2017; Yang et al., 2015). RPGRIP1L dysfunction has been associated with a loss of Y-link integrity (Jensen et al., 2015), as well as with a reduction in NPHP1 and further components in other layers (e.g. AHI1, TCTN2 and TMEM231) (Shi et al., 2017). However, a reduction in NPHP1 only has a minor effect on RPGRP1L, with the intermediate and outer layers remaining unaffected (Shi et al., 2017). Thus, it appears that RPGRP1L is the main scaffold protein of Y-links. NPHP4 is a member of the RPGRIP1L–NPHP1–NPHP4 complex located above CEP290 in the TZ (Czarnecki and Shah, 2012; Sang et al., 2011; Williams et al., 2011). We propose NPHP4 to be another component of the Y-link inner layer given that it has been reported that it mediates the interaction between RPGRIP1L and NPHP1 (Sang et al., 2011) (Fig. 4B). Moreover, NPHP4 abrogation correlates with a displacement of NPHP1 from the TZ (Jauregui and Barr, 2005; Williams et al., 2011).

Although both RPGRIP1L and NPHP1 contain specific protein domains for membrane targeting (C2 domains), super-resolution imaging data shows that they form a ring structure around MT doublets with a radius that is too small to contact the ciliary membrane (Shi et al., 2017; Yang et al., 2015). Thus, C2 domains might be responsible for establishing protein–protein interaction modules that connect the different TZ proteins, rather than acting as direct membrane anchors (Remans et al., 2014). Indeed, one of the C2 domains of RPGRIP1L is thought to be responsible for its interaction with NPHP4 (Roepman et al., 2005).

For the intermediate layer of Y-links, so far only a single component has been characterized, MKS1 (Yang et al., 2015). Super-resolution data places MKS1 outside the RPGRIP1L ring and internal to some outer-layer components (TMEM67 and TCTN2) (Yang et al., 2015). As B9D1, B9D2 and AHI1 share some protein domains (B9 and C2) with MKS1, have no transmembrane regions and form a complex with MKS1 (MKS1–B9D1–B9D2–AHI1 complex) (Dowdle et al., 2011; Remans et al., 2014; Zhang and Aravind, 2012), this suggests that AHI1, B9D1 and B9D2 are part of the intermediate layer (Fig. 4B). Similar to the inner layer, these potential components of the intermediate layer have C2- and B9-type membrane-targeting domains. As suggested above, these domains could not only anchor the protein to the membrane, but also mediate the protein–protein interactions that help maintain the integrity of the Y-link structure.

Finally, TMEM231, TMEM67 and TCTN2 are outer components of Y-links (Shi et al., 2017; Yang et al., 2015); they are transmembrane proteins that, through their intracellular domains, likely interact with intermediate layer components (Yang et al., 2015). These proteins act as anchors that connect the Y-link base with the membrane, ultimately joining the ciliary membrane to the MT doublets and regulating the access of membrane proteins to the ciliary membrane (Yang et al., 2015). Future work will further elucidate the role of TZ and basal body components in ciliary biology, how cilia regulate cell signalling, both in organ development and tissue homeostasis, and also provide a better understanding as to how these components contribute to cilia-associated diseases (ciliopathies).

## Concluding remarks and further considerations

The past decade of technological breakthroughs, including super-resolution microscopy, have paved the way for a detailed characterization of the 3D structure of the centrosome, as well as notable differences in the molecular composition of mother and daughter centrioles, thereby enhancing our understanding of relevant mechanisms underlying centrosome biology. This has led to our current view of the centrosome as a highly dynamic organelle that replicates in a semi-conservative manner in synchrony with the cell cycle. Indeed, the appendages that decorate the mother centriole are highly organized protein complexes that dynamically assemble and disassemble at the distal part of the centrioles during the late phases of the cell cycle. Because the assembly of these appendages in the new mother centriole is not fully acquired in one cell cycle, the organization of the mitotic spindle is intrinsically asymmetric. As a consequence, these built-in centrosome asymmetries establish the general rule that cell division is intrinsically asymmetric. This feature may be fundamental when cell division gives rise to two distinct cell types, such as when a stem cell divides to give rise to a stem cell and a cell that differentiates into another cell type. In addition, future research is needed to understand the mechanisms that a dividing cell utilizes to equalize these centrosome asymmetries in order to symmetrically divide.

The functional relevance of this small organelle in cell signalling, whether organized as a cilium basal body or as a mitotic spindle pole, in organ development and tissue homeostasis is only

beginning to be understood. Research in the coming years should pave the way to furthering our knowledge on the biology of this organelle and the pathological consequences of centrosome malfunction, such as seen in ciliopathies or neurodevelopmental congenital malformations.

#### Acknowledgements
The authors would like to apologise to those researchers whose primary data has not been directly cited in this Review article.

#### Competing interests
The authors declare no competing or financial interests.

#### Funding
The work in laboratory of E.M. is supported by the Spanish Ministry of Science and Innovation (grants nos PID2019-104134GB-I00 and RED2018-102553-T). J.B.A. is a recipient of a BES-2017-080050 PhD scholarship from the Spanish Ministry of Science and Innovation. P.L.F. is a recipient of a PRE2020-093886 PhD scholarship from the Spanish Ministry of Science and Innovation.

#### References
**Agircan, F. G., Schiebel, E. and Mardin, B. R.** (2014). Separate to operate: control of centrosome positioning and separation. *Philos. Trans. R. Soc. B Biol. Sci.* **369**, 20130461. doi:10.1098/rstb.2013.0461

**Alfieri, M., Iaconis, D., Tammaro, R., Perone, L., Calì, G., Nitsch, L., Dougherty, G. W., Ragnini-Wilson, A. and Franco, B.** (2020). The centrosomal/basal body protein OFD1 is required for microtubule organization and cell cycle progression. *Tissue Cell* **64**, 101369. doi:10.1016/j.tice.2020.101369

**Arquint, C., Sonnen, K. F., Stierhof, Y.-D. and Nigg, E. A.** (2012). Cell-cycle-regulated expression of STIL controls centriole number in human cells. *J. Cell Sci.* **125**, 1342-1352. doi:10.1242/jcs.099887

**Arquint, C., Gabryjonczyk, A.-M. and Nigg, E. A.** (2014). Centrosomes as signalling centres. *Philos. Trans. R. Soc. B Biol. Sci.* **369**, 20130464. doi:10.1098/rstb.2013.0464

**Augustin, A., Spenlehauer, C., Dumond, H., Ménisier-de Murcia, J., Piel, M., Schmit, A.-C., Apiou, F., Vonesch, J.-L., Kock, M., Bornens, M. et al.** (2003). PARP-3 localizes preferentially to the daughter centriole and interferes with the G1/S cell cycle progression. *J. Cell Sci.* **116**, 1551-1562. doi:10.1242/jcs.00341

**Avidor-Reiss, T. and Fishman, E. L.** (2019). It takes two to tango. *Soc. Reprod. Fertil.* **1**, 34.

**Azimzadeh, J. and Marshall, W. F.** (2010). Building the centriole. *Curr. Biol.* **20**, R816-R825. doi:10.1016/j.cub.2010.08.010

**Bahe, S., Stierhof, Y.-D., Wilkinson, C. J., Leiss, F. and Nigg, E. A.** (2005). Rootletin forms centriole-associated filaments and functions in centrosome cohesion. *J. Cell Biol.* **171**, 27-33. doi:10.1083/jcb.200504107

**Banterle, N. and Gönczy, P.** (2017). Centriole biogenesis: from identifying the characters to understanding the plot. *Annu. Rev. Cell Dev. Biol.* **33**, 23-49. doi:10.1146/annurev-cellbio-100616-060454

**Bärenz, F., Mayilo, D. and Gruss, O. J.** (2011). Centriolar satellites: busy orbits around the centrosome. *Eur. J. Cell Biol.* **90**, 983-989. doi:10.1016/j.ejcb.2011.07.007

**Bettencourt-Dias, M., Rodrigues-Martins, A., Carpenter, L., Riparbelli, M., Lehmann, L., Gatt, M. K., Carmo, N., Balloux, F., Callaini, G. and Glover, D. M.** (2005). SAK/PLK4 is required for centriole duplication and flagella development. *Curr. Biol.* **15**, 2199-2207. doi:10.1016/j.cub.2005.11.042

**Bornens, M.** (2012). The centrosome in cells and organisms. *Science* **335**, 422-426. doi:10.1126/science.1209037

**Boveri, T.** (1900). Zellen-Studien Vol. 4: Ueber die Natur der Centrosomen.

**Bowler, M., Kong, D., Sun, S., Nanjundappa, R., Evans, L., Farmer, V., Holland, A., Mahjoub, M. R., Sui, H. and Loncarek, J.** (2019). High-resolution characterization of centriole distal appendage morphology and dynamics by correlative STORM and electron microscopy. *Nat. Commun.* **10**, 993. doi:10.1038/s41467-018-08216-4

**Brunet, S., Sardon, T., Zimmerman, T., Wittmann, T., Pepperkok, R., Karsenti, E. and Vernos, I.** (2004). Characterization of the TPX2 domains involved in microtubule nucleation and spindle assembly in Xenopus egg extracts. *Mol. Biol. Cell* **15**, 5318-5328. doi:10.1091/mbc.e04-05-0385

**Burigotto, M., Mattivi, A., Migliorati, D., Magnani, G., Valentini, C., Roccuzzo, M., Offterdinger, M., Pizzato, M., Schmidt, A., Villunger, A. et al.** (2021). Centriolar distal appendages activate the centrosome-PIDDosome-p53 signalling axis via ANKRD26. *EMBO J.* **40**, 1-22. doi:10.15252/embj.2020104844

**Bystrevskaya, V. B., Lichkun, V. V., Antonov, A. S. and Perov, N. A.** (1988). An ultrastructural study of centriolar complexes in adult and embryonic human aortic endothelial cells. *Tissue Cell* **20**, 493-503. doi:10.1016/0040-8166(88)90052-3

**Bystrevskaya, V. B., Lichkun, V. V., Krushinsky, A. V. and Smirnov, V. N.** (1992). Centriole modification in human aortic endothelial cells. *J. Struct. Biol.* **109**, 1-12. doi:10.1016/1047-8477(92)90061-E

**Čajánek, L. and Nigg, E. A.** (2014). Cep164 triggers ciliogenesis by recruiting Tau tubulin kinase 2 to the mother centriole. *Proc. Natl. Acad. Sci. USA* **111**, E2841-E2850. doi:10.1073/pnas.1401777111

**Chen, C.-H., Howng, S.-L., Cheng, T.-S., Chou, M.-H., Huang, C.-Y. and Hong, Y.-R.** (2003). Molecular characterization of human ninein protein: Two distinct subdomains required for centrosomal targeting and regulating signals in cell cycle. *Biochem. Biophys. Res. Commun.* **308**, 975-983. doi:10.1016/S0006-291X(03)01510-9

**Chong, W. M., Wang, W.-J., Lo, C.-H., Chiu, T.-Y., Chang, T.-J., Liu, Y.-P., Tanos, B., Mazo, G., Tsou, M.-F. B., Jane, W.-N. et al.** (2020). Super-resolution microscopy reveals coupling between mammalian centriole subdistal appendages and distal appendages. *eLife* **9**, e53580. doi:10.7554/eLife.53580

**Clare, D. K., Magescas, J., Piolot, T., Dumoux, M., Vesque, C., Pichard, E., Dang, T., Duvauchelle, B., Poirier, F. and Delacour, D.** (2014). Basal foot MTOC organizes pillar MTs required for coordination of beating cilia. *Nat. Commun.* **5**, 4888. doi:10.1038/ncomms5888

**Comartin, D., Gupta, G. D., Fussner, E., Coyaud, É., Hasegan, M., Archinti, M., Cheung, S. W. T., Pinchev, D., Lawo, S., Raught, B. et al.** (2013). CEP120 and SPICE1 cooperate with CPAP in centriole elongation. *Curr. Biol.* **23**, 1360-1366. doi:10.1016/j.cub.2013.06.002

**Conduit, P. T., Wainman, A. and Raff, J. W.** (2015). Centrosome function and assembly in animal cells. *Nat. Rev. Mol. Cell Biol.* **16**, 611-624. doi:10.1038/nrm4062

**Craige, B., Tsao, C.-C., Diener, D. R., Hou, Y., Lechtreck, K.-F., Rosenbaum, J. L. and Witman, G. B.** (2010). CEP290 tethers flagellar transition zone microtubules to the membrane and regulates flagellar protein content. *J. Cell Biol.* **190**, 927-940. doi:10.1083/jcb.201006105

**Cunha-Ferreira, I., Rodrigues-Martins, A., Bento, I., Riparbelli, M., Zhang, W., Laue, E., Callaini, G., Glover, D. M. and Bettencourt-Dias, M.** (2009). The SCF/Slimb ubiquitin ligase limits centrosome amplification through degradation of SAK/PLK4. *Curr. Biol.* **19**, 43-49. doi:10.1016/j.cub.2008.11.037

**Cunha-Ferreira, I., Bento, I., Pimenta-Marques, A., Jana, S. C., Lince-Faria, M., Duarte, P., Borrego-Pinto, J., Gilberto, S., Amado, T., Brito, D. et al.** (2013). Regulation of autophosphorylation controls PLK4 self-destruction and centriole number. *Curr. Biol.* **23**, 2245-2254. doi:10.1016/j.cub.2013.09.037

**Czarnecki, P. G. and Shah, J. V.** (2012). The ciliary transition zone: From morphology and molecules to medicine. *Trends Cell Biol.* **22**, 201-210. doi:10.1016/j.tcb.2012.02.001

**Dammermann, A. and Merdes, A.** (2002). Assembly of centrosomal proteins and microtubule organization depends on PCM-1. *J. Cell Biol.* **159**, 255-266. doi:10.1083/jcb.200204023

**Decarreau, J., Wagenbach, M., Lynch, E., Halpern, A. R., Vaughan, J. C., Kollman, J. and Wordeman, L.** (2017). The tetrameric kinesin Kif25 suppresses pre-mitotic centrosome separation to establish proper spindle orientation. *Nat. Cell Biol.* **19**, 384-390. doi:10.1038/ncb3486

**Dobbelaere, J., Schmidt Cernohorska, M., Huranova, M., Slade, D. and Dammermann, A.** (2020). Cep97 is required for centriole structural integrity and cilia formation in Drosophila. *Curr. Biol.* **30**, 3045-3056.e7. doi:10.1016/j.cub.2020.05.078

**Dowdle, W. E., Robinson, J. F., Kneist, A., Sirerol-Piquer, M. S., Frints, S. G. M., Corbit, K. C., Zaghloul, N. A., Van Lijnschoten, G., Mulders, L., Verver, D. E. et al.** (2011). Disruption of a ciliary B9 protein complex causes meckel syndrome. *Am. J. Hum. Genet.* **89**, 589. doi:10.1016/j.ajhg.2011.09.013

**Evans, L. T., Anglen, T., Scott, P., Lukasik, K., Loncarek, J. and Holland, A. J.** (2021). ANKRD26 recruits PIDD1 to centriolar distal appendages to activate the PIDDosome following centrosome amplification. *EMBO J.* **40**, e105106. doi:10.15252/embj.2020105106

**Fang, G., Zhang, D., Yin, H., Zheng, L., Bi, X. and Yuan, L.** (2014). Centlein mediates an interaction between C-Nap1 and Cep68 to maintain centrosome cohesion. *J. Cell Sci.* **127**, 1631-1639. doi:10.1242/jcs.139451

**Fry, A. M., Mayor, T., Meraldi, P., Stierhof, Y.-D., Tanaka, K. and Nigg, E. A.** (1998). C-Nap1, a novel centrosomal coiled-coil protein and candidate substrate of the cell cycle-regulated protein kinase Nek2. *J. Cell Biol.* **141**, 1563-1574. doi:10.1083/jcb.141.7.1563

**Fry, A. M., Sampson, J., Shak, C. and Shackleton, S.** (2017a). Recent advances in pericentriolar material organization: ordered layers and scaffolding gels. *F1000Research* **6**, 1622. doi:10.12688/f1000research.11652.1

**Fry, A. M., Bayliss, R. and Roig, J.** (2017b). Mitotic regulation by NEK kinase networks. *Front. Cell Dev. Biol.* **5**, 102. doi:10.3389/fcell.2017.00102

**Fu, J. and Glover, D. M.** (2012). Structured illumination of the interface between centriole and peri-centriolar material. *Open Biol.* **2**, 120104. doi:10.1098/rsob.120104

**Garcia-Gonzalo, F. R. and Reiter, J. F.** (2017). Open Sesame: How transition fibers and the transition zone control ciliary composition. *Cold Spring Harb. Perspect. Biol.* **9**, a028134. doi:10.1101/cshperspect.a028134

**Gheghiani, L., Loew, D., Lombard, B., Mansfeld, J. and Gavet, O.** (2017). PLK1 activation in late G2 sets up commitment to mitosis. *Cell Rep.* **19**, 2060-2073. doi:10.1016/j.celrep.2017.05.031

**Gilula, N. B. and Satir, P.** (1972). The ciliary necklace: a ciliary membrane specialization. *J. Cell Biol.* **53**, 494-509. doi:10.1083/jcb.53.2.494

**Gudi, R., Haycraft, C. J., Bell, P. D., Li, Z. and Vasu, C.** (2015). Centrobin-mediated regulation of the centrosomal protein 4.1-associated protein (CPAP) level limits centriole length during elongation stage. *J. Biol. Chem.* **290**, 6890-6902. doi:10.1074/jbc.M114.603423

**Habedanck, R., Stierhof, Y.-D., Wilkinson, C. J. and Nigg, E. A.** (2005). The Polo kinase Plk4 functions in centriole duplication. *Nat. Cell Biol.* **7**, 1140-1146. doi:10.1038/ncb1320

**Hames, R. S., Crookes, R. E., Straatman, K. R., Merdes, A., Hayes, M. J., Faragher, A. J. and Fry, A. M.** (2005). Dynamic recruitment of Nek2 kinase to the centrosome involves microtubules, PCM-1, and localized proteasomal degradation. *Mol. Biol. Cell.* **16**, 1569-2127. doi:10.1091/mbc.e04-08-0688

**Hardy, T., Lee, M., Hames, R. S., Prosser, S. L., Cheary, D.-M., Samant, M. D., Schultz, F., Baxter, J. E., Rhee, K. and Fry, A. M.** (2014). Multisite phosphorylation of C-Nap1 releases it from Cep135 to trigger centrosome disjunction. *J. Cell Sci.* **127**, 2493-2506. doi:10.1242/jcs.142331

**He, R., Huang, N., Bao, Y., Zhou, H., Teng, J. and Chen, J.** (2013). LRRC45 is a centrosome linker component required for centrosome cohesion. *Cell Rep.* **4**, 1100-1107. doi:10.1016/j.celrep.2013.08.005

**Heath, I. B., Kaminskyj, S. G. and Bauchop, T.** (1986). Basal body loss during fungal zoospore encystment: evidence against centriole autonomy. *J. Cell Sci.* **83**, 135-140. doi:10.1242/jcs.83.1.135

**Helps, N. R., Luo, X., Barker, H. M. and Cohen, P. T. W.** (2000). NIMA-related kinase 2 (Nek2), a cell-cycle-regulated protein kinase localized to centrosomes, is complexed to protein phosphatase 1. *Biochem. J.* **349**, 509-518. doi:10.1042/bj3490509

**Huang, N., Xia, Y., Zhang, D., Wang, S., Bao, Y., He, R., Teng, J. and Chen, J.** (2017). Hierarchical assembly of centriole subdistal appendages via centrosome binding proteins CCDC120 and CCDC68. *Nat. Commun.* **8**, 15057. doi:10.1038/ncomms15057

**Ibrahim, R., Messaoudi, C., Chichon, F. J., Celati, C. and Marco, S.** (2009). Electron tomography study of isolated human centrioles. *Microsc. Res. Tech.* **72**, 42-48. doi:10.1002/jemt.20637

**Ishikawa, H., Kubo, A., Tsukita, S. and Tsukita, S.** (2005). Odf2-deficient mother centrioles lack distal/subdistal appendages and the ability to generate primary cilia. *Nat. Cell Biol.* **7**, 517-524. doi:10.1038/ncb1251

**Jana, S. C.** (2021). Centrosome structure and biogenesis: variations on a theme? *Semin. Cell Dev. Biol.* **110**, 123-138. doi:10.1016/j.semcdb.2020.10.014

**Jauregui, A. R. and Barr, M. M.** (2005). Functional characterization of the C. elegans nephrocystins NPHP-1 and NPHP-4 and their role in cilia and male sensory behaviors. *Exp. Cell Res.* **305**, 333-342. doi:10.1016/j.yexcr.2005.01.008

**Jean, C., Tollon, Y., Raynaud-Messina, B. and Wright, M.** (1999). The mammalian interphase centrosome: two independent units maintained together by the dynamics of the microtubule cytoskeleton. *Eur. J. Cell Biol.* **78**, 549-560. doi:10.1016/S0171-9335(99)80020-X

**Jensen, V. L., Li, C., Bowie, R. V., Clarke, L., Mohan, S., Blacque, O. E. and Leroux, M. R.** (2015). Formation of the transition zone by Mks5/Rpgrip1L establishes a ciliary zone of exclusion (CIZE) that compartmentalises ciliary signalling proteins and controls PIP2 ciliary abundance. *EMBO J.* **34**, 2537-2556. doi:10.15252/embj.201488044

**Kanie, T., Abbott, K. L., Mooney, N. A., Plowey, E. D., Demeter, J. and Jackson, P. K.** (2017). The CEP19-RABL2 GTPase complex binds IFT-B to initiate intraflagellar transport at the ciliary base. *Dev. Cell.* **42**, 22-36.e12. doi:10.1016/j.devcel.2017.05.016

**Kapitein, L. C., Peterman, E. J. G., Kwok, B. H., Kim, J. H., Kapoor, T. M. and Schmidt, C. F.** (2005). The bipolar mitotic kinesin Eg5 moves on both microtubules that it crosslinks. *Nature* **435**, 114-118. doi:10.1038/nature03503

**Kashihara, H., Chiba, S., Kanno, S.-I., Suzuki, K., Yano, T. and Tsukita, S.** (2019). Cep128 associates with Odf2 to form the subdistal appendage of the centriole. *Genes Cells* **24**, 231-243. doi:10.1111/gtc.12668

**Keller, L. C., Geimer, S., Romijn, E., Yates, J., Zamora, I. and Marshall, W. F.** (2009). Molecular architecture of the centriole proteome: the conserved WD40 domain protein POC1 is required for centriole duplication and length control. *Mol. Biol. Cell.* **20**, 1119-1267. doi:10.1091/mbc.e08-06-0619

**Keller, D., Orpinell, M., Olivier, N., Wachsmuth, M., Mahen, R., Wyss, R., Hachet, V., Ellenberg, J., Manley, S. and Gönczy, P.** (2014). Mechanisms of HsSAS-6 assembly promoting centriole formation in human cells. *J. Cell Biol.* **204**, 697-712. doi:10.1083/jcb.201307049

**Khodjakov, A., Rieder, C. L., Sluder, G., Cassels, G., Sibon, O. and Wang, C.-L.** (2002). De novo formation of centrosomes in vertebrate cells arrested during S phase. *J. Cell Biol.* **158**, 1171-1181. doi:10.1083/jcb.200205102

**Kim, S. and Dynlacht, B. D.** (2013). Assembling a primary cilium. *Curr. Opin. Cell Biol.* **25**, 506-511. doi:10.1016/j.ceb.2013.04.011

**Kim, J., Krishnaswami, S. R. and Gleeson, J. G.** (2008a). CEP290 interacts with the centriolar satellite component PCM-1 and is required for Rab8 localization to the primary cilium. *Hum. Mol. Genet.* **17**, 3796-3805. doi:10.1093/hmg/ddn277

**Kim, K., Lee, S., Chang, J. and Rhee, K.** (2008b). A novel function of CEP135 as a platform protein of C-NAP1 for its centriolar localization. *Exp. Cell Res.* **314**, 3692-3700. doi:10.1016/j.yexcr.2008.09.016

**Kim, M. K., Dudognon, C. and Smith, S.** (2012). Tankyrase 1 regulates centrosome function by controlling CPAP stability. *EMBO Rep.* **13**, 724-732. doi:10.1038/embor.2012.86

**Kim, T.-S., Park, J.-E., Shukla, A., Choi, S., Murugan, R. N., Lee, J. H., Ahn, M., Rhee, K., Bang, J. K., Kim, B. Y. et al.** (2013). Hierarchical recruitment of Plk4 and regulation of centriole biogenesis by two centrosomal scaffolds, Cep192 and Cep152. *Proc. Natl. Acad. Sci. USA* **110**, E4849-E4857. doi:10.1073/pnas.1319656110

**Kim, M., O'Rourke, B. P., Soni, R. K., Jallepalli, P. V., Hendrickson, R. C. and Tsou, M.-F. B.** (2016). Promotion and suppression of centriole duplication are catalytically coupled through PLK4 to ensure centriole homeostasis. *Cell Rep.* **16**, 1195-1203. doi:10.1016/j.celrep.2016.06.069

**Kobayashi, T., Kim, S., Lin, Y.-C., Inoue, T. and Dynlacht, B. D.** (2014). The CP110-interacting proteins talpid3 and cep290 play overlapping and distinct roles in cilia assembly. *J. Cell Biol.* **204**, 215-229. doi:10.1083/jcb.201304153

**Komesli, S., Tournier, F., Paintrand, M., Margolis, R. L., Job, D. and Bornens, M.** (1989). Mass isolation of calf thymus centrosomes: identification of a specific configuration. *J. Cell Biol.* **109**, 2869-2878. doi:10.1083/jcb.109.6.2869

**Kraatz, S., Guichard, P., Obbineni, J. M., Olieric, N., Hatzopoulos, G. N., Hilbert, M., Sen, I., Missimer, J., Gönczy, P. and Steinmetz, M. O.** (2016). The human centriolar protein CEP135 contains a two-stranded coiled-coil domain critical for microtubule binding. *Structure* **24**, 1358-1371. doi:10.1016/j.str.2016.06.011

**Kumar, D., Rains, A., Herranz-Pérez, V., Lu, Q., Shi, X., Swaney, D. L., Stevenson, E., Krogan, N. J., Huang, B., Westlake, C. et al.** (2021). A ciliopathy complex builds distal appendages to initiate ciliogenesis. *J. Cell Biol.* **220**, e202011133. doi:10.1083/jcb.202011133

**Kurtulmus, B., Yuan, C., Schuy, J., Neuner, A., Hata, S., Kalamakis, G., Martin-Villalba, A. and Pereira, G.** (2018). LRRC45 contributes to early steps of axoneme extension. *J. Cell Sci.* **131**, jcs223594. doi:10.1242/jcs.223594

**Lawo, S., Hasegan, M., Gupta, G. D. and Pelletier, L.** (2012). Subdiffraction imaging of centrosomes reveals higher-order organizational features of pericentriolar material. *Nat. Cell Biol.* **14**, 1148-1158. doi:10.1038/ncb2591

**Li, J., Kim, S., Kobayashi, T., Liang, F.-X., Korzeniewski, N., Duensing, S. and Dynlacht, B. D.** (2012). Neurl4, a novel daughter centriole protein, prevents formation of ectopic microtubule organizing centres. *EMBO Rep.* **13**, 547-553. doi:10.1038/embor.2012.40

**Lin, Y.-C., Chang, C.-W., Hsu, W.-B., Tang, C.-J. C., Lin, Y.-N., Chou, E.-J., Wu, C.-T. and Tang, T.-K.** (2013a). Human microcephaly protein CEP135 binds to hSAS-6 and CPAP, and is required for centriole assembly. *EMBO J.* **32**, 1141-1154. doi:10.1038/emboj.2013.56

**Lin, Y.-N., Wu, C.-T., Lin, Y.-C., Hsu, W.-B., Tang, C.-J. C., Chang, C.-W. and Tang, T. K.** (2013b). CEP120 interacts with CPAP and positively regulates centriole elongation. *J. Cell Biol.* **202**, 211-219. doi:10.1083/jcb.201212060

**Lo, C.-H., Lin, I.-H., Yang, T. T., Huang, Y.-C., Tanos, B. E., Chou, P.-C., Chang, C.-W., Tsay, Y.-G., Liao, J.-C. and Wang, W.-J.** (2019). Phosphorylation of CEP83 by TTBK2 is necessary for cilia initiation. *J. Cell Biol.* **218**, 3489-3505. doi:10.1083/jcb.201811142

**Loukil, A., Tormanen, K. and Sütterlin, C.** (2017). The daughter centriole controls ciliogenesis by regulating Neurl-4 localization at the centrosome. *J. Cell Biol.* **216**, 1287-1300. doi:10.1083/jcb.201608119

**Mahjoub, M. R., Xie, Z. and Stearns, T.** (2010). Cep120 is asymmetrically localized to the daughter centriole and is essential for centriole assembly. *J. Cell Biol.* **191**, 331-346. doi:10.1083/jcb.201003009

**Marshall, W. F.** (2009). Centriole Evolution. *Curr. Opin. Cell Biol.* **21**, 14-19. doi:10.1016/j.ceb.2009.01.008

**Marthiens, V. and Basto, R.** (2020). Centrosomes: the good and the bad for brain development. *Biol. Cell* **112**, 153-172. doi:10.1111/boc.201900090

**Mennella, V., Keszthelyi, B., Mcdonald, K. L., Chhun, B., Kan, F., Rogers, G. C., Huang, B. and Agard, D. A.** (2012). Subdiffraction-resolution fluorescence microscopy reveals a domain of the centrosome critical for pericentriolar material organization. *Nat. Cell Biol.* **14**, 1159-1168. doi:10.1038/ncb2597

**Meraldi, P. and Nigg, E. A.** (2002). The centrosome cycle. *FEBS Lett.* **521**, 9-13. doi:10.1016/S0014-5793(02)02865-X

**Mitchison, H. M. and Valente, E. M.** (2017). Motile and non-motile cilia in human pathology: from function to phenotypes. *J. Pathol.* **241**, 294-309. doi:10.1002/path.4843

**Mojarad, B. A., Gupta, G. D., Hasegan, M., Goudiam, O., Basto, R., Gingras, A.-C. and Pelletier, L.** (2017). CEP19 cooperates with FOP and CEP350 to drive early steps in the ciliogenesis programme. *Open Biol.* **7**, 170114. doi:10.1098/rsob.170114

**Moritz, M., Braunfeld, M. B., Guénebaut, V., Heuser, J. and Agard, D. A.** (2000). Structure of the γ-tubulin ring complex: a template for microtubule nucleation. *Nat. Cell Biol.* **2**, 365-370. doi:10.1038/35014058

**Moyer, T. C., Clutario, K. M., Lambrus, B. G., Daggubati, V. and Holland, A. J.** (2015). Binding of STIL to Plk4 activates kinase activity to promote centriole assembly. *J. Cell Biol.* **209**, 863-878. doi:10.1083/jcb.201502088

**Nabais, C., Pereira, S. G. and Bettencourt-Dias, M.** (2017). Noncanonical biogenesis of centrioles and basal bodies. *Cold Spring Harb. Symp. Quant. Biol.* **82**, 123-135. doi:10.1101/sqb.2017.82.034694

**Nakagawa, Y., Yamane, Y., Okanoue, T., Tsukita, S. and Tsukita, S.** (2001). Outer dense fiber 2 is a widespread centrosome scaffold component preferentially associated with mother centrioles: Its identification from isolated centrosomes. *Mol. Biol. Cell.* **12**, 1541-1910. doi:10.1091/mbc.12.6.1687

**Nigg, E. A. and Stearns, T.** (2011). The centrosome cycle: centriole biogenesis, duplication and inherent asymmetries. *Nat. Cell Biol.* **13**, 1154-1160. doi:10.1038/ncb2345

**Nishijima, Y., Hagiya, Y., Kubo, T., Takei, R., Katoh, Y. and Nakayama, K.** (2017). RABL2 interacts with the intraflagellar transport-B complex and CEP19 and participates in ciliary assembly. *Mol. Biol. Cell.* **28**, 1591-1711. doi:10.1091/mbc.e17-01-0017

**Ohta, M., Ashikawa, T., Nozaki, Y., Kozuka-Hata, H., Goto, H., Inagaki, M., Oyama, M. and Kitagawa, D.** (2014). Direct interaction of Plk4 with STIL ensures formation of a single procentriole per parental centriole. *Nat. Commun.* **5**, 5267. doi:10.1038/ncomms6267

**Paintrand, M., Moudjou, M., Delacroix, H. and Bornens, M.** (1992). Centrosome organization and centriole architecture: Their sensitivity to divalent cations. *J. Struct. Biol.* **108**, 107-128. doi:10.1016/1047-8477(92)90011-X

**Panic, M., Hata, S., Neuner, A. and Schiebel, E.** (2015). The centrosomal linker and microtubules provide dual levels of spatial coordination of centrosomes. *PLoS Genet.* **11**, e1005243. doi:10.1371/journal.pgen.1005243

**Park, S.-Y., Park, J.-E., Kim, T.-S., Kim, J. H., Kwak, M.-J., Ku, B., Tian, L., Murugan, R. N., Ahn, M., Komiya, S. et al.** (2014). Molecular basis for unidirectional scaffold switching of human Plk4 in centriole biogenesis. *Nat. Struct. Mol. Biol.* **21**, 696-703. doi:10.1038/nsmb.2846

**Piel, M., Meyer, P., Khodjakov, A., Rieder, C. L. and Bornens, M.** (2000). The respective contributions of the mother and daughter centrioles to centrosome activity and behavior in vertebrate cells. *J. Cell Biol.* **149**, 317-330. doi:10.1083/jcb.149.2.317

**Prosser, S. L. and Pelletier, L.** (2020). Centriolar satellite biogenesis and function in vertebrate cells. *J. Cell Sci.* **133**, jcs239566. doi:10.1242/jcs.239566

**Remans, K., Bürger, M., Vetter, I. R. and Wittinghofer, A.** (2014). C2 domains as protein-protein interaction modules in the ciliary transition zone. *Cell Rep.* **8**, 1-9. doi:10.1016/j.celrep.2014.05.049

**Robbins, E., Jentzsch, G. and Micali, A.** (1968). The centriole cycle in synchronized HeLa cells. *J. Cell Biol.* **36**, 329-339. doi:10.1083/jcb.36.2.329

**Roepman, R., Letteboer, S. J. F., Arts, H. H., Van Beersum, S. E. C., Lu, X., Krieger, E., Ferreira, P. A. and Cremers, F. P. M.** (2005). Interaction of nephrocystin-4 and RPGRIP1 is disrupted by nephronophthisis or Leber congenital amaurosis-associated mutations. *Proc. Natl. Acad. Sci. USA* **102**, 18520-18525. doi:10.1073/pnas.0505774102

**Rogers, G. C., Rusan, N. M., Roberts, D. M., Peifer, M. and Rogers, S. L.** (2009). The SCF Slimb ubiquitin ligase regulates Plk4/Sak levels to block centriole reduplication. *J. Cell Biol.* **184**, 225-229. doi:10.1083/jcb.200808049

**Saade, M., Blanco-Ameijeiras, J., Gonzalez-Gobartt, E. and Martı, E.** (2018). A centrosomal view of CNS growth. *Dev* **145**, dev170613. doi:10.1242/dev.170613

**Sang, L., Miller, J. J., Corbit, K. C., Giles, R. H., Brauer, M. J., Otto, E. A., Baye, L. M., Wen, X., Scales, S. J., Kwong, M. et al.** (2011). Mapping the NPHP-JBTS-MKS protein network reveals ciliopathy disease genes and pathways. *Cell* **145**, 513-528. doi:10.1016/j.cell.2011.04.019

**Schmidt, K. N., Kuhns, S., Neuner, A., Hub, B., Zentgraf, H. and Pereira, G.** (2012). Cep164 mediates vesicular docking to the mother centriole during early steps of ciliogenesis. *J. Cell Biol.* **199**, 1083-1101. doi:10.1083/jcb.201202126

**Schmidt, T. I., Kleylein-Sohn, J., Westendorf, J., Le Clech, M., Lavoie, S. B., Stierhof, Y. D. and Nigg, E. A.** (2009). Control of centriole length by CPAP and CP110. *Curr. Biol.* **19**, 1005-1011. doi:10.1016/j.cub.2009.05.016

**Schwarz, A., Sankaralingam, P., O'Connell, K. and Müller-Reichert, T.** (2018). Revisiting centrioles in nematodes—historic findings and current topics. *Cells* **7**, 101. doi:10.3390/cells7080101

**Shall, S. and de Murcia, G.** (2000). Poly(ADP-ribose) polymerase-1: what have we learned from the deficient mouse model? *Mutat. Res. DNA Repair* **460**, 1-15. doi:10.1016/S0921-8777(00)00016-1

**Shi, X., Garcia, G., Van De Weghe, J. C., McGorty, R., Pazour, G. J., Doherty, D., Huang, B. and Reiter, J. F.** (2017). Super-resolution microscopy reveals that disruption of ciliary transition-zone architecture causes Joubert syndrome. *Nat. Cell Biol.* **19**, 1178-1188. doi:10.1038/ncb3599

**Sillibourne, J. E., Specht, C. G., Izeddin, I., Hurbain, I., Tran, P., Triller, A., Darzacq, X., Dahan, M. and Bornens, M.** (2011). Assessing the localization of centrosomal proteins by PALM/STORM nanoscopy. *Cytoskeleton* **68**, 619-627. doi:10.1002/cm.20536

**Sillibourne, J. E., Hurbain, I., Grand-Perret, T., Goud, B., Tran, P. and Bornens, M.** (2013). Primary ciliogenesis requires the distal appendage component Cep123. *Biol. Open* **2**, 535-545. doi:10.1242/bio.20134457

**Sonnen, K. F., Schermelleh, L., Leonhardt, H. and Nigg, E. A.** (2012). 3D-structured illumination microscopy provides novel insight into architecture of human centrosomes. *Biol. Open* **1**, 965-976. doi:10.1242/bio.20122337

**Sonnen, K. F., Gabryjonczyk, A.-M., Anselm, E., Stierhof, Y.-D. and Nigg, E. A.** (2013). Human cep192 and cep152 cooperate in plk4 recruitment and centriole duplication. *J. Cell Sci.* **126**, 3223-3233. doi:10.1242/jcs.129502

**Spektor, A., Tsang, W. Y., Khoo, D. and Dynlacht, B. D.** (2007). Cep97 and CP110 suppress a cilia assembly program. *Cell* **130**, 678-690. doi:10.1016/j.cell.2007.06.027

**Tang, C.-J. C., Fu, R.-H., Wu, K.-S., Hsu, W.-B. and Tang, T. K.** (2009). CPAP is a cell-cycle regulated protein that controls centriole length. *Nat. Cell Biol.* **11**, 825-831. doi:10.1038/ncb1889

**Tanos, B. E., Yang, H.-J., Soni, R., Wang, W.-J., Macaluso, F. P., Asara, J. M. and Tsou, M.-F. B.** (2013). Centriole distal appendages promote membrane docking, leading to cilia initiation. *Genes Dev.* **27**, 163-168. doi:10.1101/gad.207043.112

**Tateishi, K., Yamazaki, Y., Nishida, T., Watanabe, S., Kunimoto, K., Ishikawa, H. and Tsukita, S.** (2013). Two appendages homologous between basal bodies and centrioles are formed using distinct Odf2 domains. *J. Cell Biol.* **203**, 417-425. doi:10.1083/jcb.201303071

**Thauvin-Robinet, C., Lee, J. S., Lopez, E., Herranz-Pérez, V., Shida, T., Franco, B., Jego, L., Ye, F., Pasquier, L., Loget, P. et al.** (2014). The oral-facial-digital syndrome gene C2CD3 encodes a positive regulator of centriole elongation. *Nat. Genet.* **46**, 905-911. doi:10.1038/ng.3031

**Tollenaere, M. A. X., Mailand, N. and Bekker-Jensen, S.** (2015). Centriolar satellites: key mediators of centrosome functions. *Cell. Mol. Life Sci.* **72**, 11-23. doi:10.1007/s00018-014-1711-3

**Tsai, J.-J., Hsu, W.-B., Liu, J.-H., Chang, C.-W. and Tang, T. K.** (2019). CEP120 interacts with C2CD3 and Talpid3 and is required for centriole appendage assembly and ciliogenesis. *Sci. Rep.* **9**, 6037. doi:10.1038/s41598-019-42577-0

**Tsou, M.-F. B. and Stearns, T.** (2006). Mechanism limiting centrosome duplication to once per cell cycle. *Nature* **442**, 947-951. doi:10.1038/nature04985

**Uzbekov, R. and Alieva, I.** (2018). Who are you, subdistal appendages of centriole? *R. Soc. Open Sci.* **8**, 180062. doi:10.1098/rsob.180062

**Veleri, S., Manjunath, S. H., Fariss, R. N., May-Simera, H., Brooks, M., Foskett, T. A., Gao, C., Longo, T. A., Liu, P., Nagashima, K. et al.** (2014). Ciliopathy-associated gene Cc2d2a promotes assembly of subdistal appendages on the mother centriole during cilia biogenesis. *Nat. Commun.* **5**, 4207. doi:10.1038/ncomms5207

**Vlijm, R., Li, X., Panic, M., Rüthnick, D., Hata, S., Herrmannsdörfer, F., Kuner, T., Heilemann, M., Engelhardt, J., Hell, S. W. et al.** (2018). STED nanoscopy of the centrosome linker reveals a CEP68-organized, periodic rootletin network anchored to a C-Nap1 ring at centrioles. *Proc. Natl. Acad. Sci. USA* **115**, E2246-E2253. doi:10.1073/pnas.1716840115

**Vorobjev, I. A. and Chentsov, Y. S.** (1982). Centrioles in the cell cycle. I. Epithelial cells. *J. Cell Biol.* **93**, 938-949. doi:10.1083/jcb.93.3.938

**Wang, L. and Dynlacht, B. D.** (2018). The regulation of cilium assembly and disassembly in development and disease. *Development* **145**, dev151407. doi:10.1242/dev.151407

**Wang, L., Failler, M., Fu, W. and Dynlacht, B. D.** (2018). A distal centriolar protein network controls organelle maturation and asymmetry. *Nat. Commun.* **9**, 3938. doi:10.1038/s41467-018-06286-y

**Williams, C. L., Li, C., Kida, K., Inglis, P. N., Mohan, S., Semenec, L., Bialas, N. J., Stupay, R. M., Chen, N., Blacque, O. E. et al.** (2011). MKS and NPHP modules cooperate to establish basal body/transition zone membrane associations and ciliary gate function during ciliogenesis. *J. Cell Biol.* **192**, 1023-1041. doi:10.1083/jcb.201012116

**Winey, M. and O'Toole, E.** (2014). Centriole structure. *Philos. Trans. R. Soc. B Biol. Sci.* **369**, 20130457. doi:10.1098/rstb.2013.0457

**Woodruff, J. B., Wueseke, O. and Hyman, A. A.** (2014). Pericentriolar material structure and dynamics. *Philos. Trans. R. Soc. B Biol. Sci.* **369**, 20130459. doi:10.1098/rstb.2013.0459

**Woodruff, J. B., Ferreira Gomes, B., Widlund, P. O., Mahamid, J., Honigmann, A. and Hyman, A. A.** (2017). The centrosome is a selective condensate that nucleates microtubules by concentrating tubulin. *Cell* **169**, 1066-1077.e10. doi:10.1016/j.cell.2017.05.028

**Wu, C., Yang, M., Li, J., Wang, C., Cao, T., Tao, K. and Wang, B.** (2014). Talpid3-binding centrosomal protein Cep120 is required for centriole duplication and proliferation of cerebellar granule neuron progenitors. *PLoS ONE* **9**, e107943. doi:10.1371/journal.pone.0107943

**Yadav, S. P., Sharma, N. K., Liu, C., Dong, L., Li, T. and Swaroop, A.** (2016). Centrosomal protein CP110 controls maturation of the mother centriole during cilia biogenesis. *Development* **143**, 1491-1501. doi:10.1242/dev.130120

**Yang, J., Adamian, M. and Li, T.** (2006). Rootletin interacts with C-Nap1 and may function as a physical linker between the pair of centrioles/basal bodies in cells. *Mol. Biol. Cell.* **17**, 555-1040. doi:10.1091/mbc.e05-10-0943

**Yang, T. T., Su, J., Wang, W.-J., Craige, B., Witman, G. B., Bryan Tsou, M.-F. and Liao, J.-C.** (2015). Superresolution pattern recognition reveals the architectural map of the ciliary transition zone. *Sci. Rep.* **5**, 14096. doi:10.1038/srep14096

**Yang, T. T., Chong, W. M., Wang, W.-J., Mazo, G., Tanos, B., Chen, Z., Tran, T. M. N., Chen, Y.-D., Weng, R. R., Huang, C.-E. et al.** (2018). Super-resolution architecture of mammalian centriole distal appendages reveals distinct

blade and matrix functional components. *Nat. Commun.* **9**, 2023. doi:10.1038/s41467-018-04469-1

**Ye, X., Zeng, H., Ning, G., Reiter, J. F. and Liu, A.** (2014). C2cd3 is critical for centriolar distal appendage assembly and ciliary vesicle docking in mammals. *Proc. Natl. Acad. Sci. USA* **111**, 2164-2169. doi:10.1073/pnas.1318737111

**Zhang, D. and Aravind, L.** (2012). Novel transglutaminase-like peptidase and C2 domains elucidate the structure, biogenesis and evolution of the ciliary compartment. *Cell Cycle* **11**, 3861-3875. doi:10.4161/cc.22068

**Zitouni, S., Francia, M. E., Leal, F., Montenegro Gouveia, S., Nabais, C., Duarte, P., Gilberto, S., Brito, D., Moyer, T., Kandels-Lewis, S. et al.** (2016). CDK1 prevents unscheduled PLK4-STIL complex assembly in centriole biogenesis. *Curr. Biol.* **26**, 1127-1137. doi:10.1016/j.cub.2016.03.055

**Zou, C., Li, J., Bai, Y., Gunning, W. T., Wazer, D. E., Band, V. and Gao, Q.** (2005). Centrobin: a novel daughter centriole-associated protein that is required for centriole duplication. *J. Cell Biol.* **171**, 437-445. doi:10.1083/jcb.200506185